Technische Universität München

Fakultät für Chemie

Arbeitskreis für Synthese und Charakterisierung innovativer Materialien

Synthesis and Characterization of Advanced Functional Materials for Photocatalytic Applications

Ebru Alime Üzer

Vollständiger Abdruck der von der Fakultät für Chemie der Technischen Universität München zur Erlangung des akademischen Grades eines

Doktors der Naturwissenschaften (Dr. rer. nat.)

genehmigten Dissertation.

Vorsitzender: Prof. Dr. Thomas Fässler

Prüfer der Dissertation:

1. Prof. Dr. Tom Nilges
2. Prof. Dr. Markus Becherer

Die Dissertation wurde am 12. Juni 2019 bei der Technischen Universität München eingereicht und durch die Fakultät für Chemie am 27.06.2019 angenommen.

Nothing in life is to be feared, it is only to be understood.
Now is the time to understand more, so that we may fear less.
Marie Skłodowska Curie

Danksagung

Hiermit danke ich Herrn Prof. Dr. Tom Nilges für die interessante Themenstellung dieser Arbeit, sein Engagement, die wissenschaftliche Unterstützung, sowie die vielen wertvollen Anregungen während der Ausführung dieser Arbeit. Darüber hinaus danke ich ihm dafür, mir beigebracht zu haben wie man mit einer wissenschaftlich aufgeschlossenen Haltung Freude und Zielstrebigkeit vereinen und gleichzeitig erfolgreiche Ergebnisse erzielen kann. Maßgeblich an dieser schönen Zeit beteiligt waren seine derzeitigen und ehemaligen Gruppenmitglieder und Mitarbeiter Claudia Ott, Dr. Ilona Krüger, Dr. Katharina Freitag, Anna Vogel, Annabelle Degg, Felix Reiter, Patrick Walke, Markus Pielmeier, Dr. Maximilian Baumgartner, Dr. André Utrap, Dr. Carolin Grotz, Dr. Daniela Pfister, Dr. Franziska Baumer, Dr. Stephanie Bretzke, Dr. Konrad Schäfer, Laura Meier, Carolin Rulofs, Vera Kragl und vor allem Lucia Weissenborn.

Ich bedanke mich auch bei meinen Forschungspraktikanten Anna Vogel, Stephan Hettich, Dominik Staude, Julian Wennmacher, Philip Lang und Daniel Baranowski für die gelungene Zusammenarbeit.

Mein weiterer besonderer Dank gilt:

- Herrn Prof. Dr. Karthik Shankar für die maßgebliche Betreuung und eine stetige wissenschaftliche Unterstützung in seiner Arbeitsgruppe während der Zeit an der UofA in Kanada, insbesondere seinen Mitarbeitern Dr. Pawan Kumar, Ryan Kisslinger, Ujwal Kumar Thakur, Arezoo Hosseini, und Dr. Piyush Kar für eine gute und stets interessante Zusammenarbeit

- Herrn Dr. Mar und seiner Arbeitsgruppe, besonders Dr. Abishek Iyer, Dr. Anton Oliynyk, Dr. Yuqiao Zhou, Dr. Lawrence Adutwum, Alex Gzyl, Dong Zhang, Vidyanshu Mishra und Dundappa Mumbaraddi, bei denen ich eine wissenschaftlich interessante und erfreuliche Zeit verbringen durfte

- Herr Prof. Dr. Fässler für die angenehme Zusammenarbeit der gemeinschaftlichen Arbeitsgruppen, insbesondere Manuela Donaubauer, Lorenz Schiegerl und Kerstin Mayer

- den ATUMS-Gründern und Organisatoren: Prof. Dr. Bernhard Rieger, Prof. Dr. Jonathan Veinot, Dr. Sergei Vagin, Dr. Carsten Troll und Leah Veinot

- den weiteren ATUMS-Mitgliedern Prof. Dr. Markus Becherer, Dr. Alina Lyuleeva, Joseph Mock, Prof. Dr. Frank Hegmann, David Purschke, Mary Narreto,

Prof. Dr. Martin Stutzmann, Andreas Zeidler, Felix Eckmann, Hannah Schamoni, Reka Csiki; Prof. Dr. Marc Tornow, Maximilian Speckbacher, Simon Pfähler; Prof. Dr. Job Boekhoven, Raphael Grötsch, Dr. Tobias Helbich, Dr. Arzu Angı, Marc Kloberg, Prof. Peter Müller-Buschbaum, Dr. Nuri Hohn und Dr. Aras Kartouzian für das große Vergnügen an der wissenschaftlichen Zusammenarbeit und der gemeinsamen Zeit während Tagungen, Konferenzen, Seminaren und der Zeit in Kanada

- Meinen ehemaligen Kollegen Andreas Tosstorff und Christoph Mähler für eine erfreuliche Zeit im Studium

- den Organisatoren des IGSSE-Teams

Meiner Familie, vor allem meiner Mutter danke ich dafür, dass sie mir bis dahin und währenddessen einen ausgesprochen liebevollen und finanziell sorgenfreien Weg bereitet haben.

Bei meinen Freunden möchte ich mich für die vielen fantastischen Momente und die wertvolle Unterstützung bedanken.

Außerdem danke ich der Naturwissenschaft, da es niemals langweilig mit ihr wurde.

Kurzfassung

Um die zukünftige Energieversorgung mit nachhaltiger und regenerativer Stromgewinnung sicherzustellen, beschäftigt sich ein großer Teil der heutigen Wissenschaft und Forschung mit der Entdeckung und Verbesserung bereits bestehender Materialien. In der vorliegenden Arbeit werden moderne Halbleitermaterialien und ihre optischen und elektronischen Eigenschaften dargestellt und optimiert. TiO_2-Nanoröhren werden bereits in der Farbstoffsolarzelle, auch Grätzel-Zelle genannt, industriell in photovoltaischen Anlagen verwendet. Sie besitzen die Fähigkeit, Lichtenergie in elektrische Energie umzuwandeln. Des Weiteren werden elektrochemisch anodisierte TiO_2-Nanoröhren in Photosensoren und zur photo-katalysierten Wasserspaltung eingesetzt. Aufgrund der begrenzten Absorptionsfähigkeit von TiO_2-Nanoröhren und zur Verbesserung der Generierungs- und Rekombinationsprozesse von Ladungsträgern werden Hybridmaterialien hergestellt. Hierzu werden 2D- und quasi-1D-phosphorbasierte Halbleiter (SnIP, $(CuI)_3P_{12}$, NaP_7, faserförmiger P, schwarzer P) mit einer angemessenen Ladungsträgermobilität sowie einem geeigneten optischen Bandlückenbereich (1.0 – 2.7 eV; 3.2 eV in TiO_2 Anatas) eingesetzt. Um einen geeigneten Kontakt zum Ladungsträgertransport zwischen Anatas und den jeweiligen 2D- und quasi-1D-Materialien herzustellen, wurde mithilfe einer Gasphasenabscheidung ein Heteroübergang erzeugt. Die resultierenden Bandlücken der Hybridmaterialien wurden ermittelt und der jeweilige Heteroübergang nach Angleichung der Ferminiveaus schematisch dargestellt. Die Anwendungsmöglichkeit der Hybridmaterialien wurde in der photo-katalytischen Wasserspaltung getestet. Hier stellt faserförmiger P die besten Abscheidungseigenschaften auf und innerhalb TiO_2-Nanoröhren dar. Das SnIP@TiO_2-Hybridmaterial weist die höchste photo-katalytische Aktivität auf. Außerdem werden die drei Seltenerd-Chalcogenid-Halogenide $RE_3Ge_2S_8I$ (*RE* = La, Ce, Pr) dargestellt. An diesen Verbindungen wurden Untersuchungen zum Kristallsystem und den optischen und magnetischen Eigenschaften durchgeführt. $RE_3Ge_2S_8I$ (*RE* = La, Ce, Pr) kristallisieren im monoklinen Kristallsystem der Raumgruppe *C*2/*c* und besitzen paramagnetische Eigenschaften. Verbindungen mit schweren Elementen zeigen aufgrund ihrer elektronischen Struktur häufig schmale Bandlücken. Ein Strukturmerkmal dieser gemischt-anionischen-Verbindungen ist die Überlappung der Halogenid- und Chalcogenid-Orbitale und eine resultierende Erweiterung der optischen Bandlücken. Dies konnte anhand von experimentellen Messungen bestätigt werden.

Abstract

To meet present needs in sustainable and regenerative energy systems, a great number of scientists are working on new advanced materials or optimization of currently used systems. This thesis focusses on synthesis and characterization of advanced semiconductors and their optical and electronic properties. Optimization and performance tests for application devices were carried out after. TiO_2 nanotubes, which are currently used in dye-sensitized solar cells are able to convert light to energy. Additionally, electrochemical anodized TiO_2 nanotubes are used as photosensors and for photocatalytic water splitting. In order to improve their light absorbing, charge carrier generation and recombination qualities, hybrid materials together with 2D- and quasi-1D-phosphorus-based semiconductors (SnIP, $(CuI)_3P_{12}$, NaP_7, fibrous red P, black P) were fabricated. To create a contact for charge carrier transport in between these materials, vapor transport reaction was used as a suitable technique. Their optical band gaps (1.0 - 2.7 eV for phosphorus-based materials and 3.2 eV for TiO_2 anatase) and charge carrier properties are promising features to generate a hybrid heterojunction system. Several characterization methods were applied to show resulting bandgaps and schematic Z-schemed band gap alignment of the hybrid materials. Straightforward transport of fibrous red P onto and into TiO_2 nanotube arrays *via* gas-phase showed most effective deposition results, whereas SnIP@TiO_2 hybrid material demonstrated highest photocatalytic performance. Furthermore, three new rare-earth chalcogenidehalide were synthesized and characterized. $RE_3Ge_2S_8I$ (*RE* = La, Ce, Pr) crystallizes monoclinically, in space group *C*2/*c*. Optical and magnetic characterization was performed, showing paramagnetism and, in contrast to other heavy element compounds, wide band gaps. However, this can be explained by structural characteristics of chalcogenidehalide-mixed-anion compounds, with halides disrupting the extensive orbital overlap of chalcogenides.

Declaration

This dissertation is written as a publication-based thesis. Relevance, scope and motivation of this work for science and research are given as introductory part in section 1. The experimental details in section 2 give information on the synthesis, characterization and computational methods of materials. Bibliographic data of articles published in peer-reviewed journals are presented in section 3. This section includes each manuscript, a summary as well as results, discussions and clarification of the author´s contributions to the respective work. An overall summary and outlook are given in section 4.

Abbreviations and Symbols

1D	One-dimensional
AES	Auger Electron Spectroscopy
AFM	Atomic Force Microscope
CB	Conduction band
CCD	Charge-coupled device
CIGS	Copper indium gallium (di)selenide
Q_n	Constant phase element
CPD	Contact potential difference
DR	Diffuse Reflectance
DSSC	Dye-sensitized solar cell
EDS	Energy Dispersive X-ray Spectroscopy
EIS	Electrochemical Impedance Spectroscopy
eV	Electronvolt
FIB	Focused ion beam
FTO	Fluorine-doped tin oxide
GC	Gas chromatography
HIM	Helium Ion Microscope
HOMO	Highest occupied molecular orbital
HOPG	Highly ordered pyrolytic graphite
KPFM	Kelvin Probe Force Microscopy
LDA	Local-density approximation
LED	Light-emitting diode
LMTO	Linear muffin-tin orbital
LUMO	Lowest unoccupied molecular orbital
Nd:YAG	Neodymium-doped yttrium aluminum garnet
NHE	Normal hydrogen electrode

PEC	Photo-electrochemical cell
RE	Rare-earth
RT	Room temperature
SEM	Scanning Electron Microscopy
STEM	Scanning Transmission Electron Microscopy
UPS	Ultraviolet Photoelectron Spectroscopy
UV-Vis	Ultraviolet-visible
VB	Valence band
XPS	X-ray Photoelectron Spectroscopy
Θ	Scattering angle
λ	Wavelength
μ_B	Magnetic moment
ω	Angular frequency

Table of Contents

1. Introduction

Our current climatic conditions are not only demanding to eliminate conventional sources, as Germany decided to no longer obtain energy from nuclear power (in 2022)[1] and coal (planed in 2038)[2], but along with this resolutions, financial circumstances associated with withdraws of economic and governmental investments oblige us to act fast. In 2008 the price of an RWE share reached 100 € and decreased to currently 24 € induced by Fukushima and following crisises.[3] But the European Commission presented a multi-annual financial framework for supporting climate protection with 29.7% of the entire budget (1.14 Mrd. €) from 2021-2027.[4] The energy production from renewable energies in 2015 amounted 26.3% and still 44.3% are still produced with coal sources.[5] In this light, a drastic development has to be achieved within the upcoming 23 years to fulfill the necessary intentions. Despite the fact that Germany is densely populated and open-fields for photovoltaic systems are limited, it is the third most used source of renewable energies, after wind and biomass energy.[6] By the end of 2018, photovoltaic modules provided a power rating of 45.9 GW in Germany.[7] If we would aim to cover our energy demands mainly or entirely by alternative sources by 2050 with 150-200 GW from solar systems (hence further 4-5 GW annually), new devices have to be installed and already existing ones need to be re-engineered in terms of their performance.[8-9] Advanced functional materials such as nanoengineered semiconductors approach such demands as their advanced properties can be employed under primary or application-optimized conditions.

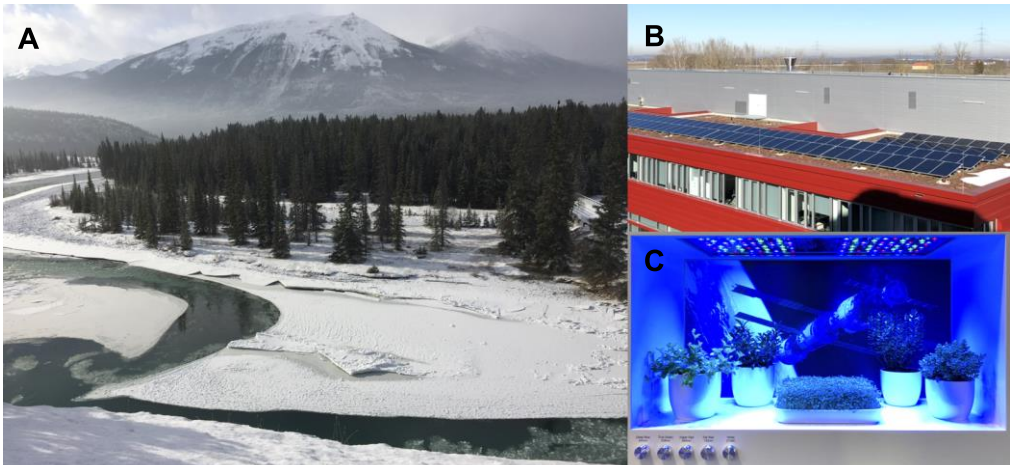

Figure 1. A) View on pristine nature in Jasper, Canada. B) Photovoltaic installation in Garching, Germany. C) Urban farming LED system for location-independent vegetable and fruit cultivation.

1.1. Advanced Functional Materials in Renewable Solar Energy Applications

The industrial efficiencies of semiconducting advanced functional materials used in solar cells were measured to be 26.7 ± 0.5% for mono- and 22.3 ± 0.4% for poly-crystalline silicon, 21 - 34% for thin film solar modules (CdTe/ GaInAsP/ GaInAs), 22.9 ± 0.5% for thin film solar cells (CIGS) and 11.9 ± 0.4% for dye-sensitized solar cells in 2019.[10] Dye-sensitized solar cells (DSSC), namely third generation solar cells, are composed of a dye coated porous layer of titanium dioxide nanoparticles (see Figure 1.1-1).[11] Titanium dioxide (anode) is immersed in a conducting electrolyte solution and bordered by a platinum catalyst (cathode). To enhance the DSSCs performances, one option is to activate the photocatalytic qualities of TiO_2. After absorption of visible light in the dye layer the electrons are excited from HOMO to LUMO level, followed by a transfer to the TiO_2 conduction band (CB). Losses during the following recombination step and insufficient visible light absorbing qualities can be reduced after careful investigation of the electronic and optical TiO_2 properties and optimization within the scope of application aspect.

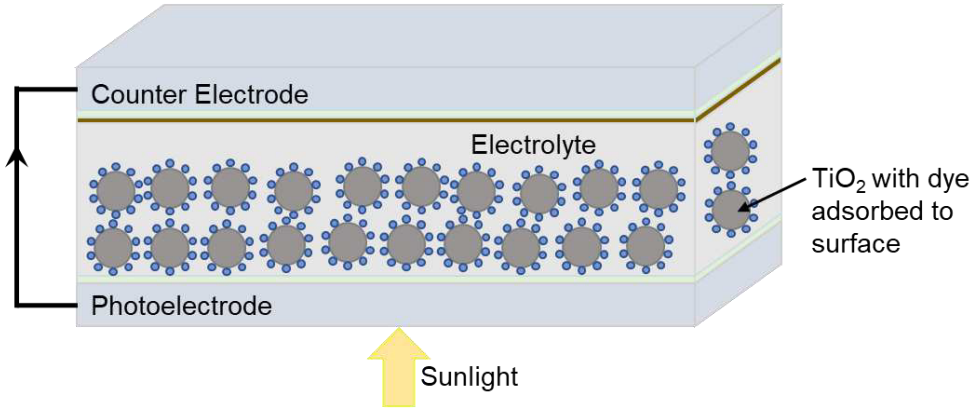

Figure 1.1-1. Schematic illustration of a dye-sensitized solar cell (Figure as described in Cit. 11).

In general, key factors such as charge transport, trapping and recombination can affect the performances and properties of optoelectronic devices. Attributed to its high surface area and orthogonalized processes of photocarrier generation and charge separation especially in highly ordered nanotube arrays, TiO_2 is used in further optoelectronic applications such as sensors, photo-electrochemical cells (PEC) (see Figure 1.1-2, left side) and photocatalysts.[12-14]

Instead of solar light to energy conversion in photovoltaic systems, materials employed for photocatalytic processes absorb light of characteristic wavelength for photoelectrochemical reactions in the presence of a co-catalyst. The photocatalytic splitting of

water into hydrogen and oxygen using TiO_2 as a photocatalyst is another example producing fuel cells from renewable energy sources. Initial significant investigations were reported by Fujishima and Honda in 1972.[15] The common principles of photovoltaic and electrochemical photocatalytic processes are photon absorption to excite electrons of sufficient lifetime from valence band (VB) to CB of a semiconductor, carrier separation of excited electrons and defect electrons (holes) followed by using the excitation energy for reduction and oxidation processes in the electrolyte (see Figure 1.1-2, right side).[16-17]

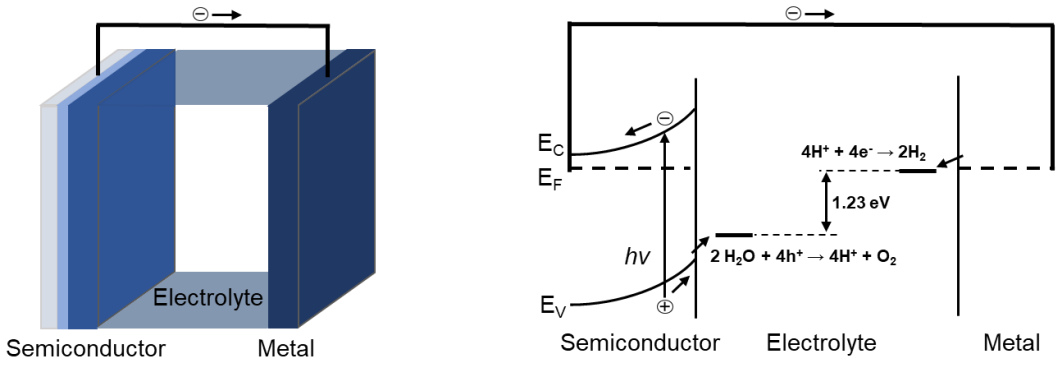

Figure 1.1-2. Left side: Schematic representation of a photoelectrochemical cell consisting of semiconductor photoanode and metal cathode. Right side: Corresponding oxidation and reduction reaction generating O_2 and H_2 in the electrolyte during light illumination (Figure as described in Cit. 17).

After photon absorption, the electrons of an occupied VB in a semiconductor need to overcome a suitable energy gap to be promoted to the CB. The precise energy of the respective band gap can be employed for further reaction sequences. In regard to harvesting an optimum amount of the electromagnetic solar radiation, crystalline Si with a band gap energy of 1.1 eV is used as photovoltaic standard material.[18] A great amount of the solar radiation can be absorbed but only the equivalent band gap energy is exploited by the intrinsic semiconductor. Titanium(IV)-oxid inhibits a large band gap energy for both polymorphs rutile (3.12 eV) and anatase (3.2 eV) and is used as standard anode material in photoelectrochemical cells mainly in anatase modification by reason of its advantageous photocurrent performance.[19-21] However, photon absorption of TiO_2 anatase is limited to short-wave components of the solar spectrum.

A first step for generation of hydrogen from water is bringing an *n*- or *p*-type semiconductor into contact with an electrolyte, both possessing dissimilar Fermi levels or electrochemical potential. In the case of PEC water oxidation the *n*-type semiconductor TiO_2 anatase complies with these requirements to transport charge carriers across the semiconductor-electrolyte interface as its VB energy lies electrochemically above (cathodic) the hydrogen potential (H^+/H_2; 0 V vs. normal hydrogen electrode (NHE) at pH = 0) and CB energy lies electrochemically below (anodic) the oxygen potential (H_2O/O_2 1.23 V vs.

NHE) (see Figure 1.1-2).[22] An utilization of TiO_2 nanotubes due to its high surface area, short travel distance to surface, orthogonalized processes of photocarrier generation and charge separation is noteworthy at this point.[23] An exchange of charge carriers creates a space charge layer in the semiconductor-electrolyte interface and band bending at the *n*- or *p*-type electrode surface. Under illumination of sunlight, a splitting to quasi-Fermi levels for building minority and majority charge carriers leads to separation through a built-in electric field and reduction of the redox system at the *p*-electrode (in this case metal counter electrode) and oxidation at the *n*-electrode (Figure 1.1-3).[17, 24] Therefore, electron-hole pairs of sufficient lifetimes have to be constituted. For successful water oxidation in a PEC a sufficient photovoltage has to be greater than the potential difference for water electrolysis, which corresponds to thermodynamic decomposition voltage of water (1.23 V). In addition to this value, diffusion-overpotential to yield sufficient current density and material-dependent kinetic overpotential to bridge the activation barriers have to be taken into account.[25] A further emerging parameter is electric potential of resistances, occurring at the semiconductor-electrolyte- and cell-contact-interfaces which have to be studied.[25] A set-up of a PEC, investigating the relevant charge-transport properties will be presented in detail in section 3.1 and 3.2 of this thesis.

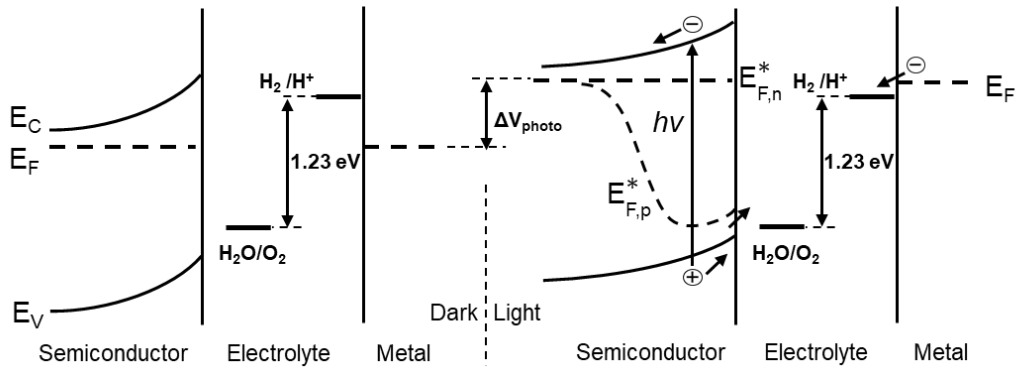

Figure 1.1-3. PEC cell with *n*-type semiconductor photoanode and metal cathode under equilibrium (left side) and illumination of light (right side) with splitting of Fermi levels to quasi-Fermi levels for charge carrier transport through semiconductor-electrolyte interface for water oxidation reactions (Figure as described in Cit. 17).

Considering the so far stated efficiency restricting effects, TiO_2 anatase nanotubes can be improved by engineering the semiconductor's optical and electrical properties but have to be approached carefully retaining its fundamental beneficial characteristics. A functional modification by hybrid heterojunction formation at the interface to another semiconductor is one way to modify TiO_2 nanotubes in such way, that its advantageous high surface area and high electron mobility can be preserved.[26] Heterojunction systems are already established in successful photoelectrochemical water splitting reactions, e.g. in nanostructured $WO_3/BiVO_4$ thin films through solvothermal deposition on fluorine-doped tin oxide (FTO) glass or Fe_2O_3/graphene/$BiV_{1-x}Mo_xO_4$ core/shell nanorods by

hydrothermal deposition onto Ti-substrate.[27-28] In this work, a novel type of inorganic semiconductor heterojunction with structural advanced functional materials possessing structural features and tunable electrical and optical properties, are introduced and discussed in section 1.2. and 1.3. Section 1.2. 'Heterojunction in Advanced Functional Materials' concentrates on band gap alignment of both semiconductors which needs to be carefully manufactured. For successful alignment, band gap energies have to be compatible which will be further discussed in section 1.3. 'Size effects in Advanced Functional Materials'.

1.2. Heterojunction in Advanced Functional Materials

After applying photovoltage in a PEC cell band bending of the photoanode at the semiconductor-electrolyte interface occurs and must remain in existence to inhibit electron-hole recombination as well as hydrogen and oxygen generation reactions in the electrolyte. An efficient way to enhance charge separation, while light harvesting and charge carrier transport across the semiconductor-electrolyte interface will not be affected, is to create a Z-schemed *p*/*n*-junction between the *n*-type semiconductor TiO_2 anatase and a *p*-type semiconductor. Therefore, the relative alignment of the heterostructure bands needs to be investigated during hydrogen generation reactions: Determination of whether CB edge of one semiconductor lies above or below the other can be obtained with respect to one value. This value is usually discerned as vacuum level energy and other energy levels are referred to it. Vacuum level energy is considered as the energy of a free stationary electron that is outside the semiconductor (green line in Figure 1.2).[29] Depending on the position of VB and CB of each semiconductors a band alignment can form either a *n*/*n*-, *p*/*p*- or *p*/*n*-type heterojunction due to charge redistribution in the depletion region, meaning depletion of majority carriers, in presence of an electric field a corresponding electrostatic potential. In contrast to junction systems, which can occur intrinsically, a heterojunction formation emerges between two distinct materials. Current PEC systems often use different electronic components biased to the photoanode to enhance the photoactive properties. In that case the photoanode is applied to a biased voltage with an integrated *p*/*n*-junction.[30]After creating a hybrid TiO_2 nanotube array heterojunction with another semiconductor, the photoanode is comprised of one constituent material and further loss of charge carriers can be avoided. During a p/n-junction electrons flow from *n*- to *p*-type semiconductor and holes from *p*- to *n*-type semiconductor while Fermi levels align. At the same time a downward band-bending of the *p*-type material and upward band-bending of the *n*-type material occurs (see Figure 1.2). A detailed determination of Fermi level alignment of the title compounds (TiO_2 nanotubes; P

allotropes and poylphosphides) with calculated energy values will be given in section 3.1. and 3.2. of this thesis.

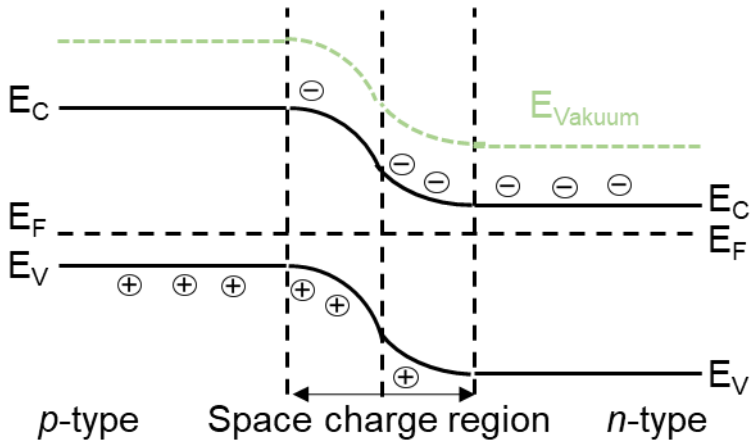

Figure 1.2. A p/n-Heterojunction semiconductor heterostructure with space charge region after depletion of majority carriers resulting in electron-flow from *n*- to *p*-type material and holes from *p*- to *n*-type material (Figure as described in Cit. 31). Referring vacuum level is highlighted as green line.

1.3. Size effects in Advanced Functional Materials

Attempts to change optical and electrical properties can be induced by changing the surface or the mere size of intrinsic semiconductors. Over recent decades, a reduction of semiconductor sizes was aimed for environmental, biomedical, electrical and photochemical applications. The sizes were cut down to two-dimensional materials in layers, thin films or stacks of thin films, to one-dimensional materials in nanorods, -tubes, and -fibers, and to zero-dimensional materials in nanoparticles.

Basic approaches to understand three dimensional semiconductors with intermolecular interactions and intramolecular bonding energies can consequently be altered because of electronic property changes by considering nanoparticles as isolated objects. The electronic excitation in a nanosized particle is fundamentally different to its periodic counterpart. While for a periodic system the energy is considered continuously, for finite atom systems the energy is discretized with individual energy levels only populated by a single electron in line with Pauli's principle (Figure 1.3-1).[32-33]

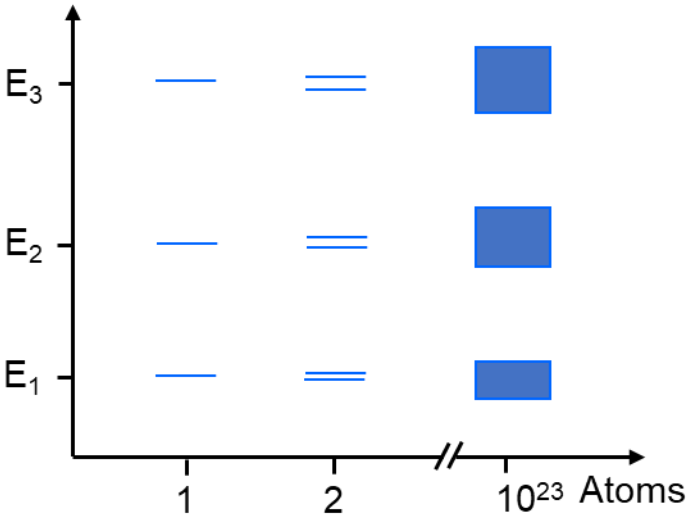

Figure 1.3-1. Energy levels for one atom and energy level transitions to a molecule consisting of two, three up to 10^{23} atoms in a molecule (Figure as described in Cit. 33).

In bulk crystals with composition-dependent energy bands a minimum energy for electronic excitation from the highest occupied VB level to lowest unoccupied CB (E_g, Figure 1.3-2) needs to be overcome. A resulting difference of individual to 'quasi-continuous' energy levels leads to a blue shift with decreasing particle size after absorption and emission of light.[34]

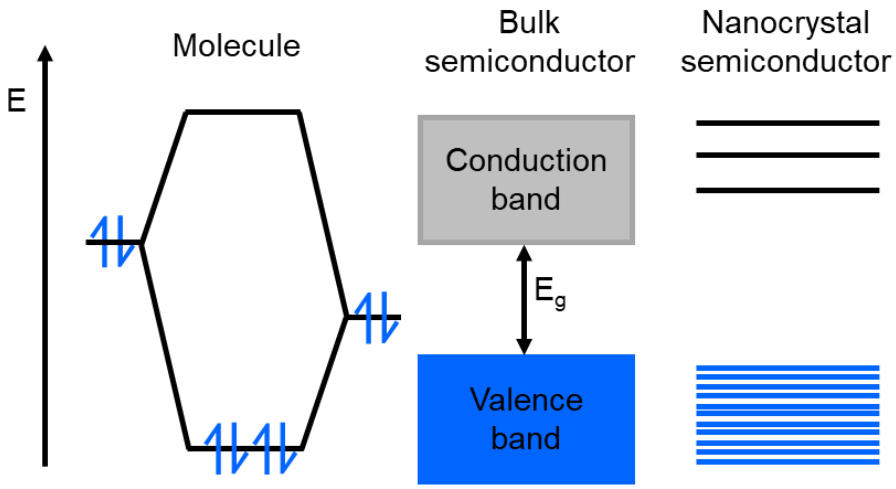

Figure 1.3-2. Electronic energy states of a molecule (left), discrete energy levels in semiconductor nanocrystals (center) and quasi-continuous energy levels in a bulk semiconductor with energy E_g for electronic excitation (right), (Figure as described in Cit.35).

The subsequent assumptions were mainly exerted from Cit. 30 (*Section 18. Nanostrukturen*), Cit. 34 (*Section 9. Optical Properties of Nanoparticles*), Cit. 35, Cit. 37. After interaction of nanosized crystals with light electronic excitation occurs creating orbital holes in the VB and excitons emerge. Excitons represent electrostatically bound electron-hole pairs in their minimum energy state.[35] The excitons Bohr radius increases

linearly with the dielectric constant of the materials and ranges from 0.1 nm to several nm.[35] If the exciton diameter is larger than the nanocrystal axis, quantum confinement, representing one of the most crucial effects in band gap engineering occurs.[37] Quantum confinement can be demonstrated by describing nanoparticles (charge carriers, excitons, electrons) as 'particle in a box with infinitely high walls' and the size of the quantum box is smaller than the particle's Bohr radius. The walls of this quantum box can be illustrated as energy barriers of higher potential energy (walls) than the nanoparticle energy and therefore can be crossed by electron tunneling.[34] Energy barriers of insulators are infinitely high but with decreasing potential the electron wave function describes a finite probability of tunneling through the barriers (Figure 1.3-3; left side).[34, 37] This effect results in a transition from continuous to discrete energy levels as well. In consequence a decrease of materials to nano-size show different energy levels and therefore change in absorption spectra in case of irradiation with light.

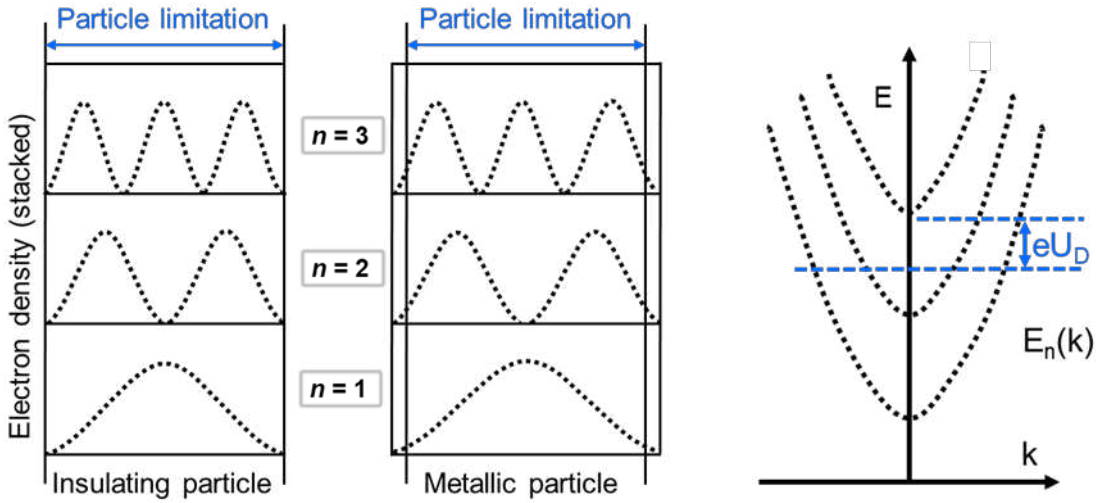

Figure 1.3-3. Left side: Electron density distribution for quantum levels 1, 2 and 3 considering a metallic nanoparticle as 'particle in a box'. There is zero probability of finding an electron outside the particle of an insulator, regardless of the quantum level, whereas in a metallic nanoparticle, surrounded by electrons, an electron can be located at a space outside the particle through tunneling effects.[34] Right side: Dispersion relations and density of sub-band states of a quasi-1D-nanofiber considered as a rectangular box, describing a parabolic in-plane dispersion (Figure as described in Cit. 30, 38).

Modification of material sizes not only affects energy level distances but also shapes, which play a role in the electron and hole relaxation pathways. To establish a determination of each individual quantized sub-band states it is useful to picture the structural changes going from regular 3D-compounds to 2D-layered and quasi-1D-fiber type materials. To understand these changes resulting from limitation of electron dispersion in individual sub-bands to two or one spatial dimensions a mathematic approach can be expressed by effective mass approximation and without taking electron-electron interactions into account. The simplest demonstration material for these approximations are quasi-1D-nanofibers where two of the three dimensions are reduced to nanoscales

similar to a rectangular box. The derivation of the Eigenstates can be simplified analog to a particle in a box.[36] Therefore, energy $\epsilon_{i,j}$ and wave function $\Psi_{i,j}(x,y)$ of quasi-1D-nanosized crystals characterized by main orientation in z-axis are described as in eqt. 1.[30]

$$\boldsymbol{\epsilon = \epsilon_{i,j} + \frac{\hbar^2 k^2}{2m}} \quad , \qquad \boldsymbol{\Psi(x,y,z) = \Psi_{i,j}(x,y)e^{ikz}} \tag{1}$$

Eigenstates x, y are defined by the quantum numbers *i*, *j* and z-axis is defined by the wave vector *k*.[30] The zero point energy $\epsilon_{i,j}$ is the energy at the bottom of the conduction sub-band and under these conditions they describe a parabolic in-plane dispersion of sub-band density of states (Figure 1.3-3; right side).[30, 39] The parabolic electron density of states is effecting optical absorption and emission as electron- and hole-relaxation to the lower sub-band side followed by a fast recombination or luminescence.[30]

Inorganic Nanosized Semiconductors

The above-mentioned one-dimensional structural features can be found in the first atomic-scale inorganic double helix **SnIP**. The compound has a minimum of recombination energy at 1.86 eV (direct band gap) and a shoulder at 1.80 eV (indirect band gap) derived from photoluminescence measurements at RT.[40] The dimensionality of SnIP can be decreased from 3D to quasi-1D by chemical delamination destruction-free up to 20 nm in width.[40] It can be synthesized in a gas-phase transport reaction from the elements.[40] Another compound of the Sn-I-P ternary phase diagram is the Zintl-phase $Sn_{24}P_{19.3}I_8$, first published by Shevelkov *et al.*[41] $Sn_{24}P_{19.3}I_8$ adopts clathrate-I type structure showing a relatively narrow band gap.[41] The quasi-1D-SnIP is crystallizing monoclinically, in space group *P*2/*c* (Nr.13) and exhibits highly anisotropic structural features with inner $^1_\infty[P^-]$- (0.32 nm) and outer $^1_\infty[SnI^+]$- (0.98 nm) helices spinning in equal directions (see Figure 1.3-4; A).[42] Electron conductivity measurements in nanofiber-direction showed 2 – 3 $\mu S \cdot m^{-1}$ at ~3 µm length and a bundle diameter of 400 – 500 nm.[40] Considering crystal bending defects, dopants or SnIP in hybrid materials can be a solution to improve the materials properties.

Further examples for ternary nano-compounds are **$(CuI)_3P_{12}$**, $(CuI)_2P_{14}$ and $(CuI)_2P_3$. Quantum-chemical computational methods on these compounds identified the following structural characteristics.[43-46] $(CuI)_3P_{12}$, $(CuI)_2P_{14}$ and $(CuI)_2P_3$ structures can be described as single P chains, related to those of Hittorf´s and Ruck´s fibrous phosphorous coordinated by a CuI-matrix.[43, 47] According to Baudler's rules the polyphosphide

substructures can be described as $^{1}_{\infty}([P10]P2[])$ in $(CuI)_3P_{12}$ (see Figure 1.3-4; B), $^{1}_{\infty}([P12(4)]P2[])$ in $(CuI)_2P_{14}$ and $^{1}_{\infty}([P8]P4(4)[])$ in $(CuI)_2P_3$.[43, 48-50] A band gap range of single isolated phosphorus chains was calculated to be 2.3 – 2.7 eV instead of 1.0 – 1.1 eV in bulk material with CuI-matrix.[43] Downsizing of particles leads to quantum confinement effects. Therefore, synthesis of these single strands can cause additional changes in electron mobility. Up to now single P chains of $(CuI)_3P_{12}$ and $(CuI)_2P_3$ allotropes were experimentally obtained without CuI-matrix, but only in an amorphous state.[51] The bulk compounds crystalize after gas-phase reactions. These polyphosphide strands could be fabricated in hetero-structured hybrid materials by support of TiO_2 nanotubular walls.

NaP_7 is a representative binary compound containing a phosphorus-rich substructure. In line with Baudler's rules $^{1}_{\infty}[P_7^-]$ -units are coordinated helically by two Na per P_7-unit (see Figure 1.3-4; C).[48, 52] The compound crystallizes tetragonally, in space group *I*4_1/*acd* after short way transport reaction from the elements using CuI as mineralizer additive.[52] Single NaP_7 strands are 0.71 nm in diameter.[52] Quantum-chemical LDA-calculations show a band gap of 1.71 eV which is in well agreement with the crystal's red-colored appearance. An electric conductivity of 1.12 µS·cm^{-1} was measured at RT.[52] Both of the latter properties can be modified in a heterostructure system.

An elemental phosphorus allotrope with nanofibrous structures is **fibrous red P**. It crystallizes at elevated temperatures using iodine as a transport mineralizer additive as first known triclinic modification of phosphorus, in space group $P\bar{1}$ (Nr. 2).[47] A short way transport reaction with Cu-halides as transport agent improved crystallization to stable and metastable phases and lead to phase pure synthesis.[53-55] According to Baudler's rules infinite $^{1}_{\infty}([P8]P2[P9]P2[])$ -chains are arranged in tubes with pentagonal cross section, in altering cages of eight and nine subunits (see Figure 1.3-4; D).[47] Band gaps were found to be in the range of 1.4 – 2.0 eV.[56] Investigations as potential water splitting agent showed steady hydrogen evolution rates of 633 µmol h^{-1} g^{-1} and 684 µmol h^{-1} g^{-1} and might be improved by modification of the electrical and optical properties.[57]

2D-nanostructures such as the phosphorus allotrope **black P** crystallizes orthorhombically, in space group *Cmce*.[58] A high carrier mobility due to in-plane anisotropy (see Figure 1.3-4; E) was found.[58] Black P is a *p*-type semiconductor and was applied in field effect transistors, photodetectors and sensors.[59-61] The electronic properties are layer number dependent as they change band gap and carrier mobility upon exfoliation to

single and bilayer sytems.[62] Its bulk material shows a direct band gap of 0.3 eV changing to 0.86 eV for four layered black P and to 1.54 eV for the monolayer sample called phosphorene.[63-65] A layer-dependent hole carrier mobility results in values of ca. 10^5 cm^2 $V^{-1}s^{-1}$.[66] In order to make use of this structural attribute, a decoration of the TiO_2 nanotube arrays which are frequently applied in industrial techniques can tune each individual features.

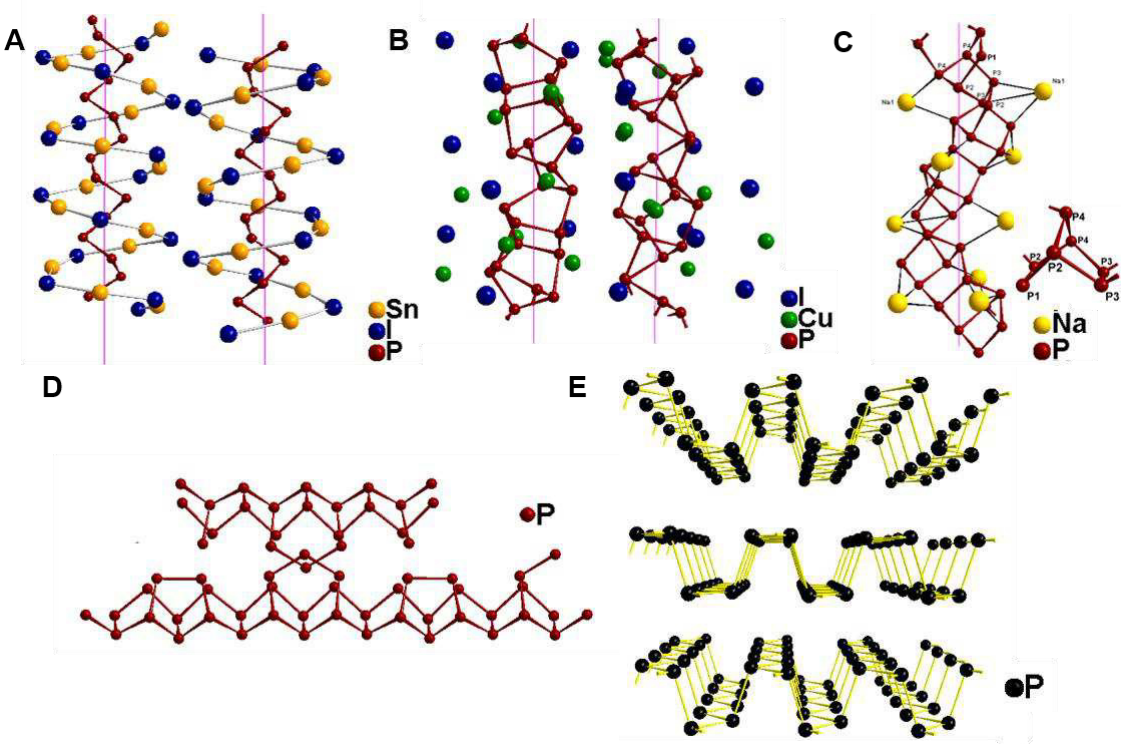

Figure 1.3-4. Crystal structure sections of A) SnIP and B) $(CuI)_3P_{12}$ with two representative strands, C) NaP_7 with representative Na-coordinated polyphosphide substructure, D) fibrous red P and E) black P.

1.4. Chemical Vapor Transport Method for Heterojunction Formation

In long range order crystalline materials heterojunction formation can only be exercised by elaborating processes to match lattice parameters, i.e. by epitaxial growth. In order to create a charge carrier contact *via* heterojunction between TiO_2 nanotubes and aforementioned compounds (see Figure 1.3-4) a simple surface deposition through gas-phase synthesis can be conducted. A coordination between surface atoms to metal centers can lead to band gap alignment and was previously corroborated in the groups of Marks and Hersam *et al.* and further research groups.[67-68] In this way, amorphous TiO_2 nanotubes can crystallize while preferable island-like surface coverage by phosphorus allotropes and polyphosphides is formed in a single synthesis step within the same temperature region (shown in Figure 1.4-1; left side). This particular advantage avoids

material degradation effects. Other thin-film deposition methods such as semiconductor lithography lead to full coating of the TiO_2 nanotube surfaces forming a blocking of Schottky-junction with charge carrier loss and reduced recombination effects.[69] However to maintain a TiO_2 nanotube semiconductor-electrolyte contact another technique should be examined. In contrast to lithography, gas-phase transport of phosphorus and polyphosphides can result in island-like deposition and preferable *p/n*-heterojunction.[70] Thus, a large area of the TiO_2-semiconductor-electrolyte contact can be preserved. Unlike thin film coating of the whole nanotube surface, quasi-1D- and 2D-materials can also be infiltrated into the pores of TiO_2 nanotube arrays for interpenetrating heterostructure *p/n*-heterojunction formation. Supplementary charge carriers created inside the infiltrated semiconductor only need to cross a short distance equal to nanotube radius (shown in Figure 1.4-1; right side). Intrinsic orthogonalization of light absorption and charge separation of TiO_2 nanotubes ensures that even weakly absorbed photons are harvested, and *p*/n-junction provides slow electron-hole recombination effects.[23]

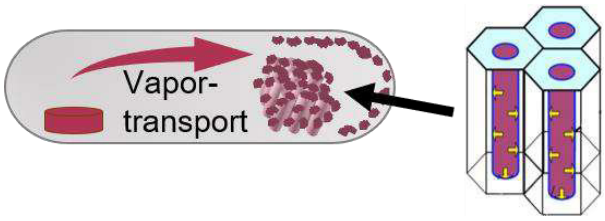

Figure 1.4-1. Left side: Chemical vapor transport of phosphorus and polyphosphides (pink pellet) onto and into TiO_2 nanotube arrays through gas-phase with starting materials. Right side: Schematic illustration of interpenetrating heterostructure (nanomaterials in pink) in outer TiO_2 nanotube arrays. Yellow narrows indicate lateral migration of excitons generated in semiconducting nanomaterials (Figure taken from Cit. 23).

Due to the enticing nanostructural, electronic and optical properties of these 1.0 – 2.7 eV semiconductors they can be applied in devices using solar light as energy source.[42-43, 52, 56, 71] A blue shift due to particle downsizing effects as it is described in section 1.3. can manipulate the band structure and can lead to improved performance.[23, 35, 60, 62, 67] To broaden the band gap engineering effects and to improve low-cost electrochemically anodized TiO_2 nanotube's charge-transport properties, a hybrid material inserting a *p*/*n*-heterojunction is aimed within this work. Key drawbacks such as limited light harvesting to only 7% of the solar spectrum and recombination effects will be addressed.[26]

1.5. Mixed-Anion Advanced Functional Materials

Intriguing optoelectronic features are also found in mixed-anion compounds containing chalcogenides and halides. In general, heavy-atom-chalcogenides own semiconducting and high-density properties. At the same time, they inhibit narrow band gaps, which lead to poor photoconductivity performance, as this precise limited amount of excitation energy can be employed for further reaction steps. Kanatzidis *et al.* presented SbSeI which

inhibits promising charge-transport properties, electrically active and carrier-trapping defects because of its low defect concentration and longe-range order structure.[72] In the case of chalcohalides, halides are able to disrupt the extensive orbital overlap in common narrow band gap nature of chalcogenides. This leads to a widening of the band gap towards 1.6 – ~2.5 eV.[72] In the instance of SbSeI, a band gap of ~1.70 eV and a density of 5.80 $g \cdot cm^{-3}$ was found.[73-74] Further compounds in the chalcohalide group were investigated such as BiSBr showing a band gap of 1.95 eV with a density of 6.57 $g \cdot cm^{-3}$ and SbSBr which shows 2.20 eV and 4.97 $g \cdot cm^{-3}$.[75-77] Another important factor is the observed one-dimensional needle-like morphology which can be useful for growth or even to intergrowth onto and into TiO_2 nanotubes with the aid of mineralizor additives.[71-72] This work deals with the investigation of rare-earth mixed-anion compounds, resulting in suitable band gap energies, and magnetic susceptibilities for optical and magnetic applications. Future experiments could be expanded to create hybrid heterojunction systems in order to combine its unusual wide chalcohalide band gap and its promising charge-transport properties with light harvesting and highly photocatalytic active TiO_2 nanotube material.

2. Materials and Methods

2.1. Reactants and Precursors

Syntheses were performed with reactants and precursors listed in Table 2.1. Further purification was not required, excluding CuI. For this purpose CuI was dissolved in concentrated hydriodic acid (57 wt.-%), precipitated with water and subsequently dried under vaccum.[78] Fluorine-doped tin oxide (FTO)-glass was cleaned by ultrasonication in water, methanol, and acetone for 10 min.

Table 2.1. Specification of reactants and precursors used for synthesis steps in this work.

Reactant	*Shape*	*Supplier*	*Purity* [%]
Ce (Cerium)	pieces	ALFA AESAR	99.8
CuI (Copper(I) iodide)	powder	CHEMPUR	98+
$C_2H_6O_2$ (97 Vol.%) (Ehylene glycol)	Liquid	MERCK	>99.0
HI (57 wt.-%) (Hydriodic acid)	liquid	RIEDEL DE HÄEN	99.99
I_2 (Iodine)	powder (re-sublim.)	CHEMPUR	99.8
La (Lanthanum)	powder	CHEMPUR	99.9
Na (Sodium)	pieces	SIGMA-ALDRICH	99.95
Pr (Praseodymium)	pieces	ALFA AESAR	99
P_{red} (red Phosphorus)	pieces	CHEMPUR	99.999
S (Sulfur)	flakes	SIGMA-ALDRICH	99.99
Sn (Tin)	shots	CHEMPUR	99.999
SnI_4 (Tin(IV) iodide)	powder	own production	crystal phase pure
Ge (Germanium)	powder	SIGMA-ALDRICH	99.99
NH_4F (Ammonium fluoride)	powder	SIGMA-ALDRICH	<99.99
Ti (Titanium)	pieces	CHEMPUR	99.98
FTO (Fluorine-doped tin oxide)	glass	HARTFORD TEC GLASS COMPANY	n.a.
Na_2SO_4 (Sodium sulfate)	powder	SIGMA-ALDRICH	99.0
Titanium (IV)-isopropoxide	powder	SIGMA-ALDRICH	99.99
KOH (Potassium hydroxide)	pieces	SIGMA-ALDRICH	99.0

2.2. Synthesis Methods

Hybrid Materials

TiO_2 Nanotubes: Arrays of self-organized oxide tubes or pores can be obtained by anodization of a suitable metal, in this instance titanium.[26] To gain nanotubes of around 100 µm length, Ti-foil employed as both, cathode (length/width/depth: 2x0.5x0.089 cm) and anode (length/width/depth: 4x1x0.089 cm), was placed 2 cm deep in an electrolyte. The electrolyte was comprised from ethylene glycol and 0.03 wt.-% of NH_4F in deionized water in a 97:3 v/v ratio. An anodic voltage of 60 V was applied by a benchtop power supply (MPJA 9312-PC) and held for 3 d while the electrolyte was cooled in a water bath (see Figure 2.2-1). After cleaning of the anodized foils in methanol, the surface was de-laminated with a razorblade and subsequent air-drying. For cleaning and opening the nanotube bottoms (Ti-metal-barrier side), gaseous reactive ion etching was performed using OXFORD PLASMAPRO NGP80 under a pressure of 20 mTorr and a forward power of 250 W for 200 s on the top side (electrolyte-exposure side) and 300 s at the bottom side of the nanotube arrays. At last both sides were cleaned using O_2 under a pressure of 150 mTorr and a forward power of 225 W for 10 min. The TiO_2 nanotube arrays were fabricated in collaboration with Ryan Kisslinger (group of Prof. Shankar, UofA).

Figure 2.2-1. Experimental setup of TiO_2 nanotube array anodization, with two Ti-foils used as anode and cathode with benchtop power supply (DC MPJA POWER SUPPLY 9312-PS) for anodization at 60 V in an electrolyte containing 97:3 v/v ethylene glycol and deionized water (0.03 wt-% NH_4F).

Nanofibers and Hybrid Materials of black P, fibrous red P, NaP_7, SnIP and $(CuI)_3P_{12}$ onto and into TiO_2 nanotube arrays were prepared *via* short way gas-phase transport reaction. This low-pressure technique was also used for the synthesis of black phosphorus, previously reported by Nilges *et al.* following the mineralizator principle.[71] Therefore, the starting materials were placed (if required pressed to a pellet with a diameter of 10 mm (MAASSEN pellet press MP150, 1 to, 15 min)) at one end of a silica glass ampoule. In the case of NaP_7-synthesis, the silica glass ampoule was graphitized beforehand by acetone decomposition using the oxidizing part of a hydrogen-oxygen flame to avoid sodium from etching the silica glass ampoule. For the hybrid materials, above-mentioned

electrochemically anodized TiO_2 nanotube arrays were placed at the opposite side of the ampoule followed by evacuation down to a pressure of $p < 10^{-3}$ mbar. The ampoule was placed horizontally, with the nanofibers starting materials located at the hot zone and TiO_2 nanotube arrays facing towards the colder zone in a muffle furnace (NABERTHERM, L3/11/330). Samples were heated to the according temperature programs known from literature.[42, 45, 47, 52, 71] Depending on the cooling process, nanofibers of different lengths were obtained, during syntheses without and with TiO_2 nanotube membranes (see Figure 2.2-2). Following these temperature programs sufficient nanofiber-growth and TiO_2 anatase crystallization was carried out, excluding major decay effects.

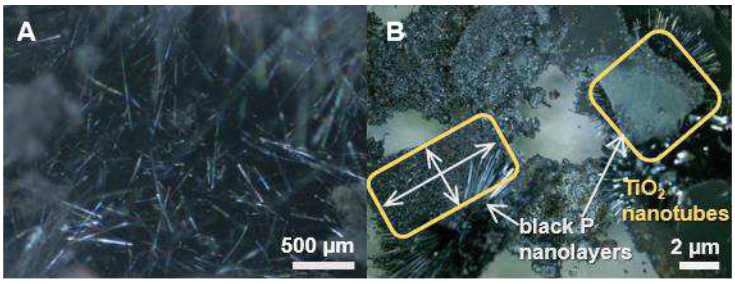

Figure 2.2-2: Samples after gas-phase transport reaction growth of **A**) nanofibers of $(CuI)_3P_{12}$ and **B**) hybrid materials of black P (deposition marked as white narrows) onto TiO_2 nanotube membranes (grey membranes marked within yellow boxes).

Single-crystal Synthesis

Single-crystals of $RE_3Ge_2S_8I$ (*RE* = La, Ce and Pr) were prepared in a similar manner, with a 10%-excess of I_2 as the mineralizing agent. The starting materials were grounded with an agate mortar to small pieces or powder and pressed to a pellet (10 mm diameter, MAASSEN pellet press MP150, 1 to, 15 min). The pellet was transferred to a silica glass ampoule, sealed under vacuum ($p < 10^{-3}$ mbar) and placed horizontally in a muffle furnace (NABERTHERM, L3/11/330). With a relatively low sulfur boiling point of 444 °C fast heat treatment can result in explosions of the ampoule caused by rapid evaporation of S. Therefore, the temperature program was selected to allow slow heating of 2°C/min to 300 °C and retention time of 2 d. The temperature was increased to 900 °C (2 °C/min), and kept at that temperature for 7 d. Afterwards, the product was slowly cooled to RT.

2.3. Characterization Techniques

Diffraction Methods

Powder Diffraction: Identification and structure of all inorganic phases was determined by powder X-ray diffraction. By grounding the samples in an agate mortar, a homogenous powder was obtained and put airtight between two stripes of SCOTCH® *Magic*™, 810, 3M tape. After placing the sample in a flat sample holder of a STOE STADI P diffractometer fitted with a DECTRIS MYTHEN 1K detector diffraction data were collected between 10 and 80° in a 2Θ range, for 15 min each using Cu-$K_{\alpha 1}$ radiation (λ = 1.54051 Å, Ge(111) monochromator) and Si (a = 5.43088 Å) added as external standard.[79] Phase analysis and indexing was carried out with the program package STOE WINXPOW and compared to literature data of PEARSON'S CHRYSTALLOGRAPHIC-database.[80-81]

Single-crystal Diffraction: Crystallographic structure data were collected using single-crystal X-ray diffraction. Single-crystals, separately mounted with glass fibers and adhered with beeswax under a light microscope (ZEISS Stemi 508, 24x magnification), were measured at room temperature. Therefore, oscillation mode with a Bruker Platform diffractometer equipped with a SMART APEX II CCS area detector (Mo-$K_{\alpha 1}$ radiation; λ = 0.7103 Å; graphite monochromator) was applied using ω scans at 7 – 8 different ϕ angles with 0.3° frame width and 10 - 12 s exposure time per frame.

Structure Refinement from X-ray data: Processing the collected data, such as standardization of atomic positions was performed using the program STRUCTURE TIDY.[82] Structure determination and refinement was carried out with the program package (version 6.12).[83] The crystal structures are represented graphically using the CRYSTAL IMPACT *Diamond* program.[84]

Magnetic Characterization Method

Magnetic Susceptibility measurements were conducted on a QUANTUM DESIGN 9T-PPMS magnetometer. The data were collected between 2 and 300 K under an applied magnetic field of 0.5 T and susceptibility values were corrected for contributions from sample holder and diamagnetism.

Microscopic/Spectroscopic Methods

Scanning Electron Microscopy (SEM) and Energy Dispersive X-ray Spectroscopy (EDS): The samples were placed on adhesive and conductive carbon tabs and analyzed with a SEM JCM-6000 NeoScop TM (JEOL, 5900LV, Si(Li) detector) along with an integrated EDS module for semi-quantitative composition determination of the samples. For

this measurement an acceleration voltage of 15 kV was applied with an integration time of 300 s at ~3 different points at homogenous material's surfaces and ~15 points at hybrid material's surfaces. Imaging and processing of the collected data was carried out with JEOL JED-2300 Analysis Station.

Scanning Transmission Electron Microscopy (STEM) and Energy Dispersive X-Ray Spectroscopy (EDS): After brief ultrasonication of the samples in methanol, the suspensions were dropped on lacey carbon films of copper grids and dried under air at RT. The copper grids were placed in a JEOL JEM-ARM200cF STEM. The microscope is equipped with a cold field-emission gun and a Cs probe corrector for high atomic resolution. For qualitative analysis of the samples, the integrated EDS including a silicon drift detector took measurements with an acceleration voltage of 200 V. Analysis of the acquired data was performed by the integrated JEOL JED-2300 Analysis Station system. STEM-EDS analysis was conducted at nanoFAB Centre (Fabrication and Characterization Centre, UofA, W1-060 ECERF Building, Edmonton, Canada T6G 2R3).

Helium Ion Microscope (HIM) with Ga-assisted focused ion beam (FIB): SEM-EDS analysis to obtain an elemental filling depth profile was enabled after removing the surface layer down to ~15 nm depth *via* focused ion beam for ultra-high-resolution imaging and operation at nanoscales. For this purpose, a ZEISS ORION NanoFab Helium ion microscope equipped with a Ga-FIB column was used. Measurements were conducted at 30 keV and beam currents of 1.5 nA. The operation technique is analogous to SEM, but instead of an electron beam a focused ion beam is used.

Auger Electron Spectroscopy (AES): AES analysis of FIB-milled areas was performed for semi-quantitative determination of the elemental composition using a JEOL JAMP-9500F Auger microprobe. The samples were cleaned with argon ion sputtering over an area of 500 μm^2 in a 15 nm^2/min rate. A standard SiO_2 thin film was used for calibration. Integrated SEM and Auger imaging were conducted at an acceleration voltage of 2 kV and an emission current of 20 mA.

Raman Spectroscopy: For Raman imaging all samples were placed on a glass slide and in case of the nanotubes' cross sections, fixed upright onto SCOTCH® *Magic*™, 810, 3M tape. The spectra were acquired with a RENISHAW inVia RE04 Raman Microscope fitted with a Nd:YAG and diode laser, (λ = 532; 785 nm) and CCD detector. The conducted laser power was 250 mW, recording 500 scans per 60 s. An integrated light microscope and camera system enabled surface point by point profiling down to 1.5 µm at 50x magnification for measurements such as along the nanotube cross sections.

X-ray Photoelectron Spectroscopy (XPS) and Ultraviolet Photoelectron Spectroscopy (UPS): After drop-casting all samples on FTO-glass, surface analysis was carried out using a KRATOS ANALYTICAL Axis-Ulra XPS-instrument equipped with monochromatic Al-Kα (E = 1486.6 eV) source at 15 kV, 50 W under ultra-high vacuum (UHV ~10^{-8} Torr). For charge correction, C1s of adventitious hydrocarbon (BE ≈ 284.4 eV) was selected. The energy of additional light sources (He-ion UV source) couples to more strongly valence-level electrons and therefore enables the instrument to perform UPS measurements. XPS and UPS analysis was performed in the laboratories of Prof. Karthik Shankar (Department of Electrical and Computer Engineering, UofA, 11-384 Donadeo Innovation Centre For Engineering, Edmonton, Canada T6G 1H9).

Diffuse Reflectance UV-Vis Spectroscopy: Optical diffuse reflectance spectra were measured with an AVASPEC 2048 spectrometer (AVANTES) with deuterium/halogen light source (AVALIGHT-DH-S-BAL) together with a reflection probe (FCR-7UV200-2ME) and a custom-made sample holder (5 mm in depth). After plotting the optical absorption spectra, band gaps were determined using the Kubelka-Munk equation (eqt. 2), where α = Kubelka-Munk absorption coefficient, S = scattering coefficient, and R is the reflectance.[85]

$$F(R) = \frac{\alpha}{S} = \frac{(1-R)^2}{2R} \quad (2)$$

With $[F(R)hv]^x$; x = 0.5 for indirect band gap and x = 2 for direct band gap.

All spectra were recorded at laboratories of Prof. Karthik Shankar (Department of Electrical and Computer Engineering, UofA, 11-384 Donadeo Innovation Centre For Engineering, Edmonton, Canada T6G 1H9).[86-87]

Kelvin Probe Force Microscopy (KPFM): Surface potential microscopy was performed to discern the charge separation dynamics using Dimension Fast Scan Atomic Force microscope (BRUKER Nanoscience Division, Santa Barbara, CA, USA). The materials were deposited on FTO, and a Pt-coated SiN-SCM-PIT served as cantilever of 2.5 µm length and 4.4 N/m stiffness in the KPFM measurements. Atomic Force Microscopy (AFM) holding chuck and conductive copper tape was used to ground all samples. The measurement was performed at zero tip bias and calibration of Pt tip were achieved by measuring the contact potential difference (CPD) of highly ordered pyrolytic graphite (HOPG) and the Pt tip was employed using following expression (eqt. 3):

$$\boldsymbol{EF\ (tip) = 4.6\ eV\ (Work\ function\ of\ HOPG) + VCPD\ (HOPG\ and\ PT\ tip)} \quad (3)$$

Chromatographic Method

Gas Chromatography (GC): Chromatographic separation and detection of reaction products were conducted on a SHIMADZU GC equipped with PORAPAK Q column, Mol Sieve column and a pulsed discharge detector. For calibration hydrogen was quantified with a standard calibration gas mixture (PRAXAIR GAS, Canada). Helium was used as carrier gas at the low rate 0.5 mL min^{-1}. The analysis started with heating the oven up to 60 °C and raising temperature up to 160 °C to remove residual water. Preset detector temperature was 160 °C.

Photo-Electrochemical Experiments

Photo-Electrochemical Properties were measured in a three-electrode set up by using a CHI660E series electrochemical workstation. The workstation consists of a working electrode as photoanode, a cathode as counter electrode, a reference electrode, respectively. To prepare the photoanode, an approximately 20 nm thick blocking layer of TiO_2 on cleaned conductive FTO-glass (transmittance 80-82%) was fabricated by spin-casting titanium isopropoxide as it has been reported previously by Shankar *et al.*[88] The samples were ultrasonicated in diluted titanium isopropoxide solution for 5 min using a VWR Ultrasonic Cleaner, drop casted onto FTO-TiO_2-glass and dried at 150 °C for 1 h. Pt sputtered glass was used as cathode and Ag/AgCl as reference electrode, respectively. Photo-electrochemical water splitting experiments were conducted by immersing the electrodes in 0.1 M KOH solution (electrolyte) and irradiated under solar simulated light (1 sun equivalent to AM1.5 G) with a power density of 100 $mW \cdot cm^{-2}$ applied at the sample surfaces.

For Linear Sweep Voltammetry, photocurrent densities were measured as function of applied voltage *vs* sweeping bias voltage from -1.0 – 0.8 V at a scan rate of 10 $mV \cdot m^{-2}$. Further experiments on LED irradiation measuring photo-response at higher wavelength (450 and 505 nm) and incident photon-to-current efficiency were carried out.

Electrochemical Impedance Spectroscopy (EIS) was performed to obtain a Nyquist EIS spectrum and an equivalent electrical circuit. EIS experiments were conducted under dark and 1 sun irradiation at a bias of -0.5 V *vs* Ag/AgCl with an AC amplitude of 0.005 V at 1 Hz – 100 kHZ frequencies.

Impedance-Potential Measurements for Mott-Schottky analysis of the semiconductor interface regions was carried out, by changing the electrolyte in the above-mentioned

electrochemical workstation to a 0.5 M Na_2SO_4 solution and performed at a potential range of -1.0 to 1.0 V at 1000 Hz frequency.

Mathematical Models

Machine Learning Technique was applied to predict expected band gaps of the compounds assigned for synthesis. Mathematical models were built systematically with the aid of in-house selection routines, implemented in the Microsoft Office Spreadsheet Excel Software [Version 2013].

3. Results

3.1. Vapor growth of binary and ternary phosphorus-based semiconductors into TiO_2 nanotube arrays and application in visible light driven water splitting

Ebru Üzer [a], Pawan Kumar [b], Ryan Kisslinger [b], Piyush Kar [b], Ujwal Kumar Thakur, [b] Karthik Shankar, [b,*] and Tom Nilges [a,*]

[a] Department of Chemistry, Technical University of Munich, Lichtenbergstr. 4, 85748 Garching b. München, Germany; E-mail: tom.nilges@lrz.tum.de

[b] Department of Electrical and Computer Engineering, 9211-116 Street NW, Edmonton, Alberta, Canada T6G 1H9; E-mail: kshankar@ualberta.ca

Nanoscale Advances Pages 26 - 56
DOI: 10.1039/C9NA00084D

The article 'Vapor growth of binary and ternary phosphorus-based semiconductors into TiO_2 nanotube arrays and application in visible light driven water splitting' was submitted to 'Nanoscale Advances' in February 2019 and published online in May 2019. Results were presented by Ebru Üzer at the 11th IGSSE Forum in Raitenhaslach, Germany in May 2017, at the 101st Canadian Chemistry Conference and Exhibition in Edmonton, Canada in May 2018, and the Annual ATUMS meeting in Jasper, Canada in November 2017.

The goal of this work was to create hybrid materials *via* an easy-accessible route, to overcome key-drawbacks of *n*-type anatase TiO_2 nanotubes, a photocatalytic active material, commercially used in photocatalytic, photovoltaic and optoelectronic sensing devices.[89-90] The results can be described in two stages: 1) Elaboration of a pertinent synthesis route, forming hetero-interfaces between prefabricated TiO_2 nanotube arrays (TiO_2 membranes fabricated by Ryan Kisslinger, group of Prof. Shankar, UofA) and semiconducting polyphosphides (NaP_7, SnIP and $(CuI)_3P_{12}$); successful deposition, enabling free carriers' generation and migration *via* physicochemical investigation of the hybrid

materials. 2) Electrochemical analysis on visible light driven applications, in this instance photocatalytic water splitting experiments were performed. Carrier's reaction on the interfacial heterostructure charge transfer were investigated. This led to an improved performance compared to pristine TiO_2 nanotubes.

1) Low-pressure gas-phase deposition of NaP_7, SnIP and $(CuI)_3P_{12}$ on TiO_2 nanotube arrays according to the mineralizator technique as previously reported by Nilges *et al.*, was applied.[71] An island-like 50% to full polyphosphide-surface coverage on electrochemically anodized TiO_2 nanotube membranes was substantiated *via* light microscope, SEM-EDX, and powder X-ray diffraction experiments. A filling of NaP_7@TiO_2 material was first analyzed by nanotube surface removal of an area of ~200x200 µm with Ga^+-assisted He-focused ion beam down to ~10 nm. A SEM-image of this FIB-milled area revealed a seemingly tube-filling of ~50%, confirmed by high-resolution elemental analysis *via* Auger electron spectroscopy. For further filling-depth profiling, Raman imaging experiments were conducted. Therefore, the Raman laser was pointed along several razor-cut cross sections. Characteristic modes of NaP_7 next to TiO_2-anatase along the full length of the tubes (~120 µm) and of $(CuI)_3P_{12}$ up to 22 µm of the tubes (full length~63 µm) were found. STEM analysis after ultrasonication of hybrid material membranes shows tubes with 60-100 nm inner diameters. According to elemental analyses after semi-quantitative EDS mapping Ti within the tube walls and all necessary elements expected for NaP_7, SnIP and $(CuI)_3P_{12}$ were detected. Surface and subsurface composition, binding energies and oxidation states of pristine and hybrid materials were derived from XPS analysis. The elemental surface scans displayed no binding energy shift or peak intensity change for pristine TiO_2, SnIP and hybrid SnIP@TiO_2, representing a hetero-structured hybrid system rather than doping of the semiconductors. A peak shift to higher binding energies in $(CuI)_3P_{12}$@TiO_2 and NaP_7@TiO_2 XPS-spectra indicates partial charge transfer between the hybrid components and additionally doping of TiO_2 with Na in the latter case. To study light-absorption capacities of TiO_2 and pristine compounds *vs* hybrid materials, diffuse reflectance UV-Vis experiments were conducted. In comparison to the optical band gap of TiO_2 which was found to be 3.05 eV (in close agreement to literature TiO_2-anatase values of 3.2 eV[91]), band gap values of the hybrid materials showed 1.87 eV for NaP_7@TiO_2, 2.22 eV for SnIP@TiO_2 and 2.73 eV for $(CuI)_3P_{12}$@TiO_2. This demonstrates a shift next to both TiO_2 and pristine polyphosphides, increasing the potential of TiO_2 nanotubes in solar light harvesting applications. Furthermore, as mentioned in section 1.3. a special structural characteristic of $(CuI)_3P_{12}$ was identified. Achieving separation of single phosphorus strands from $(CuI)_3P_{12}$ can lead to downsizing quantum confinement effects and therefore band gap widening from

commonly 1.0 eV in bulk material up to 2.3 – 2.7 eV without the CuI-matrix.[43] Powder XRD experiments revealed crystalline phases and diffuse reflectance UV-Vis resulted in a band gap of 2.84 eV, and therefore we concluded that a successful preparation of single polyphospide strands among the hybrid material due to nanocomposite growth through vapor transport method occured.

2) Photoelectrochemical hydrogen generation, including charge transport and carrier recombination analysis, was investigated in a three-terminal electrochemical cell. Thus, photoconductivity measurements to obtain of photocurrent response were applied and resulted in overall improvement of the hybrid materials compared to pristine TiO_2 (0.21 mA cm^{-2}) with a significant increase of SnIP@TiO_2 (0.84 mA cm^{-2}). Calculation of photoconversion efficiency yielded in 10-fold improvement of SnIP@TiO_2 (applied bias photon-to-current efficiency (ABPE)% 0.2 *vs* 0.02 for pristine SnIP).

In electrochemical impedance spectroscopy (EIS), photogenerated carriers' migration were investigated by periodic modulation of the potential difference across the semiconductor-electrolyte interface. Our intention was to obtain data on charge transport resistance, charge transfer resistance, space charge capacitance, and electrochemical double-layer capacitance. The electrochemical circuit component values were acquired after generating the representative equivalent circuit model containing the electrical characteristics. To describe imperfect double layer capacitances in the semiconductor-electrolyte interface a constant phase element Q_n was set in the equivalent circuit. With the aid of *Nyquist Plots* reduction in charge transfer resistance and charge transport resistance of the hybrid materials, in comparison to pristine TiO_2 could be evaluated. This suggests improved charge transfer and transport in the hybrid materials. In this regard, further charge carrier properties were calculated such as long recombination lifetime of photogenerated carriers. Due to the orthogonalized processes of photocarrier generation and charge separation in TiO_2 nanotube arrays, there is a given risk of cancelling these effects by a filling of the vertically oriented array by additional material, possessing good carrier transport capabilities. With a recombination lifetime of 2.4 µs, the SnIP@TiO_2 hybrid material lies within the range of TiO_2 nanotube arrays, effectively suppressing photogenerated electrons with holes, whereas NaP_7@TiO_2 and $(CuI)_3P_{12}$ show reduced values of 1.9 µs in both hybrid samples.

For information about charge carrier concentration and flat band potential impedance potential analysis was applied. Reciprocal squared plots of the charge capacitance *vs* potential (Mott-Schottky plots) were used to calculate charge carrier concentration using the slope. Flat band potential responds to the intersection of the according fitted straight line (see Publication Figure S14). Hybrid NaP_7@TiO_2 material showed higher charge

carrier concentration ($5.62 \cdot 10^{20}$ cm^{-3}) than pristine TiO_2 (5.1×10^{20} cm^{-3}), next to reduced values of $3.8 \cdot 10^{20}$ cm^{-3} for $(CuI)_3P_{12}@TiO_2$ and $1.1 \cdot 10^{20}$ cm^{-3} for $SnIP@TiO_2$. For successful photo-electrochemical water splitting reactions, a potential semiconductor's CB position has to be located above hydrogen potential (electron-hydrogen reduction reaction) and VB positions below oxygen potential (hole-oxygen evolution reaction).

UPS work function (WF) analysis together with KPFM analysis were performed to gain information on VB_{max} position and WF. The flat band potential values expressed in V *vs* NHE at pH=0 for the conduction band position showed a shift from pristine to hybrid $SnIP@TiO_2$ (-0.531 *vs* -1.731 V). This explains the considerable improvement of photocurrent response due to heterojunction formation. In general, calculated flat band potential and VB positions indicate an upward band bending in the Z-scheme junction formation and a downward band bending of the CB position. A Fermi level alignment in the electron flow process occurred. A hybrid formation of $SnIP@TiO_2$, displayed a greater shift to negative potential, leading to enhanced downward band bending of the TiO_2-CB position and therefore charge separation. This is additionally supported by the greater depletion width of $SnIP@TiO_2$ (923 nm) *vs* $NaP_7@TiO_2$ (119 nm) and $(CuI)_3P_{12}@TiO_2$ (157 nm) in the hybrid hetero-interface. KPFM measurements showed a uniform distribution of charge all over the sample surfaces. In addition, lowering of WF in polyphosphides were confirmed which is attributed to an uplift in Femi level energy during band gap alignment in the hybrid material heterojunction formation.

AUTHORS CONTRIBUTION: E.Ü. and R.K. synthesized the polyphosphide hybrid materials and characterized them using Helium Microscopy, SEM, and STEM-EDS. P.Ku. performed XPS, UPS and photoelectrochemical studies and involved in interpretation of obtained results. U.K. carried out KPFM experiments on the samples. P.Ka. was responsible for electrochemical characterizations. K.S. and T.N. supervised the research and wrote the manuscript with the input of all others. All authors were involved in writing their respective parts.

Nanoscale Advances

PAPER

View Article Online
View Journal

Cite this: DOI: 10.1039/c9na00084d

Vapor growth of binary and ternary phosphorus-based semiconductors into TiO_2 nanotube arrays and application in visible light driven water splitting†

Ebru Üzer,[a] Pawan Kumar,‡[b] Ryan Kisslinger,‡[b] Piyush Kar,[b] Ujwal Kumar Thakur,[b] Karthik Shankar*[b] and Tom Nilges*[a]

We report successful synthesis of low band gap inorganic polyphosphide and TiO_2 heterostructures with the aid of short-way transport reactions. Binary and ternary polyphosphides (NaP_7, SnIP, and $(CuI)_3P_{12}$) were successfully reacted and deposited into electrochemically fabricated TiO_2 nanotubes. Employing vapor phase reaction deposition, the cavities of 100 μm long TiO_2 nanotubes were infiltrated; approximately 50% of the nanotube arrays were estimated to be infiltrated in the case of NaP_7. Intensive characterization of the hybrid materials with techniques including SEM, FIB, HR-TEM, Raman spectroscopy, XRD, and XPS proved the successful vapor phase deposition and synthesis of the substances on and inside the nanotubes. The polyphosphide@TiO_2 hybrids exhibited superior water splitting performance compared to pristine materials and were found to be more active at higher wavelengths. SnIP@TiO_2 emerged to be the most active among the polyphosphide@TiO_2 materials. The improved photocatalytic performance might be due to Fermi level re-alignment and a lower charge transfer resistance which facilitated better charge separation from inorganic phosphides to TiO_2.

Received 11th February 2019
Accepted 17th May 2019

DOI: 10.1039/c9na00084d

rsc.li/nanoscale-advances

1. Introduction

Depleting fossil fuel reserves and rising atmospheric greenhouse gas concentration have motivated the search for new energy sources. Using sunlight as the energy source to generate hydrogen from water through water splitting is an enticing approach. Hydrogen is considered a clean fuel with a high calorific value; it can be stored in a solid/liquid adsorbent or transformed into hydrocarbons using CO_2 to produce a syngas mixture. Many photocatalytic materials such as ZnO, CdS, ZnS, $InVO_4$, $AgPO_4$, $SrTiO_3$ and TaON have been widely investigated to achieve water splitting.[1–4] TiO_2 has proven to be an excellent photocatalytic material due to its promising band edge potential, non-toxic and non-corrosive nature, and earth-abundance. However, issues such as its large band gap, less reductive conduction band, short lived charged carriers and poor quantum efficiency are the main obstacles preventing the successful deployment of sustainable photocatalysts.[5–7] Hybridization of TiO_2 with various low band gap semiconductors to produce direct/*Z*-scheme photocatalysts, doping, sensitization, formation of Schottky junctions and nanoscale structural modification (*i.e.*, nanotubes/nanorods/nanospikes/nanospheres) have proven to enhance photocatalytic performance and/or charge separation.[8–13] Polyphosphides are an intriguing class of low band gap semiconductors for this purpose.[14,15] We selected three polyphosphides, namely NaP_7, SnIP (ranging from 1.71–1.86 eV)[16–18] and $(CuI)_3P_{12}$ (2.84 eV, own measurement see below) because of their different band gaps and their ability to be synthesized in a mineralizer-assisted transport reaction.[19,20] NaP_7, a 2 eV-semiconductor material, plays a crucial role in the sodification and desodification processes in sodium ion batteries.[18] SnIP represents the first inorganic atomic-scale-double helix compound and $(CuI)_3P_{12}$ is an adduct phase from CuI and a neutral phosphorus chain.[21–23]

TiO_2 nanotubes are hollow nano-sized cylinders that form in vertically oriented arrays over large areas on the underlying substrate. The nanotubes are fabricated by electrochemical anodization of Ti films or foil in electrolytes typically containing F^- through the simultaneous occurrence of field-assisted Ti oxidation, field-assisted dissolution of Ti and TiO_2, and chemical dissolution of TiO_2.[24,25] The as-synthesized nanotubes are amorphous and are crystallized to n-type semiconducting anatase either by annealing in air at temperatures of 350–550 °C or by a hydrothermal treatment at lower temperatures.[26,27] TiO_2

[a]Department of Chemistry, Technical University of Munich, Lichtenbergstr. 4, 85748 Garching, Germany. E-mail: tom.nilges@lrz.tum.de

[b]Department of Electrical and Computer Engineering, 9211-116 Street NW, Edmonton, Alberta, Canada T6G 1H9. E-mail: kshankar@ualberta.ca

† Electronic supplementary information (ESI) available. See DOI: 10.1039/c9na00084d

‡ Contributed equally.

nanotubes exhibit remarkable versatility in the type of substrate they can be grown on, having been demonstrated on Si, ITO-coated glass, FTO-coated glass, quartz, polyimide and Ti foil, and also as free-standing membranes.[28–30] Likewise, the nanotube diameter can be varied over a wide range (10 to 900 nm).[31,32] These characteristics make TiO_2 nanotubes ideal for the templated growth of inorganic phosphorus-based semiconductors through diffusive chemical vapor transport into the nanotube pores at elevated temperatures.

While electrodeposition and chemical vapor deposition into nanoporous anodic aluminium oxide (AAO) templates have been previously used to form nanorods and nanofibers of CdS, CdSe, Si, Bi, *etc.* exhibiting quantum confinement effects,[33–36] the application spectrum for semiconductor nanowires formed by chemical vapor transport deposition into anodic TiO_2 nanotube arrays is much greater. This is because the TiO_2 nanotubes are n-type semiconductors (charge carrier density $\sim 10^{18}$ to 10^{19} cm^{-3})[37] and allow the formation-in-place of a semiconductor heterojunction while AAO is an insulator, precluding the formation of a useful heterojunction. Furthermore, for a heterojunction to be electronically useful in applications that rely on light harvesting (photodetectors, photovoltaics, photocatalysts, and photoelectrochemical sensors) it is essential for excess carriers to be efficiently separated and for photons to be completely harvested. In this regard, vertically oriented nanotubes and nanowires are uniquely suited because the processes of charge separation and light absorption are orthogonalized.[38] Charge carriers created in a semiconductor nanorod formed inside the nanotubes need to merely travel a distance equal to the nanotube radius before encountering a heterojunction interface for charge separation while the high aspect ratio of the nanotubes ensures that even weakly absorbed photons are harvested. Furthermore, light trapping effects such as photonic crystals and resonant Mie scattering can be easily incorporated into the nanotubes to increase their photonic strength.[32,39] Indeed, heterojunctions of TiO_2 nanotubes with solution-processed semiconductors such as CdS, CdSe, PbS, Fe_2O_3, Cu_2ZnSnS_4, g-C_3N_4, halide perovskites, *etc.* have been used to demonstrate efficient *Z*-scheme CO_2 reduction photocatalysts,[40] high performance water photolyzers,[41] selective gas sensors,[42] and high efficiency solar cells.[43,44] Herein, we introduce TiO_2–polyphosphide heterojunctions consisting of polyphosphide nanofibers formed by the hitherto unexplored process of chemical vapor transport into TiO_2 nanotube array templates.

2. Results and discussion

Section 2.1 describes the synthesis of the TiO_2 nanotubes and nanohybrids in brief. Sections 2.2 and 2.3 describe our characterization of NaP_7@TiO_2 and SnIP@TiO_2 heterostructures. Following the same principle as that for NaP_7 and SnIP, the synthesis, characterization and physical property measurement details of $(CuI)_3P_{12}$ on TiO_2 heterostructures are circumstantiated, as well as a full description of all synthesis parameters and characterization techniques in the ESI Section.† Section 2.4 and 2.5 summarize X-ray Photoelectron Spectroscopy (XPS) and UV-Vis studies of the heterostructures, with details given in the ESI† respectively. Section 2.6 deals with photocatalytic activity measurements and related characterization. Detailed interface photon-to-current efficiency performance as well as semiconductor–electrolyte interface analysis are described in the ESI† as well as sections on Electrochemical Impedance Spectroscopy (EIS), impedance-potential measurements, and Kelvin Probe Force Microscopy (KPFM).

2.1 Synthesis of polyphosphide@TiO_2 nanotube hybrids

A low-cost and easily accessible method to fabricate nanostructured photochemically active hybrid polyphosphide@TiO_2 heterostructures has been developed following a short-way transport reaction onto and into electrochemically fabricated TiO_2 nanotube membranes (Fig. 1). Synthesis details are given in the ESI.†

2.2 NaP_x@TiO_2 nanotubes

Fig. 2a displays the crystal structure of NaP_7 and a representative membrane after the gas phase deposition reaction is shown. Small crystals of NaP_7 were formed on the surface of the TiO_2 membrane (see Fig. 2b). A Scanning Electron Microscopy (SEM) image of the TiO_2 membrane cross section substantiates the growth of NaP_7 on both sides of the membrane. It is obvious from Fig. 2c that the crystal sizes are different on both sides which directly correlates with the TiO_2 nanotube pore width on either side. The cross-sectional images were taken after cutting the polyphosphides@TiO_2 nanotubes with a razor, taking the images along the cut edges. Obviously, the growth of the polyphosphide crystals started from the surface or even from inside the TiO_2 nanotube directly into the gas phase (see Fig. 3). Therefore, many crystals are grown straight out of the nanotubes. A second hint for a growth from the inside into the gas phase might be the differences in the sizes of the crystals on both sides of the membrane (corresponding SEM data in Table S1†). On the other hand, the size of the TiO_2 nanotubes can directly define the diameter of the resulting NaP_x crystals ($x = 7$, 15).

Two visually different main fractions lying on the top and bottom of the TiO_2 membrane sides were observed. The

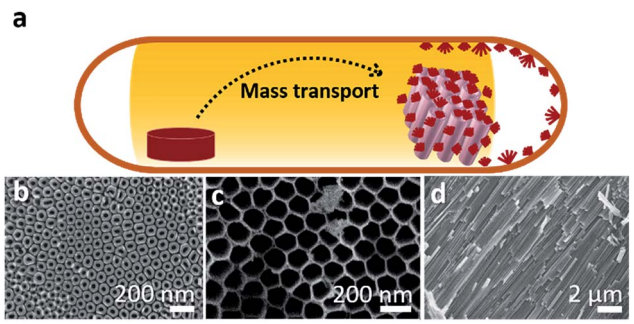

Fig. 1 (a) Starting materials (red pellet) are transported onto and into TiO_2 nanotube membranes (brown) *via* a gas phase. (b) Representative SEM pictures of the electrochemically prepared TiO_2 nanotube membranes used in a mineralizer-driven short-way transport reaction in the bottom side view, (c) top side view, and (d) side view.

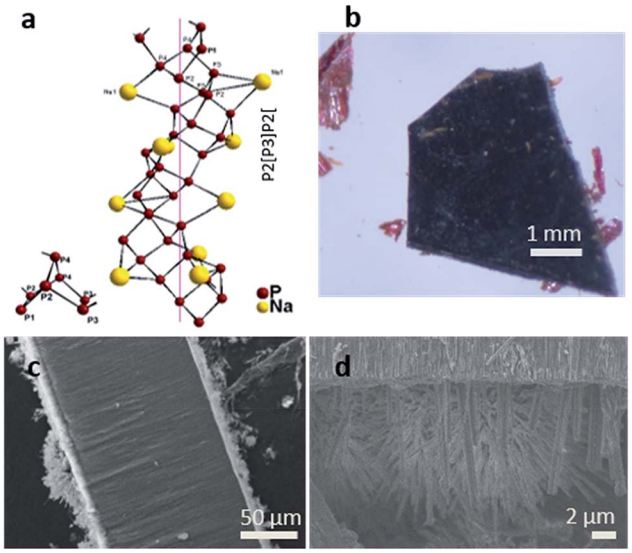

Fig. 2 (a) Structure with a representative Na-coordinated polyphosphide substructure of NaP_7. (b) A TiO_2 nanotube membrane reacted with Na and P *via* a gas phase. (c) SEM images show the cross section of a membrane. (d) Intact TiO_2 nanotubes of the membrane shown in (b) and NaP_7 crystals grown on top of the membrane surface. Many crystals have grown straight out of the nanotubes.

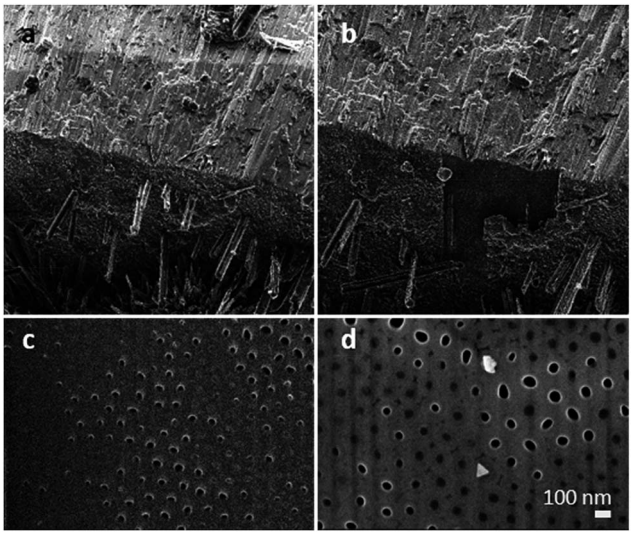

Fig. 3 FIB measurement on a NaP_x@TiO_2 nanotube membrane. FIB-SEM image (a) before and (b) after FIB-milling of the TiO_2 membrane surface area. (c) FIB-SEM and (d) SEM image of the milled area. Filled tubes show a lighter grey contrast than the non-filled appearing holes. An approx. 1 : 1 ratio was ascertained.

samples were manually separated, and data collection of powder X-ray diffraction led to a nearly phase pure pattern of NaP_7 (main fraction) and a diffraction pattern of NaP_{15} (minor fraction) reflecting distinct texture effects (see S1a and b). To verify the assumption that a significant transport of the material occurred *via* the gas phase to the inside of the nanotubes, we examined the cross section of a broken membrane by position-sensitive EDS scans (Table S1†). The data along the cross section of the membrane show a constant Na : P ratio of approx. 1 : 9 towards the top side view of the membranes (larger holes), where the crystals on the surface show a larger size and a ratio of 1 : 4 towards the bottom side of the membranes (smaller holes), where the crystals show a smaller size. This finding substantiates our hypothesis that Na and P were transported into the TiO_2 nanotubes along a certain length of the membrane. To verify the filling grade of the nanotubes, and therefore the efficiency of the gas phase transport, a FIB experiment was performed on a selected spot of the membrane. The FIB was used to cut off the upper part down to 15 nm of the membrane to facilitate an observation of the nanotube's subsurface. We found non-filled and filled tubes on the area we treated (see Fig. 3). Taking a closer look at the tubes, a filling grade of 50% can be estimated from the FIB pictures.

To determine the filling elemental depth profile, the FIB milled area (shown in Fig. 4) was analysed *via* Auger electron spectroscopy (AES) and microscopy (see Fig. 4 and AES spectra in Fig. S2†). Fig. 4a shows locally analysed FIB-milled spots with spot 1 demonstrating the analysis of a tube considered empty; notably, it is the only spot indicating the presence of carbon. Due to sample cleaning by argon ion bombardment, it is assumed that carbon has been cleaned off, as it is not present in all other spots but spot 1 being inaccessible to cleaning and therefore showing the presence of C. Spots 2–6 have much higher P contents than spot 1 even after deducting the C content (a proportionate rise of P to 18.9 at%). This suggests that the spot 2–6 nanotubes were filled, while the spot 1 tube was not; the signal at spot 1 of P is not attributed to the P content in the apparently empty nanotube but appears due to the approximately 10 nm resolution of the instrument. The most prominent Na peaks appear at 24 eV (Na KLL, overlap in AES spectra, Fig. S2†) and taking the relatively low Na to P ratio into account, a merely weak peak at 979 eV (Na LVV).

Raman spectroscopy on the surface and cross section of a membrane (cut apart with a razor) was carried out to validate the successful transport of the material into the TiO_2 nanotube membranes. We measured the depth of intake of a material by moving the Raman laser gradually along the cross section, acquiring spectra at specific spots. The laser has a standard mode spot size of 1.5 microns (at 50× magnification). From

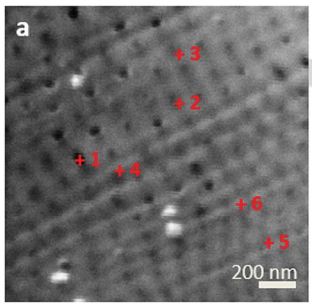

b

Atomic composition (%)

	Ti	O	P	C
1	9.3	61.1	16.4	13.1
2	14.0	57.0	29.0	0
3	14.4	57.4	28.2	0
4	11.4	51.8	36.8	0
5	15.7	57.2	27.1	0
6	13.8	54.1	32.0	0

Fig. 4 (a) Measured spots of Auger electron spectroscopy of the FIB milled NaP_x@TiO_2 nanotube specimen. (b) Detected atomic composition. Each measured composition has an error of approximately 10% of the value reported.

a series of spectra recorded at different depths and from both sides of the membrane, we found the penetration of NaP_x through the whole membrane. Raman spectra recorded along the cross section at several distances from the surface suggest two additional phases next to TiO_2 anatase after gas phase synthesis together with the nanotube membranes. The most prominent modes at 352 cm^{-1} (NaP_7) and 377 cm^{-1} (NaP_{15}) of the Raman data show the simultaneous presence of NaP_7 at 9 μm and NaP_{15} at 13 μm distance from the bottom side of the membrane surface next to a signal at 145 cm^{-1} for TiO_2 anatase (E_g) (Fig. 5). By recording along the tube length characteristic signals of less intensity confirm the presence in the centre of the nanotubes up to the top membrane side, where NaP_{15} can be found at 11 and 14 μm deep into the surface. Obviously, the crystallinity was significantly reduced going deeper into the membrane.

Representative single TiO_2 nanotubes were separated from a membrane by an ultrasonication step and STEM imaging and EDS mapping was performed to corroborate the filling of the tubes with NaP_x, as shown in Fig. 6. Na and P were detected along the full tube length. CuI was used as a transport agent and can be displayed in the elemental analysis in significant amounts. Cu was only present in defined crystals attached to the membranes and it could not be detected in reasonable amounts inside the tubes. Such defined crystals are possibly formed during the transport process as side phases or represent the remaining transport agent.

The chemical vapor deposition of NaP_7 and NaP_{15} phases onto TiO_2 nanotube membranes can be verified *via* powder XRD patterns. As SEM-EDS data show, the nanotubes are filled from both sides with NaP_x phases. This can be further proved by EDS-

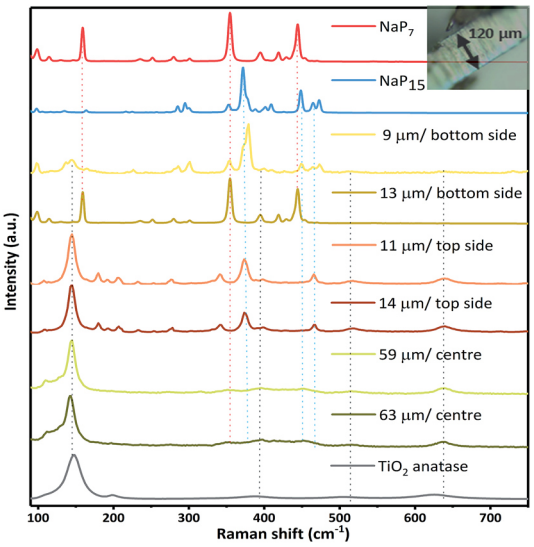

Fig. 5 Raman spectroscopy of NaP_x@TiO_2 membranes. From top to bottom: reference Raman spectrum of NaP_7 (red) and NaP_{15} (blue), and spectra of a NaP_x@TiO_2 membrane cross section measured at approx. 9 and 13 μm distance from the surface (membrane bottom side), at approx. 11 and 14 μm distance from the surface (membrane top side), at approx. 59 and 63 μm (membrane centre) and a fresh TiO_2 membrane (anatase, grey).

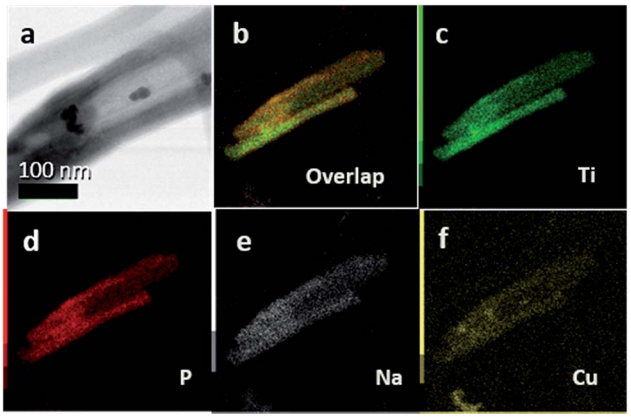

Fig. 6 (a) STEM bright-field image of TiO_2 nanotubes separated from a membrane by an ultrasonication procedure. (b) STEM-EDS shows overlaid elemental mapping of the elements Ti, P, Na and Cu. (c) Ti (representing TiO_2) nanotubes with (d) P, continuously distributed along the tubes and (e) Na substantiating the filling of the full nanotube length. (f) Cu from the mineralizer is only present in small amounts.

and Auger-results after FIB-milling into a depth of about 200 nm of the membranes. Raman spectra recorded at the center of the membrane cross section after synthesis show signals in the ranges of NaP_7 and NaP_{15} modes next to the anatase phase. After an ultrasonication process, Scanning Transmission Electron Microscopy-Energy-dispersive X-ray Spectroscopy (STEM-EDS) measurements show furthermore the presence of Na, P and Cu of the transport agent within the single tubes.

2.3 SnIP@TiO_2 nanotubes

We have further substantiated the chemical vapor deposition of the inorganic double helical semiconductor SnIP featuring a band gap of 1.86 eV on TiO_2 nanotube arrays (see Fig. 7a).[17] SnIP is anticipated to be formed from the gaseous phases of the

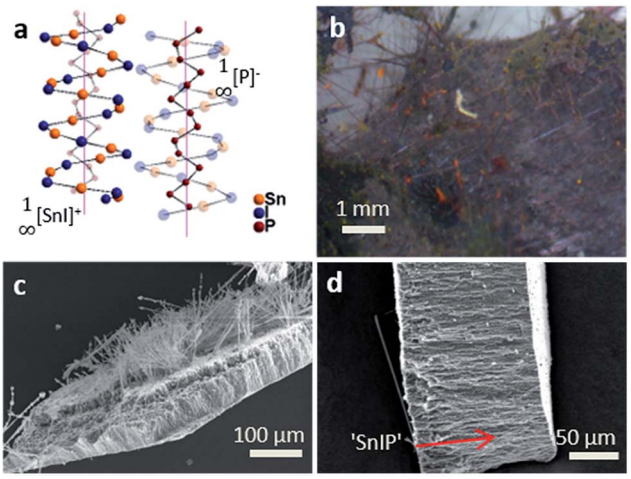

Fig. 7 (a) Structure of SnIP with two representative strands. (b) A TiO_2 nanotube membrane reacted with SnIP *via* a gas phase. (c) Cross section and surface of SnIP@TiO_2 nanotube membranes. (d) EDS of the cross section showing SnIP along the nanotubes.

precursors and a comproportionation reaction of Sn and SnI_4 to SnI_2. Therefore, no additional mineralizer was needed to cover the surface of the TiO_2 nanotube membranes with SnIP as depicted in the microscopy images in Fig. 7b and c. The SEM image substantiates the growth of SnIP on the nanotube, when detecting the elemental composition *via* EDS measurements. The detection of Sn and I was diminished going further into the tubes (Table S2†). A possible explanation is that during the transport reaction through a gas phase the formation of pure phosphorus species deeper in the nanotubes can be more likely than the double helical structure of $^1_\infty[SnI^+]$– and $^1_\infty[P^-]$– chains. Powder X-ray diffraction verifies the formation of crystalline SnIP on the TiO_2 membranes (Fig. S3†).

STEM imaging after the separation of the TiO_2 nanotubes by an ultrasonication process shows a set of nanotubes with a size of ~80–100 nm per tube. Elemental mapping confirms Ti (representing TiO_2), P, Sn, and I with a distribution of P along the tube length. Sn and I appear to be present in smaller amounts in a TiO_2 tube (Fig. 8).

SnIP was grown successfully onto and into TiO_2 nanotube arrays *via* a gas phase as verified using powder X-ray diffraction and SEM-EDS. The transportation of the ternary compounds into the nanotubes was demonstrated with STEM-EDS analysis.

2.4 XPS studies

We performed XPS studies on the pure semiconductors NaP_x, SnIP and $(CuI)_3P_{12}$ and the three semiconductor@TiO_2 nanotube heterostructures in order to verify the surface compositions, binding energies and oxidation states of the materials (Fig. S7–S9 and Table S6†). All oxidation states in the heterostructure systems are consistent with the ones observed for the pure compounds along with surface oxidized phosphates (P_xO_y). In the case of (NaP_7, NaP_{15})@TiO_2 we found a shift of the Na1s peak in NaP_7@TiO_2 to higher binding energy which might be due to partial charge transfer from NaP_7 to the surface of TiO_2 and doping of the TiO_2 surface with Na^+ ions to some extent. The peak positions of Ti and O remained unchanged upon semiconductor loading into the tubes (Fig. S7†). A comparable charge transfer behaviour was observed for the $(CuI)_3P_{12}$@TiO_2 heterostructure compound (see Fig. S8†).

XPS spectra of SnIP@TiO_2 do not show any significant change of the Sn, I and P peaks which we interpret as the absence of significant bonding interaction between the two phases (shown in Fig. S9†).

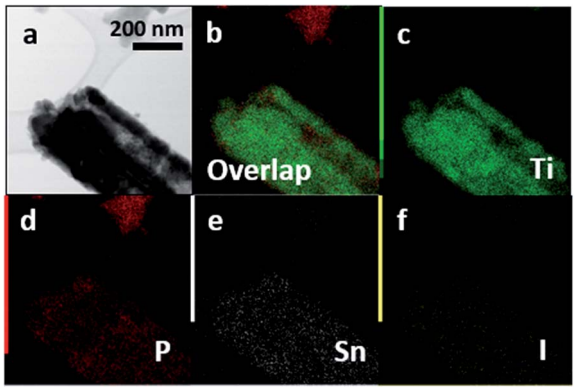

Fig. 8 (a) STEM bright-field image of TiO_2 nanotubes separated from a membrane by an ultrasonication procedure. (b) Elemental mapping of overlaid elements Ti (representing TiO_2), P, Sn and I. (c) Ti and (d) P substantiating P distributed along the length of TiO_2 nanotubes with (e) Sn and (f) I in small amounts.

2.5 UV-Vis spectra

The absorption properties of materials in the UV-Vis region were determined by diffuse reflectance UV-Vis spectroscopy (Fig. S6a†). The absorption spectra of TiO_2 nanotubes show an intense band at 330 nm with band tailing up to 384 nm, which corresponds to a valence band to conduction band (O2p → Ti3d) transition.[45,46] The UV-Vis spectra of NaP_7 displayed broad absorption in the visible region extended up to 800 nm, which is attributed to charge generation in the phosphide chain motif. The NaP_7@TiO_2 heterostructures displayed an absorption band which corresponded to TiO_2 along with an absorption profile in the visible region due to the presence of NaP_7. Pristine SnIP displayed a broad absorption edge up to 700 nm which is shifted up to 500 nm in SnIP@TiO_2, with a slight increase in the absorption profile at higher wavelengths (Fig. S10†). The UV-Vis spectra of pristine $(CuI)_3P_{12}$ show an intense absorption edge extended up to 440 nm which is slightly decreased in $(CuI)_3P_{12}$@TiO_2 samples (Fig. S10†). To probe the visible light absorption of the samples, the optical band gap of each material was determined using a Tauc plot by plotting a graph of $(\alpha h\nu)^{1/2}$ *vs.* $h\nu$ followed by extrapolation of a linear tangent to the abscissa, where α is the absorption coefficient, h is the Planck constant, and ν is the light frequency (Fig. S10†). The band gaps for TiO_2, NaP_7, NaP_7@TiO_2, SnIP, SnIP@TiO_2, $(CuI)_3P_{12}$ and $(CuI)_3P_{12}$@TiO_2 (see Table 1) are in close agreement with reported values. Due to the band gap values a certain absorption in the visible light region is present (Fig. S6†).

2.6 Photocatalytic activity measurement

The photocatalytic performance of the hybrid materials was discerned by photoelectrochemical water splitting experiments. A three-electrode configuration was used, composed of pristine/hybrid materials deposited on FTO glass as the photoanode, Pt as the cathode and Ag/AgCl as the reference electrode, all immersed in a 0.1 M KOH electrolyte. The photoanode was irradiated with AM1.5 G solar simulated light having a power density of 100 mW cm^{-2} on the surface of the sample. The photocurrent density per cm^2 was measured in linear sweep voltammetry (LSV) mode by switching the applied bias from −1.0 V to +0.8 V *vs.* Ag/AgCl. The dark current was also measured to compare the photoelectrochemical response. At an applied bias of 0.6 V *vs.* Ag/AgCl (1.23 V *vs.* RHE which is the water oxidation potential), the photocurrent density values of TiO_2, NaP_7, NaP_7@TiO_2, SnIP, SnIP@TiO_2, $(CuI)_3P_{12}$ and $(CuI)_3P_{12}$@TiO_2 are shown in Table 1. Under dark conditions the current density remains almost zero, while after irradiation under solar simulated light bare TiO_2 shows extremely low photocurrent (0.21 mA cm^{-2}) which is in good agreement with

Table 1 Energies of band gaps, values of photocurrent density, maximum ABPE, IPCE, and APCE in % of TiO_2 nanotubes, NaP_7, NaP_7@TiO_2, SnIP, SnIP@TiO_2, $(CuI)_3P_{12}$ and $(CuI)_3P_{12}$@TiO_2 obtained by UV-Vis, linear sweep voltammetry and corresponding calculations

Sample	Band gap [eV]	Photocurrent density [mA cm^{-2}]	Max ABPE [%]	IPCE [%]	APCE [%]
TiO_2	3.05	0.21	0.07	0.007	0.01
NaP_7	1.28	0.20	0.04	0.04	0.06
NaP_7@TiO_2	1.87	0.22	0.05	0.36	0.43
SnIP	1.84	0.20	0.02	2.0	0.46
SnIP@TiO_2	2.22	0.84	0.20	0.20	3.2
$(CuI)_3P_{12}$	2.84	0.41	0.06	0.46	0.78
$(CuI)_3P_{12}$@TiO_2	2.73	0.43	0.09	0.48	1.19

its large band gap (~3.2 eV), as shown in Fig. 9a. Similarly, the photocurrent density for bare NaP_7, $(CuI)_3P_{12}$ and SnIP remained low due to the inability of poorly oxidative holes to facilitate water splitting. Thus, the order of performance is SnIP > $(CuI)_3P_{12}$ > NaP_7. Furthermore, the hybrids NaP_7@TiO_2 and $(CuI)_3P_{12}$@TiO_2 also displayed a small improvement in photocatalytic performance over the pristine phosphide material which might be due to unfavourable Fermi level alignment resulting in sluggish charge separation. However, hybrids of SnIP phosphides with TiO_2 (SnIP@TiO_2) demonstrated a much higher photocurrent density (0.82 mA cm^{-2}) than individual components and NaP_7@TiO_2 and $(CuI)_3P_{12}$@TiO_2; this suggests the formation of a heterojunction and feasible transfer of electrons and holes. The higher photocurrent for SnIP@TiO_2 is attributed to better coverage of the TiO_2 surface by SnIP and more long-range ordering of the SnIP helix which facilitates faster charge injection into the conduction band of TiO_2. To validate the photoresponse of materials, the photocurrent was measured during a light on–off cycle, which clearly demonstrated the materials' photo-responsive nature (Fig. S11†). Furthermore, the ability to drive water splitting at longer wavelengths was proved by measuring the photocurrent response of the materials under 425 nm and 505 nm wavelength light irradiation having a power density of 54.15 and 40.48 mW cm^{-2}, respectively, at the surface of the samples (Fig. 9b). Again, the highest photocurrent density (0.32 mA cm^{-2} at 450 nm and 0.34 mA cm^{-2} at 505 nm) was obtained for the SnIP@TiO_2 composite (Fig. 9b). Furthermore, on–off experiments clearly confirmed the higher wavelength response of the SnIP@TiO_2 composite (Fig. S12†).

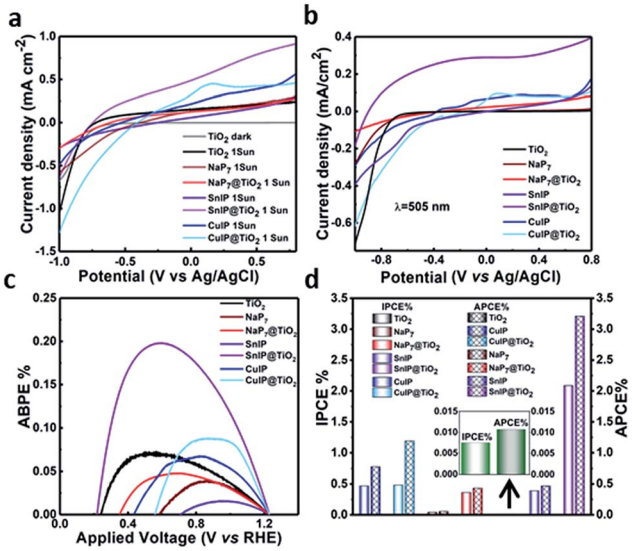

Fig. 9 (a) Linear sweep voltammogram of TiO_2 under dark conditions and under 1 solar simulated AM1.5 G light irradiation (100 mW cm^{-2}) for bare TiO_2 nanotubes, NaP_7, NaP_7@TiO_2, SnIP, SnIP@TiO_2, $(CuI)_3P_{12}$, and $(CuI)_3P_{12}$@TiO_2. (b) Photocurrent density *vs.* applied voltage plot under 505 nm LED light irradiation (40.5 mW cm^{-2}) of TiO_2 nanotubes, NaP_7, NaP_7@TiO_2, SnIP, SnIP@TiO_2, $(CuI)_3P_{12}$, and $(CuI)_3P_{12}$@TiO_2. (c) ABPE% *vs.* RHE plot under AM1.5 G light irradiation (100 mW cm^{-2}) for TiO_2 nanotubes, NaP_7, NaP_7@TiO_2, SnIP, SnIP@TiO_2, $(CuI)_3P_{12}$, and $(CuI)_3P_{12}$@TiO_2. (d) IPCE% under 505 nm LED light irradiation (40.5 mW cm^{-2}) for TiO_2, NaP_7, NaP_7@TiO_2, SnIP, SnIP@TiO_2, $(CuI)_3P_{12}$, and $(CuI)_3P_{12}$@TiO_2 and APCE% under 505 nm LED light irradiation (40.5 mW cm^{-2}) for TiO_2 nanotubes, $(CuI)_3P_{12}$, $(CuI)_3P_{12}$@TiO_2, NaP_7, NaP_7@TiO_2, SnIP, and SnIP@TiO_2. Color: TiO_2 under dark conditions (black), TiO_2 and under AM1.5 G light irradiation TiO_2 nanotubes (grey), NaP_7 (brown), NaP_7@TiO_2 (red), SnIP (violet), SnIP@TiO_2 (pink), $(CuI)_3P_{12}$ (deep blue), and $(CuI)_3P_{12}$@TiO_2 (light blue) (CuIP ⇒ $(CuI)_{12}P_3$).

To quantify the material system/interface performance, the following diagnostic efficiencies were measured according to derivations given in the ESI.† The maximum applied bias photon-to-current efficiency percentage (ABPE%) for TiO_2, NaP_7, NaP_7@TiO_2, SnIP, SnIP@TiO_2, $(CuI)_3P_{12}$ and $(CuI)_3P_{12}$@TiO_2 was calculated and is listed in Table 1 (Fig. 9c). SnIP@TiO_2 nanohybrids show the highest performance (3.2%) which was much higher than that of the other hybrids. Furthermore, the ABPE% of SnIP@TiO_2 was 10 times higher than that of pristine SnIP which demonstrates that hybrid material formation with TiO_2 increased photocatalytic performance significantly.

The incident photon-to-current efficiency percentage (IPCE%) and absorbed photon-to-current efficiency percentage (APCE%) for TiO_2, NaP_7, NaP_7@TiO_2, SnIP, SnIP@TiO_2, $(CuI)_3P_{12}$ and $(CuI)_3P_{12}$@TiO_2, listed in Table 1, demonstrate that heterostructure formation overall improves the photocatalytic performance of materials in the visible regime.

To gain insight into the charge transfer mechanisms in the materials and determine the band structure of the materials, work function spectra and valence band spectra were recorded using ultraviolet photoelectron spectroscopy (UPS). The work

function was calculated using the expression WF (ϕ) = 21.21 − $E_{cut\text{-}off}$, where 21.21 eV is the energy of the incident He(I) line of a He discharge lamp, and $E_{cut\text{-}off}$ is the cut-off energy of secondary electrons. The point of intersection after extrapolation of the linear regions of the graphs results in the cut-off energy values. From the graph, the cut-off energy and value of work function for TiO_2, NaP_7, NaP_7@TiO_2, $(CuI)_3P_{12}$, $(CuI)_3P_{12}$@TiO_2, SnIP and SnIP@TiO_2 are listed in Table 2 (Fig. 10 and insets). It should be noted that unexpectedly, we observe that the WF of the NaP_7@TiO_2 and SnIP@TiO_2 hybrids falls above and below that of the pristine materials, respectively. This may be due to small amounts of metal-ion surface doping in the hybrids, where Na^+ decreases the charge density on TiO_2 and Sn^{2+} increases the charge density on TiO_2; on the other hand, Cu^+ is a closed-shell d-block element with a similar charge distribution to Ti^{4+}, which may explain why this effect does not seem to be observed as strongly in this case. Furthermore, based on the P 2p region in NaP_7, a higher degree of oxidation seems to occur in the pristine material compared to its hybrid here, changing the charge distribution on the phosphide backbone, and shifting the WF. The position of valence band maxima (VB_{max}) obtained from UPS valence band spectra of NaP_7, NaP_7@TiO_2, $(CuI)_3P_{12}$, $(CuI)_3P_{12}$@TiO_2, SnIP and SnIP@TiO_2 is also shown in Table 2 (Fig. 10, inset). Furthermore, the valence band position of bare TiO_2 nanotubes determined from XPS valence band spectra was found to be 3.15 eV below the Fermi level (Fig. S9†).

On the basis of the obtained band structure and band gap, we have proposed a plausible mechanism of improved photocatalytic performance of polyphosphide@TiO_2 materials (Fig. 10). In general, to achieve efficient water splitting the conduction band position of the semiconductor should be more negative than 0.00 V *vs.* NHE at pH-0 (reduction potential of protons, H^+/H_2) and overpotential, while the valence band position should be more positive than +1.23 V *vs.* NHE at pH-0 (oxidation potential of water, H_2O/O_2). So, the band gap of the materials should be wider than 1.23 eV. TiO_2 has a wide band gap of approximately 3.2 eV with appropriate band positions (conduction band, E_{CB}; −0.26 V and valence band, E_{VB}; +2.94 V *vs.* NHE at pH 0) to drive the water splitting reaction; however, its large band gap means the photocatalytic response of TiO_2 remains too low under visible irradiation. On the other hand, inorganic phosphides (NaP_7, $(CuI)_3P_{12}$ and SnIP) absorb

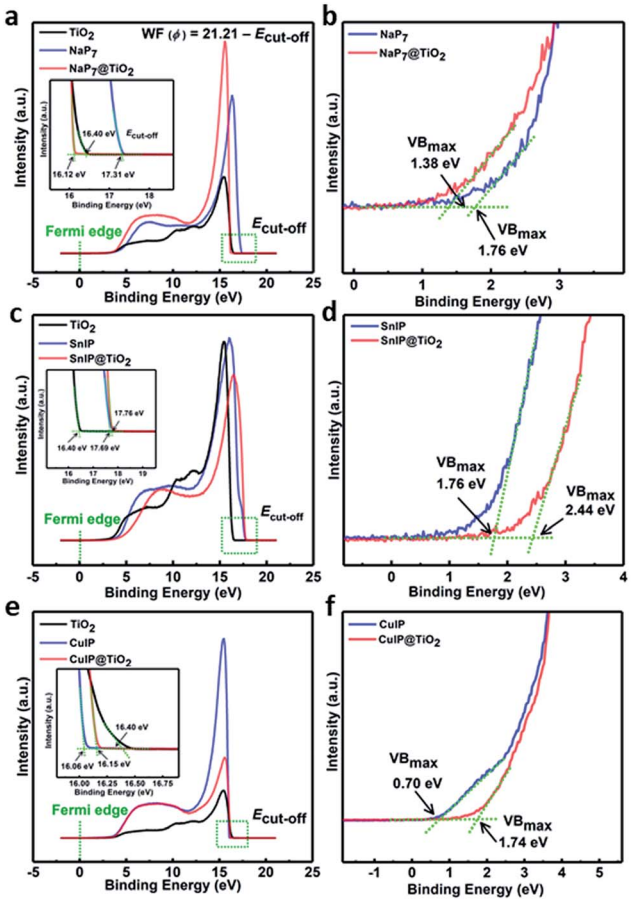

Fig. 10 UPS work function spectra and inset showing the cut-off energy ($E_{cut\text{-}off}$) of (a) TiO_2 nanotube membranes, NaP_7 and NaP_7@TiO_2, (c) TiO_2 nanotube membranes, SnIP and SnIP@TiO_2, and (e) TiO_2 nanotube membranes, $(CuI)_3P_{12}$ and $(CuI)_3P_{12}$@TiO_2. The value of work function (WF) was determined from the UPS work function spectra by using the equation WF (ϕ) = 21.21 − $E_{cut\text{-}off}$, where 21.21 eV is the energy of the incident He(I) line of a He discharge lamp used for UPS. UPS valence band spectra showing valence band maxima below the Fermi level of (b) NaP_7 and NaP_7@TiO_2, (d) SnIP and SnIP@TiO_2 and (f) $(CuI)_3P_{12}$ and $(CuI)_3P_{12}$@TiO_2) (CuIP ⇒ $(CuI)_{12}P_3$).

Table 2 Secondary electron cut-off energies ($E_{cut\text{-}off}$), values of work function (WF) and valence band maxima (VB_{max}) obtained from UPS measurements of TiO_2 nanotubes, NaP_7, NaP_7@TiO_2, SnIP, SnIP@TiO_2, $(CuI)_3P_{12}$ and $(CuI)_3P_{12}$@TiO_2

Sample	$E_{cut\text{-}off}$ [eV]	WF [eV]	VB_{max}
TiO_2	16.40	4.81	3.15
NaP_7	17.31	3.90	1.76
NaP_7@TiO_2	16.12	5.09	1.38
SnIP	17.69	3.52	1.76
SnIP@TiO_2	17.76	3.45	2.44
$(CuI)_3P_{12}$	16.06	5.15	0.70
$(CuI)_3P_{12}$@TiO_2	16.15	5.06	1.74

well in the UV-Vis region to generate electron–hole pairs due to their low band gap (1.28, 2.84 and 1.86 eV) (Fig. S6†). From the Mott–Schottky measurements, the flat band potential values for NaP_7, $(CuI)_3P_{12}$ and SnIP were found to be −0.670, −0.721 and −0.730 V, respectively, *vs.* Ag/AgCl, which might be considered the position of the conduction band, E_{CB} (Table 2). As the band position is usually expressed on the NHE scale in water splitting, the conduction band position of NaP_7, $(CuI)_3P_{12}$ and SnIP was calculated to be −0.471, −0.522 and −0.531 V, respectively, *vs.* NHE at pH 0. By taking the band gap and conduction band position into account, the estimated valence band position for NaP_7, $(CuI)_3P_{12}$ and SnIP was found to be +0.809, +2.318 and +1.309 V, respectively, *vs.* NHE at pH 0. These values indicate that the valence band positions of NaP_7 and SnIP are not positive enough to afford water oxidation, while the valence band position of $(CuI)_3P_{12}$ was slightly more positive than the water oxidation potential and thus generates poorly oxidizing

holes. This explains the observed negligibly small photocurrent for pristine NaP_7 and SnIP, and the slightly improved photocurrent for $(CuI)_3P_{12}$. After hybrid material formation, the photocatalytic performance of NaP_7@TiO_2, $(CuI)_3P_{12}$@TiO_2 and SnIP@TiO_2 was improved (Fig. 9d). However, SnIP@TiO_2 displayed a much greater rise in photocurrent compared to the other hybrid nanostructures. The improved photocurrent response can possibly be explained based on the Fermi level alignment between heterojunctions, charge carrier concentration, flat band potential and position of the valence band. This feature has been observed for fibrous red phosphorus@TiO_2 and black phosphorus@TiO_2 hybrids.[47] A drastic improvement of the photocatalytic activity was also reported for SnIP@C_3N_4 heterostructures where an ideal contact between the two materials is realized by a self-assembly process.[48] Additional experiments are planned to substantiate this assumption for the titular compounds. Mott–Schottky analysis shows a shift in the flat band potential from −0.471 and −0.522 V *vs.* NHE in pristine NaP_7 and $(CuI)_3P_{12}$ to −0.581 and −0.493 V *vs.* NHE in NaP_7@TiO_2 and $(CuI)_3P_{12}$@TiO_2 which implies a possible Fermi level alignment (flow of electrons from one semiconductor to another for equilibrating the Fermi level position), and the conduction band shifted slightly due to downward band bending in NaP_7 and $(CuI)_3P_{12}$ and upward band bending in TiO_2, respectively, (see Fig. S17 in the ESI†). Interestingly, the conduction band position (E_{CB}) of SnIP (−0.531 V) was shifted drastically toward a more negative potential in SnIP@TiO_2 (−1.731 V), which reveals more prominent band bending. The higher band bending and more negative conduction band position in SnIP@TiO_2 lead to more efficient charge separation, which facilitated superior water splitting.

From the UPS VB spectra, the VB_{max} position of SnIP@TiO_2 was found to be deeper than that of NaP_7@TiO_2 and $(CuI)_3P_{12}$@TiO_2 which suggests the generation of more oxidative holes in the SnIP@TiO_2 heterostructure to drive water splitting (Fig. 10). Additionally, the depletion width for SnIP@TiO_2 was found to be 922.89 nm which demonstrates an effective inbuilt electrical field in the space charge region; this value was much higher than that of NaP_7@TiO_2 (118.95 nm) and $(CuI)_3P_{12}$@TiO_2 (157.14 nm), and clearly supports better charge transfer in SnIP@TiO_2 (Table 2). Furthermore, the recombination lifetime of photoexcited species plays an important role in photocatalysis and a long lifetime is expected for better photocatalytic performance. The longer recombination lifetime of SnIP@TiO_2 (2.40 μs) in comparison to NaP_7@TiO_2 (1.90 μs) and $(CuI)_3P_{12}$@TiO_2 (1.90 μs) signifies the availability of more electrons and holes to drive hydrogen evolution and water oxidation reactions (Table 2). The morphological and surface coverage might be responsible for the higher performance of the SnIP@TiO_2 nanostructure. SnIP has a helical structure composed of an inner P helix $^1_\infty[P^-]$ chain and an outer helical $^1_\infty[SnI^+]$ helix winding together in long range ordering which generates a rod like structure. Due to long range ordering in 1D SnIP, better charge mobility can be achieved relative to short range NaP_7 and $(CuI)_3P_{12}$ resulting in better charge transfer to TiO_2. The occupancy of the nanotubes was also much higher in NaP_7@TiO_2 and $(CuI)_3P_{12}$@TiO_2 than SnIP@TiO_2, which might reduce the effective exposed surface area to light and electrolyte semiconductor interface contact leading to lower photocatalytic performance.

3. Conclusions

A gas-phase transport reaction was employed as an effective method to deposit complex binary and ternary polyphosphide compounds into TiO_2 nanotube arrays. The underlying short-way transport reaction by mineralization is a viable approach for the synthesis of hybrid materials. Three different substances, binary sodium polyphosphides, ternary SnIP, and $(CuI)_3P_{12}$, were successfully reacted with electrochemically fabricated TiO_2 nanotube membranes. The synthesized polyphosphides onto and into the TiO_2 nanotubes were analyzed with several spectroscopic and diffraction methods such as XRD, EDS-analysis, XPS, Auger electron and Raman spectroscopy and STEM analysis. SEM, HR-TEM, Auger electron spectroscopy, and elemental mapping of intact and cross sections of nanohybrids substantiated the successful deposition of materials inside the tube with excellent occupancy (a filling grade of ~50%).

STEM followed by EDS analysis proved the presence of the binary NaP_x phase as well as $(CuI)_3P_{12}$ along the full length of the TiO_2 nanotubes. STEM-EDS experiments of the ternary phase SnIP showed a higher distribution of P than Sn and I along TiO_2 nanotubes. Raman spectra recorded at the surface and along the razor-cut cross section of the nanotubes can verify the growth of NaP_x phases continuously along the nanotubes (120 μm in length) and $(CuI)_3P_{12}$ up to 22 μm into the nanotubes (63 μm in length). The herein reported hybrid materials displayed enhanced photoelectrochemical water splitting performance under visible light compared to individual components due to the possible formation of a heterojunction facilitating better charge separation. Considering the unusual values of the WF of NaP_7@TiO_2 and SnIP@TiO_2, further study of the interfaces may be warranted. Nevertheless, lower electronic bandgaps, negative conduction band positions of the composites, long recombination lifetime, better charge carrier mobility and deep valence band positions were responsible for improved visible light performance. This feature may lead to higher conversion efficiencies for optoelectronic applications such as in photodetectors, photovoltaics, photo-electrochemical catalysts and sensors. With a special focus on the mineralization concept, further heterostructures between 1D semiconductors and nanostructured materials are being prepared.

Authors contribution

E. Ü. and R. K. synthesized the polyphosphide hybrid materials and characterized them using Helium Microscopy, SEM, and STEM-EDS. P. Kumar performed XPS, UPS and photoelectrochemical studies and was involved in the interpretation of the obtained results. U. K. T. carried out the KPFM measurements. P. Kar was responsible for the electrochemical characterization. K. S. and T. N. supervised the research and edited the manuscript. All authors were involved in writing their respective parts.

Conflicts of interest

There are no conflicts to declare.

Abbreviations

CuIP	$(CuI)_3P_{12}$
SEM	Scanning electron microscopy
EDS	Energy dispersive X-ray spectroscopy
FIB	Focused ion beam
HR-TEM	High resolution transmission electron microscopy
XRD	X-ray diffraction
XPS	X-ray photoelectron spectroscopy
STEM	Scanning transmission electron microscopy
ITO	Indium-doped tin oxide
FTO	Fluorine-doped tin oxide
UV-Vis	Ultraviolet-visible spectroscopy
NHE	Normal hydrogen electrode

Acknowledgements

This work has been performed as part of the international graduate school ATUMS (IRTG 2022) funded by the DFG and NSERC. The assistance in Helium ion microscopy (with Ga-FIB), AES, and STEM-EDS by Peng Li, Shihong Xu and Anqiang He from the nanoFab at the University of Alberta is gratefully acknowledged. We like to thank Anna Vogel for Raman spectroscopy of the samples. The authors would like to thank the Natural Sciences and Engineering Research Council of Canada (NSERC), the National Research Council Canada (NRC), Future Energy Systems (FES) and CMC Microsystems for direct and indirect (equipment use) financial support. Pawan Kumar is thankful to Future Energy systems for providing the post-doctoral fellowship. Dr Kazi Alam is kindly acknowledged for the DR UV-Vis measurement. The use of Prof. Thomas Thundat's scanning probe microscope for the KPFM measurements is gratefully acknowledged.

References

1 T. Hisatomi, J. Kubota and K. Domen, *Chem. Soc. Rev.*, 2014, **43**, 7520–7535.
2 P. Kalisman, Y. Nakibli and L. Amirav, *Nano Lett.*, 2016, **16**, 1776–1781.
3 K. Iwashina and A. Kudo, *J. Am. Chem. Soc.*, 2011, **133**, 13272–13275.
4 M. Higashi, K. Domen and R. Abe, *J. Am. Chem. Soc.*, 2012, **134**, 6968–6971.
5 J. Schneider, M. Matsuoka, M. Takeuchi, J. Zhang, Y. Horiuchi, M. Anpo and D. W. Bahnemann, *Chem. Rev.*, 2014, **114**, 9919–9986.
6 Y. Ma, X. Wang, Y. Jia, X. Chen, H. Han and C. Li, *Chem. Rev.*, 2014, **114**, 9987–10043.
7 J. Tang, J. R. Durrant and D. R. Klug, *J. Am. Chem. Soc.*, 2008, **130**, 13885–13891.
8 S. J. A. Moniz, S. A. Shevlin, D. J. Martin, Z.-X. Guo and J. Tang, *Energy Environ. Sci.*, 2015, **8**, 731–759.
9 K. Iwashina, A. Iwase, Y. H. Ng, R. Amal and A. Kudo, *J. Am. Chem. Soc.*, 2015, **137**, 604–607.
10 Z. Yu, F. Li and L. Sun, *Energy Environ. Sci.*, 2015, **8**, 760–775.
11 Y.-C. Pu, G. Wang, K.-D. Chang, Y. Ling, Y.-K. Lin, B. C. Fitzmorris, C.-M. Liu, X. Lu, Y. Tong, J. Z. Zhang, Y.-J. Hsu and Y. Li, *Nano Lett.*, 2013, **13**, 3817–3823.
12 M. Ge, Q. Li, C. Cao, J. Huang, S. Li, S. Zhang, Z. Chen, K. Zhang, S. S. Al-Deyab and Y. Lai, *Adv. Sci.*, 2017, **4**, 1600152.
13 R. Singh, R. Bapat, L. Qin, H. Feng and V. Polshettiwar, *ACS Catal.*, 2016, **6**, 2770–2784.
14 M. Bawohl and T. Nilges, *Z. Anorg. Allg. Chem.*, 2015, **641**, 304–310.
15 M. Bawohl, P. Schmidt and T. Nilges, *Inorg. Chem.*, 2013, **52**, 11895–11901.
16 M. P. Baumgartner, Dissertation (Dr. rer. nat.), Technische Universität München, 2017.
17 D. Pfister, K. Schäfer, C. Ott, B. Gerke, R. Poettgen, O. Janka, M. Baumgartner, A. Efimova, A. Hohmann, P. Schmidt, S. Venkatachalam, L. van Wuellen, U. Schürmann, L. Kienle, V. Duppel, E. Parzinger, B. Miller, J. Becker, A. Holleitner, R. Weihrich and T. Nilges, *Adv. Mater.*, 2016, **28**, 9783–9791.
18 C. Grotz, M. Köpf, M. Baumgartner, L. A. Jantke, G. Raudaschl-Sieber, T. F. Fässler and T. Nilges, *Z. Anorg. Allg. Chem.*, 2015, **641**, 1395–1399.
19 M. Schöneich, A. Hohmann, P. Schmidt, F. Pielnhofer, F. Bachhuber, R. Weihrich, O. Osters, M. Köpf and T. Nilges, *Z. Kristallogr. - Cryst. Mater.*, 2017, **232**, 91–105.
20 S. Lange, M. Bawohl, R. Weihrich and T. Nilges, *Angew. Chem., Int. Ed.*, 2008, **47**, 5654–5657.
21 A. Utrap, N. Y. Xiang and T. Nilges, *J. Cryst. Growth*, 2017, **475**, 341–345.
22 C. Grotz, K. Schäfer, M. Baumgartner, R. Weihrich and T. Nilges, *Inorg. Chem.*, 2015, **54**, 10794–10800.
23 A. Pfitzner and E. Freudenthaler, *Angew. Chem., Int. Ed.*, 1995, **34**, 1647–1649.
24 D. Regonini, C. R. Bowen, A. Jaroenworaluck and R. Stevens, *Mater. Sci. Eng., R*, 2013, **74**, 377–406.
25 R. Hahn, J. Macak and P. Schmuki, *Electrochem. Commun.*, 2007, **9**, 947–952.
26 P. Kar, Y. Zhang, S. Farsinezhad, A. Mohammadpour, B. D. Wiltshire, H. Sharma and K. Shankar, *Chem. Commun.*, 2015, **51**, 7816–7819.
27 B. M. Rao and S. C. Roy, *J. Phys. Chem. C*, 2013, **118**, 1198–1205.
28 V. Galstyan, A. Vomiero, E. Comini, G. Faglia and G. Sberveglieri, *RSC Adv.*, 2011, **1**, 1038–1044.
29 S. Farsinezhad, A. Mohammadpour, A. N. Dalrymple, J. Geisinger, P. Kar, M. J. Brett and K. Shankar, *J. Nanosci. Nanotechnol.*, 2013, **13**, 2885–2891.
30 S. Farsinezhad, A. N. Dalrymple and K. Shankar, *Phys. Status Solidi A*, 2014, **211**, 1113–1121.
31 X. Chen, M. Schriver, T. Suen and S. S. Mao, *Thin Solid Films*, 2007, **515**, 8511–8514.

32 A. Mohammadpour and K. Shankar, *J. Mater. Chem.*, 2010, **20**, 8474–8477.
33 D. Routkevitch, T. Haslett, L. Ryan, T. Bigioni, C. Douketis and M. Moskovits, *Chem. Phys.*, 1996, **210**, 343–352.
34 Y. Peng, D.-H. Qin, R.-J. Zhou and H.-L. Li, *Mater. Sci. Eng., B*, 2000, **77**, 246–249.
35 D. Xu, X. Shi, G. Guo, L. Gui and Y. Tang, *J. Phys. Chem. B*, 2000, **104**, 5061–5063.
36 M. Lu, M.-K. Li, L.-B. Kong, X.-Y. Guo and H.-L. Li, *Composites, Part B*, 2004, **35**, 179–184.
37 A. Mohammadpour, P. Kar, B. D. Wiltshire, A. M. Askar and K. Shankar, *Curr. Nanosci.*, 2015, **11**, 593–614.
38 N. S. Lewis, *Science*, 2007, **315**, 798–801.
39 X. Zhang, F. Han, B. Shi, S. Farsinezhad, G. P. Dechaine and K. Shankar, *Angew. Chem., Int. Ed.*, 2012, **51**, 12732–12735.
40 D. Zhou, Z. Chen, Q. Yang, C. Shen, G. Tang, S. Zhao, J. Zhang, D. Chen, Q. Wei and X. Dong, *ChemCatChem*, 2016, **8**, 3064–3073.
41 X. Fu, Z. Ji, C. Li and Z. Zhou, *J. Alloys Compd.*, 2016, **688**, 1013–1018.
42 Z. Lou, F. Li, J. Deng, L. Wang and T. Zhang, *ACS Appl. Mater. Interfaces*, 2013, **5**, 12310–12316.
43 P. Qin, M. Paulose, M. I. Dar, T. Moehl, N. Arora, P. Gao, O. K. Varghese, M. Grätzel and M. K. Nazeeruddin, *Small*, 2015, **11**, 5533–5539.
44 U. K. Thakur, R. Kisslinger and K. Shankar, *Nanomaterials*, 2017, **7**, 95.
45 Z. Xiong, H. Wang, N. Xu, H. Li, B. Fang, Y. Zhao, J. Zhang and C. Zheng, *Int. J. Hydrogen Energy*, 2015, **40**, 10049–10062.
46 J. Low, B. Cheng and J. Yu, *Appl. Surf. Sci.*, 2017, **392**, 658–686.
47 E. Üzer, P. Kumar, R. Kisslinger, P. Kar, U. K. Thakur, S. Zeng, K. Shankar and T. Nilges, *ACS Appl. Nano Mater.*, 2019, DOI: 10.1021/acsanm.9b00221.
48 C. Ott, F. Reiter, M. Baumgartner, M. Pielmeier, A. Vogel, P. Walke, S. Burger, M. Ehrenreich, G. Kieslich, D. Daisenberger, J. Armstrong, U. K. Thakur, P. Kumar, S. Chen, D. Donadio, L. S. Walter, R. T. Weitz, K. Shankar and T. Nilges, *Adv. Funct. Mater.*, 2019, **29**, 1900233.

Supporting Information

Vapor growth of binary and ternary phosphorus-based semiconductors into TiO_2 nanotube arrays and application in visible light driven water splitting

Ebru Üzer,[a] Pawan Kumar,[b†] Ryan Kisslinger,[b†] Piyush Kar,[b] Ujwal Kumar Thakur,[b] Karthik Shankar, [b,*] and Tom Nilges [a,*]

[a.] *Department of Chemistry, Technical University of Munich, Lichtenbergstr. 4, 85748 Garching b. München, Germany; E-mail: tom.nilges@lrz.tum.de*
[b.] *Department of Electrical and Computer Engineering, 9211-116 Street NW, Edmonton, Alberta, Canada T6G 1H9; E-mail: kshankar@ualberta.ca*
†Contributed equally

1. Experimental details

Fabrication of TiO_2 nanotube membranes

TiO_2 nanotube membranes were fabricated through anodization.[1] Titanium foil was used as both the anode and cathode; the anode was 4 cm long and 1 cm wide, while the cathode was 2 cm long and 0.5 cm wide. Both the cathode and anode were 0.89 mm thick. The electrolyte was comprised of 97:3 v/v ethylene glycol and deionized water, with 0.03 wt.% NH_4F added in. The electrolyte was stirred vigorously before anodization. The anode and cathode were spaced 2 cm in the solution, and the 100 mL beaker containing the electrolyte submerged in a water bath for cooling. A voltage of 60 V was applied for 3 d to create the nanotube arrays; they were then dipped in methanol for cleaning, and the 0.89 mm thick sides of the anodized pieces scratched off with a razor to allow them to delaminate during subsequent air drying. To open the bottoms of the nanotubes and clean the tops of any debris, the delaminated nanotube arrays (membranes) were subjected to reactive ion etching using Oxford PlasmaPro NGP80. An SF_6 etch using a pressure of 20 mTorr and a forward power of 250 W was used for 200 s on the top and 300 s on the bottom (see Results and Discussion for explanation of our top versus bottom terminology). An oxygen cleaning using a pressure of 150 mTorr and a forward power of 225 W for 10 min was used on each side.

Synthesis of hybrid NaP_x@TiO_2 nanotube membranes

The chemical vapour deposition of NaP_7 and NaP_{15} on TiO_2 nanotube membranes was synthesized according to literature procedures.[2] A mixture of the elements sodium and red phosphorus in the atomic ratio of 1:7 was prepared by transferring red Phosphorus (452.1 mg, 99.999+%, Chempur) and Sodium (47.9 mg, 99,95% in oil, Aldrich) into a silica-glass tube (0.8 cm inner diameter, 8 cm length). Into the previously graphitized glass tube, purified CuI (10 mg) together with TiO_2 nanotube membranes was added. The ampoule was sealed under vacuum ($p < 10^{-3}$ mbar) and placed horizontally in the chamber of a muffle furnace to obtain a temperature gradient of approx. 10 K. By locating the starting materials in the hot zone of a Nabertherm muffle furnace (L3/11/330) and TiO_2 nanotube membranes in the colder zone, a dissolution *via* gas phase and deposition on the TiO_2 nanotube membranes was attempted. The furnace was set to 823 K within 10 h and held at this temperature for 7 d. The products were formed after cooling down by switching off the furnace. Deposition of thin red-brown fibres on the TiO_2 nanotube arrays were observed. Red, block-like crystals of NaP_7 were formed simultaneously.
Purification of the mineralizer CuI was carried out by solving CuI (98+%, Chempur) in concentrated HI (57 %, Riedel de Häen) and following precipitation in water. The precipitate was purified by washing twice with water and ethanol and subsequently dried under vacuum.

Synthesis of hybrid SnIP@TiO_2 nanotube membranes

The preparation of hybrid SnIP@TiO_2 nanotube membranes was carried out following the bulk-SnIP literature procedure.[3] The starting materials Sn (107.8 mg, 99,999%, Chempur), SnI_4 (189.6 mg, synthesized according to literature procedures),[4] and red phosphorus (37.5 mg, 99.999+%, Chempur) were pressed into a pellet (diameter: 10 mm, 25 MPa for 15 min). The pellet and TiO_2 nanotube membranes were transferred into a silica glass tube, the ampoule was sealed under vacuum ($p < 10^{-3}$ mbar) and placed horizontally in a Nabertherm muffle furnace (L3/11/330). The materials were located at the hot zone at 923 K and the membranes at the colder zone of the furnace. Cooling the melt down to 773 K within 15 h at a rate of 2 K h^{-1} and of 1 K h^{-1} to room temperature led to deposition of SnIP onto the TiO_2 nanotube membranes.

Synthesis of $(CuI)_3P_{12}$@TiO_2 nanotube membranes

The synthesis of $(CuI)_3P_{12}$@TiO_2 nanotube membranes was attained according to literature procedures.[5] Purified CuI (181.8 mg) and red Phosphorus (118.2 mg, 99.999+%, Chempur) were pressed into a pellet (diameter 10 mm, 25 MPa for 15 min). The pellet was placed in a silica glass tube (0.8 cm inner diameter, 8 cm length) with TiO_2 nanotube membranes, located at the opposite side. The ampoule was sealed under vacuum ($p < 10^{-3}$ mbar) and laid horizontally in a Nabertherm muffle furnace (L3/11/330) so that the starting materials are located at the hot zone of the furnace and the TiO_2 nanotube membranes at the colder zone. The furnace was heated to 773 K within 8 h, with a holding period of 48 h, cooled down to 673 K within 24 h and held at this temperature for 11 d. Room temperature was reached within 24 h.
CuI was purified as it was mentioned in a previous paragraph.

Synthesis of polyphosphide@TiO_2 nanotube hybrids

TiO_2 nanotube membranes were prepared by electrochemical anodization of titanium foil to produce an ordered array of parallel-aligned TiO_2 nanotubes. The membranes had two distinct sides: a side that was exposed to the electrolyte during the anodization process (top side) and a side that was delaminated from the underlying titanium substrate (bottom side). Owing to the fluoride etching process during anodization, the top side had thinner sidewalls and thus large inner tube diameter. The nanotube bottoms had an average inner diameter of 67±9 nm (n = 50 nanotubes), shown in Figure 1b; the nanotube tops had an average inner diameter of 120±13 nm (n = 50 nanotubes), shown in Figure 1c. To maximize the probability of deposition inside of the tubes, the nanotubes were placed top side up in the ampoule. To fabricate hybrid semiconducting materials, we succeeded in filling the anatase-type TiO_2 nanotubes with binary NaP_7/NaP_{15}, and ternary $(CuI)_3P_{12}$, SnIP using a short-way transport reaction; this reaction is adapted from the so-called mineralization-principle used for the synthesis of a plethora of phosphorus-containing compounds. Notably, owing to the TiO_2 nanotube structure necessary to deposit sodium polyphosphides on and inside the membranes, the structure withstood the thermal treatment and led to deposition of respective polyphosphides onto and into the membranes.

1.1 Physicochemical characterization

X-ray powder diffraction

X-ray powder data were collected on a Stoe STADI P diffractometer (Cu-$K_{\alpha1}$ radiation, λ = 1.54060 Å, Ge-monochromator) fitted with a Mythen 1 K detector (Fa. Dectris). An external calibration was performed using a silicon standard (a = 5.43088 Å). Phase analysis and indexing was carried out with the program package Stoe WinXPOW.[6]

Scanning Electron Microscopy (SEM) and Energy Dispersive X-ray spectroscopy (EDS).

TiO_2 nanotubes and according nanofibers were investigated *via* Scanning Electron Microscopy with a SEM JCM-6000 NeoScop TM (JEOL, 5900LV, Si(Li) detector). The compositions of the hybrid compounds were determined semi-quantitatively by EDS measurements (Energy Dispersive X-ray Spectroscopy, Röntec). The samples were applied with an acceleration voltage of 15 kV. The measured composition is in good agreement with the composition achieved from structure refinement.

Scanning Transmission Electron Microscope (STEM) and Energy Dispersive X-ray spectroscopy (EDS).

STEM-EDS analysis was performed on a JEOL JEM-ARM200cF STEM, which is equipped with a cold Field-Emission Gun (cFEG) and a probe Cs corrector. EDS maps were acquired with a Silicon Drift (SDD) EDS detector at an acceleration voltage of 200 kV.

Helium Ion Microscope (with Ga-FIB)

For SEM and Auger analysis, samples were prepared using a Zeiss ORION NanoFab Helium Ion Microscope, equipped with a Ga-FIB column. The cross section of TiO_2 nanotubes was milled and polished with a 30 keV Ga-FIB at beam currents of 1.5 nA.

Raman spectroscopy

Raman studies were performed at 300 K by using a Renishaw inVia RE04 Raman Microscope fitted with a Nd:YAG laser (λ = 532 nm) and a CCD detector. A laser power of 250 mW was applied recording a total number of 500 scans.

Auger electron spectroscopy

SEM and Auger measurements were performed using a JAMP-9500F Auger microprobe (JEOL) at the Alberta Centre for Surface Engineering and Science, University of Alberta. A Schottky Field emitter was used to generate an electron probe diameter of about 3 to 8 nm at the sample. Sample cleaning was conducted using argon ion sputtering, over an area of 500 μm^2 with a sputtering rate of 15 nm/min as calibrated using SiO_2. The SEM and Auger imaging were performed at an accelerating voltage of 2 kV and emission current of 20 mA. The working distance used was 24 mm. The sample was rotated 30 degrees away from the primary electron beam to face the electron energy analyzer. For the Auger spectroscopy and imaging a M5 lens with 0.6 % energy resolution was applied.

X-ray Photoelectron spectroscopy (XPS) and ultraviolet photoelectron spectroscopy (UPS)

The surface chemical composition and oxidation state of materials was determined with X-ray photoelectron spectroscopy (XPS) by using Axis-Ultra, Kratos Analytical instrument equipped with monochromatic Al-Kα source (15 kV, 50 W) and photon energy of 1486.7 eV under ultra-high vacuum (UHV $\sim 10^{-8}$ Torr). The binding energy of C1s of adventitious hydrocarbon (BE ≈ 284.8 eV) was used as standard to assign binding energy (BE) of other elements by carbon correction. The obtained raw data was deconvoluted in various peak components using CasaXPS and acquired .csv file were plotted using origin 8.5. To determine the band structure of materials the work function spectra and valence band spectra of materials were determined by using ultraviolet photoemission spectroscopy (UPS) with Axis-Ultra, Kratos Analytical instrument and He I line (21.21 eV) of He discharge lamp source.
Additionally, valence band position of bare TiO_2 nanotubes was determined with XPS valence band spectra acquired on Axis-Ultra, Kratos Analytical instrument under ultrahigh vacuum conditions.

Diffuse reflectance UV-Vis (DR-UV-Vis)

Diffuse reflectance UV-Vis spectra to determine UV-Vis absorption profile of materials was acquired on a Perkin Elmer Lambda-1050 UV–Vis-NIR spectrophotometer equipped with an integrating sphere accessory.

Kelvin Probe Force Microscopy (KPFM)

To discern the charge separation dynamics and validate formation of heterojunction between polyphosphides and TiO_2, the surface potential (SP) or contact potential difference (CPD) of materials was measured using peak force KPFM (Kelvin probe force microscopy) using Dimension Fast Scan Atomic Force microscope (Bruker Nanoscience Division, Santa Barbara, CA, USA). For measurements, the materials were deposited on FTO, and a Pt-coated SiNSCM-PIT cantilever of 2.5 4.4 N/m stiffness was employed to perform the KPFM experiments. Samples were grounded with the AFM chuck with the help of conductive copper tape. The measurement was performed at zero tip bias and Pt tip was calibrated by measuring the CPD of HOPG and the Pt tip using following expression:
EF (tip) = 4.6 eV (Work function of HOPG) + VCPD (HOPG and Pt tip)

1.2 Electrochemical characterization

Analytical grade KOH (99.0%), anhydrous Na_2SO_4 (99.0%), titanium (IV)-isopropoxide (99.99%), were procured from Sigma Aldrich and used without any further purification. Conductive Fluorine doped tin oxide (FTO) glass (transmittance 80-82%) was purchased from Hartford Tec Glass Company. The surface of FTO was cleaned by ultrasonication in water, methanol and acetone for 10 min to remove any residual organics. All the solvent/water used in the measurements were of HPLC grade.

Photo-electrochemical measurements

The electrochemical properties of the materials were determined by using a CHI660E series electrochemical workstation in a three-electrode configuration. The photoactive materials deposited on FTO glass containing a TiO_2 blocking layer was assigned as anode (working electrode), while Pt sputtered glass and Ag/AgCl was used as cathode (counter electrode) and as reference electrode respectively. To ensure an equal amount of photocatalytic materials on the photoanodes, an identical amount of materials, dispersed in methanolic solution was drop-casted on the exact same area of TiO_2 seed layer containing FTO glass. The photoelectrochemical measurements were performed in 0.1 M KOH aqueous electrolyte. Linear sweep voltammetry (LSV) to measure the materials photocurrent density was performed by sweeping voltage from –1.0 V to +0.8 V vs Ag/AgCl at a scan rate of 10 mV/sec. The photoanode was irradiated with solar simulated light (AM1.5 G) having a power density of 100 mW m^{-2} at the sample surface by using Newport, Oriel instrument USA, model 67005, solar simulator. To determine visible light response at higher wavelengths and incident photon-to-current efficiency (IPCE) the samples were irradiated with monochromatic 450 and 505 nm wavelength LEDs having 54.15 and 40.48 mW cm^{-2} incident power density at the sample surface. Mott-Schottky plots to calculate flat band potential were extracted from impedance-potential values measure in 0.5 M Na_2SO_4 solution in a potential range of –1.0 to +1.0 V at 1 K frequency. Electrochemical impedance spectroscopy (EIS) to draw Nyquist plots and equivalent circuit under dark and 1 Sun irradiation was performed using a three

electrodes configuration at a bias of –0.5 V vs Ag/AgCl in 0.1 M KOH, with an AC amplitude of 0.005 V at frequency value 1 Hz - 100 kHz.

To investigate the photo-electrochemical performance an approx. 20 nm thick TiO_2 blocking layer was spin casted on cleaned FTO glass using titanium isopropoxide solution according to our previous report just by changing the dilution of the solution three times.[6] The deposition of photoactive materials on TiO_2 coated FTO was done by dispersing materials in very dilute aqueous solution of titanium isopropoxide and drop casting followed by heating at approx. 150 ºC for 1 h. In this way the materials stick strongly on the TiO_2 coated FTO substrate. The materials deposited on FTO glass function as photoanode (working electrode) and Pt and Ag/AgCl was used as counter (cathode) and reference electrodes, respectively. The photo-electrochemical water splitting experiments were performed by immersing the electrodes in 0.1 M KOH solution. The samples were irradiated under solar simulated light (AM1.5 G) having a power density of 100 mW cm^{-2} at the sample surface and photocurrent density was measured in function of applied voltage by sweeping bias from –1.0 V to +0.8 V. Further, photocurrent response at higher wavelength (monochromatic 450 and 505 nm light) was measured using LEDs and with power density on the sample surface was 54.15 and 40.48 mW cm^{-2}.

2. Results

NaP_7@TiO_2 nanotubes

P-XRD analysis

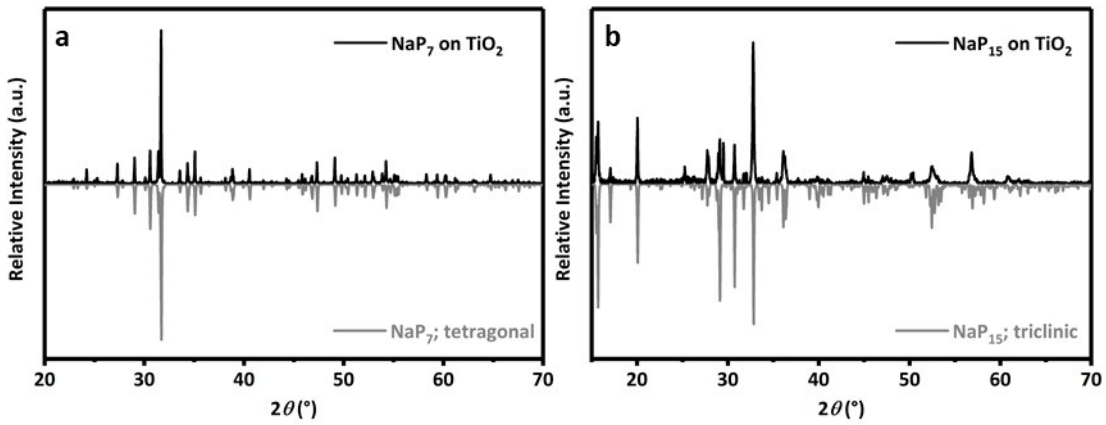

Figure S1. a) and **b)** Powder X-ray diffraction patterns of NaP_7 (main fraction) and NaP_{15} (minor fraction) substantiate the formation of the two polyphosphides on the membrane.

AES analysis

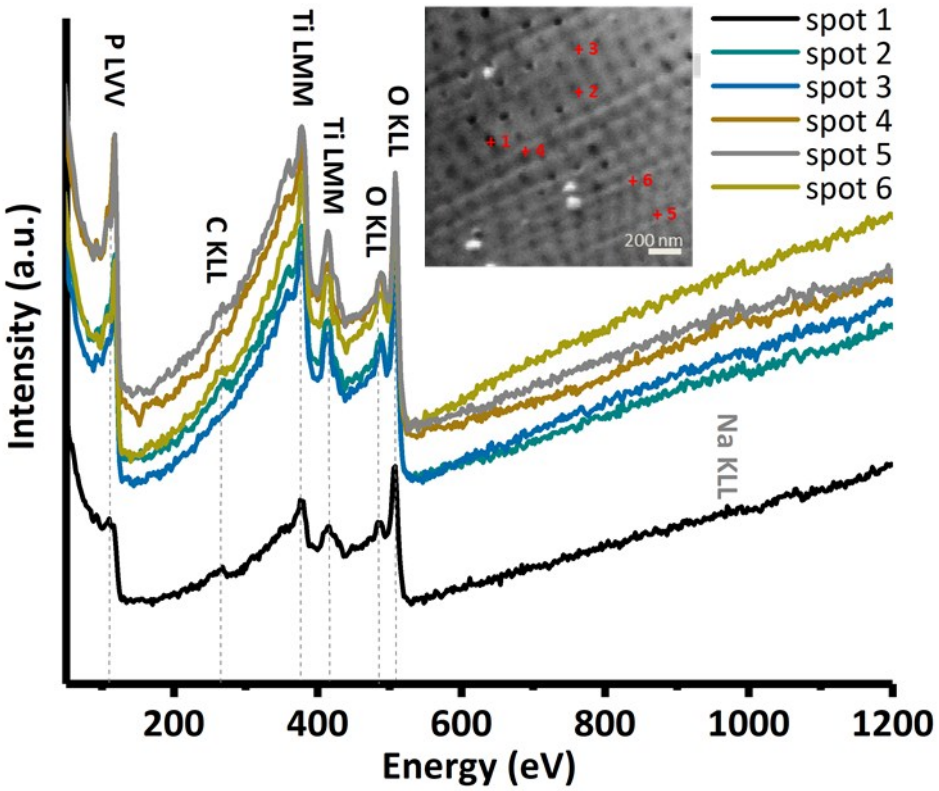

Figure S2. Selected point AES spectra on FIB-milled NaP_x@TiO_2 nanotube specimen. The according peaks at spot 1 (seeming hole) are P LVV (115 eV), C KLL (266 eV), Ti LMM (381 eV, 416 eV), O KLL (482 eV, 503 eV), a weak peak at 979 eV potentially caused by Na KLL.

SnIP@TiO_2 nanotubes

P-XRD analysis

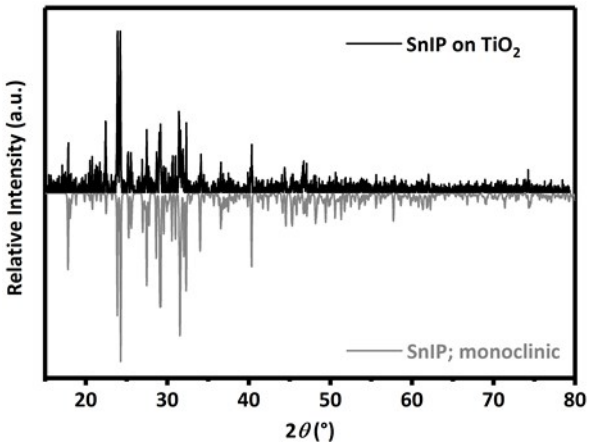

Figure S3. Powder X-ray diffraction patterns confirm the formation of crystalline SnIP onto the membrane.

$(CuI)_3P_{12}$@TiO_2 nanotubes

The gas-phase based synthesis was furthermore applied for the ternary polyphosphide $(CuI)_3P_{12}$. According to calculations $(CuI)_3P_{12}$ and its structurally related compounds $Cu_2I_3P_3$, and $(CuI)_2P_{14}$ show a band gap range of 1.0 - 1.1 eV.[7] Downsizing quantum confinement effects such as in single and isolated phosphorus ${}^{1}_{\infty}[P10]P2[$ strands without the CuI-matrix lead to bandgaps of 2.3 - 2.9 eV.[7] A growth of such isolated strands can be achieved by the infiltration in hollow TiO_2 nanotubes.

The polyphosphide substructure consists of condensed five- and six-membered ring fragments attached to a polymer subunit in the CuI matrix.[5] In line with Baudler's rules the one-dimensional infinite phosphorus chains ${}^{1}_{\infty}([P10]P2[)^{0}$ in the $(CuI)_3P_{12}$ structure are more stable than the structurally related $Cu_2I_3P_3$ with infinite chains ${}^{1}_{\infty}[P^{0}_{12}]$ inhibiting additional four-membered rings.[8-11] In Figure S4a the $(CuI)_3P_{12}$ - crystal structure consisting of separated CuI and polymeric phosphorus tubes along the b-axis is demonstrated. A microscopic image of the TiO_2 nanotube membranes show the surface covered with dark blue fibres of $(CuI)_3P_{12}$ (Figure S4b). The SEM image in Figure S4c confirms preservation of the nanotube structure after gas phase synthesis procedure as well as the according elemental composition (Table S3). Powder X-ray diffraction verifies the growth of $(CuI)_3P_{12}$ on top of the TiO_2 nanotube membranes (Figure S4d).

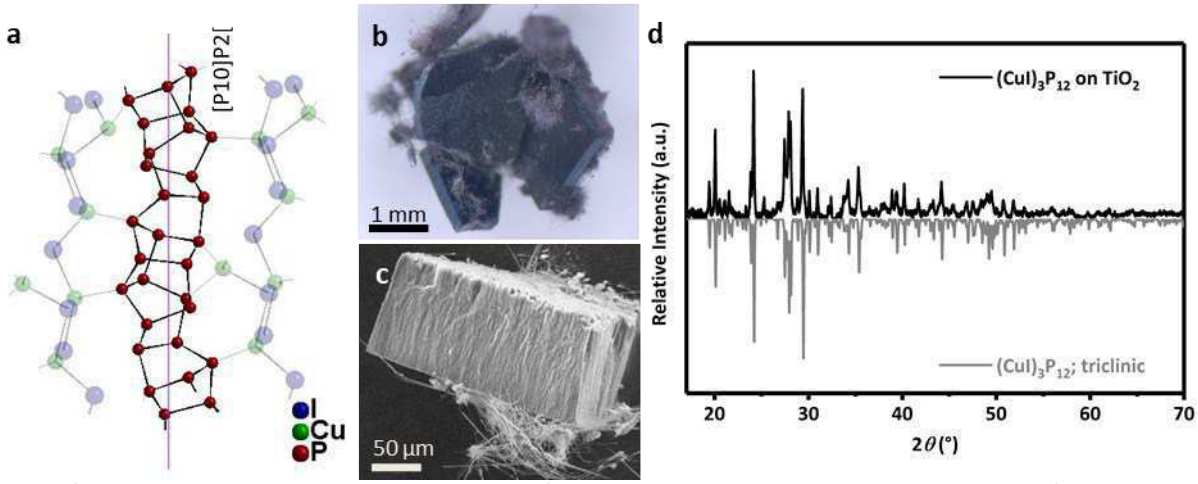

Figure S4. **a)** Crystal structure of $(CuI)_3P_{12}$ with CuI and polymeric P units. **b)** A TiO_2 nanotube membrane reacted with $(CuI)_3P_{12}$ *via* gas phase. **c)** Cross section and surface of $(CuI)_3P_{12}$@TiO_2 nanotube membranes. **d)** Powder X-ray diffraction patterns confirm the formation of crystalline $(CuI)_3P_{12}$ onto the membrane.

Raman imaging of the razor-cut cross section of hybrid $(CuI)_3P_{12}$@TiO_2 nanotube membranes cutting demonstrates the successful growth of $(CuI)_3P_{12}$ crystals up to 22 µm in distance to the membrane-top side (Figure S5).

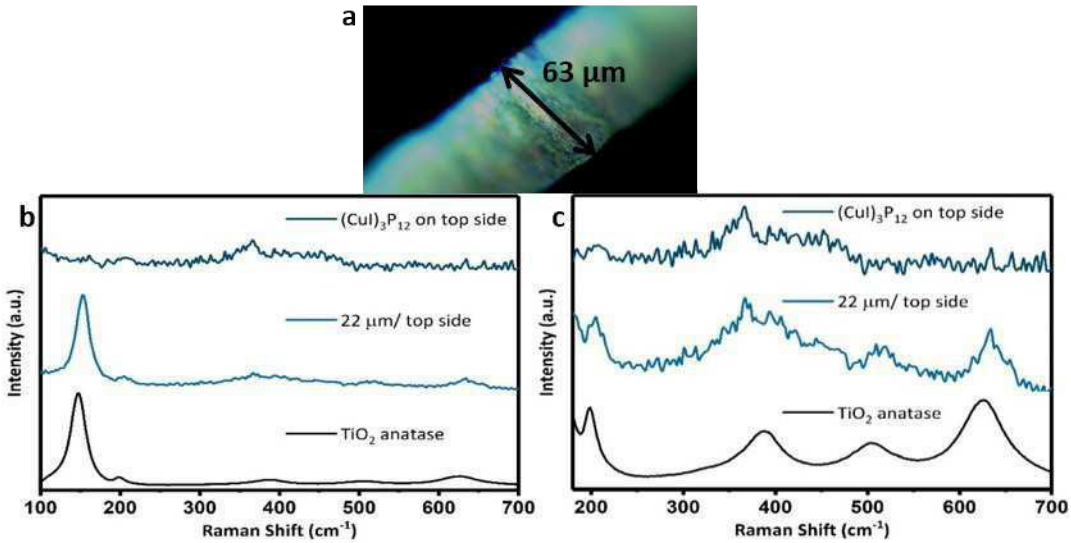

Figure S5. Raman spectroscopy on $(CuI)_3P_{12}@TiO_2$ membranes. **a)** Corresponding membrane cross section of measured specimen. **b)** From top to down: Reference Raman spectrum of measured $(CuI)_3P_{12}$ crystals, spectra of a $(CuI)_3P_{12}@TiO_2$ membrane cross section measured at approx. 22 µm in distance to the surface (membrane-top side and a fresh TiO_2 membrane (anatase, grey). **c)** A zoom in into the significant bands between 300 and 550 cm-1 of the $(CuI)_3P_{12}$ Raman spectrum.

STEM images show a ranged bundle of non-decayed TiO_2 nanotubes taken after separation by an ultrasonication process. The image scale displays a size of ~90-100 nm per tube. An infiltration is shown by distribution of Ti and P along, with Cu and I according to elemental mapping is illustrated along the tube length of the nanotube bundle (see Figure S6a).

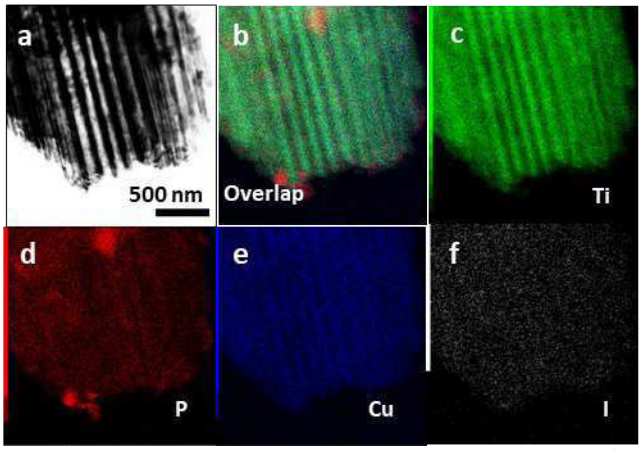

Figure S6. a) STEM bright-field image of TiO_2 nanotubes separated from a membrane by an ultrasonication procedure. **b)** Elemental mapping of overlaid elements Ti (representing TiO_2), P, Cu and I. The elemental mapping images of **c)** Ti, d) P, e) Cu and f) I substantiating P, Cu and I distributed along the length of a TiO_2 nanotube bundle.

XPS analysis

High resolution X-ray photoelectron spectroscopy (HR-XPS) was performed to investigate the surface chemical composition, binding energy and oxidation state of the elements. XPS elemental survey scan of NaP_7, TiO_2 and $NaP_7@TiO_2$ reveals the presence of all elements in NaP_7 (Na1s, P2p), TiO_2 (Ti2p, O1s) and $NaP_7@TiO_2$ (Na1s, P2p, Ti2p, O1s) (Figure S7a). HR-XPS in Ti2p region for TiO_2 reveal two peak components at BE ≈ 459.46 and 465.27 eV assigned to $Ti2P_{3/2}$ and $Ti2p_{1/2}$ splitting, demonstrating presence of anatase form TiO_2 with Ti^{4+} in crystal lattice (Figure S7b).[12] The peak position of $Ti2P_{3/2}$ and $Ti2p_{1/2}$ components does not change in hybrid $NaP_7@TiO_2$ suggesting anatase phase TiO_2 remains intact during deposition step. The deconvoluted HR-XPS spectra of TiO_2 nanotubes in O1s region shows two peak components at 530.98 and 532.70 eV. The strong peak at 530.98 eV was originated from lattice oxygens bonded to Ti in crystal (Ti-O-Ti), while relatively weak shoulder peak at 532.70 eV was assigned to non-lattice adventitious oxygen and surface –OH groups. Additionally, two peak components in O1s spectra cantered at 530.98 and 532.70 eV for TiO_2 remains unchanged in and $NaP_7@TiO_2$ which reveal robust nanotube

structure even after vapor phase deposition of NaP_7 on TiO_2 (Figure S7c).[13] However, the increase in peak intensity of 532.70 eV exhibit increase in adventitious oxygen which might be due to partial surface oxidation of phosphide to various P-O moieties (P_xO_y). The peak positioned at 1063.74 eV in Na1s HR-XPS spectra for NaP_7 originated from electrostatically bonded Na^+ to the phosphide backbone.[14-17] Surprisingly, The Na1s peak in NaP_7@TiO_2 was shifted to higher binding energy which might be due to partial charge transfer from NaP_7 to the surface of TiO_2 and partial doping of TiO_2 surface with Na ions (Figure S7d). Additionally, HR-XPS of NaP_7 in P 2p region show two peaks centred at BE ≈ 130.15 and 134.16 eV. The peak at 129.86 eV can be further deconvoluted into two peak components located at BE≈129.90 and 130.77 eV and might have originated due to coexistence of two phases NaP_7 (dominant fraction) and NaP_{15} (both responsible for the 129.86 eV peak due to comparable polyphosphide substructures and crystallographically non-equivalent P species)[16, 17] The peak at 134.16 eV was originated due to partially oxidized surfaces (phosphate formation, P_xO_y). A significant increase of the peak positioned at 130.15 eV appears in the NaP_7@TiO_2 nanocomposite. The increase signal intensity might be due to a reduced oxidation tendency of the polyphosphide in the hybrid (Figure S7e).

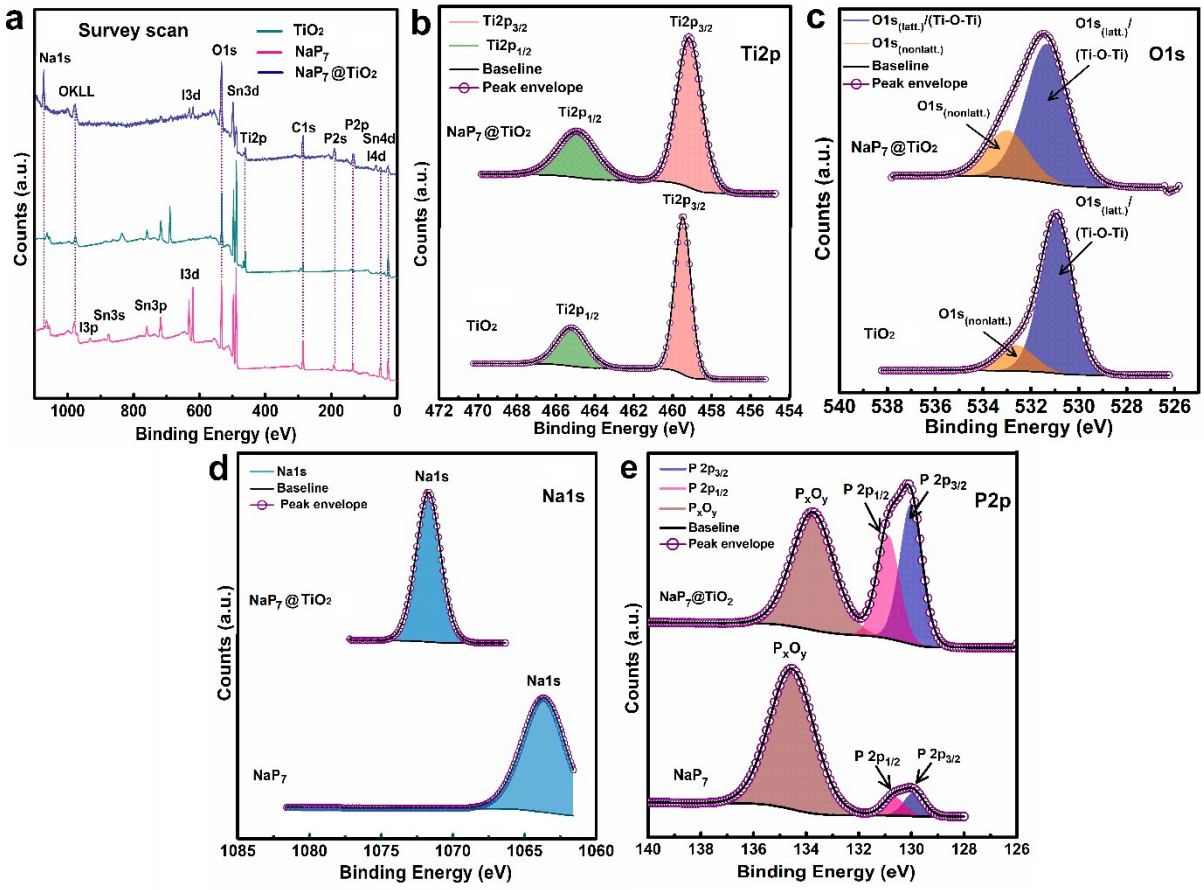

Figure S7. a) Elemental survey scan of TiO_2 nanotube membranes (green), NaP_7 (pink) and NaP_7@TiO_2 (navy blue) and HR-XPS spectra of TiO_2 and NaP_7@TiO_2, **b)** in Ti2p region, **c)** in O1s region, **d)** in Na1s region, **e)** in P2p region.

Like NaP_7, the elemental survey scan of $(CuI)_3P_{12}$, TiO_2 nanotube membrane and hybrid $(CuI)_3P_{12}$@TiO_2 confirms presence of all the relevant elements in $(CuI)_3P_{12}$ (Cu, I and P), TiO_2 and $(CuI)_3P_{12}$@TiO_2 (Cu, I, P, Ti and O) (Figure S8a). The high resolution XPS (HR-XPS) core level spectra of TiO_2 in Ti2p region can be deconvoluted into two peak components located at binding energy 459.46 and 465.27 eV assigned to $Ti2p_{3/2}$ and $Ti2p_{1/2}$ components of Ti^{4+} oxidation state of anatase phase TiO_2 (Figure S8b).[18, 19] After solid state vapour phase deposition of $(CuI)_3P_{12}$ on TiO_2 nanotube membranes ($(CuI)_3P_{12}$@TiO_2) the binding energy of $Ti2p_{3/2}$ and $Ti2p_{1/2}$ components doesn't change, which confirms that the chemical nature of TiO_2 doesn't change during deposition of $(CuI)_3P_{12}$. The HR-XPS spectra of TiO_2 in O1s region can be deconvoluted into two peak components at 530.48 and 532.64 eV. The origin of the stronger peak at BE ≈ 530.48 eV was attributed to lattice oxygens (Ti-O-Ti), while smaller peak component located at 532.68 eV was originated due to presence of non-lattice adventitious oxygen and surface –OH groups (Figure S8c).[20] For $(CuI)_3P_{12}$@TiO_2, the binding energy of O1s peak components corresponding to lattice oxygen and adventitious oxygens remains identical; however, the intensity of non-lattice bounded peak components are increased significantly which might be due to the affinity of $(CuI)_3P_{12}$ to moisture and oxidation of surface phosphorous to

phosphates (P_xO_y). HR-XPS spectra of bare $(CuI)_3P_{12}$ in Cu2p region displayed two peak components at BE ≈ 932.91 eV and 952.55 eV, attributed to $Cu2p_{3/2}$ and $Cu2p_{1/2}$ components of Cu present in the +1 oxidation state (Figure S8d).[21, 22] Furthermore, the absence of any shoulder peak in Cu2p XPS at higher binding energies confirms the presence of Cu^{1+} atoms in identical chemical environment.[23] The Cu2p HR-XPS remains the same for the hybrid of $(CuI)_3P_{12}@TiO_2$, which demonstrates successful solid-state deposition of $(CuI)_3P_{12}$ on TiO_2 nanotubes. Two peak components in HR-XPS scan in I3d region corresponded to $I3d_{5/2}$ and $I3d_{3/2}$ at BE of 631.42 and 619.94 eV show a presence of I^- coordinated to Cu^{1+} composing Cu-I-Cu bridges of polymeric structure (Figure S8e).[24, 25] The binding energy of the I3d peak component in $(CuI)_3P_{12}@TiO_2$ gets shifted slightly to higher binding energy which might be due to chemical interaction of outer coordinated iodine with electronegative oxygen of TiO_2. Additionally, the single peak component in P2p region (134.95 eV) of $(CuI)_3P_{12}$ might be originated due contribution from oxidized P atoms present in the form of phosphate (P_xO_y) and the presence single phase Cu and iodine bonded phosphide chain (Figure S8f).[26, 27] However, considering high signal intensity we inferred phosphides were main contributor to this signal. Further the peak located at 134.95 eV can be split into two peak components centred at 134.39 and 135.27 eV for $2p_{3/2}$ and $2p_{1/2}$ peak components. Similar to the I3d peak, the P2p peak component gets shifted to higher binding energies due to the slight charge transfer from phosphorous helix to TiO_2 surface.

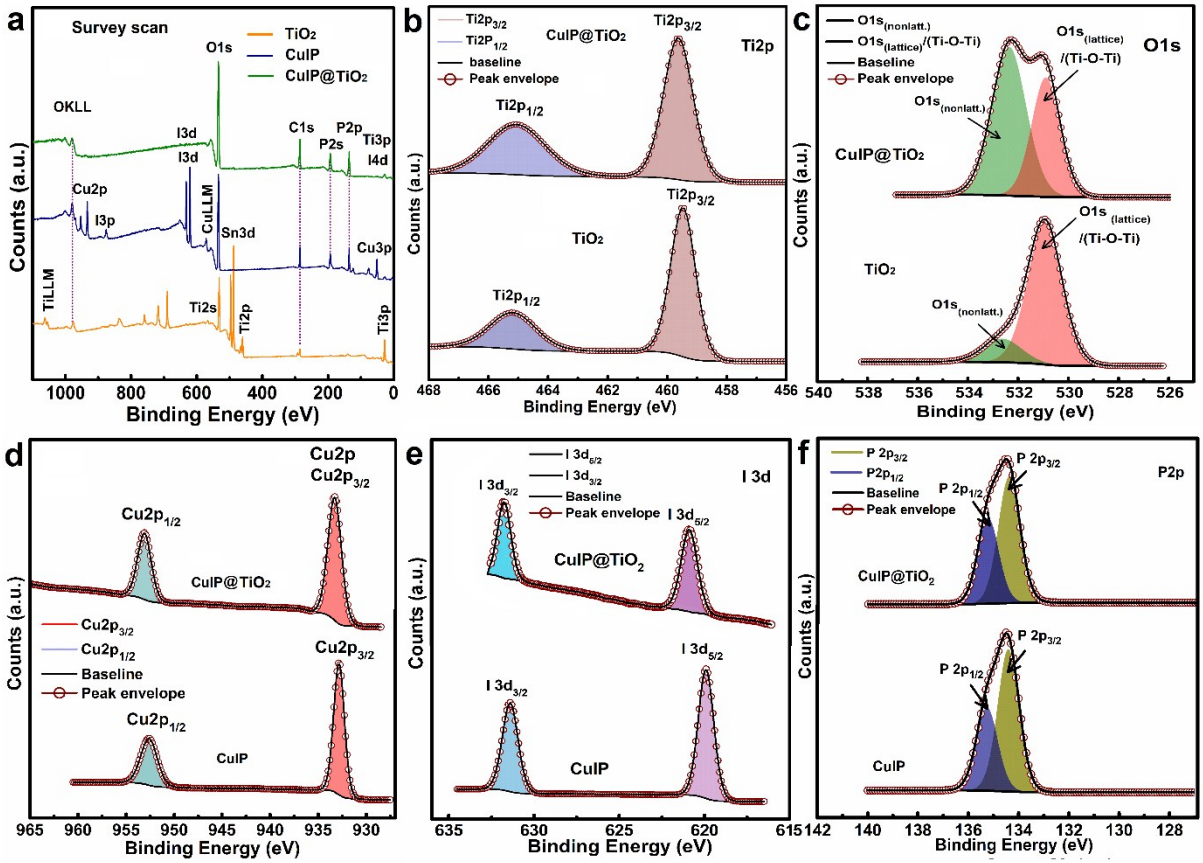

Figure S8. a) Elemental survey scan of TiO_2 nanotube membranes (orange), $(CuI)_3P_{12}$ (navy blue) and $(CuI)_3P_{12}@TiO_2$ (green), HR-XPS core level spectra of TiO_2 and $(CuI)_3P_{12}@TiO_2$, **b)** in Ti2p region, **c)** in O1s region, and HR-XPS spectra of $(CuI)_3P_{12}$ and $(CuI)_3P_{12}@TiO_2$ **d)** in Cu2p region, **e)** in I3d region and **f)** in P2p region. (CuIP ⇒ $(CuI)_{12}P_3$).

The elemental survey scan of SnIP, TiO_2 and $SnIP@TiO_2$ displayed all peaks of composing elements present in SnIP (Sn3d, I3d, P2p), TiO_2 (Ti2p, O1s) and $SnIP@TiO_2$ (Sn3d, I3d, P2p, Ti2p, O1s) (Figure S9a). The HR-XPS spectra of the bare SnIP samples in Sn3d region displayed two deconvoluted peaks at 487.51 and 495.88 eV attributed to $Sn3d_{5/2}$ and $Sn3d_{3/2}$ components, revealing a presence of chemically equivalent Sn present in +2 oxidation state (Figure S9b).[28, 29] The HR-XPS spectra of SnIP showed two peak components at binding energies 619.87 and 631.37 eV in I3d region assigned to $I3d_{5/2}$ and $I3d_{3/2}$ peak component of I- composing the SnIP helix (Figure S9c).[30, 31] Additionally, HR-XPS spectra of SnIP in P2p region show two peaks at 134.01 eV (deconvoluted into two components, $2p_{3/2}$-133.73 eV and $2p_{1/2}$-134.71 eV) for crystallographic non-equivalent P of SnIP and 139.77 eV (Phosphate, surface oxidation product P_xO_y) (Figure S9d).[32, 33] The binding energies corresponding to Sn2p, I3d and P2p peak components remain fairly constant after fabrication of SnIP on TiO_2 ($SnIP@TiO_2$) which signify the absence of any chemical interaction between SnIP and TiO_2 (Figure S9b-d). The HR-XPS core level spectra in Ti2p region for TiO_2

nanotubes displays two peak components at 466.43 and 465.23 eV assigned to $Ti2p_{3/2}$ and $Ti2p_{1/2}$, revealing the Ti^{4+} states in anatase TiO_2 lattice (Figure S9e).[34] The HR-XPS spectra in O1s region of TiO_2 deconvoluted into two peak components gave peak at BE≈ 531.86 and 532.74 eV corresponding to lattice bounded oxygen and adventitious surface adsorbed oxygen (Figure S9f).[35] After gas-phase deposition of SnIP on TiO_2 nanotube membranes the signal for Ti2p disappeared which was assumed due to coverage of TiO_2 nanotube membrane with SnIP materials resulting in suppression of the signals at the measured area (Figure S9e). While the O1s signal get slightly shifted to lower binding energies (530.98 eV) and the peak component at 532.74 eV gets increased, showing some oxidation of SnIP phosphorus to P-O (P_xO_y) functionalities and surface adsorbed adventitious oxygen.[36]

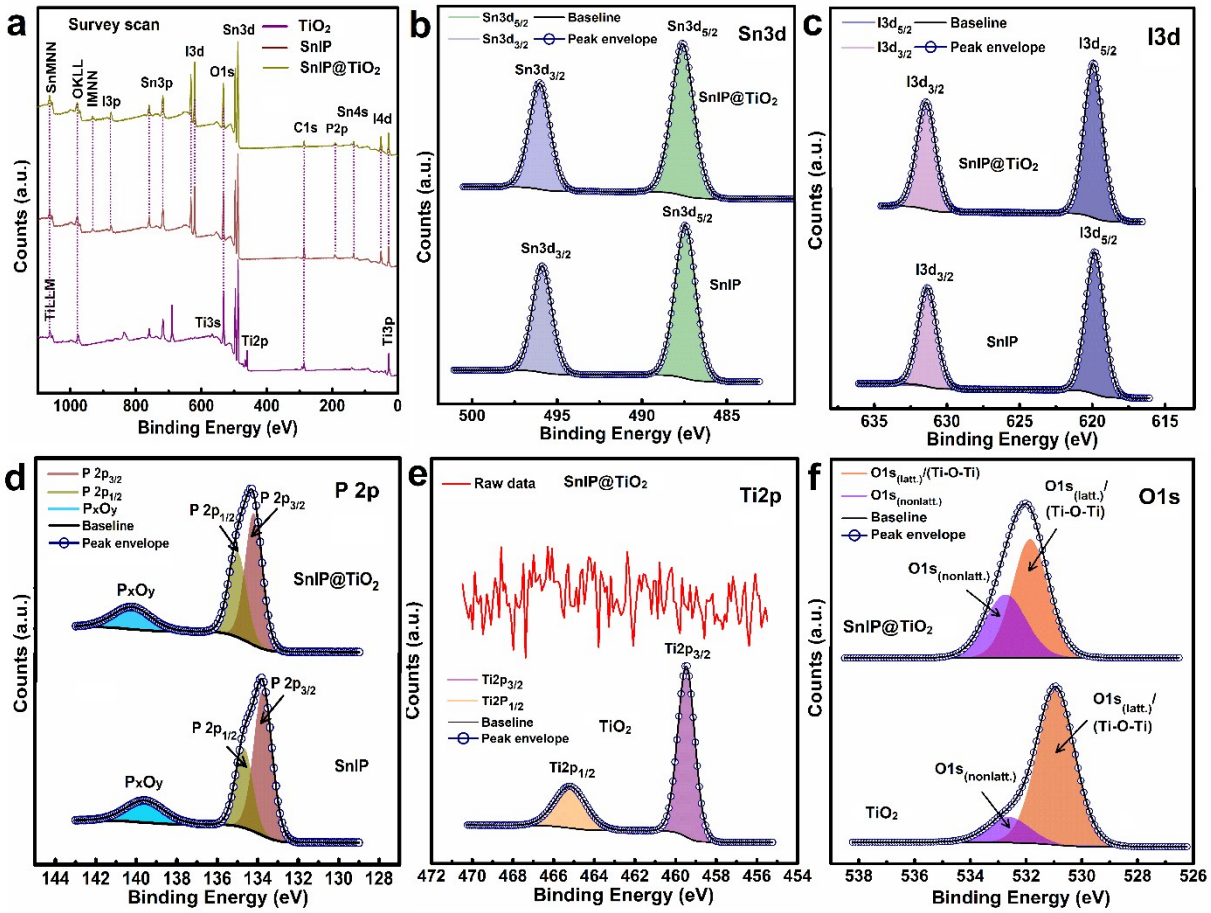

Figure S9. a) Elemental survey scan of TiO_2 nanotube membranes (purple), SnIP (red) and SnIP@TiO_2 (yellow) and HR-XPS core level spectra of TiO_2 and SnIP@TiO_2, **b)** in Sn3d region, **c)** in I3d region, **d)** in P2p region, **e)** in Ti2p region and **f)** in O1s region.

Diffuse reflectance spectroscopy

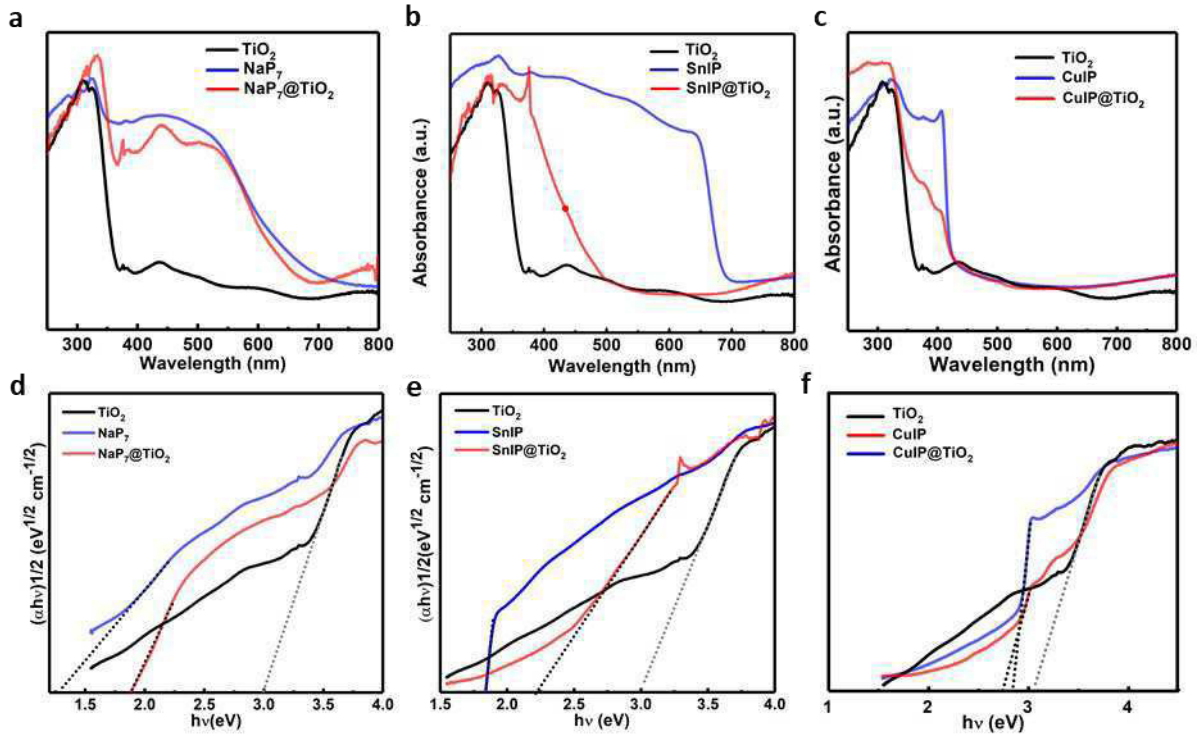

Figure S10. UV-Vis DRS spectra of **a)** TiO_2 nanotubes (black),NaP_7 (blue), NaP_7@TiO_2 (red), **b)** TiO_2 (black), SnIP (blue), SnIP@TiO_2 (red), **c)** TiO_2 (black), $(CuI)_3P_{12}$ (blue), $(CuI)_3P_{12}$@TiO_2 (red) and Tauc plot for determination of optical band gap of **d)** TiO_2 (black), NaP_7 (blue), NaP_7@TiO_2 (red) **e)** TiO_2 (black), SnIP (blue), SnIP@TiO_2 (red), **f)** TiO_2 (black), $(CuI)_3P_{12}$ (red), $(CuI)_3P_{12}$@TiO_2 (blue). (CuIP ⇒ $(CuI)_{12}P_3$).

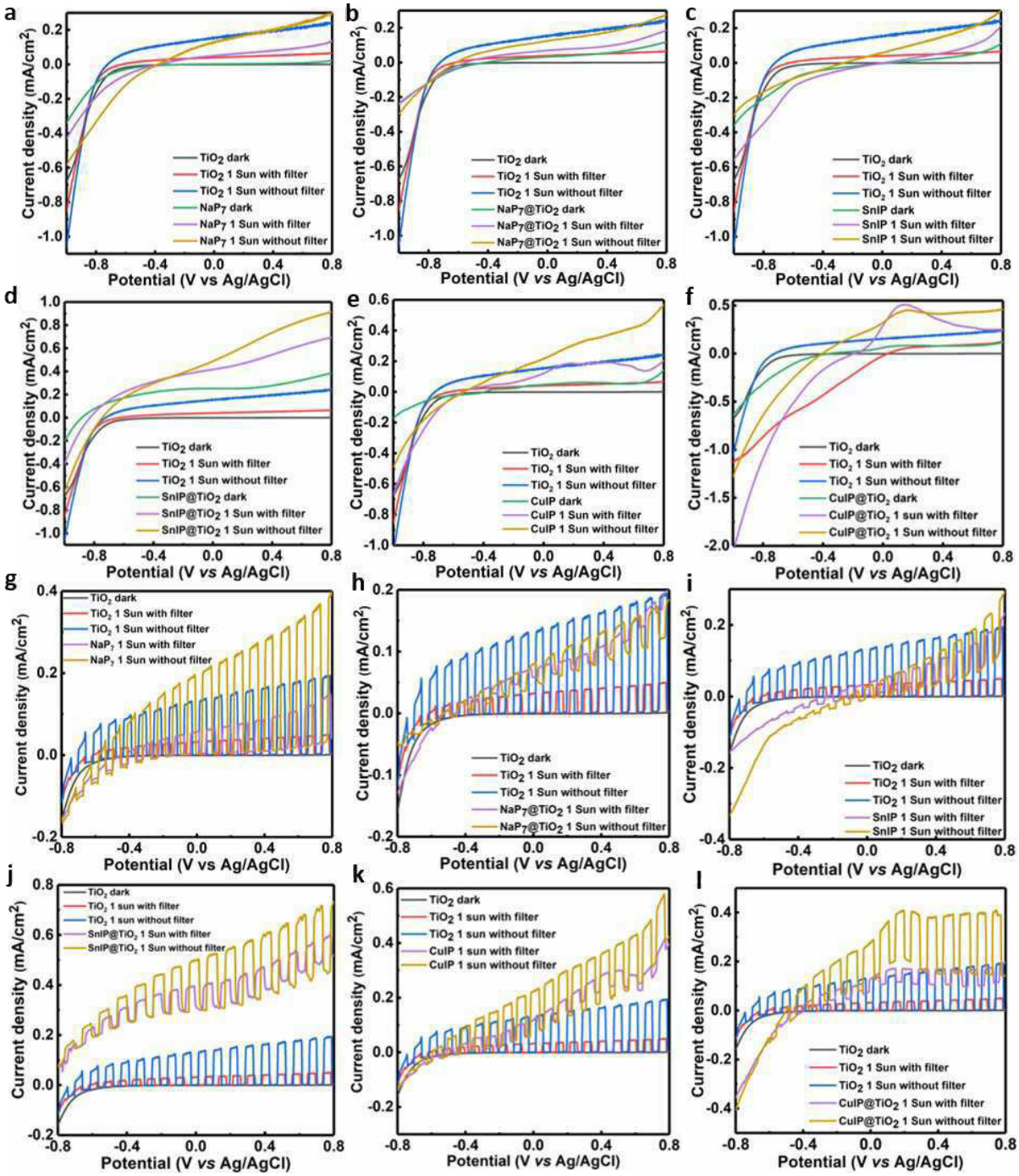

Figure S11. a) - l) Photocurrent density *vs* applied voltage plot with on-off cycles of TiO_2 nanotubes *vs* NaP_7, NaP_7@TiO_2, SnIP, SnIP@TiO_2, $(CuI)_3P_{12}$, $(CuI)_3P_{12}$@TiO_2. (CuIP ⇒ $(CuI)_{12}P_3$).

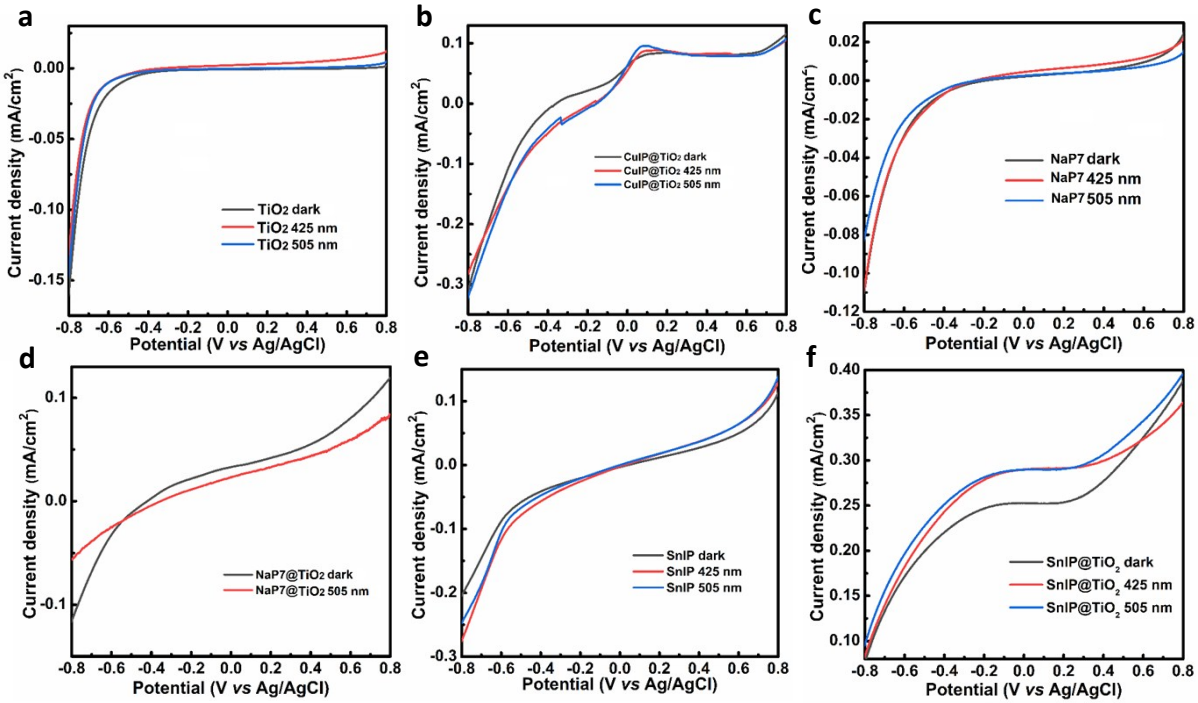

Figure S12. **a) – f)** Photocurrent density *vs* applied voltage plot of TiO_2 nanotubes, $(CuI)_3P_{12}@TiO_2$, NaP_7, $NaP_7@TiO_2$, SnIP and $SnIP@TiO_2$ under the illumination of LED 425 and 505 nm. (CuIP ⇒ $(CuI)_{12}P_3$).

Interface photon-to-current performance

Investigations on semiconductor/interface performance revealed following diagnostic efficiencies of the materials.[37, 38]

Applied bias photon-to-current efficiency (ABPE):

The applied bias photon-to-current efficiency percentage (ABPE%) which demonstrates photo-conversion efficiency under applied bias of the photoanode was determined by plotting a graph between ABPE% and applied voltage on RHE (reversible hydrogen electrode) scale. The ABPE% was calculated by using following expression:

$$ABPE\ (\%) = [J\ (mA\ cm^{-2}) \times (1.23 - V_b) / P\ (mW\ cm^{-2})] \times 100 \quad (1)$$

Where, J is the current density, V_b is the applied voltage at RHE scale and P is the power density of the incident light.

The applied voltage on Ag/AgCl scale was converted to RHE scale by using following expression.

$$V_{RHE} = V_{Ag/AgCl} + 0.059\ pH + V^0_{Ag/AgCl} \quad (2)$$

Where $V^0_{Ag/AgCl}$ = 0.197 V.

Incident photon-to-current efficiency (IPCE) also referred as external quantum efficiency (EQE):

The IPCE which is a measure of the obtained photocurrent (number of electrons collected) per incident photon flux as a function of wavelength was calculated at 0.6 V *vs* Ag/AgCl (1.23 V *vs* RHE, thermodynamic water splitting potential) by irradiating samples with a 505 nm wavelength LED (40.48 mW cm^{-2}). The IPCE values were calculated using the following expression.

$$IPCE\% = [1240 \times J\ (mA\ cm^{-2}) / \lambda\ (nm) \times P\ (mW\ cm^{-2})] \times 100 \quad (3)$$

Where, J is the photocurrent density, λ is the wavelength of incident light in nm, and P is the power density of the incident light.

Absorbed photon-to-current efficiency percentage (APCE%) also referred to as internal quantum efficiency (IQE):

Since IPCE is a measure to incident photons conversion efficiency, it doesn't take the loss of photons being unabsorbed by the materials into account. So, absorbed photon-to-current efficiency percentage (APCE%) which

define the photocurrent collected per incident photon absorbed is used to demonstrate device performances. The APCE% can be calculated by following formulas:

$$\text{APCE\%} = (\text{IPCE/LHE}) \times 100 \tag{4}$$

Where, *LHE* is the light harvesting efficiency or absorbance which is a number of electron-hole pairs produced as fraction per incident photon flux. By considering that each absorbed photon produces equal electron hole pairs, the value of LHE or absorptance calculated by Beer's law can be expressed by following equation.

LHE or absorptance = $(1\text{-}10^{-A})$

$$\text{APCE\%} = [1240 \times J\ (\text{mA cm}^{-2})/\lambda\ (\text{nm}) \times P\ (\text{mW cm}^{-2}) \times (1\text{-}10^{-A})] \times 100 \tag{5}$$

Where, J is photocurrent density, λ is wavelength of incident light in nm, P is the power density of incident light, *LHE* is light harvesting efficiency and A is absorbance at measured wavelength.

Semiconductor-electrolyte interface

Electrochemical impedance spectroscopy

Semiconductor electrolyte interfacial (SEI) behaviour of NaP_7 and NaP_7@TiO_2, SnIP, SnIP@TiO_2, $(CuI)_3P_{12}$, $(CuI)_3P_{12}$@TiO_2 were analysed using electrochemical impedance spectroscopy (EIS), whereby Nyquist plots were obtained, between frequencies of 1 and 10,000 Hz at -0.4 V vs Ag/AgCl, using dark and one-sun conditions. EIS Nyquist plots (Figure S13a, b and c) clearly indicate higher charge transfer resistance in dark conditions when compared to those in one-sun illumination condition. Equivalent circuit diagram representing the Nyquist plots is shown in Figure S13d, wherein in $\boldsymbol{R_S}$, $\boldsymbol{R_C}$, $\boldsymbol{R_T}$, $\boldsymbol{C_{SC}}$, and $\boldsymbol{C_H}$ are electrolyte resistance, charge transfer resistance, charge transport resistance, space charge capacitance, and electrochemical double-layer (Helmholtz) capacitance, respectively. $\boldsymbol{Q}$ is a constant phase element with coefficient $\boldsymbol{n}$. The values of circuit parameters are listed in Table S4. As obtained by equivalent circuit model, $\boldsymbol{R_C}$ was the same (i.e. 10 ohms) $(CuI)_3P_{12}$ and SnIP, as it was (i.e. 1 ohm) for SnIP@TiO_2 and NaP_7@TiO_2. RC for $(CuI)_3P_{12}$@TiO_2 and NaP_7 were rather high at 50 and 30 ohms, respectively. Calculated recombination lifetime (τ, using (6) values are listed in Table S5, and indicate reasonably long-lived holes for all samples, and particularly for SnIP and NaP_7.

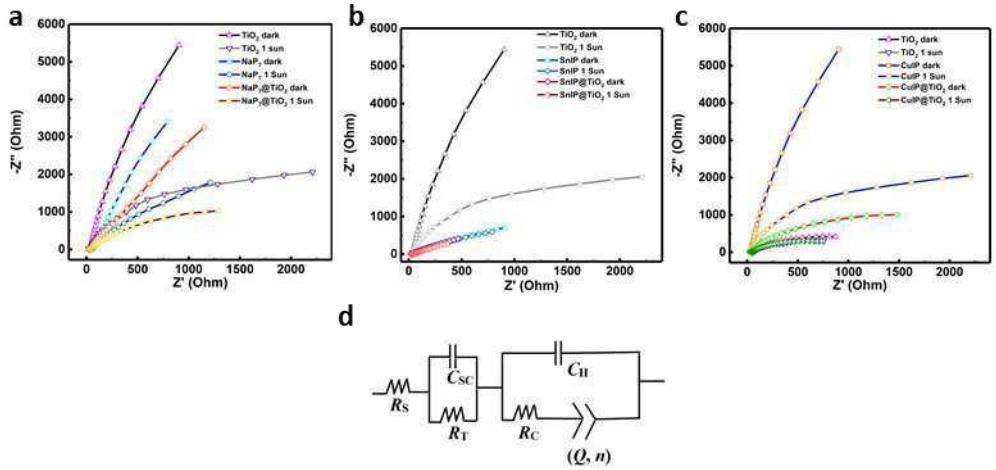

Figure S13. Nyquist plots measured in 0.1 M KOH, under dark conditions and AM1.5 G light irradiation (100 mW cm^{-2}) **a)** TiO_2 nanotubes (black and magenta), NaP_7 (light and dark blue), NaP_7@TiO_2 (light and dark red), **b)** TiO_2 (black and magenta), SnIP (dark and light green), SnIP@TiO_2 (light and dark red), **c)** TiO_2 (black and magenta), $(CuI)_3P_{12}$ (light and dark blue), $(CuI)_3P_{12}$@TiO_2 (light and dark red). **d)** Equivalent circuit diagram of the EIS Nyquist plots shown in a, b and c. (CuIP ⇒ $(CuI)_{12}P_3$).

$$\tau = R_T C_{SC} \tag{6}$$

$$\frac{1}{C_{SC}^2} = \frac{2}{\varepsilon_0 \varepsilon_r N_D}\left\{(V - V_{FB}) - \frac{kT}{e}\right\} \tag{7}$$

$$N_D = \frac{2}{\varepsilon_0 \varepsilon_r}\left\{\frac{dV}{dC_{SC}^2}\right\} \tag{8}$$

$$W = \{\frac{2\varphi\varepsilon_0\varepsilon_r}{eN_D}\}^{\mathfrak{G}} \quad (9)$$

Impedance-potential analysis

Further insights about SEI of the samples were gained *via* Mott Schottky's equations (eq. (7) and (8)), which were used to calculate charge carrier concentration (N_D), and flat band potential (V_{FB}). In eq. (7) and (8), C_{SC} is space-charge capacitance per unit area; ε_r the dielectric constant of the samples, which may be assumed to be 45, i.e. same as that of anatase TiO_2.[39, 40] N_D is carrier concentration; ε_0 is the vacuum permittivity (8.854 ×10^{-14} F cm^{-1}); k is the Boltzmann constant (1.381 ×10^{-23} J K^{-1}); ***T*** is the temperature in (298 K); ***e*** is the electron charge (1.602×10^{-19} C); V_{FB} is the flat band potential; and ***V*** is the applied potential. N_D, the charge carrier concentration, is calculated from the slope (term within the bracket in eq. (8) of the Mott Schottky's plots (Figure S14), using eq. (8). V_{FB}, is the point of intersection of the slope of the Mott Schottky's plot with the potential axis, as shown in Figure S14. N_D and V_{FB} of the samples are listed in Table S5. N_D of the order of 1020 cm^{-3}, is well known for anatase TiO_2[41] N_D of the composites of $(CuI)_3P_{12}$ and SnIP with TiO_2 decreased, as it did for bare $(CuI)_3P_{12}$ and SnIP, while that of NaP_7@TiO_2 increased slightly from bare TiO_2 nanotube arrays, while that for bare NaP_7 decreased slightly. Width of depletion layer, ***W***, is calculated using eq. (9) at 1.23 V *vs* RHE in eq. (9), where φ is the potential drop across the space layer. ***W*** is highest for SnIP and SnIP@TiO_2 indicating maximum band bending in those samples due to the lower carrier concentration.

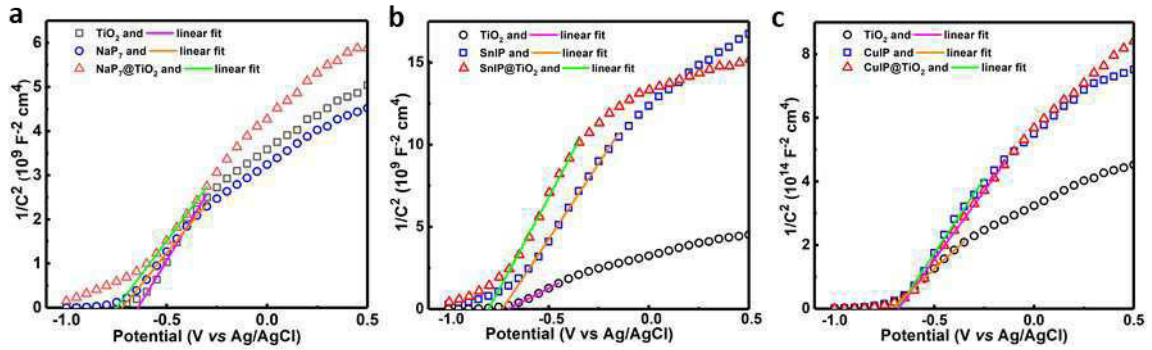

Figure S14. Mott-Schottky plots, linear fit of plot intersecting on abscissa reveal flat band potential of **a)** TiO_2 nanotubes (black), NaP_7 (blue), NaP_7@TiO_2 (red), **b)** TiO_2 (black), SnIP (blue), SnIP@TiO_2 (red), **c)** TiO_2 (black), $(CuI)_3P_{12}$ (blue), $(CuI)_3P_{12}$@TiO_2 (red) in 0.5 M Na_2SO_4. (CuIP ⇒ $(CuI)_{12}P_3$).

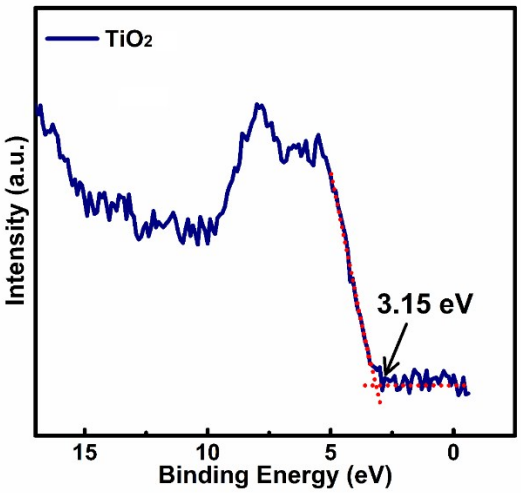

Figure S15. XPS valance band spectra of TiO_2 nanotube membranes showing the position of valance band maxima (VB_{max}) below Fermi level.

Kelvin Probe Force Microscopy (KPFM) Mesurement

To understand the dynamics of charge carrier separation and probe heterojunction formation between polyphosphides and TiO_2, surface potential (SP) difference of materials was determined using Kelvin Probe Force

Microscopy (KPFM) (Figure S16). The AFM topographical images of the samples displayed rough morphology and evidential presence of nanotube arrays (Figure S16a-d). The surface potential (SP) map of bare TiO_2, NaP_7@TiO_2, CuIP@TiO_2 and SnIP@TiO_2 deposited on FTO under dark condition is displayed in Figure S16a-d. The surface potential map of the samples shows uniform charge distribution at all sample surfaces. For bare TiO_2 nanotubes some bright region was observed which demonstrates electron rich surface of *n*-type TiO_2 nanotubes. Furthermore, the surface potential map contrast of SnIP@TiO_2 sample was slightly higher than other hybrid materials (NaP_7@TiO_2 and CuIP@TiO_2) which demonstrates higher electronic density of these materials. The surface potential distribution of bare TiO_2 was found to be ~38 mV, while SP of polyphosphide@TiO_2 hybrids, NaP_7@TiO_2, CuIP@TiO_2 and SnIP@TiO_2 was calculated to be ~ 27, 26, and 31 mV. A slightly negative shift of SP distribution of hybrid samples was corroborated to the lowering of work function value of nanohybrids. The lowering of WF (work function) value is attributed to the uplifting of the Fermi level of polyphosphides during Fermi level alignment in heterojunction formation because of charge carrier gradients (in-built electric field). The evident change in WF values and band structure clearly suggests successful formation of heterojunction between the materials.

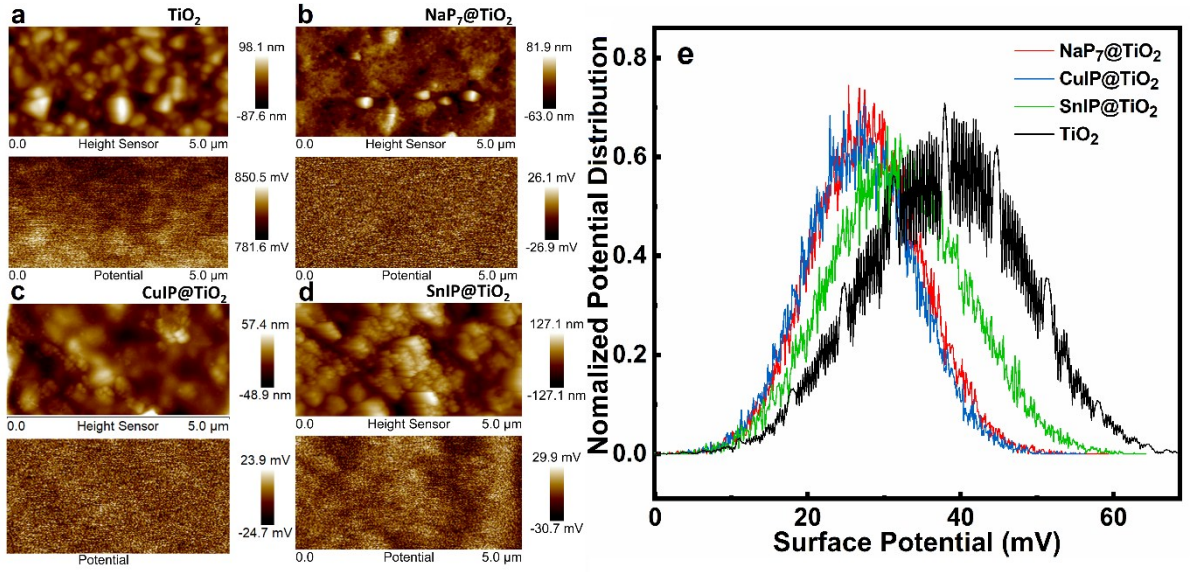

Figure S16. Topographical AFM images and surface potential map of **a)** TiO_2 nanotube, **b)** NaP_7@TiO_2, **c)** $(CuI)_3P_{12}$@TiO_2, **d)** SnIP@TiO_2 and **e)** surface potential distribution of bare TiO_2 nanotubes (black), NaP_7@TiO_2 (red), $(CuI)_3P_{12}$@TiO_2 (blue) and SnIP@TiO_2 (green) samples deposited on FTO under dark conditions.

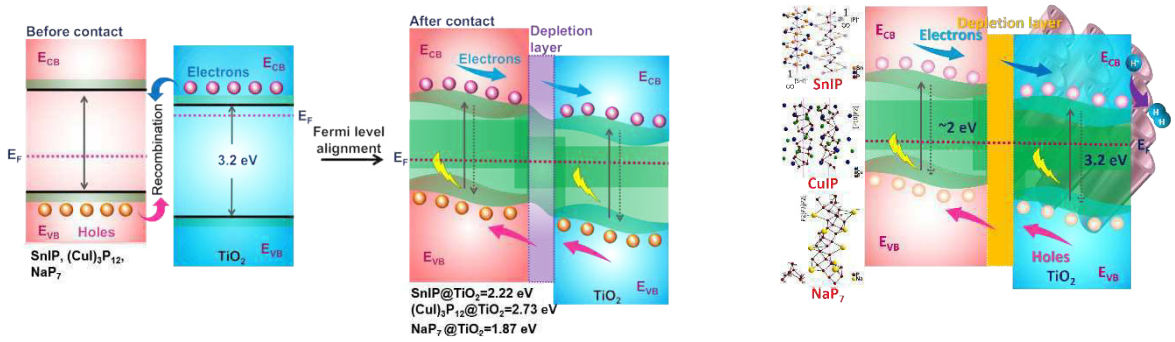

Figure S17. Left side: Plausible mechanism of charge separation in inorganic phosphides@TiO_2 heterojunction. Right side: Hybrid materials including heterojunction formation between TiO_2 nanotubes and different polyphosphides (NaP_7, SnIP and $(CuI)_3P_{12}$) for PEC-water-oxidation. (CuIP ⇒ $(CuI)_{12}P_3$).

EDS analysis

Table S1. Elemental analysis of deposited crystals found on both sides of the membranes and different spots along the razor cut cross section of NaP_x@TiO_2 membranes *via* EDS-measurements. Elemental composition in at.% with corresponding molar ratio deriving from the Na and P content and normalized to the Na content. Atomic percent of Ti is representing Ti in TiO_2.

EDS - NaP_x	**Na (at%)**	**P (at%)**	**Ti (at%)**	
NaP_7	12.5	87.5		NaP_7
NaP_{15}	6.25	93.75		NaP_{15}
NaP_7 measured, crystal	12.0(4)	87.9(1)	-	$Na_{0.96}P_{7.03}$
NaP_{15} measured, crystal	5.6(8)	94.4(2)	-	$Na_{0.9}P_{15.1}$
NaP_x@TiO_2 cross section 1	3.6(2)	16.4(2)	80.1(2)	$NaP_{4.5}$
NaP_x@TiO_2 cross section 2	1.5(1)	13.5(1)	85.0(3)	NaP_9

Table S2. Elemental analysis of deposited crystals found on both sides of the membranes and different spots along the razor cut cross section of SnIP@TiO_2 membranes *via* EDS-measurements. Elemental composition in at% with corresponding molar ratio deriving from the Sn, I and P content and normalized to the P content. Atomic percent of Ti is representing Ti in TiO_2.

EDS - SnIP	**Sn (at%)**	**I (a%)**	**P (at%)**	**Ti (at%)**	
SnIP	1	1	1		SnIP
SnIP measured, crystal	37.8(3)	26.3(3)	35.7(1)	-	$SnI_{0.7}P$
SnIP@TiO_2 cross section 1	13.2(2)	9.4(2)	20.2(2)	57.1(4)	$SnI_{0.7}P$
SnIP@TiO_2 cross section 2	10.5(6)	7.4(4)	18.6(8)	63.5(2)	$Sn_{0.6}I_{0.4}P$

Table S3. Elemental analysis of deposited crystals found on both sides of the membranes and different spots along the razor cut cross section of $(CuI)_3P_{12}$@TiO_2 membranes *via* EDS-measurements. Elemental composition in at% with corresponding molar ratio deriving from the Cu, I and P content and normalized to the P content. Atomic percent of Ti is representing Ti in TiO_2.

EDS - $(CuI)_3P_{12}$	**Cu (at%)**	**I (at%)**	**P (at%)**	**Ti (at%)**	
$CuI)_3P_{12}$	16.67	16.67	66.67		$Cu_3I_3P_{12}$
$(CuI)_3P_{12}$ measured, crystal	14.7(4)	16.1(3)	69.1(3)	-	$Cu_{2.6}I_{2.8}P_{12}$
$(CuI)_3P_{12}$@TiO_2 cross section 1	2.4(3)	2.5(3)	24.5(3)	72.6(5)	$Cu_{1.2}I_{1.2}P_{12}$
$(CuI)_3P_{12}$@TiO_2 cross section 2	16.5(5)	13.2(6)	69.0(5)	73.0(8)	$Cu_{2.9}I_{2.3}P_{12}$

Electrochemical impedance spectroscopy and impedance-potential analysis

Table S4. Values of electrolyte resistance R_S, charge transfer resistance R_C, charge transport resistance R_T, space charge capacitance C_{SC}, electrochemical double-layer (Helmholtz) capacitance C_H and constant phase element Q with coefficient n for $(CuI)_3P_{12}$, $(CuI)_3P_{12}$@TiO_2, SnIP, SnIP@TiO_2, NaP_7, NaP_7@TiO_2, obtained by fitting the Nyquist plots to the equivalent circuit (**Figure S13**).

Sample	R_S (Ohm)	C_{SC} (F)	R_T (Ohm)	C_H (F)	R_C (Ohm)	Q (Fs^{-1+n})	n
$(CuI)_3P_{12}$	16	9.00×10^{-8}	21	1.25×10^{-5}	10	5.50×10^{-4}	0.35
$(CuI)_3P_{12}$@TiO_2	16	6.00×10^{-8}	31	1.85×10^{-5}	50	5.80×10^{-4}	0.39
SnIP	16	1.00×10^{-7}	30	1.00×10^{-5}	10	4.75×10^{-4}	0.45
SnIP@TiO_2	16	1.10×10^{-7}	22	6.00×10^{-6}	1	9.50×10^{-4}	0.50
NaP_7	16	2.00×10^{-7}	16	1.50×10^{-5}	30	2.00×10^{-4}	0.54
NaP_7@TiO_2	16	8.50×10^{-8}	22	1.50×10^{-5}	1	2.10×10^{-4}	0.52

Table S5. Values of charge carrier concentration N_D, flat band potential V_{FB}, width of depletion layer W and calculated recombination lifetime τ for $(CuI)_3P_{12}$, $(CuI)_3P_{12}$@TiO_2, SnIP, SnIP@TiO_2, NaP_7, NaP_7@TiO_2 and TiO_2, obtained by fitting the Nyquist plots to the equivalent circuit (**Figure S13**).

Sample	N_D (cm^{-3})	V_{FB} (V *vs* Ag/AgCl)	V_{FB} (V *vs* NHE at pH-0)	W (nm)	τ (µs)
$(CuI)_3P_{12}$	3.88×10^{20}	-0.721	-0.522	113.18	1.90
$(CuI)_3P_{12}$@TiO_2	3.83×10^{20}	-0.692	-0.493	157.14	1.90
SnIP	1.69×10^{20}	-0.730	-0.531	712.80	3.00
SnIP@TiO_2	1.05×10^{20}	-1.930	-1.731	922.89	2.40
NaP_7	4.75×10^{20}	-0.670	-0.471	376.09	3.20
NaP_7@TiO_2	5.62×10^{20}	-0.780	-0.581	118.95	1.90
TiO_2	5.05×10^{20}	-0.702	-0.503	197.42	-

Table S6. Binding energies of different element and species present in TiO_2 nanotubes, NaP_7, NaP_7@TiO_2, $(CuI)_3P_{12}$, $(CuI)_3P_{12}$@TiO_2, SnIP, SnIP@TiO_2.

Sample	Ti2p ($Ti2p_{3/2}$) ($Ti2p_{1/2}$)	O1s ($O_{latt.}$) (-OH)	Na1s (Na1s)	Cu2p ($Cu\ 2p_{3/2}$) ($Cu2p_{1/2}$)	Sn3d ($Sn3d_{5/2}$) ($Sn3d_{3/2}$)	I3d ($I3d_{5/2}$) ($I3d_{3/2}$)	P2p ($P2p_{3/2}$) ($P2p_{1/2}$) (P_xO_y)
TiO_2	459.46 465.27	530.98 532.70	-	- -	- -	- -	- - -
NaP_7	- -	- -	1063.74	- -	- -	-	129.90 130.77 134.56
NaP_7@TiO_2	459.46 465.27	530.98 532.70	1071.83	- -	- -	-	130.00 130.98 133.82
$(CuI)_3P_{12}$	- -	- -	-	932.91 952.55	- -	619.94 631.42	134.39 135.27 -
$(CuI)_3P_{12}$@TiO_2	459.46 465.27	530.48 532.64	-	932.91 952.55	- -	620.30 631.89	134.40 135.33 -
SnIP	- -	- -	-	- -	487.51 495.88	619.87 631.37	133.73 134.71 139.77
SnIP@TiO_2	- -	530.98 532.74	-	- -	487.51 495.88	619.87 631.37	133.94 134.83 139.77

All binding energy values are in eV.

References

1. G. K. Mor, K. Shankar, M. Paulose, O. K. Varghese and C. A. Grimes, *Nano Lett.*, 2006, **6**, 215-218.
2. C. Grotz, M. Köpf, M. Baumgartner, L. A. Jantke, G. Raudaschl-Sieber, T. F. Fässler and T. Nilges, *Z. Anorg. Allg. Chem.*, 2015, **641**, 1395-1399.
3. D. Pfister, K. Schaefer, C. Ott, B. Gerke, R. Poettgen, O. Janka, M. Baumgartner, A. Efimova, A. Hohmann, P. Schmidt, S. Venkatachalam, L. van Wuellen, U. Schuermann, L. Kienle, V. Duppel, E. Parzinger, B. Miller, J. Becker, A. Holleitner, R. Weihrich and T. Nilges, *Adv. Mater. (Weinheim, Ger.)*, 2016, **28**, 9783-9791.
4. W. G. Palmer, *Experimental inorganic chemistry*, Cambridge University Press, Cambridge, 1962.
5. A. Pfitzner and E. Freudenthaler, *Angew. Chem. Int. Ed.*, 1995, **34**, 1647-1649.
6. U. K. Thakur, A. M. Askar, R. Kisslinger, B. D. Wiltshire, P. Kar and K. Shankar, *Nanotechnology*, 2017, **28**, 274001.
7. M. P. Baumgartner, Technische Universität München, 2017.
8. M. Baudler, *Angew. Chem.*, 1982, **94**, 520-539.
9. M. Baudler, *Angew. Chem.*, 1987, **99**, 429-451.
10. M. Baudler and K. Glinka, *Chem. Rev.*, 1993, **93**, 1623-1667.
11. S. Böcker and M. Häser, *Z. Anorg. Allg. Chem.*, 1995, **621**, 258-286.
12. G. Yang, D. Chen, H. Ding, J. Feng, J. Z. Zhang, Y. Zhu, S. Hamid and D. W. Bahnemann, *Appl. Catal. B*, 2017, **219**, 611-618.
13. M. Wang, B. Nie, K.-K. Yee, H. Bian, C. Lee, H. K. Lee, B. Zheng, J. Lu, L. Luo and Y. Y. Li, *Chem. Commun.*, 2016, **52**, 2988-2991.
14. W.-J. Kwak, Z. Chen, C. S. Yoon, J.-K. Lee, K. Amine and Y.-K. Sun, *Nano Energy*, 2015, **12**, 123-130.
15. T. Kajita and T. Itoh, *Phys. Chem. Chem. Phys.*, 2018, **20**, 2188-2195.
16. J. Song, C. Zhu, B. Z. Xu, S. Fu, M. H. Engelhard, R. Ye, D. Du, S. P. Beckman and Y. Lin, *Adv. Energy Mater.*, 2017, **7**, 1601555.
17. X. Zhong, Y. Jiang, X. Chen, L. Wang, G. Zhuang, X. Li and J.-g. Wang, *J. Mater. Chem. A*, 2016, **4**, 10575-10584.
18. Y. Zhou, C. Chen, N. Wang, Y. Li and H. Ding, *J. Phys. Chem. C*, 2016, **120**, 6116-6124.
19. R. Kumar, S. Govindarajan, R. K. Siri Kiran Janardhana, T. N. Rao, S. V. Joshi and S. Anandan, *ACS Appl. Mater. Interfaces*, 2016, **8**, 27642-27653.
20. F. Amano, M. Nakata, A. Yamamoto and T. Tanaka, *J. Phys. Chem. C*, 2016, **120**, 6467-6474.
21. I.-H. Tseng, W.-C. Chang and J. C. Wu, *Appl. Catal., B*, 2002, **37**, 37-48.
22. C. S. Chen, A. D. Handoko, J. H. Wan, L. Ma, D. Ren and B. S. Yeo, *Catal. Sci. Technol.*, 2015, **5**, 161-168.
23. C. S. Chen, J. H. Wan and B. S. Yeo, *J. Phys. Chem. C*, 2015, **119**, 26875-26882.
24. D. S. Bhachu, S. J. Moniz, S. Sathasivam, D. O. Scanlon, A. Walsh, S. M. Bawaked, M. Mokhtar, A. Y. Obaid, I. P. Parkin and J. Tang, *Chem. Sci.*, 2016, **7**, 4832-4841.
25. M. J. Islam, D. A. Reddy, N. S. Han, J. Choi, J. K. Song and T. K. Kim, *Phys. Chem. Chem. Phys.*, 2016, **18**, 24984-24993.
26. D. Hanlon, C. Backes, E. Doherty, C. S. Cucinotta, N. C. Berner, C. Boland, K. Lee, A. Harvey, P. Lynch and Z. Gholamvand, *Nat. Commun.*, 2015, **6**, 8563.
27. Z. Niu, J. Jiang and L. Ai, *Electrochem. Commun.*, 2015, **56**, 56-60.
28. G. G. Ninan, C. S. Kartha and K. Vijayakumar, *Sol. Energy Mater. Sol. Cells*, 2016, **157**, 229-233.
29. W. Gao, K. Zielinski, B. N. Drury, A. D. Carl and R. L. Grimm, *J. Phys. Chem. C*, 2018, **122**, 17882-17894.
30. M. Yan, Y. Hua, F. Zhu, W. Gu, J. Jiang, H. Shen and W. Shi, *Appl. Catal. B*, 2017, **202**, 518-527.
31. J. C.-R. Ke, D. J. Lewis, A. S. Walton, B. F. Spencer, P. O'Brien, A. G. Thomas and W. R. Flavell, *J. Mater. Chem. A*, 2018.
32. X.-D. Wang, Y.-F. Xu, H.-S. Rao, W.-J. Xu, H.-Y. Chen, W.-X. Zhang, D.-B. Kuang and C.-Y. Su, *Energy Environ. Sci.*, 2016, **9**, 1468-1475.
33. H. Tabassum, W. Guo, W. Meng, A. Mahmood, R. Zhao, Q. Wang and R. Zou, *Adv. Energy Mater.*, 2017, **7**, 1601671.
34. S. G. Ullattil and P. Periyat, *J. Mater. Chem. A*, 2016, **4**, 5854-5858.
35. H. Zhao, M. Wu, J. Liu, Z. Deng, Y. Li and B.-L. Su, *Appl. Catal. B*, 2016, **184**, 182-190.
36. M. S. Milien, U. Tottempudi, M. Son, M. Ue and B. L. Lucht, *J. Electrochem. Soc.*, 2016, **163**, A1369-A1372.
37. Z. Chen, H. N. Dinh and E. Miller, *Photoelectrochemical water splitting*, Springer, 2013.
38. X. Zhang, B. Zhang, K. Cao, J. Brillet, J. Chen, M. Wang and Y. Shen, *J. Mater. Chem. A*, 2015, **3**, 21630-21636.
39. H. Wang, Y. Liang, L. Liu, J. Hu and W. Cui, *J. Hazard. Mater.*, 2018, **344**, 369-380.
40. A. Muñoz, Q. Chen and P. Schmuki, *J. Solid State Electrochem.*, 2007, **11**, 1077-1084.
41. F. Y. Oliva, L. a. B. Avalle, E. Santos and O. R. Cámara, *J. Photochem. Photobiol., A*, 2002, **146**, 175-188.

3.2. Vapor Deposition of Semiconducting P Allotropes into TiO_2 Nanotube Arrays for Photo-Electrocatalytic Water Splitting

Ebru Üzer,[a] Pawan Kumar,[b] Ryan Kisslinger,[b] Piyush Kar,[b] Ujwal Kumar Thakur, [b] Sheng Zeng, [b] Karthik Shankar,[b,*] and Tom Nilges [a,*]

[a] Synthesis and Characterization of Innovative Materials group, Department of Chemistry, Technical University Munich, Lichtenbergstr. 4, Garching bei München 85748, Germany

[b] Department of Electrical and Computer Engineering, University of Alberta, 9211 - 116 St, Edmonton, Alberta, Canada T6G 1H9

ACS Applied Nano Materials Pages 60 - 94
DOI: 10.1021/acsanm.9b00221

The article 'Vapor growth of semiconducting P allotropes into TiO_2 nanotube arrays for photo-electrocatalytic water splitting applications' was submitted to 'ACS Applied Nano Materials' in February 2019 and published online in May 2019. Results were presented by Ebru Üzer at the 101st Canadian Chemistry Conference and Exhibition in Edmonton, Canada in May 2018 and the Annual ATUMS meeting in Raitenhaslach, Germany in November 2018.

The objective of this work was a modification of TiO_2 nanotube properties by band gap engineering and optimization of key factors required for photocatalytic hydrogen and oxygen evolution in water-splitting experiments. In a similar manner as presented in paragraph 3.1., hybrid materials of semiconducting P allotropes, namely black P and fibrous red P were fabricated, following a simple low-pressure vapor deposition onto and into TiO_2 nanotube arrays.

Previously electrochemically anodized TiO_2 nanotube membranes of 40 – 150 µm nanotube length and ~100 nm inner tube diameter were successfully covered by fibrous red P and black P, confirmed by light microscope imaging, SEM-EDS analysis, and powder X-ray diffraction. STEM-EDS images displayed individual and bundle-TiO_2 nanotubes corroborating fibrous red P and black P. Filling of the tubes was additionally

approved by point-by-point Raman analysis. A 1.5 µm resolution laser was run along a razor cut cross section of hybrid membranes. The detected data resulted in characteristic fibrous red P Raman modes next to TiO_2 anatase down to 20 µm and crystalline black P down to 7 µm both from the membrane top side.

Elemental binding energies, oxidation states and surface composition indicated the similar characteristics for pristine fibrous red P, black P, TiO_2 and the hybrid materials, tested in HR-XPS analyses. A peak change in the P2p region, sparsely in fibrous red P@TiO_2 and significant in black P@TiO_2 implied partial reaction to phosphorus oxides. Initiated engineering of optical properties was observed after gas-phase transport reactions onto TiO_2 nanotube arrays, showing an initial optical band gap value of 2.97 eV (*vs.* 3.2 eV in pristine TiO_2 anatase[91]). Band gap values of pristine fibrous red P and black P were found to be 1.97 eV and 1.67 eV. In hybrid materials we found slightly shifted peak wavelengths toward the long wavelength region for (2.1 eV in fibrous red P@TiO_2; 1.54 eV in black P@TiO_2). Thus, an effect of improved visible light absorption could be identified beneficial for solar light harvesting applications.

Efficiency of potential photocatalytic water-splitting agents (commercially used TiO_2 nanotubes, pristine P allotropes and hybrid materials) were compared. Photocurrent density was tested in linear sweep voltammetry which resulted in values of 0.22 $mA \cdot cm^{-2}$ for pristine TiO_2, 0.25 $mA \cdot cm^{-2}$ for fibrous red P, and 0.19 $mA \cdot cm^{-2}$ for black P at 0.6 V *vs* Ag/AgCl (1.23 V *vs* RHE). Hybrid fibrous red P@TiO_2 exhibited a three-fold improvement of 0.6 $mA \cdot cm^{-2}$ compared to 0.20 $mA \cdot cm^{-2}$ of black P@TiO_2. Suggesting a successful heterojunction generation in fibrous red P@TiO_2 and reduced photocatalytic performance effects of black P@TiO_2 presumably based on undesirable P_xO_y formation. Calculated photoconversion efficiency of hybrid fibrous red P@TiO_2 was found to be ~3.5 times higher than for pristine TiO_2.

EIS investigation of mobile charge carriers in the semiconductor-electrolyte interfaces revealed reduction of charge transfer resistance, charge transport resistance and electrochemical double-layer capacitance of hybrid materials compared to pristine TiO_2 nanotubes. The latter component is indicating a formation of a wider depletion region at the fibrous red P-TiO_2 interface. Longest recombination lifetime of the measured compounds could be accounted for pristine TiO_2 nanotubes with 2.8 µs at highest. Due to interfacial effects in hybrid allotrope P materials as detected in HR-XPS data, a larger impact on fibrous red P@TiO_2 than black P@TiO_2 is implied.

Charge carrier concentration derived from impedance potential analysis was improved in both hybrid fibrous red P@TiO_2 ($1.9 \cdot 10^{21}$ cm^{-3}) and black P@TiO_2 ($3.4 \cdot 10^{21}$ cm^{-3}) than in hollow TiO_2 nanotubes. Including UPS results, an energy level

diagram was constructed, describing a Z-scheme junction formation during energy level alignment at the semiconductor-hetero interface. Deeper VB_{max} energy values in hybrid phosphorus allotrope@TiO_2 compared to pristine compounds suggest successful heterojunction formation and p-type characteristics for the P allotropes and therefore the formation of a *p*/*n*-heterojunction system. In the charge carrier flow process at the P allotrope-titania interface, an upward band bending in the P allotrope band structure and a downward band bending in TiO_2 was demonstrated.

AUTHORS CONTRIBUTION: E.Ü. and R.K. performed synthesis and characterization of P allotrope-TiO_2 hybrid materials. P.Ku. was involved in XPS, UPS, and photoelectrochemical studies and compilating the results. P.Ka. was responsible for electrochemical characterizations. K.S. and T.N. planned and supervised all research studies. All authors were involved in writing their respective parts.

ACS APPLIED NANO MATERIALS
Cite This: ACS Appl. Nano Mater. XXXX, XXX, XXX−XXX
Article
www.acsanm.org

Vapor Deposition of Semiconducting Phosphorus Allotropes into TiO_2 Nanotube Arrays for Photoelectrocatalytic Water Splitting

Ebru Üzer,[†] Pawan Kumar,[‡,§] Ryan Kisslinger,[‡,§] Piyush Kar,[‡] Ujwal Kumar Thakur,[‡] Sheng Zeng,[‡] Karthik Shankar,*[,‡] and Tom Nilges*[,†]

[†]Department of Chemistry, Technical University of Munich, Lichtenbergstrasse 4, Garching 85748, Germany

[‡]Department of Electrical and Computer Engineering, Faculty of Engineering, University of Alberta, 9211 116th Street NW, Edmonton, Alberta T6G 1H9, Canada

Supporting Information

ABSTRACT: Recent evidence of exponential environmental degradation will demand a drastic shift in research and development toward exploiting alternative energy resources such as solar energy. Here, we report the successful low-cost and easily accessible synthesis of hybrid semiconductor@TiO_2 nanotube photocatalysts. In order to realize its maximum potential in harvesting photons in the visible-light range, TiO_2 nanotubes have been loaded with earth-abundant, low-band-gap fibrous red and black phosphorus (P). Scanning electron microscopy− and scanning transmission electron microscopy−energy-dispersive X-ray spectroscopy, X-ray diffraction, Raman spectroscopy, X-ray photoelectron microscopy, and UV−vis measurements have been performed, substantiating the deposition of fibrous red and black P on top and inside the cavities of 100-μm-long electrochemically fabricated nanotubes. The nanotubular morphology of titania and a vapor-transport technique are utilized to form heterojunctions of P and TiO_2. Compared to pristine anatase 3.2 eV TiO_2 nanotubes, the creation of heterojunctions in the hybrid material resulted in 1.5−2.1 eV photoelectrocatalysts. An enhanced photoelectrochemical water-splitting performance under visible light compared with the individual components resulted for the P@TiO_2 hybrids. This feature is due to synergistically improved charge separation in the heterojunction and more effective visible-light absorption. The electronic band structure and charge-carrier dynamics are investigated in detail using ultraviolet photoelectron spectroscopy and Kelvin probe force microscopy to elucidate the charge-separation mechanism. A Fermi-level alignment in P@TiO_2 heterojunctions leads to a more reductive flat-band potential and a deeper valence band compared to pristine P and thus facilitates a better water-splitting performance. Our results demonstrate effective conversion efficiencies for the nanostructured hybrids, which may enable future applications in optoelectronic applications such as photodetectors, photovoltaics, photoelectrochemical catalysts, and sensors.

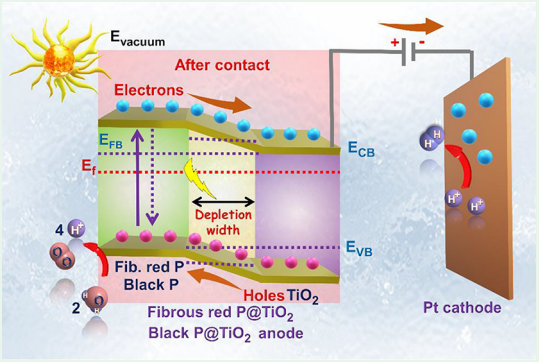

KEYWORDS: *phosphorus, TiO_2, vapor-phase deposition, low-band-gap materials, photocatalyst, heterojunction, sunlight-driven water splitting*

INTRODUCTION

Limited reserves of carbon-emitting fossil fuels and their associated negative environmental impact have triggered research into finding alternative self-sustainable technologies. Sunlight-driven water splitting to generate hydrogen fuels is a promising approach as an alternate energy technology. However, photosplitting of water to generate hydrogen is unfavorable because of a high positive Gibbs free-energy change (+237 kJ mol^{-1}) and the need for a process requiring a photocatalyst (usually semiconductor) with appropriate conduction band (CB) and valence band (VB) positions.[1] Various nanostructured semiconductor materials have been extensively investigated for application in photochemical and photoelectrochemical water splitting, i.e., $BiVO_4$, WO_3, Fe_2O_3, MoS_2, CoO, g-C_3N_4, CdS, $Ga_{1-x}Zn_xN_{1-x}O_x$, SnS_2, $SrTiO_3$, etc.[2−7] However, meeting the broad range of required properties in one single material to actuate water splitting remains a challenge; such properties include visible-light absorptivity, long-lived charge carriers, high quantum efficiency, electrochemical resiliency, low cost, and nontoxicity with the appropriateness of the CB (<0.00 V vs NHE) and VB (>1.23 V vs NHE) edges for electron transfer and the formation of hydrogen (reduction) and oxygen from water (oxidation), respectively. TiO_2, which meets many of the aforementioned requirements, nevertheless suffers from poor visible-light absorption and fast recombination of photogenerated charge carriers. Band-structure manipulation of TiO_2 via approaches such as doping, sensitization, hetero-

Received: February 5, 2019
Accepted: May 9, 2019
Published: May 9, 2019

DOI: 10.1021/acsanm.9b00221
ACS Appl. Nano Mater. XXXX, XXX, XXX−XXX

junction formation, etc., and morphological engineering are enticing approaches to improve the quantum efficiency.[8−11] One-dimensional (1D) TiO_2 nanostructures like nanorods, nanotubes, nanocones, etc., are particularly interesting because of their large accessible surface areas, vectorial charge-transport pathways, and a carrier retrieval length comparable to that of the smallest dimension of the nanostructure. Thus, they have emerged as excellent candidates for heterojunction formation with low-band-gap semiconductors.[12−17]

Low-cost TiO_2 nanotube layers fabricated via electrochemical anodization present varied applications in photocatalytic, photovoltaic, and optoelectronic sensing devices.[18−20] By maximization of the specific surface area from bulk to nanoparticulate TiO_2, improvement of the photoelectrochemical water-splitting performance using solar light can be achieved.[21] To broaden the application spectrum and overcome key drawbacks of TiO_2 nanotubes, our intention is band-gap engineering and semiconductor/electrolyte contact optimization, which play a major role in efficient photocatalytic water splitting.[22,23] Therefore, we utilize a hybrid system of semiconductor materials between highly ordered self-organized TiO_2 nanotube membranes and inexpensive phosphorus (P) allotropes, 1D fibrous red P and two-dimensional (2D) black P, which leads to higher-efficiency composite photocatalysts. As-prepared hollow nanosized cylinders of TiO_2 nanotubes were formed by electrochemical, field-aided, three-step anodization of titanium (Ti) films or foils in electrolytes containing $F^-/I^-/ClO_3^-$ ions. Both P allotropes were deposited via low-pressure chemical vapor deposition (CVD).[24,25] In order to prevent the semiconductor−semiconductor hybrid from material degradation during long thermal treatment processes, the vapor deposition or so-called mineralization technique allows crystallization of amorphous TiO_2 to anatase. At the same time, the desirable growth of P nanorods inside and onto the nanotubes in one annealing step (at ∼500 °C) takes place. The intrinsic band gap for the n-type semiconductor anatase TiO_2 in the UV range at 3.2 eV limits light absorption to only <5% of the solar spectrum.[26] To much better exploit the solar spectrum, heterojunction systems with two P allotropes were investigated: (a) fibrous red P, exhibiting a band gap of 2.25 eV based on our experimental results and (b) p-type semiconducting black P due to a direct band gap of 0.3 eV for bulk material in the near-IR region. The latter is characterized by a high, layer-dependent hole-carrier mobility of ca. 10^5 $cm^2/(V\ s)$.[27−29] Fibrous red P is being investigated regarding its potential as a water-splitting agent and black P as a field-effect transistor, a photodetector, and a sensor.[30−32] In a heterojunction system, the photogenerated carrier mechanism can induce the formation of a built-in potential (V_{bi}) and hinder electron−hole pair recombination.[33−36] The dense hybrid structure supports the fast charge separation of carriers, created inside the nanorods, and migration of a short distance equal to the nanotube radius to cross the heterojunction interface. Excellent quantum yields can be obtained from the suitable nanotube structure because of a high aspect ratio, which ensures efficient photon harvesting, orthogonalized processes of charge separation and light absorption, and improved light trapping by Mie scattering.[37−39] Modification of the TiO_2 nanotubes has been approached by the decoration of surfaces with noble-metal nanoparticles, such as gold, silver, and platinum. A solid interface occurs, in which a Schottky contact is formed that is less preferable than a p/n-semiconductor contact in terms of charge-carrier recombination loss.[23,38,40,41] Recently, the desired Z-scheme junction formation has been successfully carried out with CdS, g-C_3N_4, MoS_2, $ZnIn_2S_4$, Fe_2O_3, halide perovskites, etc., for use in extensive photocatalytic applications such as CO_2 photoreduction, high-performance photoanodes for water-splitting devices, selective gas sensors, and high-efficiency solar cells.[42−47] In this work, we introduce a vapor-transport process to grow hybrid semiconductor−semiconductor 1D and 2D materials to form heterojunctions capable of realizing enhanced photoelectrochemical water splitting.

RESULTS AND DISCUSSION

This section is divided into two main chapters: (1) structural characterization of fibrous red and black P deposited into and onto the TiO_2 nanotube arrays and (2) the photocatalytic activity of the P allotrope@TiO_2 hybrid materials. Spectroscopic [X-ray photoelectron spectroscopy (XPS), UV−vis, Raman, and Kelvin probe force microscopy (KPFM) studies in the Supporting Information, SI] and X-ray diffraction (XRD; see the SI) experiments were applied to characterize the bare and hybrid materials. A brief photoelectrocatalytic investigation of the P allotrope@TiO_2 hybrid materials contains the full electrochemical characterization [hydrogen and oxygen evolution and calculation of the efficiencies, i.e., ABPE, IPCE, APCE, and Faradaic efficiency (FE) in the SI], including a plausible mechanism for the water-splitting activity of the title compounds.

Structural Characterization of P Allotrope@TiO_2 Nanotube Hybrids. In order to fabricate hybrid semiconducting materials, we succeeded in filling the anatase-type TiO_2 nanotubes with fibrous red and black P using a short-way transport reaction (Figure 1; experimental details are given in the SI). This reaction is adapted from the so-called mineralization principle used for the synthesis of a plethora of P-containing compounds, as in fibrous solely, binary, and ternary P compounds like NaP_7 and SnIP.[48−50]

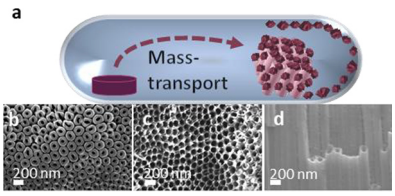

Figure 1. (a) Fibrous P (purple pellet) reacted onto and into TiO_2 nanotube membranes (pink). Representative SEM pictures of the electrochemically prepared TiO_2 nanotube membranes used in a mineralizer-driven short-way transport reaction along the (b) bottom, (c) top, and (d) normal side views.

The TiO_2 nanotube structure could be preserved after the deposition of P allotropes via thermal treatment during the transport reactions.

Fibrous Red P@TiO_2 Nanotubes. The mineralization method can be applied to prepare element allotropes and binary and ternary compounds. An example is the successful deposition of fibrous red P onto and into TiO_2 nanotube membranes via the gas phase, as shown in Figure 2. Pure fibrous P exhibits photocatalytic activity and has the potential for water-splitting applications.[20] Fibrous red P has been formed everywhere on the TiO_2 nanotube membrane (Figure 2b). Noticeably, fibrous P is distributed on the whole surface of the membranes, as scanning electron microscopy−energy-

DOI: 10.1021/acsanm.9b00221
ACS Appl. Nano Mater. XXXX, XXX, XXX−XXX

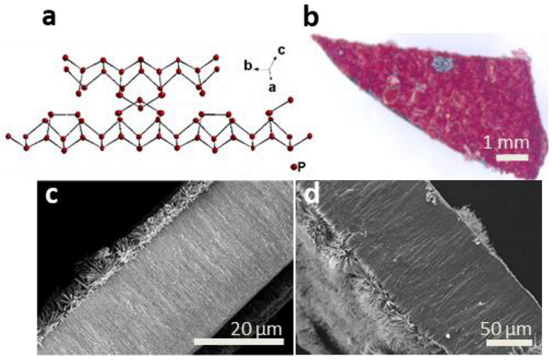

Figure 2. (a) Crystal structure of fibrous red P. (b) TiO_2 nanotube membrane covered with fibrous red P after reaction via gas phase. (c and d) SEM images of the cross section and surface of fibrous P@TiO_2 nanotube membranes. Fibrous P covers the surface of the membrane. EDS of the cross section shows P all along the nanotubes (Table S1).

dispersive X-ray spectroscopy (SEM–EDS) measurements exhibit in Figure 2c,d and Table S1. According to powder XRD data, the growth of fibrous red P on top of the TiO_2 nanotube membranes was confirmed (Figure S1).

Scanning transmission electron microscopy (STEM) images taken after separation of the TiO_2 nanotubes by an ultrasonication process show a bundle of nanotubes with diameters of ~90–100 nm. Elemental mapping confirms Ti, oxygen (O), and P with a distribution of P along the full tube length (Figure 3).

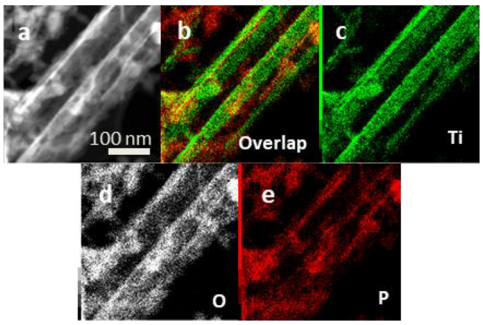

Figure 3. (a) STEM bright-field image of TiO_2 nanotubes separated from a membrane by an ultrasonication procedure. (b) Elemental mapping of the overlaid elements Ti, O, and P. (c and d) Ti and O of the TiO_2 nanotubes, (e) with P distributed along the full length of the tubes.

The successful growth of a fibrous red P structure up to a certain depth into the TiO_2 nanotube arrays can be verified via Raman measurements. Therefore, TiO_2 nanotube membranes were cut along the cross section after CVD of fibrous red P, and imaging at specific spots from the surface of a TiO_2 nanotube array downward along a vertical line was acquired. The laser has a standard mode spot size of 1.5 μm (at 50× magnification). Raman spectra were recorded at several spots along the 65-μm-long cross section of the membranes. The experimental frequencies of bulk fibrous red P match the significant modes between 352 and 462 cm^{-1} recorded up to 20 μm in distance to the surface from the top side and 15 μm in distance to the surface from the bottom side along the cross section of the membranes (shown in Figure S2). A systematic detection of spots further into the 65-μm-long tubes shows the expected modes for pure anatase and the additional characteristic modes of fibrous P up to 15 μm recorded from the top side of the nanotube array and 15 μm from the bottom side (Figure 4). A reduction of the crystallinity of fibrous red P upon going deeper into the tubes can be observed.

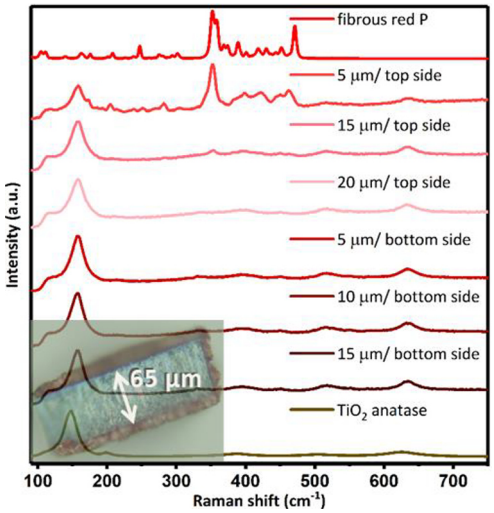

Figure 4. Raman spectroscopy on fibrous red P@TiO_2 membranes. From the top down: reference Raman spectrum of fibrous red P and spectra of a fibrous red P@TiO_2 membrane cross section measured at approximately 5, 15, and 20 μm in distance to the surface (membrane top side) and at approximately 5, 10, and 15 μm in distance to the surface (membrane bottom side) and a blank TiO_2 membrane (anatase, brown).

After the successful growth of fibrous red P onto and into TiO_2 nanotube arrays was demonstrated via powder XRD, SEM–EDS, Raman spectroscopy, and STEM–EDS analysis, the growth of partially crystalline fibrous P into the membrane was realized, whereas nicely crystallized fibrous P was found at the surface of the membranes.

Black P@TiO_2 Nanotubes. A similar successful gas-phase deposition has been performed with black P, another element allotrope of P. Black P is characterized by a structure (on the number of neighboring P layers)-dependent band-gap value covering a wide range of the electromagnetic spectrum.[51] Thus, black P has potential in applications such as field-effect transistors, p–n junctions, photodetectors, etc.[52] This orthorhombic allotrope of P crystallizes in space group *Cmca* (crystal structure in Figure 5a) shows a high carrier mobility and in-plane anisotropy, playing a role in hydrogen and oxygen generation in photocatalytic water splitting.[51] Moreover, a broadening of the absorption fraction toward the visible-light range of 3.2 eV TiO_2 anatase can be provided by a heterojunction formation with the narrow-band-gap semiconductor black P. Depending on the number of neighboring layers stacked onto each other, a band gap of 0.3 eV in bulk black P to ~2 eV for the monolayer (called phosphorene) can be realized. The overall efficiency of the existing narrow-band-gap water-splitting photocatalysts is affected by photocorrosion, which results from the chemical bond strength of the given system.[53] This fact can be avoided by the fabrication of a heterojunction hybrid system between black P and TiO_2 nanotube arrays, where the chemical bond strength of the bulk material (TiO_2 anatase) will remain and only an alignment of the Fermi levels between the materials during charge-carrier-

DOI: 10.1021/acsanm.9b00221
ACS Appl. Nano Mater. XXXX, XXX, XXX–XXX

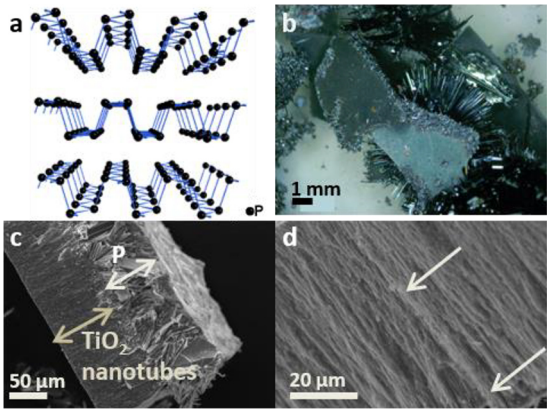

Figure 5. (a) Crystal structure of black P. (b) TiO_2 nanotube membranes with black P needles on the front and back sides after reaction via the gas phase. (c and d) SEM images of the cross section and covered surface of black P@TiO_2 nanotube membranes. There is visible horizontal growth along the vertical tube axis between white arrows. EDS of the cross section shows P all along the nanotubes.

transport reactions within the hybrid occurs.[23] A visual deposition of characteristic flat metallic-colored needles, spreading out gradually on the TiO_2 nanotube membranes (reversed side), can be seen in Figure 5b. A SEM image in Figure 5c shows the successful deposition of a thick black P layer covering the surface of this cut cross-sectional part of a TiO_2 nanotube membrane. The second SEM image in Figure 5d is displaying a gradual growth of small horizontally aligned black P crystals between the two arrows, which is confirmed by EDS measurements (Table S2). A reason for this unusual growth can be the unique 2D structure of black P. Powder XRD data can confirm the formation of black P on top of the TiO_2 nanotube arrays (Figure S3).

After separation of the TiO_2 nanotubes in an ultrasonication process, STEM imaging displays a singular tube with a width of ~150 nm. P was detected inside the tube besides Ti from the TiO_2 membrane after elemental mapping. Furthermore, analysis of tin (Sn) and iodine (I) inside the tubes was carried out because of the fact that SnI_4 was used during the transport reaction for synthesis. The formation of SnIP, as a possible side product, in such a transport reaction was ruled out (Figure 6).[50]

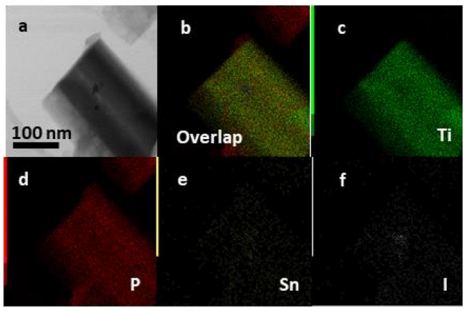

Figure 6. (a) STEM bright-field image of TiO_2 nanotubes separated from a membrane by an ultrasonication procedure. (b) Elemental mapping of overlaid elements Ti (representing TiO_2), P, Sn, and I. (c) Ti and (d) P substantiating P distributed along the full length of a TiO_2 nanotube, with (e) Sn and (f) I coming from the mineralizer only present in small amounts.

To verify the successful growth of black P into TiO_2 nanotubes, several Raman spectra were recorded after cutting the nanotube membranes at the cross section after synthesis. A simultaneous presence at the membrane surface of black P (main phase), with the most prominent modes at 360, 436, and 464 cm^{-1} next to anatase with a characteristic mode at 145 cm^{-1}, can be confirmed. A gradual change is detectable when the laser is pointed down to a depth of 7 μm into the nanotubes, where black P next to anatase (main phase) still can be confirmed (Figure 7). The crystallinity of the black P phase

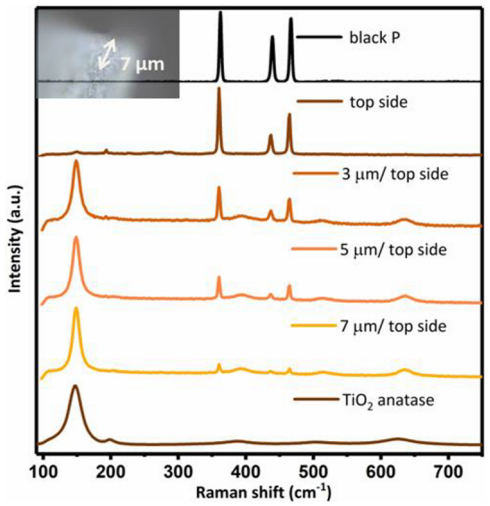

Figure 7. Raman spectroscopy on black P@TiO_2 membranes. From the top down: reference Raman spectrum of black P, spectra of a black P@TiO_2 membrane cross section measured at the surface and approximately 3, 5, and 7 μm in distance to the surface (membrane top side), and a fresh TiO_2 membrane (anatase, brown).

remains unchanged, in comparison to Raman imaging of fibrous red P@TiO_2 nanotubes. This is an additional proof of the assumption of distinct P needles in the SEM image in Figure 5d.

XPS. Characterization of the surface composition, binding energies, and oxidation states of fibrous red and black P next to blank TiO_2 samples, hybrid fibrous red P@TiO_2, and black P@TiO_2 was investigated via high-resolution XPS studies. The heterostructure systems reveal consistent oxidation states along with the pure samples. A shift of the binding energies in the O 1s region of fibrous red P@TiO_2 and black P@TiO_2 compared to pristine TiO_2 can be primarily attributed to the formation of P−O bonds in the heterostructure system (Figures S5 and S6).

UV−Vis Spectroscopy. The optical properties of the samples were determined using UV−vis in diffuse-reflectance mode (Figure S4). A sharp peak around 320 nm in the UV−vis spectrum of TiO_2 with a band tailing up to 380 nm arises from a O 2p → Ti 3d transition of electrons, demonstrating a VB to CB transition. The absorption spectrum of fibrous red P shows a broad absorption band extending to the visible range. Fibrous red P deposited on wide-band-gap TiO_2 shows improved absorption in the visible region because of the presence of moderate-band-gap fibrous red P. The UV−vis spectrum of black P shows three absorption bands at 315, 374, and 438 nm, with broadening of the absorption bands in the IR region. This is in line with findings in the published literature.[54,55] After the deposition of black P on TiO_2 nanotubes, the visible-light and

DOI: 10.1021/acsanm.9b00221
ACS Appl. Nano Mater. XXXX, XXX, XXX−XXX

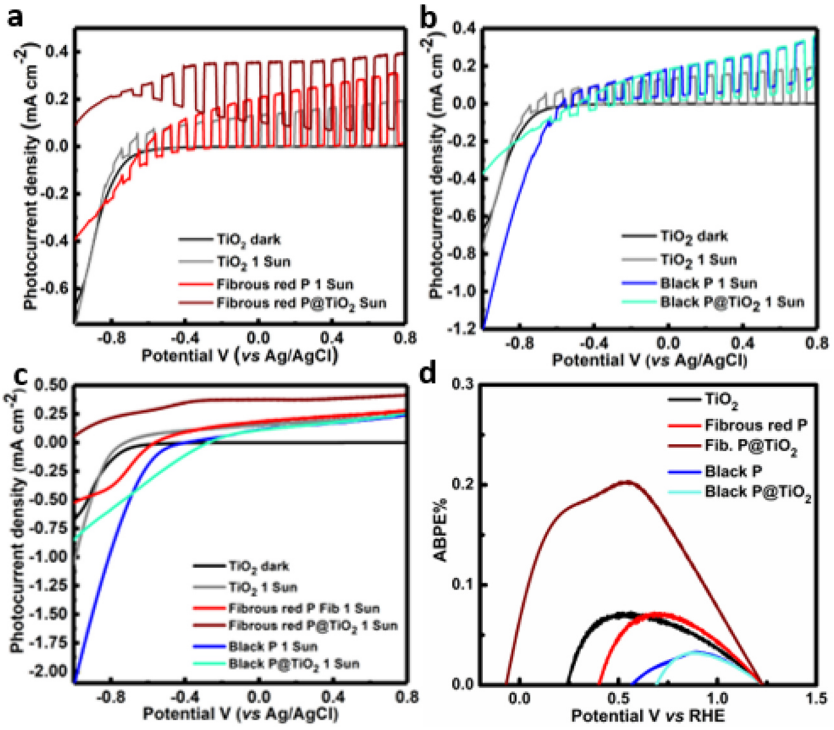

Figure 8. (a and b) Linear-sweep voltammograms of TiO_2, fibrous red P, fibrous red P@TiO_2, black P, and black P@TiO_2, under dark conditions and 1 solar simulated AM1.5 G light irradiation (100 mW cm^{-2}) showing the photoresponse during on−off and (c) standard mode cycling. (d) ABPE % versus RHE plot under AM1.5 G light irradiation (100 mW cm^{-2}). Color code: TiO_2 under dark conditions, black; TiO_2 under AM1.5 G light irradiation, grey; fibrous red P, red; fibrous red P@TiO_2, brown; black P, blue; black P@TiO_2, light blue.

IR absorption range was increased, which demonstrates a better visible-light response of the samples.

Visible-light absorption of the samples was investigated in detail using Tauc plots by plotting a graph of $(\alpha h\nu)^{1/2}$ versus $h\nu$, followed by extrapolation of a linear tangent to the X axis, where α is the absorption coefficient, h is the Planck constant, and ν is the light frequency (Figure S4). The values of the optical band gaps from the Tauc plots were found to be 2.97 eV for TiO_2, 1.97 eV for fibrous red P, 2.1 eV for fibrous red P@TiO_2, 1.67 eV for black P, and 1.54 eV for black P@TiO_2, respectively, which are in close agreement with the reported values and clearly demonstrate absorption in the visible region by the heterojunction hybrids (Figure S4).

Photocatalytic Activity of P Allotrope@TiO_2 Nanotube Hybrids. The photoelectrochemical water splitting performance of all compounds was tested using a three-electrode system. In this setup, the specimens, deposited on fluorine-doped tin oxide, formed the anode (working electrode), while platinum and Ag/AgCl were used as the cathodes (counter electrode) and reference electrode, respectively. The photoanode was irradiated with AM1.5 G simulated sunlight with a power density of 100 mW cm^{-2} (1 sun) at the sample surface. The current density (mA cm^{-2}) was measured using linear-sweep voltammetry (LSV) by sweeping the applied voltage from −0.1 to +0.8 V versus Ag/AgCl at a scan rate of 0.1 V s^{-1}. To compare the photoresponses, the dark current was also measured. The photocurrent response during light on−off cycles shows a rise and drop in the photocurrent, which substantiates the photogeneration of charge carriers in the samples under light irradiation (Figure 8a,b). The photocurrent densities for TiO_2, fibrous red P, fibrous red P@TiO_2, black P, and black P@TiO_2, at 0.6 V versus Ag/AgCl (1.23 V vs RHE; water oxidation potential), were measured to be 0.22, 0.25, 0.60, 0.19, and 0.20 mA cm^{-2} respectively (Figure 8c). Under dark conditions, a negligible current was observed. The photocurrent densities of pristine black P, bare TiO_2, and pristine fibrous red P were almost identical because of the poor carrier separation in P and the lack of visible-light absorption in TiO_2. Further, black P@TiO_2 does not show a noticeable increase in the photocurrent density, which can be attributed to the lack of a synergistic photocatalytic process, which is likely due to the higher degree of oxidation of P in black P to P_xO_y, which was evident in the XPS data (Figure S5). Interestingly, the fibrous red P@TiO_2 hybrid exhibited a relatively high photocurrent density (0.60 mA cm^{-2}), suggesting the successful formation of a heterojunction and better charge transfer between fibrous red P and TiO_2 (Figure 8a). The viability of the photocatalytic system to perform under visible light was tested by irradiating the specimens with a 425 nm LED light and a power density of 54.15 mW cm^{-2}. The increase in the photocurrent under 425 nm of irradiation clearly demonstrates the applicability of the system to perform at longer wavelengths (Figure S11). The highest applied bias photon-to-current efficiency percentage (ABPE %; calculation details are given in the SI) was found for a fibrous red P@TiO_2 nanohybrid, which was approximately 3.0 times higher than that for TiO_2 and pristine fibrous red P, and demonstrates that heterojunction formation with TiO_2 increases the photoelectrocatalytic performance significantly (Figure 8d).[56,57] Further, action spectra, showing IPCE and APCE % of materials as a function of the wavelength, demonstrate that a fibrous red P@TiO_2 nanohybrid outperformed and calculated IPCE and APCE % at 450 nm were found to be 1.30 and 1.65%, respectively (see the SI). To verify that the generated photocurrent originated from the photoelectrochemical water splitting and not from side reactions or

DOI: 10.1021/acsanm.9b00221
ACS Appl. Nano Mater. XXXX, XXX, XXX−XXX

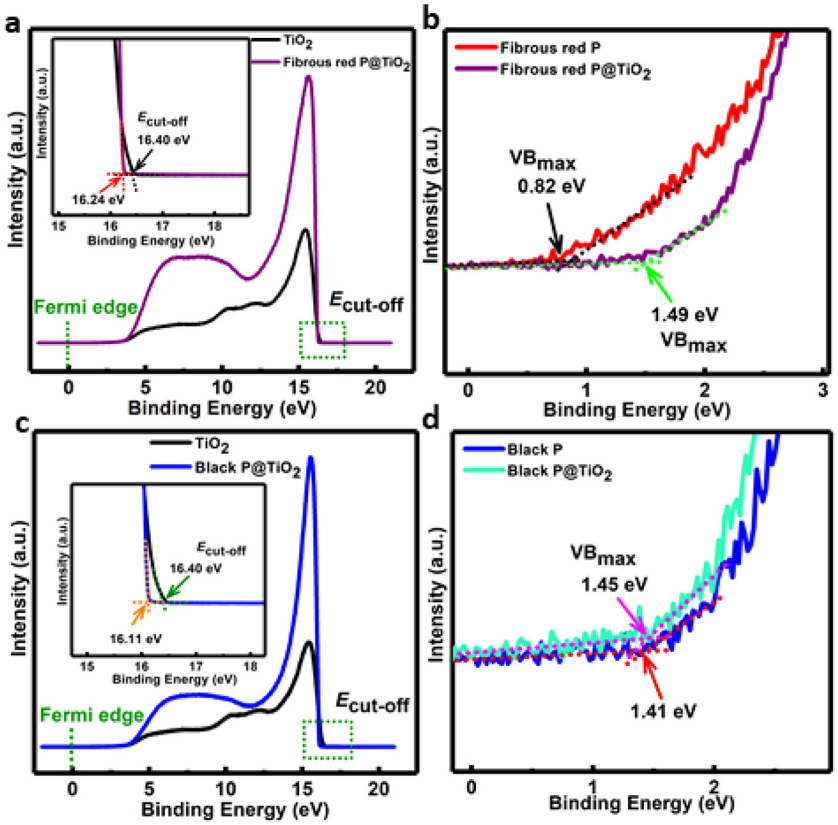

Figure 9. UPS WF spectra of (a) TiO_2 and fibrous red P@TiO_2 and (c) TiO_2 and black P@TiO_2. Inset: E_{cutoff}. The value of the WF was determined from the UPS WF spectra by using the equation WF(Φ) = 21.21 − E_{cutoff}, where 21.21 eV is the energy of the incident He I line of a He discharge lamp used for UPS. UPS VB spectra of (b) fibrous red P and fibrous red P@TiO_2 and (d) black P and black P@TiO_2 Color code: TiO_2, black; fibrous red P, red; fibrous red P@TiO_2, purple; black P, blue; black P@TiO_2, light blue.

photocorrosion of the electrodes, evolved hydrogen at the platinum counter electrode was collected to calculate the Faradaic efficiency (FE; see section 2.6 in the SI). The black P@TiO_2 hybrid displayed the highest FE (90.61%), demonstrating the origin of the photocurrent from water splitting and negligible photocorrosion of the materials.

The band-edge energies with respect to the vacuum levels of all samples were determined from the work function (WF) and VB spectra acquired using ultraviolet photoelectron spectroscopy (UPS; Figure 9). The WF was calculated by subtracting the energy of the emitted secondary electrons (cutoff energy E_{cutoff}) from the energy of the incident UV light (He I line of a He discharge lamp: 21.21 eV) using the expression WF(Φ) = 21.21 − E_{cutoff}. The extrapolation of the linear region of the WF spectrum on the X and Y scales and their point of intersection gave the value of the cutoff energy. The E_{cutoff} values of TiO_2, fibrous red P@TiO_2, and black P@TiO_2 were found to be 16.40, 16.24, and 16.11 eV, respectively. Hence, the values of WF were calculated to be 4.81, 4.97, and 5.10 eV (Figure 9a,c and insets). The increase of the WF value demonstrates depletion region formation with concomitant band bending at the solid-state heterointerface, which leads to a deepening of the Fermi level of TiO_2 in P@TiO_2 hybrids. Additionally, the valence-band maximum (VB_{max}) values calculated via linear extrapolation of the leading edges of the UPS VB spectra for fibrous red P, fibrous red P@TiO_2 black P, and black P@TiO_2 were found to be 0.82, 1.49 1.41, and 1.45 eV below the Fermi level. The small difference in the energies between the Fermi level and VB_{max} (E_F − $E_{VB_{max}}$) for fibrous red P (0.82 eV) and black P (1.41 eV) reveals that the Fermi level was close to VB_{max} and the samples were moderately p-type. Further, XPS VB spectra of TiO_2 gave the value of VB_{max} as 3.15 eV below the Fermi level (Figure S4). The increase in VB_{max} in black P@TiO_2 and fibrous red P@TiO_2 implies a slightly uplifted Fermi level of P in the heterojunction during Fermi-level alignment and band bending (Figure 10). From the WF and VB_{max} results, it can be concluded that heterojunction formation between P and TiO_2 was facilitated by upward band bending in TiO_2 and downward band bending in P allotropes (black P and fibrous red P), as expected for a p−n heterojunction. Further, surface potential measurement of materials under dark and light conditions provides evidence of Fermi-level alignment and better charge transport due to the formation of a heterojunction (see section 2.8 in the SI for more details).

Plausible Mechanism. The water-splitting process proceeds via the absorption of light by the semiconductors, generating electron−hole pairs, which drive proton reduction and water oxidation reactions. In photoelectrochemical water splitting, electrons in the CB of the semiconductors move toward the platinum cathode, where they reduce protons, while holes in the VB of the semiconductors oxidize water to produce oxygen at the anode. Wide band gaps (>1.23 eV) and aligned positions of the CB and VB (CB < 0.00 eV and VB > +1.23 eV vs NHE at pH 0) are required to achieve proton reduction and water oxidation, respectively. TiO_2 has a large band gap, and electron−hole pairs can only be produced under UV irradiation, which demonstrates the origin of very small photocurrent density in LSV. However, from DR UV−vis, the

DOI: 10.1021/acsanm.9b00221
ACS Appl. Nano Mater. XXXX, XXX, XXX−XXX

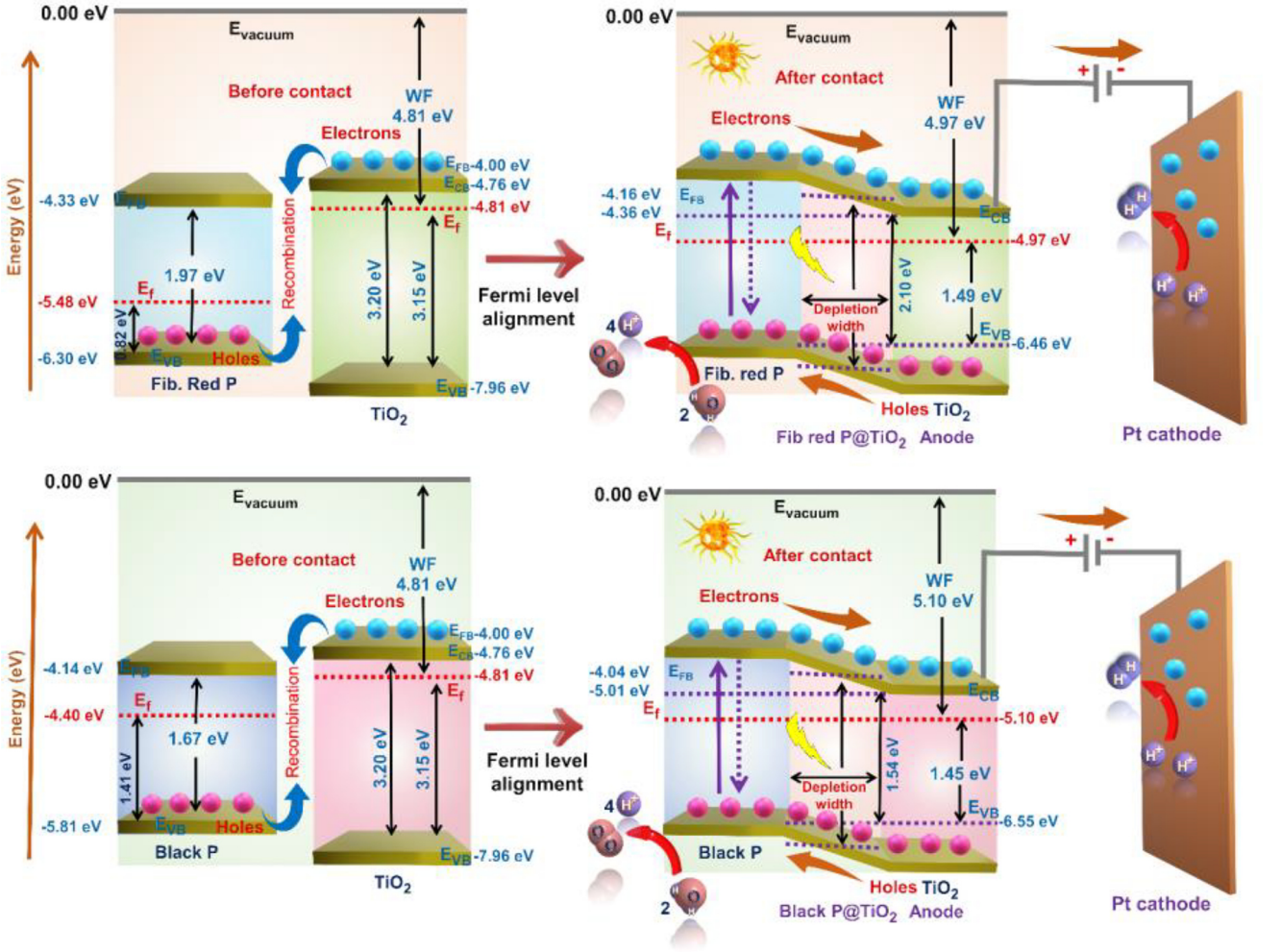

Figure 10. Energy-level diagrams illustrating a plausible charge-separation mechanism in P allotrope@TiO_2 heterojunctions.

value of the optical band gap was found to be 2.97 eV, which corresponds to 417 nm; in other words, a small visible-light fraction can be absorbed by TiO_2. The decrease in the band gap of TiO_2 might be explained as the presence of a few Ti^{3+} defects, oxygen vacancies, and trap sites. Moreover, because of the low band gaps of pristine black P and fibrous red P, the generation of sufficient reductive and oxidative electrons and holes to facilitate the water-splitting reaction can be affected.[58,59] However, a hybrid material, consisting of fibrous red P with TiO_2, was found to be an efficient photocatalyst as a result of the formation of a heterojunction and efficient charge transfer between fibrous red P and TiO_2. Heterojunction formation leads to Fermi-level alignment. During Fermi-level alignment, electrons flow from one semiconductor to another, which equilibrates the Fermi-level position between the semiconductors. Measurements of the flat-band potential for TiO_2, pristine fibrous red P, and black P were carried out via Mott−Schottky analysis (Figure S12b), and the positions were found to be −0.70, −0.37, and −0.56 V versus Ag/AgCl (−4.00, −4.14, and −4.33 eV on the E_{vac} scale); however, we note that the n-type behavior found for pristine fibrous red P and black P is attributed to a compact TiO_2 layer used during measurements and should be discounted. This indicates an electron transfer from TiO_2 to black P or fibrous red P, respectively, during Fermi-level alignment. After hybrid heterojunction formation and equilibrium was reached, the positions of the flat-band potentials of fibrous red P@TiO_2 and black P@TiO_2 were found to be −0.54 and −0.66 V versus Ag/AgCl (−4.16 and −4.04 eV at the E_{vac} scale; Figure 10). The downshifting of the flat-band potential of TiO_2 in hybrid systems suggests downward band bending of the CB edge of fibrous red and black P while upward band bending in TiO_2 occurs. This clearly demonstrates the formation of a p−n-type heterojunction between P allotropes and TiO_2. These observations were also supported by WF values (position of the Fermi level in a vacuum), where the WF of TiO_2 changed from 4.97 versus vacuum in fibrous red P@TiO_2 to 4.81−5.10 eV in black P@TiO_2 (Figure 10), which is a sufficiently positive potential for water oxidation to occur (−5.72 eV vs E_{vac} or +1.23 V vs NHE at pH 0). The increase in the WF value in hybrid materials demonstrates lower shifting of the Fermi level, which agrees well with heterojunction formation.

Additionally, a deeper VB_{max} in hybrid P allotrope@TiO_2 compounds than in pristine P allotropes suggests the successful formation of a heterojunction and generation of more oxidative holes to facilitate water splitting. On the basis of the above findings, we have sketched a band-structure diagram of the hybrid materials, which demonstrates that more efficient water splitting was possible because of p−n heterojunction formation and better charge separation (Figure 10). Further, Nyquist plots demonstrate that charge-transfer resistance and charge-transport resistance of hybrids are lower in comparison to

DOI: 10.1021/acsanm.9b00221
ACS Appl. Nano Mater. XXXX, XXX, XXX−XXX

pristine TiO_2, which suggests better charge transfer and transport in hybrid materials (Figure S12). The cavities of the TiO_2 nanotube membranes are evidently filled with visible-light-absorbing P allotropes. Thus, generated electron−hole pairs can be transferred to TiO_2. Because of a short path distance and TiO_2 exhibiting a high carrier mobility, carrier recombination can be prevented and a fast transit of the charge carriers toward the semiconductor−electrolyte interface is enabled.

CONCLUSION

Hybrid heterojunction systems for optoelectronic applications were designed, fabricated, characterized, and tested. The so-called mineralization principle for short-way gas-phase transport of solids was performed to grow semiconductors on TiO_2 nanotube arrays. Fibrous red and black P were successfully deposited onto and into electrochemically produced TiO_2 nanotube membranes. The formation of hybrid nanostructures was analyzed with several spectroscopic and diffraction methods such as XRD, STEM−EDS, Raman spectroscopy, UV−vis, and XPS. The effectiveness of the vapor transport was verified through SEM, STEM, and elemental mapping of the surface and cross section of nanohybrids, showing deposition of the materials inside the tubes.

Raman spectroscopy taken at the surface and along the razor-cut cross section of the nanotubes confirmed the penetration and growth of fibrous red P up to 15 μm (65 μm in length) and black P up to 7 μm into the nanotubes (60 μm in length). The fibrous red P@TiO_2 and black P@TiO_2 hybrid materials displayed an improved photoelectrochemical performance for water splitting in the visible-light regime because of successful p−n heterojunction formation. UPS WF spectra demonstrate band alignment, the Fermi level of TiO_2 gets downshifted, and an upshift was observed for the P allotropes during heterojunction formation. This formation enables carrier transportation from the VB of downshifted TiO_2 to P allotropes, resulting in successful oxidation in the water splitting. At the same time, Mott−Schottky plots corroborate the occurrence of more reductive flat bands in hybrid P allotrope@TiO_2 materials, which facilitate the effective reduction of hydrogen. The increased charge-carrier mobility, lower charge-transfer resistance, and lower charge-transport resistance of such hybrid materials lead to better charge separation and an improved photoelectrochemical performance.

ASSOCIATED CONTENT

Supporting Information

The Supporting Information is available free of charge on the ACS Publications website at DOI: 10.1021/acsanm.9b00221.

Experimental details on the synthesis and physicochemical and photoelectrochemical characterization, additional characterization on powder XRD, Raman and EDS analyses, DR UV−vis, high-resolution XPS, photocurrent density, electrochemical impedance spectroscopy, Nyquist and Mott−Schottky plots, and XPS VB spectra (PDF)

AUTHOR INFORMATION

Corresponding Authors

*E-mail: kshankar@ualberta.ca.
*E-mail: tom.nilges@lrz.tum.de.

ORCID

Pawan Kumar: 0000-0003-2804-9298
Ryan Kisslinger: 0000-0003-2456-396X
Karthik Shankar: 0000-0001-7347-3333
Tom Nilges: 0000-0003-1415-4265

Author Contributions

§These authors contributed equally.

Author Contributions

E.Ü. and R.K. performed the synthesis and characterization of P/hybrid materials. P.Ku. was involved in the XPS, UPS, and photoelectrochemical studies and compiled the results. P.Ka. performed the electrochemical characterizations. K.S. and T.N. planned and supervised the research. All authors were involved in writing their respective parts.

Notes

The authors declare no competing financial interest.

ACKNOWLEDGMENTS

This work has been performed as part of the international graduate school ATUMS (IRTG 2022) funded by Deutsche Forschungsgemeinschaft and Natural Sciences and Engineering Research Council of Canada (NSERC). The performance and assistance in STEM−EDS by Peng Li, Shihong Xu, and Anqiang He from nanoFAB at the University of Alberta are gratefully acknowledged. We thank Anna Vogel for Raman spectroscopy of the samples. K.S. acknowledges NSERC, National Research Council Canada, Future Energy Systems (FES). and CMC Microsystems for research funding and allowances for tool usage. P.Ku. is thankful to FES for a postdoctoral research fellowship. We kindly acknowledge Dr. Kazi Alam for DR UV−vis measurements.

ABBREVIATIONS

black P@TiO_2 = hybrid of black phosphorus and TiO_2
CB = conduction band
DR UV−vis = diffuse-reflectance ultraviolet−visible spectroscopy
fibrous red P@TiO_2 = hybrid of fibrous red phosphorus and TiO_2
IR = infrared radiation
KPFM = Kelvin probe force microscopy
LSV = linear sweep voltammetry
NHE = normal hydrogen electrode
SEM = scanning electron microscopy
STEM−EDS = scanning transmission electron microscopy−energy-dispersive X-ray spectroscopy
VB = valence band
UPS = ultraviolet photoelectron spectroscopy
WF = work function
XPS = X-ray photoelectron spectroscopy
XRD = X-ray diffraction

REFERENCES

(1) Yuan, Y.-P.; Ruan, L.-W.; Barber, J.; Joachim Loo, S. C.; Xue, C. Hetero-nanostructured suspended photocatalysts for solar-to-fuel conversion. *Energy Environ. Sci.* **2014**, *7*, 3934−3951.
(2) Liao, L.; Su, Z.; Wang, Y.; Li, Y.; Lu, X.; Zhang, Q.; Zhao, Z.; Wei, D.; Feng, G.; Yu, Q.; Cai, X.; Baldelli, S.; Zhao, J.; Ren, Z.; Fang, H.; Robles-Hernandez, F.; Bao, J. Efficient solar water-splitting using a nanocrystalline CoO photocatalyst. *Nat. Nanotechnol.* **2014**, *9*, 69−73.
(3) Liu, J.; Liu, Y.; Liu, N.; Han, Y.; Zhang, X.; Huang, H.; Lifshitz, Y.; Lee, S.-T.; Zhong, J.; Kang, Z. Metal-free efficient photocatalyst for

DOI: 10.1021/acsanm.9b00221
ACS Appl. Nano Mater. XXXX, XXX, XXX−XXX

stable visible water splitting via a two-electron pathway. *Science* **2015**, *347*, 970−974.
(4) Roger, I.; Shipman, M. A.; Symes, M. D. Earth-abundant catalysts for electrochemical and photoelectrochemical water splitting. *Nat. Rev. Chem.* **2017**, *1*, 0003.
(5) Maeda, K.; Teramura, K.; Lu, D.; Takata, T.; Saito, N.; Inoue, Y.; Domen, K. Photocatalyst releasing hydrogen from water. *Nature* **2006**, *440*, 295.
(6) Sun, Y.; Cheng, H.; Gao, S.; Sun, Z.; Liu, Q.; Liu, Q.; Lei, F.; Yao, T.; He, J.; Wei, S.; Xie, Y. Freestanding tin disulfide single-layers realizing efficient visible-light water splitting. *Angew. Chem.* **2012**, *124*, 8857−8861.
(7) Wang, Q.; Hisatomi, T.; Jia, Q.; Tokudome, H.; Zhong, M.; Wang, C.; Pan, Z.; Takata, T.; Nakabayashi, M.; Shibata, N.; Li, Y.; Sharp, I. D.; Kudo, A.; Yamada, T.; Domen, K. Scalable water splitting on particulate photocatalyst sheets with a solar-to-hydrogen energy conversion efficiency exceeding 1%. *Nat. Mater.* **2016**, *15*, 611.
(8) Habisreutinger, S. N.; Schmidt-Mende, L.; Stolarczyk, J. K. Photocatalytic reduction of CO_2 on TiO_2 and other semiconductors. *Angew. Chem., Int. Ed.* **2013**, *52*, 7372−7408.
(9) Sheridan, M. V.; Hill, D. J.; Sherman, B. D.; Wang, D.; Marquard, S. L.; Wee, K.-R.; Cahoon, J. F.; Meyer, T. J. All-in-One Derivatized Tandem p+n-Silicon−SnO_2/TiO_2 Water Splitting Photoelectrochemical Cell. *Nano Lett.* **2017**, *17*, 2440−2446.
(10) Moniz, S. J.; Shevlin, S. A.; Martin, D. J.; Guo, Z.-X.; Tang, J. Visible-light driven heterojunction photocatalysts for water splitting−a critical review. *Energy Environ. Sci.* **2015**, *8*, 731−759.
(11) Jaafar, S. N. H.; Minggu, L. J.; Arifin, K.; Kassim, M. B.; Wan, W. R. D. Natural dyes as TiO_2 sensitizers with membranes for photoelectrochemical water splitting: An overview. *Renewable Sustainable Energy Rev.* **2017**, *78*, 698−709.
(12) Ge, M.; Li, Q.; Cao, C.; Huang, J.; Li, S.; Zhang, S.; Zhang, K.; Lai, Y.; Chen, Z.; Al-Deyab, S. S. One-dimensional TiO_2 Nanotube Photocatalysts for Solar Water Splitting. *Adv. Sci.* **2017**, *4*, 1600152.
(13) Park, J. H.; Kim, S.; Bard, A. J. Novel carbon-doped TiO_2 nanotube arrays with high aspect ratios for efficient solar water splitting. *Nano Lett.* **2006**, *6*, 24−28.
(14) Pu, Y.-C.; Wang, G.; Chang, K.-D.; Ling, Y.; Lin, Y.-K.; Fitzmorris, B. C.; Liu, C.-M.; Lu, X.; Tong, Y.; Zhang, J. Z.; Hsu, Y.-J.; Li, Y. Au nanostructure-decorated TiO_2 nanowires exhibiting photoactivity across entire UV-visible region for photoelectrochemical water splitting. *Nano Lett.* **2013**, *13*, 3817−3823.
(15) Lee, C. Y.; Taylor, A. C.; Beirne, S.; Wallace, G. G. 3D-Printed Conical Arrays of TiO_2 Electrodes for Enhanced Photoelectrochemical Water Splitting. *Adv. Energy Mater.* **2017**, *7*, 1701060.
(16) de Brito, J. F.; Tavella, F.; Genovese, C.; Ampelli, C.; Zanoni, M. V. B.; Centi, G.; Perathoner, S. Role of CuO in the modification of the photocatalytic water splitting behavior of TiO_2 nanotube thin films. *Appl. Catal., B* **2018**, *224*, 136−145.
(17) Ning, X.; Li, J.; Yang, B.; Zhen, W.; Li, Z.; Tian, B.; Lu, G. Inhibition of photocorrosion of CdS via assembling with thin film TiO_2 and removing formed oxygen by artificial gill for visible light overall water splitting. *Appl. Catal., B* **2017**, *212*, 129−139.
(18) Mor, G. K.; Shankar, K.; Paulose, M.; Varghese, O. K.; Grimes, C. A. Use of highly-ordered TiO_2 nanotube arrays in dye-sensitized solar cells. *Nano Lett.* **2006**, *6*, 215−218.
(19) Mor, G. K.; Varghese, O. K.; Paulose, M.; Shankar, K.; Grimes, C. A. A review on highly ordered, vertically oriented TiO_2 nanotube arrays: Fabrication, material properties, and solar energy applications. *Sol. Energy Mater. Sol. Cells* **2006**, *90*, 2011−2075.
(20) Wang, F.; Ng, W. K. H.; Yu, J. C.; Zhu, H.; Li, C.; Zhang, L.; Liu, Z.; Li, Q. Red phosphorus: an elemental photocatalyst for hydrogen formation from water. *Appl. Catal., B* **2012**, *111-112*, 409−414.
(21) Kudo, A.; Miseki, Y. Heterogeneous photocatalyst materials for water splitting. *Chem. Soc. Rev.* **2009**, *38*, 253−278.
(22) Roy, P.; Berger, S.; Schmuki, P. TiO_2 nanotubes: synthesis and applications. *Angew. Chem., Int. Ed.* **2011**, *50*, 2904−2939.
(23) Schock, H.; Meissner, D., *Solarzellen-Physikalische Grundlagen und Anwendungen in der Photovoltaik*; Vieweg & Sohn: Wiesbaden, Germany, 1993.
(24) Regonini, D.; Bowen, C. R.; Jaroenworaluck, A.; Stevens, R. A review of growth mechanism, structure and crystallinity of anodized TiO_2 nanotubes. *Mater. Sci. Eng., R* **2013**, *74*, 377−406.
(25) Hahn, R.; Macak, J.; Schmuki, P. Rapid anodic growth of TiO_2 and WO_3 nanotubes in fluoride free electrolytes. *Electrochem. Commun.* **2007**, *9*, 947−952.
(26) Ravi, P.; Navakoteswara Rao, V.; Shankar, M.; Sathish, M. $CuOCr_2O_3$ core-shell structured co-catalysts on TiO_2 for efficient photocatalytic water splitting using direct solar light. *Int. J. Hydrogen Energy* **2018**, *43*, 3976−3987.
(27) Keyes, R. W. The electrical properties of black phosphorus. *Phys. Rev.* **1953**, *92*, 580.
(28) Morita, A. Semiconducting black phosphorus. *Appl. Phys. A: Solids Surf.* **1986**, *39*, 227−242.
(29) Yan, J.; Ji, Y.; Kong, L.; Li, Y.; Navlani-García, M.; Liu, S.; Kuwahara, Y.; Mori, K.; Che, M.; Yamashita, H. Black Phosphorus-Based Compound with Few Layers for Photocatalytic Water Oxidation. *ChemCatChem* **2018**, *10*, 3424−3428.
(30) Li, L.; Yu, Y.; Ye, G. J.; Ge, Q.; Ou, X.; Wu, H.; Feng, D.; Chen, X. H.; Zhang, Y. Black phosphorus field-effect transistors. *Nat. Nanotechnol.* **2014**, *9*, 372.
(31) Yuan, H.; Liu, X.; Afshinmanesh, F.; Li, W.; Xu, G.; Sun, J.; Lian, B.; Curto, A. G.; Ye, G.; Hikita, Y.; Shen, Z.; Zhang, S.-C.; Chen, X.; Brongersma, M.; Hwang, H. Y.; Cui, Y. Polarization-sensitive broadband photodetector using a black phosphorus vertical p−n junction. *Nat. Nanotechnol.* **2015**, *10*, 707.
(32) Viti, L.; Hu, J.; Coquillat, D.; Knap, W.; Tredicucci, A.; Politano, A.; Vitiello, M. S. Black-phosphorus Terahertz photodetectors. *Adv. Mater.* **2015**, *27*, 5567−5572.
(33) Zhou, Y.; Zhang, Y.; Lin, M.; Long, J.; Zhang, Z.; Lin, H.; Wu, J. C.-S.; Wang, X. Monolayered Bi_2WO_6 nanosheets mimicking heterojunction interface with open surfaces for photocatalysis. *Nat. Commun.* **2015**, *6*, 8340.
(34) Chen, S.; Qi, Y.; Hisatomi, T.; Ding, Q.; Asai, T.; Li, Z.; Ma, S. S. K.; Zhang, F.; Domen, K.; Li, C. Efficient Visible Light-Driven Z-Scheme Overall Water Splitting Using a $MgTa_2O_{6-x}N_y$/TaON Heterostructure Photocatalyst for H_2 Evolution. *Angew. Chem.* **2015**, *127*, 8618−8621.
(35) Shang, L.; Tong, B.; Yu, H.; Waterhouse, G. I. N.; Zhou, C.; Zhao, Y.; Tahir, M.; Wu, L.-Z.; Tung, C.-H.; Zhang, T. CdS Nanoparticle-Decorated Cd Nanosheets for Efficient Visible Light-Driven Photocatalytic Hydrogen Evolution. *Adv. Energy Mater.* **2016**, *6*, 1501241.
(36) Nguyen, C. C.; Vu, N. N.; Do, T.-O. Recent advances in the development of sunlight-driven hollow structure photocatalysts and their applications. *J. Mater. Chem. A* **2015**, *3*, 18345−18359.
(37) Lewis, N. S. Toward cost-effective solar energy use. *Science* **2007**, *315*, 798−801.
(38) Zhang, X.; Han, F.; Shi, B.; Farsinezhad, S.; Dechaine, G. P.; Shankar, K. Photocatalytic conversion of diluted CO_2 into light hydrocarbons using periodically modulated multiwalled nanotube arrays. *Angew. Chem., Int. Ed.* **2012**, *51*, 12732−12735.
(39) Mohammadpour, A.; Kar, P.; Wiltshire, B. D.; Askar, A. M.; Shankar, K. Electron transport, trapping and recombination in anodic TiO_2 nanotube arrays. *Curr. Nanosci.* **2015**, *11*, 593−614.
(40) Macak, J.; Barczuk, P.; Tsuchiya, H.; Nowakowska, M.; Ghicov, A.; Chojak, M.; Bauer, S.; Virtanen, S.; Kulesza, P.; Schmuki, P. Self-organized nanotubular TiO_2 matrix as support for dispersed Pt/Ru nanoparticles: Enhancement of the electrocatalytic oxidation of methanol. *Electrochem. Commun.* **2005**, *7*, 1417−1422.
(41) Paramasivam, I.; Macak, J.; Ghicov, A.; Schmuki, P. Enhanced photochromism of Ag loaded self-organized TiO_2 nanotube layers. *Chem. Phys. Lett.* **2007**, *445*, 233−237.
(42) Yang, G.; Chen, D.; Ding, H.; Feng, J.; Zhang, J. Z.; Zhu, Y.; Hamid, S.; Bahnemann, D. W. Well-designed 3D $ZnIn_2S_4$ nanosheets/TiO_2 nanobelts as direct Z-scheme photocatalysts for CO_2

DOI: 10.1021/acsanm.9b00221
ACS Appl. Nano Mater. XXXX, XXX, XXX−XXX

photoreduction into renewable hydrocarbon fuel with high efficiency. *Appl. Catal., B* **2017**, *219*, 611−618.
(43) Zhou, D.; Chen, Z.; Yang, Q.; Shen, C.; Tang, G.; Zhao, S.; Zhang, J.; Chen, D.; Wei, Q.; Dong, X. Facile Construction of g-C_3N_4 Nanosheets/TiO_2 Nanotube Arrays as Z-Scheme Photocatalyst with Enhanced Visible-Light Performance. *ChemCatChem* **2016**, *8*, 3064−3073.
(44) Pi, Y.; Li, Z.; Xu, D.; Liu, J.; Li, Y.; Zhang, F.; Zhang, G.; Peng, W.; Fan, X. 1T-Phase MoS_2 Nanosheets on TiO_2 Nanorod Arrays: 3D Photoanode with Extraordinary Catalytic Performance. *ACS Sustainable Chem. Eng.* **2017**, *5*, 5175−5182.
(45) Qin, P.; Paulose, M.; Dar, M. I.; Moehl, T.; Arora, N.; Gao, P.; Varghese, O. K.; Grätzel, M.; Nazeeruddin, M. K. Stable and efficient perovskite solar cells based on titania nanotube arrays. *Small* **2015**, *11*, 5533−5539.
(46) Thakur, U.; Kisslinger, R.; Shankar, K. One-dimensional electron transport layers for perovskite solar cells. *Nanomaterials* **2017**, *7*, 95.
(47) Lou, Z.; Li, F.; Deng, J.; Wang, L.; Zhang, T. Branch-like hierarchical heterostructure (α-Fe_2O_3/TiO_2): a novel sensing material for trimethylamine gas sensor. *ACS Appl. Mater. Interfaces* **2013**, *5*, 12310−12316.
(48) Eckstein, N.; Hohmann, A.; Weihrich, R.; Nilges, T.; Schmidt, P. Synthesis and Phase Relations of Single-Phase Fibrous Phosphorus. *Z. Anorg. Allg. Chem.* **2013**, *639*, 2741−2743.
(49) Grotz, C.; Köpf, M.; Baumgartner, M.; Jantke, L. A.; Raudaschl-Sieber, G.; Fässler, T. F.; Nilges, T. Synthesis, Structure, and Properties of NaP_7, a Phosphorus-rich Polyphosphide. *Z. Anorg. Allg. Chem.* **2015**, *641*, 1395−1399.
(50) Pfister, D.; Schaefer, K.; Ott, C.; Gerke, B.; Poettgen, R.; Janka, O.; Baumgartner, M.; Efimova, A.; Hohmann, A.; Schmidt, P.; Venkatachalam, S.; van Wuellen, L.; Schuermann, U.; Kienle, L.; Duppel, V.; Parzinger, E.; Miller, B.; Becker, J.; Holleitner, A.; Weihrich, R.; Nilges, T. Inorganic Double Helices in Semiconducting SnIP. *Adv. Mater.* **2016**, *28*, 9783−9791.
(51) Castellanos-Gomez, A. Black phosphorus: narrow gap, wide applications. *J. Phys. Chem. Lett.* **2015**, *6*, 4280−4291.
(52) Abbas, A. N.; Liu, B.; Chen, L.; Ma, Y.; Cong, S.; Aroonyadet, N.; Köpf, M.; Nilges, T.; Zhou, C. Black phosphorus gas sensors. *ACS Nano* **2015**, *9*, 5618−5624.
(53) Grätzel, M. Photoelectrochemical cells. *Nature* **2001**, *414*, 338.
(54) Guo, Z.; Zhang, H.; Lu, S.; Wang, Z.; Tang, S.; Shao, J.; Sun, Z.; Xie, H.; Wang, H.; Yu, X. F.; Chu, P. K. From black phosphorus to phosphorene: basic solvent exfoliation, evolution of Raman scattering, and applications to ultrafast photonics. *Adv. Funct. Mater.* **2015**, *25*, 6996−7002.
(55) Wang, H.; Yang, X.; Shao, W.; Chen, S.; Xie, J.; Zhang, X.; Wang, J.; Xie, Y. Ultrathin black phosphorus nanosheets for efficient singlet oxygen generation. *J. Am. Chem. Soc.* **2015**, *137*, 11376−11382.
(56) Chen, Z.; Dinh, H. N.; Miller, E. *Photoelectrochemical Water Splitting*; Springer: Berlin, 2013.
(57) Zhang, X.; Zhang, B.; Cao, K.; Brillet, J.; Chen, J.; Wang, M.; Shen, Y. A perovskite solar cell-TiO_2@$BiVO_4$ photoelectrochemical system for direct solar water splitting. *J. Mater. Chem. A* **2015**, *3*, 21630−21636.
(58) Hoang, S.; Berglund, S. P.; Hahn, N. T.; Bard, A. J.; Mullins, C. B. Enhancing visible light photo-oxidation of water with TiO_2 nanowire arrays via cotreatment with H_2 and NH_3: synergistic effects between Ti^{3+} and N. *J. Am. Chem. Soc.* **2012**, *134*, 3659−3662.
(59) Chen, X.; Liu, L.; Yu, P. Y.; Mao, S. S. Increasing solar absorption for photocatalysis with black hydrogenated titanium dioxide nanocrystals. *Science* **2011**, *331*, 746−750.

DOI: 10.1021/acsanm.9b00221
ACS Appl. Nano Mater. XXXX, XXX, XXX−XXX

Supporting Information

Vapor Deposition of Semiconducting Phosphorus Allotropes into TiO_2 Nanotube Arrays for Photoectrocatalytic Water Splitting

Ebru Üzer,[a] Pawan Kumar,[b†] Ryan Kisslinger,[b†] Piyush Kar,[b] Ujwal Kumar Thakur,[b] Sheng Zeng,[b] Karthik Shankar,[b,] and Tom Nilges[a,*]*

Department of Chemistry, Technical University of Munich, Lichtenbergstrasse 4, 85748 Garching, Germany; E-mail: tom.nilges@lrz.tum.de

Department of Electrical and Computer Engineering, 9211-116 Street NW, Edmonton, Alberta, Canada T6G 1H9; E-mail: kshankar@ualberta.ca.

†Contributed equally

1 EXPERIMENTAL DETAILS

1.1 Synthesis of TiO_2 nanotube membranes

The anodization method was used to fabricate TiO_2 nanotube membranes.[1] Titanium foil 0.5 cm wide and 2 cm long was used as the cathode, and titanium foil 1 cm wide and 4 cm long was used as the anode; both titanium pieces had thicknesses of 0.89 mm. The electrolyte was comprised of ethylene glycol with the addition of 3 Vol.-% deionized water and 0.03 wt% NH_4F. The electrolyte was well-mixed before anodization. The cathode and anode were spaced 2 cm apart in a 100 mL beaker filled with electrolyte; this beaker was submerged in an ice-water bath for cooling. A constant voltage of 60 V was applied for 3 days. Afterwards, samples were removed and submerged in methanol for cleaning, and a razor was used to scratch off the anodized 0.89 mm thick sides of the titanium piece to enable delamination of the membranes. The membranes were left to dry, which caused delamination of the membrane to occur. The inner pores of the nanotubes were then exposed by reactive ion etching, followed by a cleaning step for each side of the membrane. An SF_6 etch using a pressure of 20 mTorr and a forward power of 250 W was utilized, followed immediately by an O_2 clean using a pressure of 150 mTorr and a forward power of 225 W. The side of the membrane that was exposed directly to electrolyte was subjected to the SF_6 etch for 200 s followed by the O_2 clean for 10 min; the membrane was then flipped, and the side of the membrane that formed the barrier layer of TiO_2/Ti foil was subjected to the SF_6 etch for 300 s followed by the O_2 etch for 10 min.

1.2 Synthesis of hybrid fibrous P@TiO_2 nanotube membranes

Chemical vapor deposition of fibrous red P on TiO_2 nanotube membranes was attained according to literature procedures.[2] Red phosphorus (300 mg, ultrahigh grade, 99.999+%, Chempur) and purified CuI (15 mg) were transferred into a silica-glass tube (0.8 cm inner diameter, 8 cm length). TiO_2 nanotube membranes were subsequently added. The ampoule was sealed under vacuum ($p < 10^{-3}$ mbar) and placed horizontally in a Nabertherm muffle furnace (L3/11/330) by locating the precursors in the hot zone of the furnace and the TiO_2 nanotube membranes to the colder zone. The furnace was heated to 773 K within 8 h, with a holding period of 48 h, cooled down to 673 K within 24 h and held at this temperature for 11 d. Room temperature was reached within 24 h.

Purification of CuI was carried out by solving CuI (98+%, Chempur) in concentrated HI (57 %, Riedel de Häen) and a following precipitation in water. The precipitate was purified by washing twice with water and ethanol and dried under vacuum.

1.3 Synthesis of black P@TiO_2 nanotube membranes

The preparation of black P@TiO_2 nanotube membranes can be carried out through *in situ* growth from amorphous red phosphorus following a short way transport reaction following the literature procedures.[3] The precursors Sn (20 mg, 99.999%, Chempur) and SnI_4 (189.6 mg, synthesized according to literature procedures)[4] were added as mineralization additives. Red phosphorus (500 mg, Chempur, 99.999+%) were placed together with Sn and SnI_4 in a silica-glass tube (0.8 cm inner diameter, 8 cm length, 0.25 cm wall thickness) and TiO_2 nanotube membranes in short distance. The ampoule was sealed under vacuum ($p < 10^{-3}$ mbar) and then

put horizontally, with the precursors located at the hot end and the TiO_2 nanotube membranes located towards the colder zone of the Nabertherm muffle furnace (L3/11/330). The furnace was heated to 923 K and then cooled down within 7.5 h to 773 K.

1.4 Photo-/electrochemical characterization

To determine the electrochemical properties of the samples a CHI660E series electrochemical workstation equipped with a three-electrode configuration was used. A FTO glass deposited sample was assigned as working electrode (photoanode) while Pt and Ag/AgCl electrodes were used as counter (cathode) and reference electrode respectively. To fabricate the photoanode a 20 nm thick layer of TiO_2 compact layer was deposited on FTO by following our previous recipe after three times dilution of titanium di-isopropoxide solution.[5] The thin TiO_2 layer serves as blocking layer by preventing direct contact between solvent and FTO. After that the materials, dispersed in very dilute solution of titanium di-isopropoxide, were drop-casted on TiO_2 followed by heating up to 150 °C for 1 h which allows robust binding of the materials on the surface of FTO/TiO_2. To measure the photo-electrochemical performance 0.1 M KOH was used as electrolyte. Three electrodes were immersed in KOH electrolyte and photoelectrochemical performance was investigated by sweeping the applied voltage from –1.0 V to +0.8 V *vs* Ag/AgCl at 10 mV/s scan rate. A solar simulator (Newport, Oriel instrument USA, model 67005, solar simulator) equivalent to AM1.5 G spectrum having a power density of 100 mW m^{-2} at the sample surfaces was used for photo-irradiation. The photo-response of the materials at higher wavelength and respective efficiencies (IPCE and APCE%) were determined using monochromatic 425 nm (54.15 mW cm^{-2}), 420, 505, 580 and 620 nm wavelength LED having a power density of 21.00 mW cm^{-2} on the electrode surface. For the measurements of evolved hydrogen on the Pt counter electrode a photoelectrochemical water splitting H-cell was used. The samples from the Pt electrode containing arm was withdrawn after 2 h interval using a gas tight syringe and injected in a GC (gas chromatographer). See Figure S16 for an image of the experimental setup. To confirm oxygen evolution occured due to photoelectrochemical water splitting, the gaseous sample from the photoanode was analyzed using GC-PDD (gas chromatographer pulsed discharge detector) before photoirradiation (after purging with N_2 for 30 min) and after photoirradiation for 1 h. Flat band potential and charge carrier concentration of the materials were determined from Mott-Schottky analysis obtained from impedance-potential measurements using 0.5 M Na_2SO_4 solution in –1.0 to +1.0 V range at 1 K frequency. Nyquist plotting to draw equivalent circuit and to determine the value of charge transfer resistance, space charge capacitance, carrier lifetime etc. was obtained using electrochemical impedance spectroscopy (EIS) under dark and 1 sun irradiation on the applied potential of –0.5 V *vs* Ag/AgCl in 0.1 M KOH, with an AC amplitude of 0.005 V at frequency value 1 Hz to 100 kHz.

Chemicals and reagents. Anhydrous Na_2SO_4 (99.0%), KOH (99.0%), titanium(IV)-isopropoxide (99.99%), were purchased from Sigma Aldrich and used as received. Fluorine doped tin oxide (FTO) glass (transmittance 80-82%) was purchased from Hartford Tec Glass Company. The surface of FTO was degreased by ultrasonication in water, methanol and acetone for 10 min each. HPLC grade solvents were used throughout studies.

Structural and physicochemical characterization

X-ray powder diffraction. X-ray powder data were applied on a Stoe Stadi P diffractometer (Cu-$K_{\alpha 1}$ radiation, λ = 1.5406 Å, Ge-monochromator) fitted with a Mythen 1 K detector (Fa. Dectris) and calibrated externally using (a = 5.43088 Å). Phase analysis and indexing was carried out with the program package of Stoe Winxpow 2011.[6]

Scanning Electron Microscopy (SEM) and Energy Dispersive X-ray spectroscopy (EDS). Scanning Electron Microscopy imaging on TiO_2 nanotubes and according nanofibers were performed *via* JEOL [SEM 5900LV, Si (Li) detector]. The composition of the hybrid compounds was determined semi-quantitatively by EDS measurements (Energy Dispersive X-ray Spectroscopy, Röntec). The samples were applied with an acceleration voltage of 15 kV. The measured composition is in good agreement with the composition achieved from structure refinement.

Scanning Transmission Electron Microscope (STEM) and Energy Dispersive X-ray spectroscopy (EDS). STEM-EDS analysis data were collected on a JEOL JEM-ARM200cF STEM, along with a cold Field-Emission Gun (cFEG) and a probe Cs corrector. EDS scans were applied with a Silicon Drift (SDD) EDS detector at an acceleration voltage of 200 kV.

Raman spectroscopy. The hybrid semiconductor@TiO_2 nanotube arrays were investigated by Raman spectroscopy at 300 K using a Renishaw inVia RE04 Raman Microscope fitted with a Nd:YAG and diode laser (λ = 532 nm; 785 nm) and a CCD detector. The applied laser power was 250 mW, recording a total number of 500 scans. Scans along a razor cut cross section of the membranes were conducted by moving the focused Raman beam from the outside to the center of the membrane *via* a x-y stage. One Raman spectrum was recorded for each individual step.

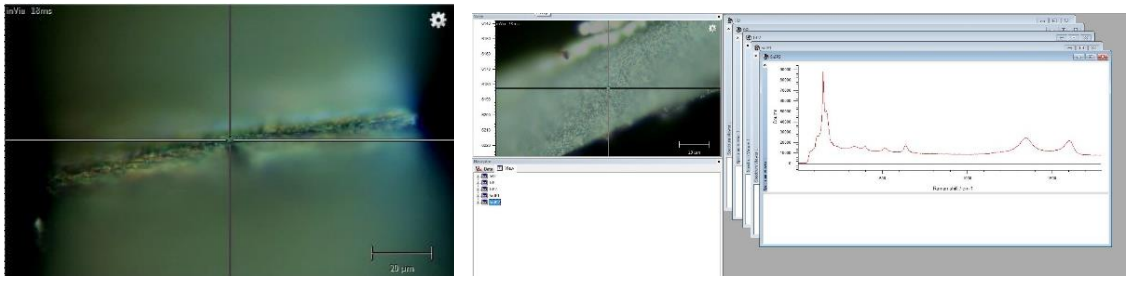

Scheme S1. Left: Raman microscope focus on a cross section of a membrane used for Raman spectroscopic investigations. Right: Consecutive Raman spectra were recorded along the cross section.

X-ray Photoelectron spectroscopy (XPS) and Ultraviolet photoelectron spectroscopy (UPS). To determine the surface chemical nature and binding energy of elements XPS was performed on all samples using Axis-Ultra, Kratos Analytical instrument equipped with monochromatic Al-Kα source (15 kV, 50 W) with an incident X-ray energy of 1486.7 eV operating under ultra-high vacuum (UHV ~10^{-8} Torr). To assign the binding energy of the

elements the binding energy of C1s of adventitious hydrocarbon (BE ≈ 284.8 eV) was used as standard (carbon correction). The acquired raw data in the form of .vms files was deconvoluted in various peak components using CasaXPS and extracted .csv files were plotted in origin 8.5. The electronic band structure of all materials was determined using ultraviolet photoelectron spectroscopy (UPS) using a 21.21 eV He I line of a He discharge lamp to collect work function and valence band spectra.

Diffuse reflectance UV-Vis spectroscopy (DR UV-Vis). The absorption spectra of all materials in UV-Vis region was recorded on a Perkin Elmer Lambda-1050 UV–Vis-NIR spectrophotometer working in diffuse reflectance mode equipped with an integrating sphere accessory.

Kelvin Probe Force Microscopy (KPFM). The nature of charge carrier transport to probe the successful formation of heterojunction between infiltrated phosphorous and TiO_2 nanotubes, surface potential (SP) of bare and hybrid materials were determined using peak force KPFM on a Dimension Fast Scan Atomic Force microscope (Bruker Nanoscience Division, Santa Barbara, CA, USA). To perform KPFM measurements, samples were deposited on FTO and a Pt coated SiNSCM-PIT cantilever of 2.5 4.4 N/m stiffness was used. Samples containing FTO were grounded with the AFM chuck using a conductive copper tape. The surface potential of the samples was measured at 100 nm x 75 nm lift height at 12 kHz lockin bandwidth and a scan speed of 0.51 Hz. To investigate charge carrier dynamics under light irradiation conditions samples were irradiated with 450 and 635 nm LEDs and dark and light conditions were maintained for 5 min, to achieve equilibrium condition. The measurements were performed at zero tip bias and Pt tip was calibrated by measuring the contact potential difference (CPD) of highly oriented pirolytic graphite (HOPG) and the Pt tip using following expression.

EF (tip) = 4.6 eV (Work function of HOPG) + VCPD (HOPG and Pt tip)

Gas chromatography (GC). The identification and quantification of reaction product was done by gas chromatography using custom made Shimadzu GC equipped with Porapak Q column and Mol Sieve column, and a pulsed discharge detector (PDD). Conditions: He carrier flow rate: 0.5 mL min^{-1}, detector temperature: 160 °C, oven temp: started from 60 °C and raised up to 160 °C to expel water vapor. A standard calibration gas mixture (Praxair gas, Canada) was used for the quantification of hydrogen.

2 STRUCTURAL CHARACTERIZATION

2.1 Fibrous red P@TiO2 nanotube hybrids

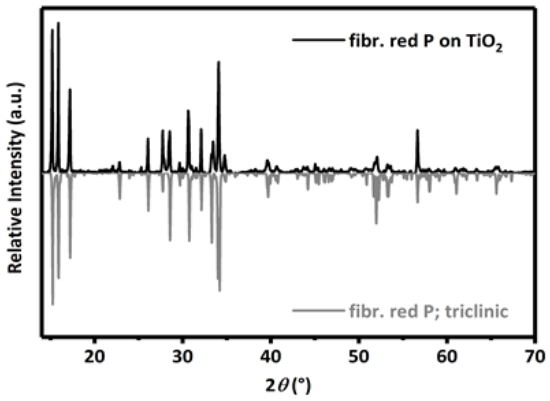

Figure S1. Powder X-ray diffraction substantiates the formation of crystalline fibrous red phosphorus onto the membrane. A calculated diffractogram based on the structure data of fibrous red phosphorus[2] is drawn with negative intensities. Slight variations in intensity are due to texture effects.

In Figure S2 Raman modes were detected 5 µm in distance to the membrane surface. The formation of fibrous red Phosphorus was confirmed at this depth. Significant shifts are found for the 158 cm^{-1} E_g mode, which is located at 145 cm^{-1} in the hybrid material. The whole spectrum of anatase is slightly shifted towards higher wavenumbers, which can be due to doping or defect formation in TiO_2.

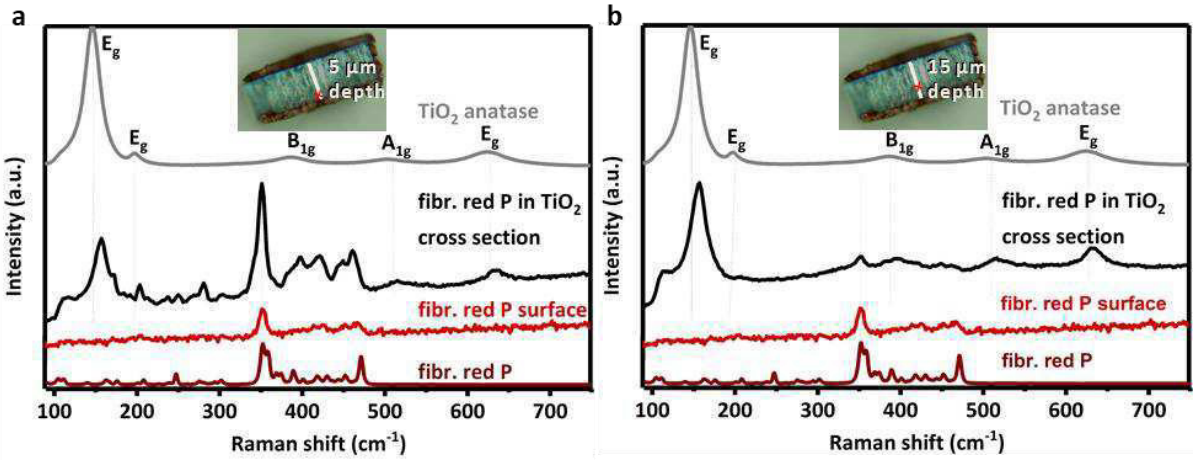

Figure S2. Raman spectroscopy on fibrous red P@TiO_2 membranes **a)** Raman spectra of a fresh TiO_2 membrane (anatase, grey), fibrous red P@TiO_2 membrane cross section measured approx. 5 µm in distance to the surface (black), fibrous red P (red), recorded at the surface and reference spectrum of fibrous red P (dark red). Raman-microscope picture of the fibrous red P@TiO_2 membrane where the Raman spectrum was recorded at the top. **b)** Raman spectra of a fresh TiO_2 membrane (anatase, grey), fibrous red P@TiO_2 membrane cross section measured approx. 15 ⌈m in distance to the surface (black), fibrous red P (red), recorded at the surface and reference spectrum of fibrous red P (dark red). Raman-microscope images of fibrous red P@TiO_2 membranes, recorded during the measurement show the laser path along the cross section.

2.2 Black P@TiO_2 nanotube hybrids

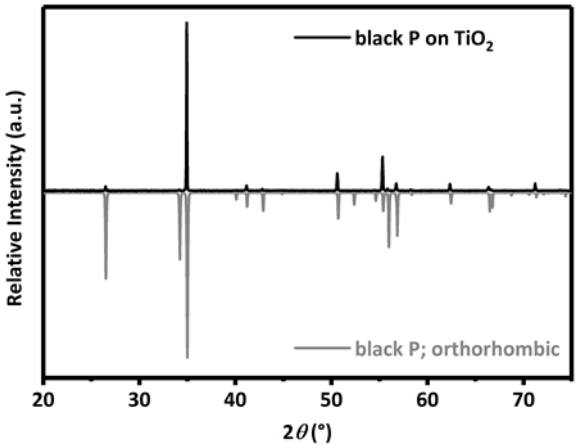

Figure S3. Powder X-ray diffraction confirms formation of crystalline black phosphorus onto the membrane. A calculated diffractogram based on the structure data of black phosphorus[3] is drawn with negative intensities. Slight variations in intensity are due to texture effects.

2.3 EDS analysis

Table S1. Elemental analysis of deposited crystals found on both sides of the membranes and different spots along the razor cut cross section of fibrous red P@TiO_2 membranes *via* EDS-measurements. Elemental composition in at% deriving from P and Ti were found whereas Cu and I (originated from the mineralizer used during synthesis) could not be detected. Atomic percent of Ti is representing Ti in TiO_2.

EDS	P (at%)	Ti (at%)	Cu (at%)	I (at%)
Fibrous red P@TiO_2 cross section 1	75.7(6)	24.3(4)	—	—
Fibrous red P@TiO_2 cross section 2	37.5(4)	62.5(6)	—	—

Table S2. Elemental analysis of deposited crystals found on both sides of the membranes and different spots along the razor cut cross section of black P@TiO_2 membranes *via* EDS-measurements. Elemental composition in at% deriving from P and Ti were found whereas Sn and I (originated from the mineralizer used during synthesis) was present in small amounts. Atomic percent of Ti is representing Ti in TiO_2.

EDS	P (at%)	Ti (at%)	Sn (at%)	I (at%)
Black P@TiO_2 cross section 1	26.8(3)	72.0(6)	1.1(1)	—
Black P@TiO_2 cross section 2	75.4(6)	19.7(3)	3.5(2)	1.3(2)

2.4 UV-Vis analysis

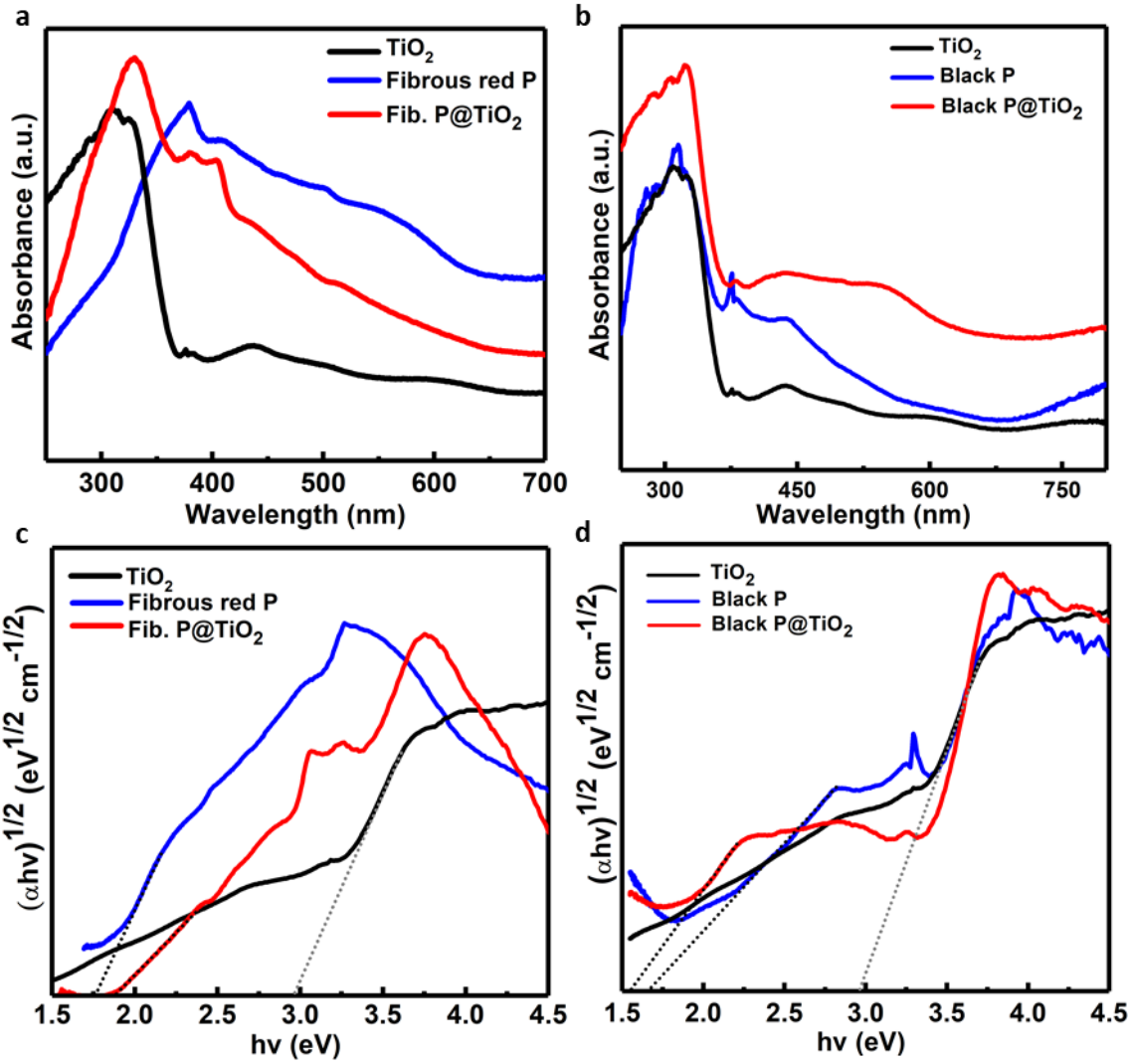

Figure S4. DRS UV-Vis spectra of **a)** TiO_2, fibrous red P, and fibrous red P@TiO_2. **b)** TiO_2, black P, and black P@TiO_2. Tauc plot for **c)** TiO_2, fibrous red P, and fibrous red P@TiO_2. **d)** black P, TiO_2, and black P@TiO_2. **Color**: TiO_2 (black), black P, fibrous red P (red), black P@TiO_2 and fibrous red P@TiO_2 (blue).

2.5 XPS analysis of phosphorus allotrope@TiO_2 membranes

The nature of the chemical species present in the materials and their binding energies were determined using high resolution X-ray photoelectron spectroscopy (HR-XPS). Survey scan for elemental analysis gave peaks corresponding to all the elements in TiO_2 (Ti2p, O1s), black P (P2p), black P@TiO_2 (P2p, Ti2p, O1s), fibrous red P (P2p) and fibrous red P@TiO_2 (P2p, Ti2p, O1s) (Figure S5a and b). The deconvoluted core-level HR-XPS spectra of TiO_2 gave two peak components centred at BE ≈ 459.7 and 465.3 eV, originating from $Ti2p_{3/2}$ and $Ti2p_{1/2}$ components of Ti^{4+} present in anatase phase TiO_2 (Figure S5a).[7-9] The position of $Ti2p_{3/2}$ and $Ti2p_{1/2}$ components does not change after vapor phase growth of black P and fibrous red P on and inside TiO_2 nanotube membranes which implies, the oxidation state of Ti in TiO_2 lattice remains equal (4+) during deposition conditions (Figure S5a and b). Further, the absence of any

shoulder peak in Ti2p region overrules any possibility of phosphorus doping in TiO_2 lattice. HR-XPS spectra of TiO_2 in O1s region was deconvoluted in two peaks components located at 530.9 and 532.2 eV, assigned to Ti^{4+} coordinated oxygen atoms present in TiO_2 crystal lattice and surface adsorbed non-lattice oxygen (adventitious and –OH oxygens).[10-11] After vapor phase deposition of black P on TiO_2 the O1s peak get shifted toward higher binding energies and new peaks were situated at 532.6 and 533.8 eV. The shifting of O1s peak was attributed due to transformation of certain fraction of black P into P-O (bridging and dangling oxygen bonding) and coordination of P atoms in black P with Ti^{4+} present on the surface of TiO_2 which change coordination environment of lattice bounded oxygen on the surface of TiO_2 (Figure S5c).[12-13] Previous studies demonstrated that three P atoms in black P can coordinate tetragonally with surface metals centre which provides more stable configuration due to satisfaction of tetravalency of undercoordinated Ti^{4+} present on the surface of TiO_2.[14-16] It should be noted that XPS gives information of only surface chemical composition up to 5-10 nm and bulk chemical composition of TiO_2 was preserved as confirmed by XRD analysis and Raman spectra. For the fibrous red P@TiO_2 the XPS peak position in O1s region was found at relatively higher BE ≈ 532.0 and 533.5 eV again due to lattice O atoms bonded with P coordinated Ti and adventitious oxygen (Figure S5d). HR-XPS scan of black P in P2p region gave two peaks located at 130.9 and 134.5 eV corroborated to contribution from P2p of P atom in the sheets and oxidized P (P_xO_y) respectively (Figure S5e).[17] After deposition of black P on the TiO_2 nanotube membranes the intensity of P 2p peak component at 130.4 eV was diminished which demonstrate higher degree of oxidation of P in black P@TiO_2.[12] Further, pristine fibrous red P show only one peak at BE ≈ 134.9 in P2p region due to P atoms in fibrous P and absence of any peak corresponding to P-O suggest better stability of fibrous red P than black P (Figure S5f), possibly caused by the structural preference of black P reacting with air. The peak position and intensity of P2p peak remains the same in fibrous red P@TiO_2 revealing the unaffected chemical nature of fibrous red P deposited on TiO_2 (Figure S5f). Additionally, HR-XPS of pristine black P and black P@TiO_2 show I3d ($I3d_{5/2}$ BE ≈ 619.6 and $I3d_{3/2}$ BE ≈ 631.7) and Sn3d ($Sn3d_{3/2}$ BE ≈ 488.1 and $Sn3d_{1/2}$ BE ≈ 496.6) peaks which was originated from SnI_4, used as transporting materials for vapor deposition (Figure S6).

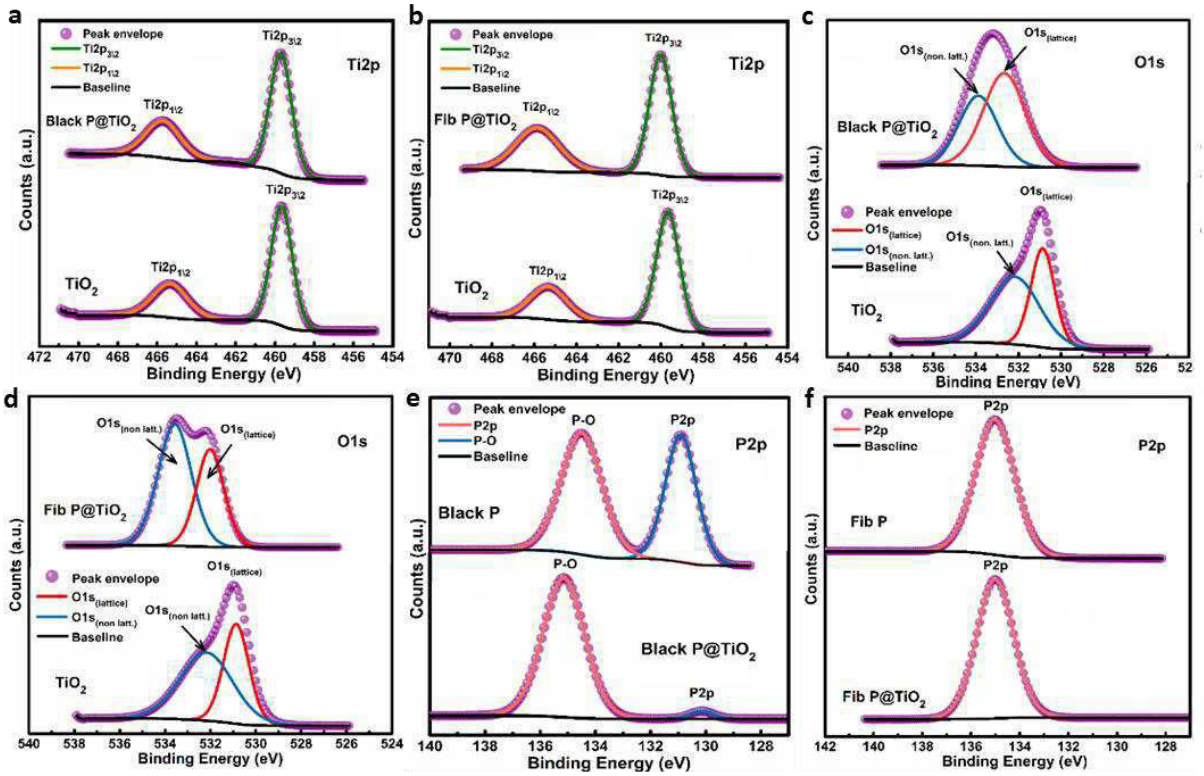

Figure S5. Core level HR-XPS spectra of TiO_2 and black P@TiO_2 **a)** in Ti2p region, **b)** in Ti2p region, **c)** O1s region and HR-XPS spectra of TiO_2 fibrous red P and fibrous red P@TiO_2 **d)** in O1s region, **e)** in P 2p region, **f)** in P 2p region.

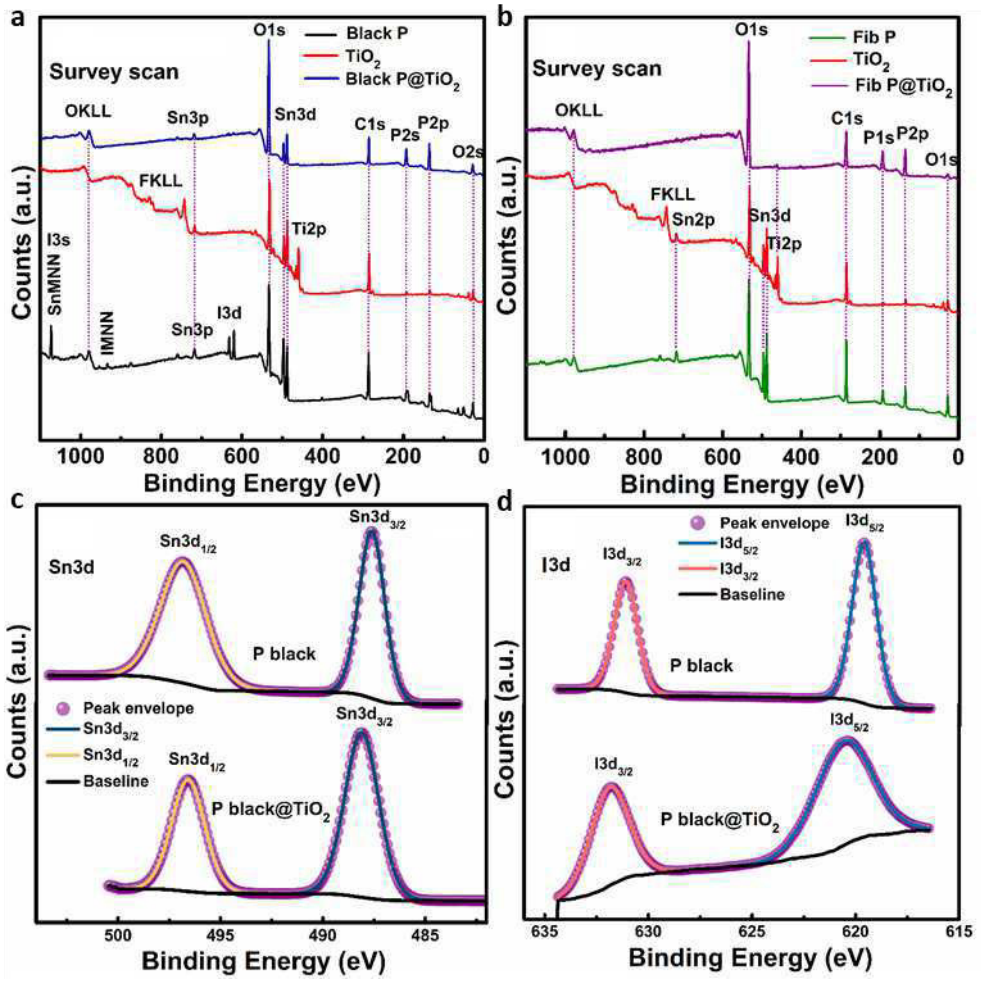

Figure S6. XPS elemental survey scan of **a)** black P, TiO_2, black P@TiO_2, **b)** fibrous red P, TiO_2, fibrous red P@TiO_2, and HR-XPS spectra of black P and black P@TiO_2 **c)** in Sn3d region and **d)** in I3d region showing presence of Sn and I as mass transporting agents. **Color**: black P (black), TiO_2 (red), black P@TiO_2 (blue), fibrous red P (olive), fibrous red P@TiO_2 (magenta).

2.6 Calculation of Efficiencies:

To discern materials/interface performance of materials, diagnostic efficiencies of materials were calculated.

Applied Bias Photon-to-current Efficiency (ABPE%)

Since external bias is applied in photoelectrochemical measurements, the electrical energy must be subtracted during efficiency calculation. Applied Bias Photon-to-current Efficiency (ABPE%), which demonstrate photo-conversion efficiency under applied bias conditions and provides information of materials system/interface performance, was determined by plotting a graph between ABPE% at different applied voltage on a reversible hydrogen electrode (RHE) scale. To ABPE% was calculated by using following expression:

$$ABPE\ (\%) = [J\ (mA\ cm^{-2}) \cdot \frac{1.23 - V_b}{P(mW\ cm^{-2})}] \cdot 100 \quad (1)$$

Where, J is the current density, V_b is applied voltage at RHE scale and P is power density of the incident light.

The applied voltage on Ag/AgCl scale was converted to RHE scale by using following expression:

$$RHE = V_{Ag/AgCl} + 0.059\,pH + V^{0}_{Ag/AgCl} \quad (2)$$

Where $V^{0}_{Ag/AgCl}$ = 0.197 V.

The optimum ABPE% for TiO_2, black P, black P@TiO_2, fibrous red P and fibrous red P@TiO_2 was calculated to be 0.07, 0.03, 0.03, 0.07 and 0.20 respectively (Figure 8d).

Incident photon-to-current efficiency (IPCE%)

Incident photon-to-current efficiency (IPCE) also referred as external quantum efficiency (EQE) measured at fixed incident wavelengths to evaluate performance of a photoelectrode for water splitting (Figure S7d). The IPCE is defined as the number of photogenerated charge carriers per incident photon flux as a function of wavelength contributing to the photocurrent. The IPCE% of materials were calculated at an applied bias of +0.6 V *vs* Ag/AgCl (1.23 V *vs* RHE, thermodynamic water splitting potential) using 420, 505, 580, 620 nm wavelength LEDs having 21.00 mW cm^{-2} power density at the surface of samples. IPCE% was calculated using the following expression.

$$IPCE\ (\%) = \left[\frac{1240.J\ (mA\ cm^{-2})}{\lambda\ (\mathrm{nm}).\mathrm{P}\ (mW\ cm^{-2}).}\right] \cdot 100 \quad (3)$$

Where, J is photocurrent density, λ is wavelength of incident light in nm and P is the power density of incident light.

The IPCE action spectra of samples is given in Figure S7d. The calculated value of IPCE% at 420, 505, 580 and 620 nm for TiO_2 (0.20, 0.16, 0.11, 0.08), black P@TiO_2 (0.66, 0.39, 0.16 and 0.11) and fibrous red P@TiO_2 (1.30, 0.43, 0.23 and 0.02) respectively.

Absorbed photon-to-current efficiency (APCE%)

Absorbed photon-to-current efficiency (APCE) is also referred as internal quantum efficiency (IQE) (Figure S7d). Since IPCE measurements demonstrate incident photons conversion efficiency and loss of photon being unabsorbed by the materials is not considered during calculation. A parameter of efficiency which takes unabsorbed photons into account should be used. So, APCE which defines the photocurrent collected per incident photon absorbed seem to be a suitable parameter to designate performance of devices. The APCE% can be calculated by following formulas:

APCE% = (IPCE/LHE) x 100 (4)

Where, LHE is light harvesting efficiency or absorptance which is numbers of electron hole pairs produced per incident photon flux. Considering each absorbed photon produces equal numbers of electron hole pairs, the value of LHE or absorptance can be calculated by Beer's law using following expression.

LHE or absorptance = $(1\text{-}10^{-A})$

So

$$APCE\ (\%) = \left[\frac{1240.J\ (mA\ cm^{-2})}{\lambda\ (\mathrm{nm}).\mathrm{P}\ (mW\ cm^{-2}).(1-10^{-A})}\right] \cdot 100 \quad (5)$$

Where, *J* is photocurrent density, λ is wavelength of incident light in nm, P is the power density of incident light, LHE is light harvesting efficiency and A is absorbance at measured wavelength.

The calculated value of APCE% at 420, 505, 580 and 620 nm for TiO_2 (0.28, 0.23, 0.16, 0.11), black P@TiO_2 (1.04, 0.67, 0.26 and 0.20) and fibrous red P@TiO_2 (1.65, 0.57, 0.32 and 0.03) respectively (Figure S7d).

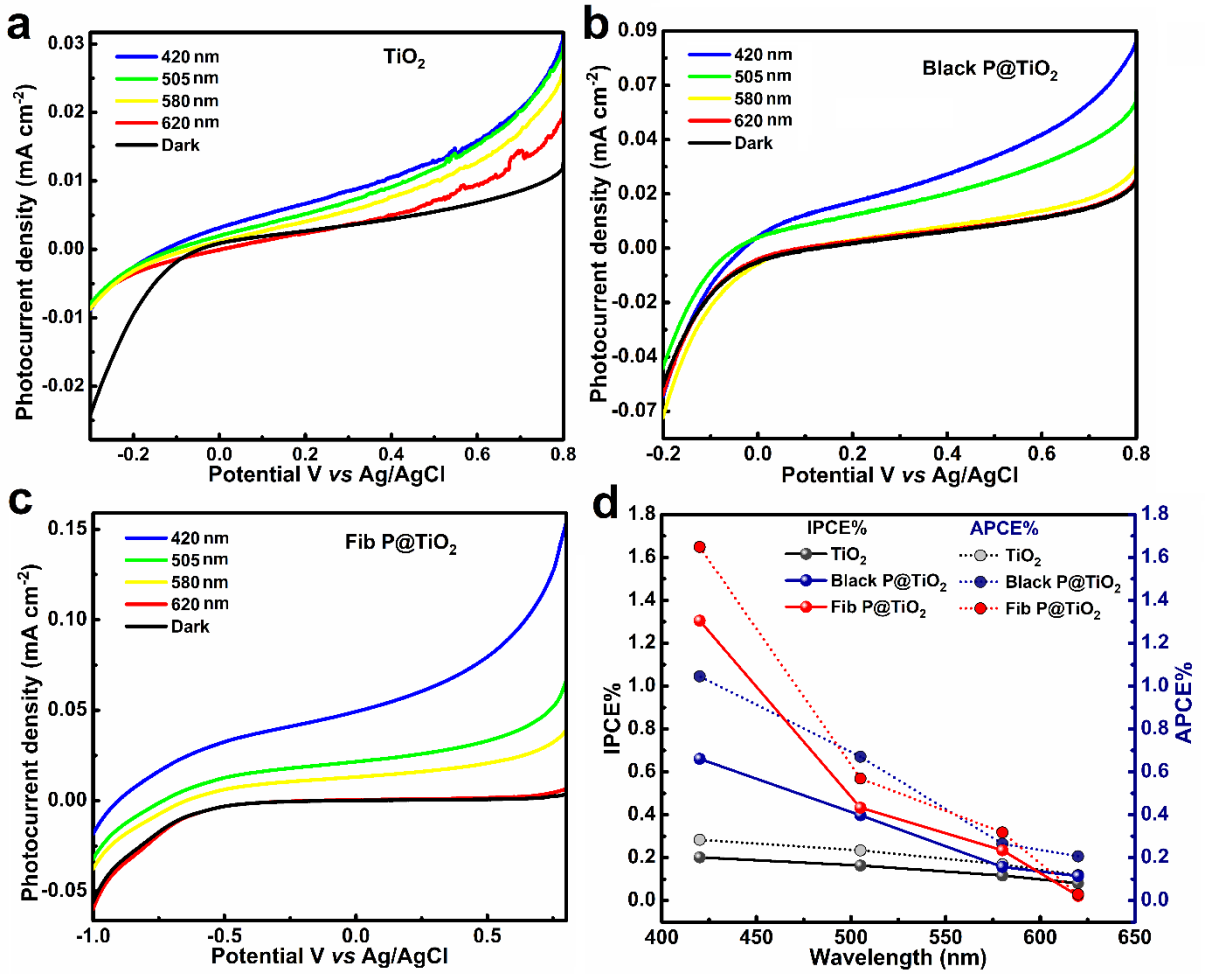

Figure S7 Photocurrent density *vs* applied voltage plot for a) TiO_2, b) black P@TiO_2, b) fibrous red P@TiO_2 under dark (black), 420 (blue), 505 (green), 580 (yellow), 620 (red) nm wavelength LEDs (21.00 mW cm^{-2}) and d) IPCE and APCE% TiO_2 (black), black P@TiO_2 (blue), fibrous red P@TiO_2 (red).

Faradaic Efficiency (FE%)

Faradaic Efficiency (FE%) was determined to verify the generated photocurrent. It is originated due to photoelectrochemical water splitting and not due the side reactions or photo-corrosion of the electrodes. Faradaic Efficiency can be defined as ratio of observed hydrogen in experimental condition divided by the theoretically evolved H_2 calculated from photocurrent density.

$$Faradaic\ efficiency\ (\%) = \left[\frac{Experimental\ gas\ evolution\ (measured\ H_2)}{Theoretical\ H_2\ gas\ evolution\ (based\ on\ photocurrent)}\right] \cdot 100 \quad (6)$$

$$Faradaic\ efficiency\ (\%) = \left[\frac{H_2\ evolution\ measured\ (mol)}{\frac{J\,(A\ cm^{-2}).A\ (cm^2).T\ (sec)}{2.e\ (C).N_A\ (mol^{-1})}}\right] \cdot 100 \quad (7)$$

Where, J is the photocurrent density (A cm^{-2}), A is the irradiation area of the photoelectrode (cm^2), T is time of measurement (seconds), e is the charge of an electron (1.602 x 10^{-19} C) and N_A is the Avogadro number (6.02 x 10^{23} mol^{-1}), the amount of hydrogen generated during PEC is expressed in moles.

For the measurements of evolved hydrogen, a three electrode H-cell was used and produced hydrogen at Pt cathode was analyzed by gas chromatography using a PDD detector (Figure S8). The experimental rate of hydrogen evolution per cm^2 was found to be 1.37, 3.38 and 8.15 for TiO_2, black P@TiO_2 and fibrous red P@TiO_2, respectively. Further, calculated Faradaic efficiency for TiO_2, black P@TiO_2 and fibrous red P@TiO_2 was calculated to be 33.41, 90.61 and 72.83 respectively (Figure S9, Table S3). The obtained faradaic efficiencies demonstrate populated side reaction and photo-corrosion of TiO_2 electrode while black P@TiO_2 shows excellent FE% which demonstrates true origin of photocurrent from water splitting reaction. Furthermore, to validate origin of photocurrent due to water splitting at anode not because of self oxidation of photoanode materials, oxygen concentration on black P@TiO_2 photoanode was also determined before reaction and after reaction. The gaseous sample was analyzed using GC-PDD equipped with Porapak Q column and Mol Sieve column. After 1 h the GC chromatogram of product clearly demonstrate significantly increased oxygen peak area/concentration. The increase peak area of oxygen collected at the photoanode suggest the origin of photocurrent/hydrogen at counter electrode from water splitting (Figure S10 a and b).

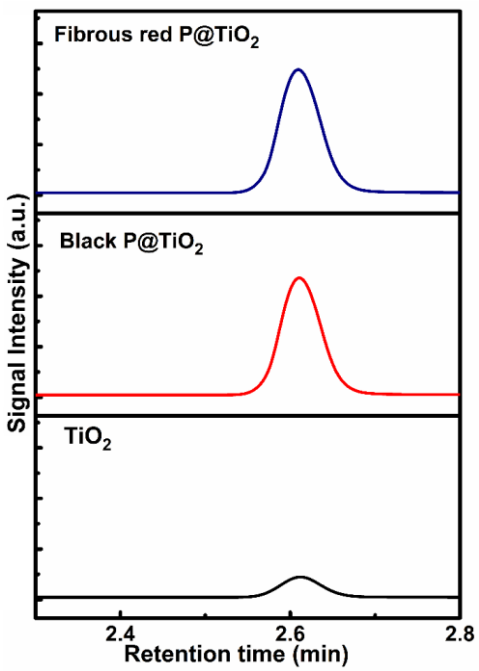

Figure S8. GC chromatogram of photoelectrochemically evolved H_2 collected at the Pt counter electrode.

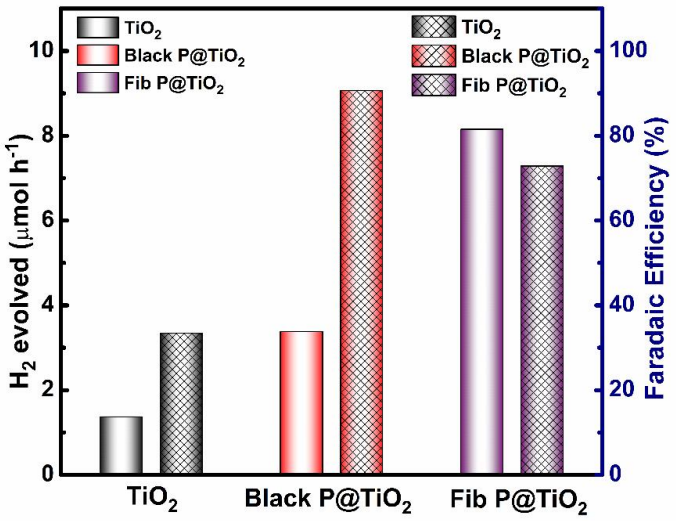

Figure S9. Graph of amount of H_2 evolved during PEC measurements (AM1.5 G) and corresponding Faradaic efficiencies.

Table S3. Experimentally observed amount of H_2 and theoretically calculated H_2 in PEC measurements and corresponding Faradaic efficiencies.

Sample	H_2 evolved (μmol h^{-1} cm^{-2})	Theoretical H_2 (μmol h^{-1} cm^{-2})	Faradaic Efficiency (%)
TiO_2	1.37	4.10	33.41
black P@TiO_2	3.38	3.73	90.61
fib. red P@TiO_2	8.15	11.193	72.83

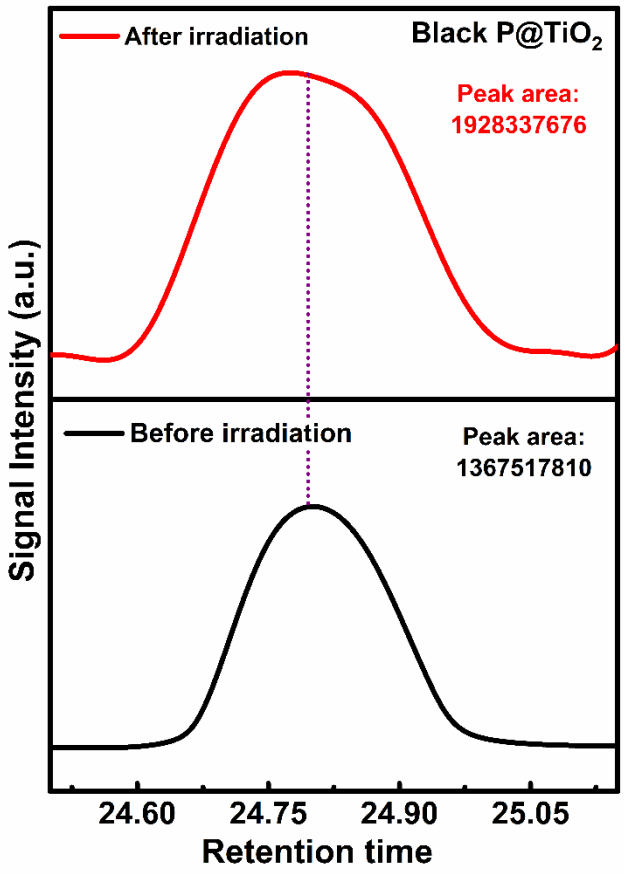

Figure S10. GC chromatogram of gaseous sample collected at black P@TiO_2 photoanode (a) before photoreaction after purging N_2 for 30 min and (b) after 1 h photoreaction under AM1.5 G irradiation.

2.7 Electrochemical characterization of phosphorus allotrope@TiO_2 membranes

Charge transfer resistance (R_C) at the semiconductor electrolyte interface (SEI), charge transport resistance (R_T) and space-charge capacitance (C_{SC}) were determined using electrochemical impedance spectroscopy (EIS) under AM1.5 G irradiation as well as under dark conditions (Figure S12a). EIS was performed at room temperature in a sodium sulfate electrolyte at pH 7 and at a potential of -0.4 V vs Ag/AgCl in a frequency range of 10 Hz and 105 Hz. EIS Nyquist plots, obtained under AM1.5 G illumination condition, for blank TiO_2, fibrous red P, fibrous red P@TiO_2, black P and black P@TiO_2 are shown Figure S12 and under dark conditions in Figure S13. Generally larger diameters of the Nyquist plots obtained under dark conditions confirm a higher charge transfer resistance in dark. From Nyquist plotting under irradiation an equivalent circuit diagram shown in Figure S12c could be obtained. As mentioned in the equivalent circuit, R_S, R_C, R_T, C_{SC} and C_H are electrolyte resistance, charge transfer resistance, charge transport resistance, space charge capacitance, and electrochemical double-layer capacitance, respectively. The equivalent circuit also comprises of a constant phase element, Q, with coefficient n. Resistive circuit elements, R_S, R_C, are R_T are independent of frequency and have the same magnitude as the resistances itself. The frequency-dependent impedances due to capacitances (Z_C_{SC} and Z_C_H) and the constant phase element (Z_Q) are given by eqt. (8) to (10).

$$\boldsymbol{Z_{C_{SC}}} = \frac{1}{\boldsymbol{i} \cdot (2\boldsymbol{\pi f}) \cdot \boldsymbol{C_{SC}}} \tag{8}$$

$$\boldsymbol{Z\_C_H} = \frac{1}{\boldsymbol{i} \cdot (2\boldsymbol{\pi f}) \cdot \boldsymbol{C_H}} \tag{9}$$

$$\boldsymbol{Z\_Q_1} = \frac{1}{i \cdot (2\pi f) \cdot C_{SC}} \tag{10}$$

$$\boldsymbol{Z} = \boldsymbol{R_S} + \boldsymbol{R_C} + \boldsymbol{R_{CT}} + \boldsymbol{Z\_C_{SC}} + \boldsymbol{Z\_C_H} + \boldsymbol{Z_Q} \tag{11}$$

$$\boldsymbol{\tau} = \boldsymbol{R_C} \cdot \boldsymbol{C_{SC}} \tag{12}$$

In eqt. (8) to (11), $i = \sqrt{-1}$, $\boldsymbol{Z}$ is the total impedance of the system. The magnitude of $\boldsymbol{Z}$ is the sum of impedance of all circuit elements and given by eqt. (11). The values of the circuit elements are obtained by fitting $\boldsymbol{Z}$ with experimentally obtained Nyquist plots, and are listed in Table S4. R_C (i.e. 200 Ω) of blank TiO_2 is much higher than those for fibrous red P, fibrous red P@TiO_2, black P, black P@TiO_2. Also notable is that the smallest $\boldsymbol{R_C}$ is of fibrous red P. Alike $\boldsymbol{R_C}$, $\boldsymbol{R_T}$ of the blank TiO_2 is also the highest among the sample studied, with black P being an exception. Recombination lifetime ($\boldsymbol{\tau}$, calculated using eqt. (12)) values are generally similar, with blank TiO_2 exhibiting the longest recombination lifetime (i.e. 2.8 μs) and fibrous red P@TiO_2 exhibiting the shortest lifetime (i.e. 1.7 μs). The lower recombination lifetimes of the semiconductor blends are expected because of interfacial defects, which may be caused by recombination effects.

$$\frac{1}{\boldsymbol{C_{sc}^2}} = \frac{\boldsymbol{2}}{\boldsymbol{e\varepsilon_0\varepsilon_r N_D}}\left\{(\boldsymbol{V} - \boldsymbol{V_{FB}}) - \frac{\boldsymbol{kT}}{\boldsymbol{e}}\right\} \tag{13}$$

$$N_d = \frac{2}{e\varepsilon_0\varepsilon_r}\left\{\frac{dV}{dC_{SC}^2}\right\} \tag{14}$$

Carrier concentration ($\boldsymbol{N_D}$) and flat band potential ($\boldsymbol{V_{FB}}$) values were calculated using Mott–Schottky analysis as described by eqt. (13) and eqt. (14), wherein $\boldsymbol{\varepsilon_r}$ is the semiconductor dielectric constant; $\boldsymbol{\varepsilon_r}$ of fibrous red P and black P are expected to be 8.5;[18] and blank TiO_2 as 30,[19] and dielectric constant of the blends of black P and TiO_2 (black P@TiO_2) as well as fibrous red P and TiO_2 (fibrous red P/TiO_2) are expected to be an intermediate value of 15. $\boldsymbol{\varepsilon_0}$ is the vacuum permittivity (8.854×10^{-12} F m^{-1}); $\boldsymbol{k}$ is the Boltzmann constant (1.381×10^{-23} J K^{-1}); $\boldsymbol{T}$

is the temperature in (298 K); e is the electron charge (1.602×10^{-19} C); and V is the applied potential. N_D of the samples were obtained using eqt. (12), where slopes of the Mott-Schottky plots (Figure S12b) were factored into. Positive slopes indicate *n*-type conductivity and electrons as the majority carrier. The *n*-type slope in Mott-Schottky measurements for fibrous red P and black P was attributed to the contribution in charge transport from underlying compact TiO_2 used during measurements; note that pristine fibrous red P and black P graphs are less steep compared to pristine TiO_2. We note *p*-type behaviour from UPS measurements, which is considered to the actual behaviour of the fibrous red P and black P. The values of N_D are indicated within the plot. V_{FB} was determined from the intersection of the slope of the Mott-Schottky's plot with the horizontal axis, which denotes potential with respect to Ag/AgCl. V_{FB} values for TiO_2, fibrous red P, black P, fibrous red P@TiO_2 and black P@TiO_2 was calculated to be to be -0.70, -0.37, -0.56, -0.54 and -0.66 V *vs* Ag/AgCl respectively (Figure S12b). Interestingly, N_D of blank TiO_2 is the least among the samples while its V_{FB} is the most negative as well. In photocatalysis, the band potential is usually expressed at the scale of vacuum energy level (E_{vacuum}). So, we have first converted the value of flat band potential from Ag/AgCl scale to RHE (reversible hydrogen electrode) followed by conversion to vacuum level by following equation:

$$E_{(RHE)} = E_{Ag/AgCl} + 0.059\,pH + E_{Ag/AgCl} \tag{15}$$

$$E_{vacuum} = -(E_{(RHE)} + 4.5) \tag{16}$$

Where, $E^{o}_{Ag/AgCl} = 0.199$ V at 25 °C, $E_{Ag/AgCl}$ is working potential and E_{vacuum} (eV) is the potential at vacuum scale. From the eqt. (15) and (16) the position of flat band potential of TiO_2, fibrous red P, black P, fibrous red P@TiO_2 and black P@TiO_2 was estimated to be -4.00, -4.33, -4.14, -4.16 and -4.04 eV respectively.

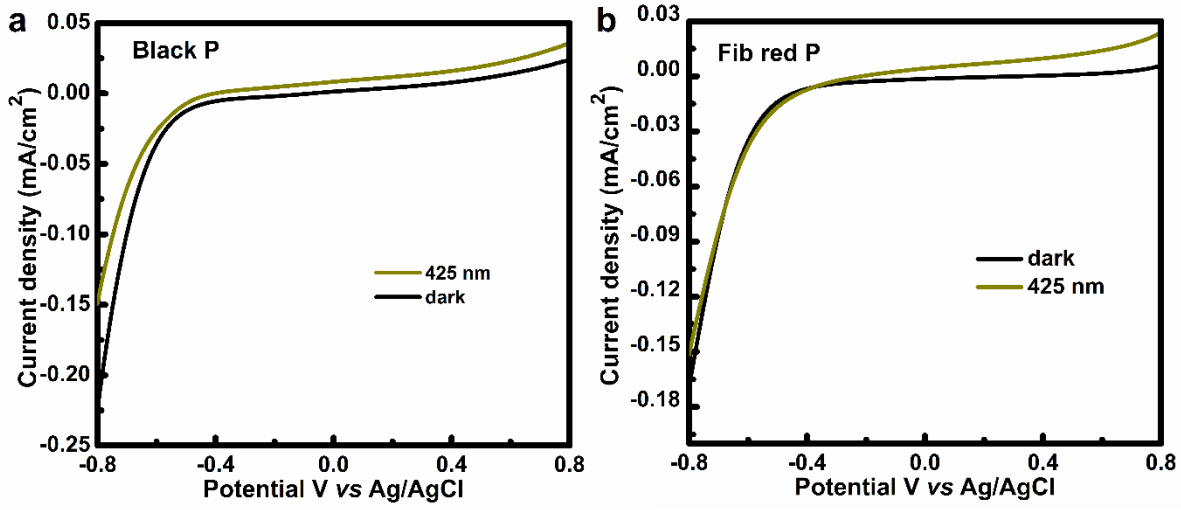

Figure S11. Photocurrent density *vs* applied voltage plot at 425 nm wavelength for **a)** black P **b)** fibrous red P.

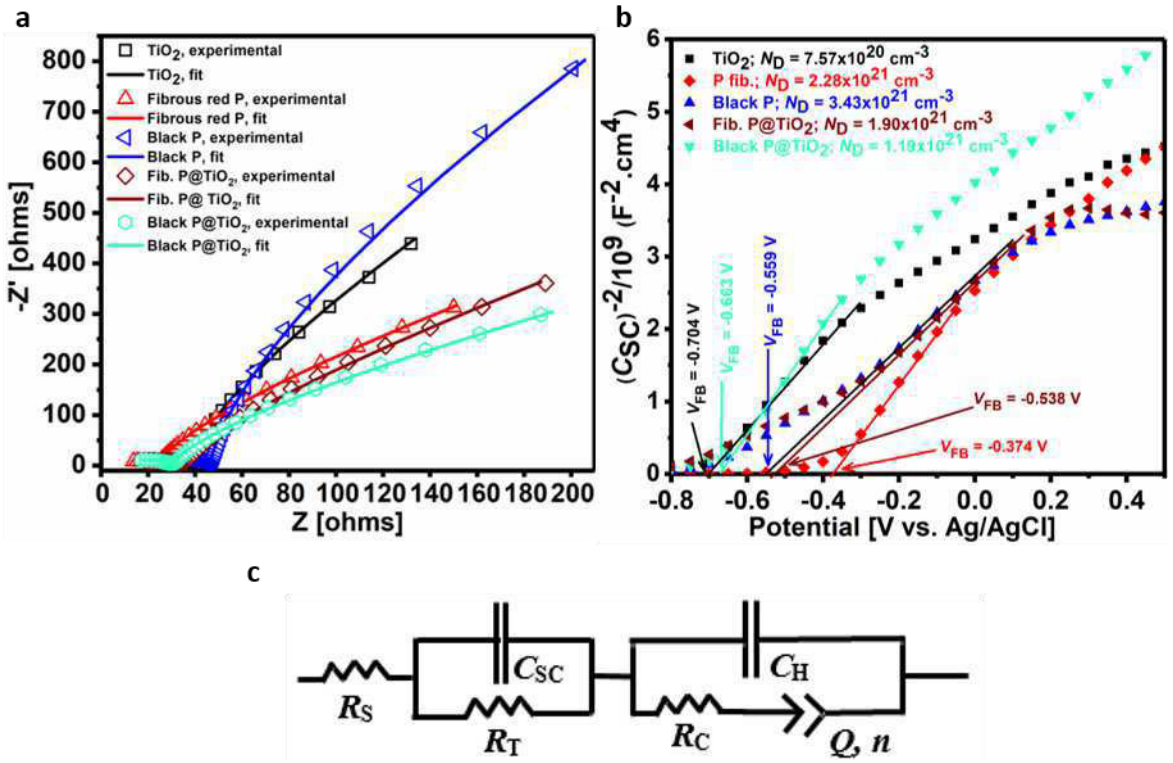

Figure S12. **a)** Experimental and fitted EIS Nyquist plots of blank TiO_2, fibrous red P, fibrous red P@TiO_2, black P and black P@TiO_2 under AM1.5 G irradiation **b)** Mott Schottky plots of fibrous red P, fibrous red P@TiO_2, black P, black P@TiO_2 and blank TiO_2. V_{FB} and N_D are mentioned within the plot. **c)** Equivalent circuit of EIS data. Color: TiO_2 (black), fibrous red P (red), fibrous red P@TiO_2 (brown), black P (blue) and black P@TiO_2 (light green).

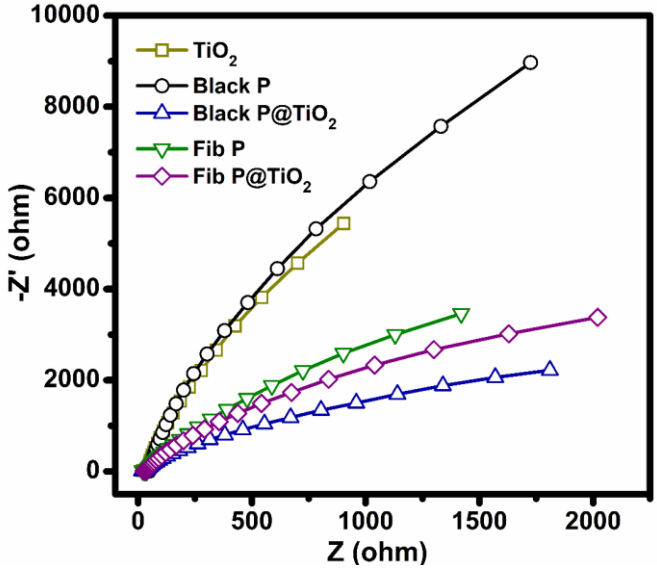

Figure S13. Nyquist plots of fibrous red P, fibrous red P@TiO_2, black P, black P@TiO_2 and blank TiO_2 under dark conditions.

Table S4. Values of R_S, R_C, R_T, C_{SC}, C_H, Q and n, obtained by fitting the Nyquist plots to the equivalent circuit.

Sample	R_S (Ω)	C_{SC} (F)	R_T (Ω)	C_H (F)	R_C (Ω)	Q ($F.s^{-1+n}$)	n	τ (μs)
TiO_2	9	$1.00x10^{-7}$	28	$2.20x10^{-5}$	200	$6.00x10^{-5}$	0.57	2.8
fibrous red P	5	$1.20x10^{-8}$	18	$1.90x10^{-5}$	1	$1.55x10^{-4}$	0.55	2.2
fib. red P@TiO_2	12	$8.10x10^{-8}$	21	$1.70x10^{-5}$	70	$1.30x10^{-4}$	0.57	1.7
black P	5	$3.10x10^{-8}$	40	$1.25x10^{-5}$	50	$3.65x10^{-5}$	0.52	1.3
black P@TiO_2	7	$1.10x10^{-7}$	22	$1.60x10^{-5}$	15	$2.15x10^{-4}$	0.51	2.4

2.8 Kelvin Probe Force Microscopy (KPFM) Measurement

To understand the mechanism of charge carrier transport and verify successful heterojunction formation between phosphorous materials (black P and fibrous red P) and TiO_2 nanostructures, change in surface potential (SP) was determined using Kelvin Probe Force Microscopy (KPFM) under dark and irradiation conditions (Figure S14). The surface topographical AFM image of TiO_2, black P, black P@TiO_2, fibrous red P and fibrous red P@TiO_2 samples exhibit rough surface features (Figure S14 a-e). The surface potential map of samples under dark condition, 450 and 635 nm irradiation are given in Figure S13a-e. The surface potential (SP) map of bare TiO_2 displayed nonuniform charge distribution due to the uneven morphology of TiO_2 nanotubes, while, SP distribution of pristine black P and fibrous red P and hybrids were comparatively uniform. The hybrid materials (black P@TiO_2 and fibrous red P@TiO_2) displayed intermediate SP distribution. Under dark condition, the SP map image of bare TiO_2 samples show bright contrast in comparison to pristine black P and fibrous red P which demonstrates electron rich surface of *n*-type TiO_2 nanotubes. However, SP map of hybrid materials show slightly increased contrast in comparison to pristine materials due to reduced surface charge, suggesting a transfer of electronic charge from the surface of TiO_2 due to the formation of heterojunction. Further, after illumination with 450 nm laser, the contrast of red regions was further increased for all samples which was corroborated due to the transfer of photogenerated electrons on the surface phosphorous to TiO_2's surface. The hybrid materials (particularly black P@TiO_2) displayed the highest change in SP which clearly verifies heterojunction formation between the materials leading to improved charge carrier generation under illuminated condition. Further, under 635 nm illumination similar pattern was followed suggesting improved charge carrier creation and separation in hybrid P@TiO_2 heterojunction even at a higher wavelength.

The measured surface potential distribution or contact potential difference (CPD) for TiO_2, black P, black P@TiO_2, fib. red P and fib. red P@TiO_2 under dark condition was found to be +36, +86, +39, +16 and +14 mV, respectively (Figure S14f-j). A slight negative shift of SP distribution of hybrid samples in comparison to pristine phosphorous reveals a decrease in the work function (WF) value. The observed decrease in WF suggest uplifting of Fermi level of phosphorous in hybrid due to Fermi level alignment leading to the formation of heterojunction. As expected after irradiation with 450 and 635 nm laser, the CPD of TiO_2, black P, black P@TiO_2, fibrous red P and fibrous red P@TiO_2 show a slight negative shift due to the accumulation of photogenerated negative charge on the sample's surface. Bare TiO_2 and fibrous red P displayed extremely small SP shift under 450 and 635 nm illumination which demonstrate poorly generated charge in TiO_2 and faster recombination rate in fibrous red P respectively. While, black P show relatively higher shift under illumination conditions which might be due to longer lifetime of generated charge on 2D phosphorous structure. A similar pattern was followed for fibrous P@TiO_2 and black P@TiO_2 heterojunction which demonstrate visible responsive nature of hybrid materials (Figure S14).

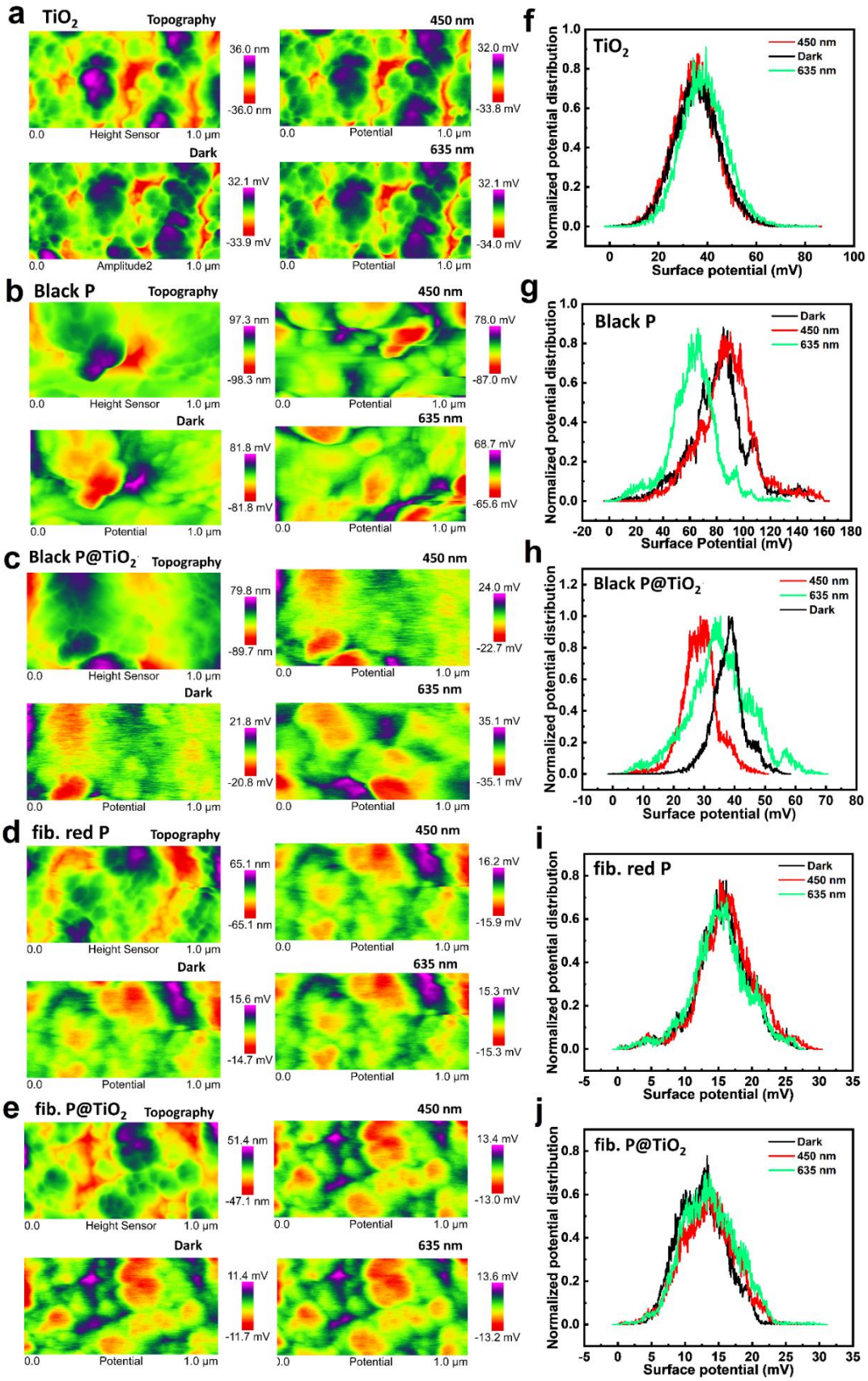

Figure S14. Topographical AFM images and surface potential map of a) TiO_2 nanotubes, b) black P, c) fibrous red P, d) black P@TiO_2, e) fibrous red P@TiO_2 under dark, 450 and 635 nm illumination conditions and e) surface potential distribution of bare TiO_2 nanotubes, black P, fibrous red P, black P@TiO_2, fibrous red P@TiO_2, samples deposited on FTO under dark (black), 450 nm (red) and 635 nm (green) illumination condition.

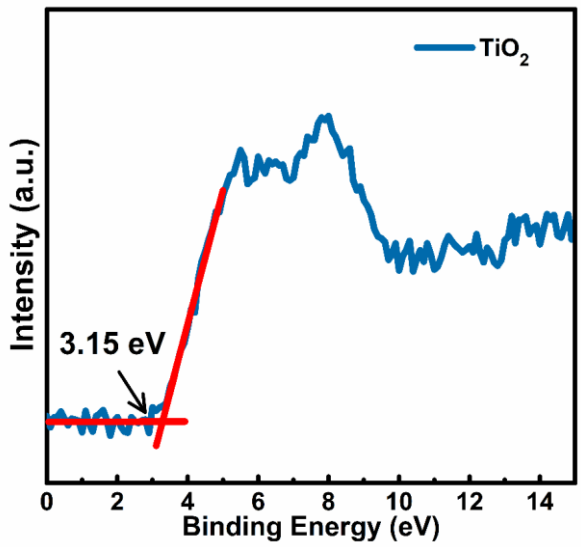

Figure S15. XPS valence band spectra of TiO_2. The point of intersection display position of valence band maxima (VB_{max}) below Fermi level.

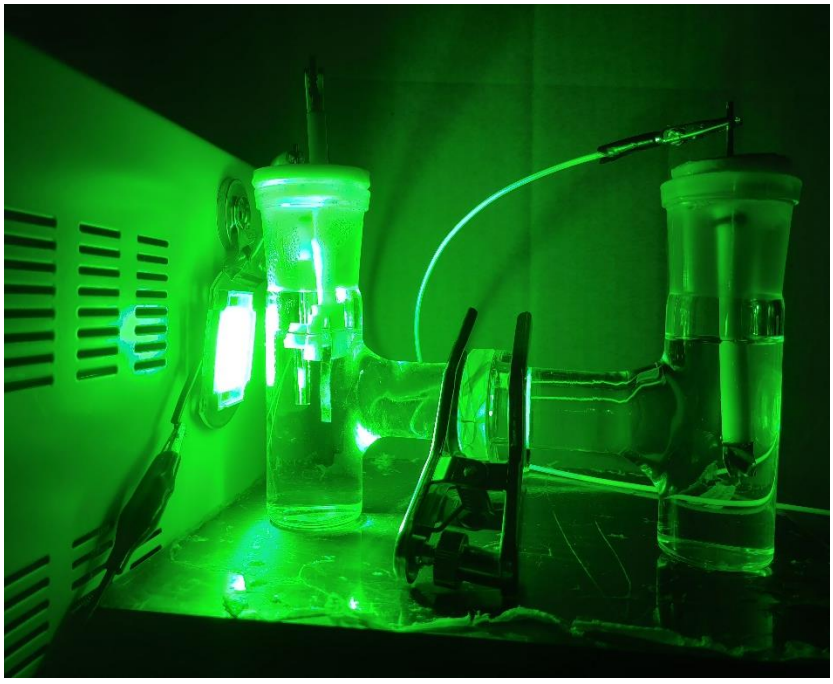

Figure S16. Photograph of photoelectrochemical water splitting cell irradiated under 505 nm LED.

REFERENCES

1. Mor, G. K.; Shankar, K.; Paulose, M.; Varghese, O. K.; Grimes, C. A., Use of Highly-Ordered TiO_2 Nanotube Arrays in Dye-Sensitized Solar Cells. *Nano Lett.* **2006,** *6*, 215-218.
2. Eckstein, N.; Hohmann, A.; Weihrich, R.; Nilges, T.; Schmidt, P., Synthesis and Phase Relations of Single- Phase Fibrous Phosphorus. *Z. Anorg. Allg. Chem.* **2013,** *639*, 2741-2743.
3. Köpf, M.; Eckstein, N.; Pfister, D.; Grotz, C.; Krüger, I.; Greiwe, M.; Hansen, T.; Kohlmann, H.; Nilges, T., Access and In Situ Growth of Phosphorene-Precursor Black Phosphorus. *J. Cryst. Growth* **2014,** *405*, 6-10.
4. Palmer, W. G., *Experimental Inorganic Chemistry*. Cambridge University Press: Cambridge, 1962; p 577 s.
5. Thakur, U.; Kisslinger, R.; Shankar, K., One-Dimensional Electron Transport Layers for Perovskite Solar Cells. *Nanomaterials* **2017,** *7*, 95.
6. WinXPOW, S., Version 3.0. 2.1. *STOE & Cie GmbH: Darmstadt* **2011**.
7. Ni, J.; Fu, S.; Wu, C.; Maier, J.; Yu, Y.; Li, L., Self- Supported Nanotube Arrays of Sulfur- Doped TiO_2 Enabling Ultrastable and Robust Sodium Storage. *Adv. Mater.* **2016,** *28*, 2259-2265.
8. Tong, Z.; Yang, D.; Xiao, T.; Tian, Y.; Jiang, Z., Biomimetic Fabrication of g-C_3N_4/TiO_2 Nanosheets with Enhanced Photocatalytic Activity Toward Organic Pollutant Degradation. *Chem. Eng. J.* **2015,** *260*, 117-125.
9. Zhang, Y.; Zhao, Z.; Chen, J.; Cheng, L.; Chang, J.; Sheng, W.; Hu, C.; Cao, S., C-Doped Hollow TiO_2 Spheres: In Situ Synthesis, Controlled Shell Thickness, and Superior Visible-Light Photocatalytic Activity. *Appl. Catal., B* **2015,** *165*, 715-722.
10. Feng, J. X.; Xu, H.; Dong, Y. T.; Lu, X. F.; Tong, Y. X.; Li, G. R., Efficient Hydrogen Evolution Electrocatalysis using Cobalt Nanotubes Decorated with Titanium Dioxide Nanodots. *Angew. Chem. Int. Ed.* **2017,** *56*, 2960-2964.
11. Zheng, L.; Han, S.; Liu, H.; Yu, P.; Fang, X., Hierarchical MoS_2 Nanosheet@TiO_2 Nanotube Array Composites with Enhanced Photocatalytic and Photocurrent Performances. *Small* **2016,** *12*, 1527-1536.
12. Gómez-Pérez, J.; Barna, B.; Tóth, I. Y.; Kónya, Z.; Kukovecz, A., Quantitative Tracking of the Oxidation of Black Phosphorus in the Few-Layer Regime. *ACS Omega* **2018,** *3*, 12482-12488.
13. Edmonds, M.; Tadich, A.; Carvalho, A.; Ziletti, A.; O'Donnell, K.; Koenig, S.; Coker, D.; Ozyilmaz, B.; Neto, A. C.; Fuhrer, M., Creating a Stable Oxide at the Surface of Black Phosphorus. *ACS Appl. Mater. Interfaces* **2015,** *7*, 14557-14562.
14. Ling, Z.-P.; Zhu, J.-T.; Liu, X.; Ang, K.-W., Interface Engineering for the Enhancement of Carrier Transport in Black Phosphorus Transistor with Ultra-Thin High-*k* Gate Dielectric. *Sci. Rep.* **2016,** *6*, 26609.
15. Zhu, J.; Xu, S.; Ning, J.; Wang, D.; Zhang, J.; Hao, Y., Gate-Tunable Electronic Structure of Black Phosphorus/HfS_2 P–N van der Waals Heterostructure with Uniformly Anisotropic Band Dispersion. *J. Phys. Chem. C* **2017,** *121*, 24845-24852.
16. Zhou, L.; Zhang, J.; Zhuo, Z.; Kou, L.; Ma, W.; Shao, B.; Du, A.; Meng, S.; Frauenheim, T., Novel Excitonic Solar Cells in Phosphorene–TiO_2 Heterostructures with Extraordinary Charge Separation Efficiency. *J. Phys. Chem. C* **2016,** *7*, 1880-1887.
17. Luo, W.; Zemlyanov, D. Y.; Milligan, C. A.; Du, Y.; Yang, L.; Wu, Y.; Peide, D. Y., Surface Chemistry of Black Phosphorus Under a Controlled Oxidative Environment. *Nanotechnology* **2016,** *27*, 434002.
18. Morita, A., Semiconducting Black Phosphorus. *Appl. Phys. A* **1986,** *39* (4), 227-242.
19. Asahina, H.; Morita, A., Band Structure and Optical Properties of Black Phosphorus. *J. Phys. C* **1984,** *17*, 1839.

3.3. Synthesis, structure, and properties of rare-earth germanium sulfide iodides $RE_3Ge_2S_8I$ (*RE* = La, Ce, Pr)

Dundappa Mumbaraddi [a], Abishek K. Iyer [a], Ebru Üzer [b], Vidyanshu Mishra [a], Anton O. Oliynyk [a], Tom Nilges [b], Arthur Mar [a, *]

[a] Department of Chemistry, University of Alberta, Edmonton, Alberta, Canada T6G 2G2

[b] Department of Chemistry, Technische Universität München, 85747 Garching, Germany

Journal of Solid State Chemistry Pages 97 - 103
DOI: 10.1016/j.jssc.2019.03.034

The article 'Synthesis, structure, and properties of rare-earth germanium sulfide iodides $RE_3Ge_2S_8I$ (*RE* = La, Ce, Pr)' was submitted to 'Journal of Solid State Chemistry' in January 2019 and published online in June 2019. The main results were presented by Dr. Abishek Iyer at the Annual ATUMS meeting in Jasper, Canada in November 2017 and by Dundappa Mumbaraddi and Ebru Üzer at the 101st Canadian Chemistry Conference and Exhibition in Edmonton, Canada in May 2018.

An extended study on chalcogenides as optical materials was conducted through mathematical models in machine-learning to support property prediction for systematical approaches. A solid-state synthesis and characterization of three quarternary sulfide iodides was carried out after. $RE_3Ge_2S_8I$ (*RE* = La, Ce, Pr) were prepared from melting and annealing processes at elevated temperatures (900 °C). The rare-earth chalcogenidehalide compounds crystallize monoclinically, in space group *C*2/c. In Table 3.3 cell parameters are listed.

Table 3.3. Unit cell parameters of $RE_3Ge_2S_8I$ (*RE* = La, Ce, Pr).

Formula	*a* (Å)	*b* (Å)	*c* (Å)	V (Å^3)
$La_3Ge_2S_8I$	16.156(6)	7.9776(18)	11.018(3)	1405.6(6)
$Ce_3Ge_2S_8I$	16.054(2)	7.9233(11)	10.9624(15)	1379.9(3)
$Pr_3Ge_2S_8I$	15.9760(9)	7.8786(5)	10.9281(6)	1360.56(14)

Isostructural to the $La_3(SiO_4)Cl$-type the title compounds contain isolated $[GeS_4]^{4-}$-tetrahedrons, stacked along the *c*-axis and separated by RE^{3+} cations. Mixed-anion compounds exhibit structure control advantages. In this way, large tunnels are formed, where I^--anions are located along the stacking direction. Each RE site is occupied by one I and eight S atoms, forming an almost regular to tricapped trigonal prism.

Optical band gap properties were determined using diffuse reflectance UV-Vis spectroscopy. Tauc-plotting the converted absorption spectra by extrapolation resulted in an optical band gap of 3.1 eV for $La_3Ge_2S_8I$, 2.7 eV for $Ce_3Si_2S_8I$, and 2.9 eV for $Pr_3Ge_2S_8I$ which is in close agreement to the nearly colorless appearance of the compound. A significantly larger band gap was calculated using LMTO approximation for $La_3Ge_2S_8I$ (3.9 eV).[92] In contrast to $La_3Ge_2S_8I$, LMTO calculations were underestimating the experimentally found band gap for $Ce_3Si_2S_8I$ (calculated: 2.9 eV).[93]

Magnetic susceptibility measurements on $Ce_3Ge_2S_8I$ and $Pr_3Ge_2S_8I$ showed Curie-Weiss paramagnetism for both compounds, with no magnetic ordering down to 2 K. Effective magnetic moments were found to be 4.51(1) μ_B/f.u. for $Ce_3Ge_2S_8I$ and 6.20(1) μ_B/f.u. for $Pr_3Ge_2S_8I$.

AUTHORS CONTRIBUTION: A.I. and E.Ü. performed synthesis and XRD studies on $RE_3Ge_2S_8I$ (*RE* = La, Ce, Pr). D.M. and V.M. investigated optical band gap and magnetic properties of the compounds. A.O. was involved in crystal structure refinement. A.M. and T.N. planned and supervised research studies. All authors were involved in writing their respective parts of the manuscript.

Journal of Solid State Chemistry 274 (2019) 162–167

Contents lists available at ScienceDirect

Journal of Solid State Chemistry

journal homepage: www.elsevier.com/locate/jssc

Synthesis, structure, and properties of rare-earth germanium sulfide iodides $RE_3Ge_2S_8I$ (RE = La, Ce, Pr)

Dundappa Mumbaraddi [a], Abishek K. Iyer [a], Ebru Üzer [b], Vidyanshu Mishra [a], Anton O. Oliynyk [a], Tom Nilges [b], Arthur Mar [a,*]

[a] Department of Chemistry, University of Alberta, Edmonton, Alberta, T6G 2G2, Canada
[b] Department of Chemistry, Technische Universität München, 85747, Garching, Germany

ARTICLE INFO

Keywords:
Rare earths
Mixed-anion compounds
Crystal structure
Electronic structure
Magnetic properties

ABSTRACT

The rare-earth germanium sulfide iodides $RE_3Ge_2S_8I$ (RE = La, Ce, Pr) have been prepared by reaction of the elements at 900 °C. They adopt the monoclinic $La_3(SiO_4)_2Cl$-type structure (space group $C2/c$, $Z = 4$; $a = 16.156(4)$–$15.9760(9)$ Å, $b = 7.9776(18)$–$7.8786(5)$ Å, $c = 11.081(3)$–$10.9281(6)$ Å, $\beta = 98.192(5)$–$98.4525(10)°$ on progressing from La to Pr for the RE component) consisting of isolated thiogermanate tetrahedral groups $[GeS_4]^{4-}$ separated by RE^{3+} and I^- ions. The optical band gaps fall in the range of 2.7–3.1 eV. Magnetic measurements indicated simple paramagnetic behaviour for $Ce_3Ge_2S_8I$ and $Pr_3Ge_2S_8I$.

1. Introduction

Mixed-anion compounds, which contain more than one type of anion, offer ways to control the structures and properties of solids that are not accessible in single-anion or mixed-cation compounds [1]. The local environment around cations can be changed to create coordination polyhedra with different symmetries, the bonding character can be adjusted by introducing intermediate degrees of electron transfer, and the band gap can be varied to desired magnitudes. Well-known examples of mixed-anion compounds typically contain oxide with fluoride (e.g., $LiFeSO_4F$ as cathode materials in batteries [2]), other chalcogenide (e.g., $LaCuChO$ (Ch = S, Se) as transparent conductors [3]), and pnictide ions (e.g., $Ca_{1-x}La_xTaO_{2-x}N_{1+x}$ as inorganic pigments [4], LaFeAsO as superconductors [5]). Mixed-anion compounds containing heavier chalcogenide and halide ions are less common [6], but they have also emerged as attractive candidates for various applications (e.g., Ag_5Te_2Cl as ionic conductors [7], BiSI and BiSeI as photovoltaic materials [8], $Ba_4ZnGa_4Se_{10}Cl_2$ as infrared nonlinear optical materials [9], and Tl_6SI_4 as hard radiation detectors [10]).

Chalcogenide halides containing rare-earth metals are relatively scarce but may be interesting because of their potential as optical and magnetic materials [6]. Narrow-band optical spectra and large magnetic moments may be expected from the presence of unpaired electrons in highly localized f-orbitals. Within the systems RE–Tt–Ch–X (RE = rare-earth metal; Tt = Si, Ge, Sn (tetrel), Ch = S, Se, Te; X = F, Cl, Br, I), the only known quaternary phases so far are $RE_3Si_2S_8X$ (RE = early rare-earth metals; X = Cl, Br, I) [11–17] and RE_3SiS_6Cl (RE = Nd, Sm) [18,19], first discovered nearly 20 years ago. The compound $Ce_3Si_2S_8I$ luminesces in the blue region and may be useful in electroluminescent devices [13].

As part of our ongoing investigations of chalcogenides as optical materials, we are examining these RE–Tt–Ch–X systems to ascertain if other quaternary phases can be found. In particular, we hypothesize that the Ge-substituted analogues of $RE_3Si_2S_8X$ may be viable targets to prepare. The existence of $Ce_3Ge_2S_8I$ has been mentioned but no publication has been forthcoming [13]. Here, we present the synthesis and full structural characterization of the Ge-containing members $RE_3Ge_2S_8I$, their electronic band structure, and their optical and magnetic properties.

2. Experimental

2.1. Synthesis

Starting materials were freshly filed rare-earth metal pieces (RE = La, Ce, Pr; 99.9%, Hefa), germanium powder (99.999%, Sigma-Aldrich), sulfur flakes (99.998%, Sigma-Aldrich), and iodine crystals (99.8%, Anachemia). The elements were combined in stoichiometric ratios on a 0.5-g scale to target the composition $RE_3Ge_2S_8I$, with a 10% excess (by weight) of I_2 added. The mixtures were finely ground, cold-pressed into pellets, and loaded into fused-silica tubes (12 mm diameter and 15 cm

* Corresponding author.
E-mail address: arthur.mar@ualberta.ca (A. Mar).

https://doi.org/10.1016/j.jssc.2019.03.034
Received 15 January 2019; Received in revised form 12 March 2019; Accepted 17 March 2019
Available online 18 March 2019

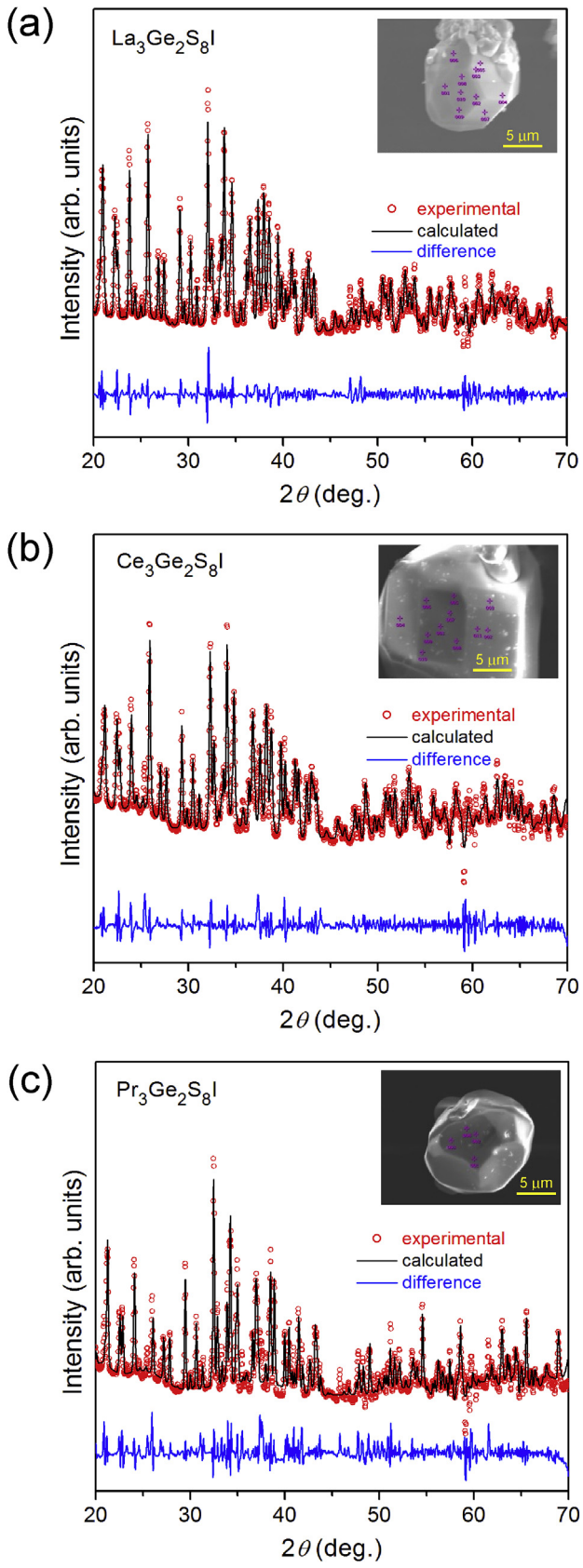

Fig. 1. Powder XRD patterns (with Pawley fittings) and SEM images of typical crystals (insets) for $RE_3Ge_2S_8I$.

Table 1
Crystallographic data for $RE_3Ge_2S_8I$.

formula	$La_3Ge_2S_8I$	$Ce_3Ge_2S_8I$	$Pr_3Ge_2S_8I$
formula mass (amu)	945.29	948.92	951.29
space group	*C*2/*c* (No. 15)	*C*2/*c* (No. 15)	*C*2/*c* (No. 15)
a (Å)	16.156(4)	16.054(2)	15.9760(9)
b (Å)	7.9776(18)	7.9233(11)	7.8786(5)
c (Å)	11.018(3)	10.9624(15)	10.9281(6)
β (°)	98.192(5)	98.262(3)	98.4525(10)
V (Å^3)	1405.6(6)	1379.9(3)	1360.56(14)
Z	4	4	4
T (K)	296(2)	296(2)	296(2)
ρ_{calcd} (g cm^{-3})	4.467	4.568	4.644
crystal dimensions (mm)	0.05 × 0.04 × 0.04	0.07 × 0.05 × 0.04	0.05 × 0.04 × 0.04
μ(Mo Kα) (mm^{-1})	16.49	17.41	18.36
transmission factors	0.511–0.558	0.331–0.531	0.471–0.553
2*θ* limits	5.09–66.33°	5.13–66.56°	5.16–66.54°
data collected	$-24 \le h \le 24$, $-12 \le k \le 12$, $-16 \le l \le 16$	$-24 \le h \le 24$, $-12 \le k \le 12$, $-16 \le l \le 16$	$-24 \le h \le 24$, $-12 \le k \le 12$, $-16 \le l \le 16$
no. of data collected	9974	9823	9815
no. of unique data, including $F_o^2 < 0$	2654	2634	2605
no. of unique data, with $F_o^2 > 2\sigma(F_o^2)$	1767	1874	1946
no. of variables	65	65	65
R(*F*) for $F_o^2 > 2\sigma(F_o^2)$[a]	0.048	0.043	0.041
$R_w(F_o^2)$[b]	0.128	0.108	0.104
goodness of fit	1.02	1.02	1.07
$(\Delta\rho)_{max}$, $(\Delta\rho)_{min}$ (e Å^{-3})	3.70, −2.52	3.13, −2.08	3.47, −2.21

[a] $R(F) = \sum||F_o| - |F_c||/\sum|F_o|$.
[b] $R_w(F_o^2) = [\sum[w(F_o^2 - F_c^2)^2]/\sum wF_o^4]^{1/2}$; $w^{-1} = [\sigma^2(F_o^2) + (Ap)^2 + Bp]$, where $p = [\max(F_o^2, 0) + 2F_c^2]/3$.

Table 2
Atomic coordinates and equivalent isotropic displacement parameters (Å^2)[a] for $RE_3Ge_2S_8I$.

Atom	Wyckoff position	*x*	*y*	*z*	U_{eq} (Å^2)[a]
$La_3Ge_2S_8I$					
La1	8*f*	0.30365(3)	0.12072(6)	0.32098(4)	0.0144(1)
La2	4*e*	0	0.10242(9)	1/4	0.0166(2)
Ge	8*f*	0.15867(6)	0.03916(11)	0.02736(8)	0.0139(2)
S1	8*f*	0.0650(1)	0.1575(3)	0.5404(2)	0.0163(4)
S2	8*f*	0.1446(1)	0.2501(3)	0.1496(2)	0.0166(4)
S3	8*f*	0.2160(1)	0.4296(3)	0.4133(2)	0.0155(4)
S4	8*f*	0.3507(1)	0.4014(3)	0.1684(2)	0.0153(4)
I	4*e*	0	0.5186(1)	1/4	0.0273(2)
$Ce_3Ge_2S_8I$					
Ce1	8*f*	0.30319(3)	0.12132(5)	0.32094(4)	0.0147(1)
Ce2	4*e*	0	0.10510(8)	1/4	0.0173(1)
Ge	8*f*	0.15843(5)	0.03936(10)	0.02651(7)	0.0143(2)
S1	8*f*	0.0649(1)	0.1602(2)	0.5395(2)	0.0187(4)
S2	8*f*	0.1445(1)	0.2522(2)	0.1496(2)	0.0179(4)
S3	8*f*	0.2152(1)	0.4299(2)	0.4133(2)	0.0162(3)
S4	8*f*	0.3510(1)	0.4020(2)	0.1703(2)	0.0163(3)
I	4*e*	0	0.5193(1)	1/4	0.0267(2)
$Pr_3Ge_2S_8I$					
Pr1	8*f*	0.30270(2)	0.12199(4)	0.32111(3)	0.0131(1)
Pr2	4*e*	0	0.10822(7)	1/4	0.0156(1)
Ge	8*f*	0.15808(4)	0.03975(9)	0.02567(6)	0.0125(2)
S1	8*f*	0.0647(1)	0.1618(2)	0.5380(2)	0.0165(3)
S2	8*f*	0.1441(1)	0.2534(2)	0.1490(2)	0.0160(3)
S3	8*f*	0.2151(1)	0.4306(2)	0.4131(2)	0.0147(3)
S4	8*f*	0.3516(1)	0.4019(2)	0.1723(2)	0.0145(3)
I	4*e*	0	0.5203(1)	1/4	0.0241(2)

[a] U_{eq} is defined as one-third of the trace of the orthogonalized U_{ij} tensor.

Table 3
Interatomic distances (Å) in $RE_3Ge_2S_8I$.

	$La_3Ge_2S_8I$	$Ce_3Ge_2S_8I$	$Pr_3Ge_2S_8I$
*RE*1–S4	2.963(2)	2.937(2)	2.914(2)
*RE*1–S3	2.976(2)	2.960(2)	2.948(2)
*RE*1–S1	3.007(2)	2.982(2)	2.967(2)
*RE*1–S3	3.016(2)	2.998(2)	2.988(2)
*RE*1–S4	3.062(2)	3.038(2)	3.024(2)
*RE*1–S2	3.077(2)	3.047(2)	3.030(2)
*RE*1–S3	3.086(2)	3.068(2)	3.049(2)
*RE*1–S2	3.139(2)	3.117(2)	3.103(2)
*RE*1–I	3.4708(9)	3.4565(6)	3.4499(4)
*RE*2–S4 (× 2)	2.930(2)	2.910(2)	2.896(2)
*RE*2–S2 (× 2)	2.967(2)	2.947(2)	2.928(2)
*RE*2–S1 (× 2)	3.252(2)	3.224(2)	3.193(2)
*RE*2–S1 (× 2)	3.381(2)	3.394(2)	3.415(2)
*RE*2–I	3.3190(14)	3.282(1)	3.246(1)
Ge–S2	2.187(2)	2.191(2)	2.188(2)
Ge–S4	2.192(2)	2.191(2)	2.195(2)
Ge–S1	2.199(2)	2.200(2)	2.197(2)
Ge–S3	2.217(2)	2.218(2)	2.212(2)

length), which were evacuated to 10^{-3} mbar and sealed. To minimize volatilization losses of sulfur and iodine, and to avoid catastrophic failure of the tubes, the samples were heated slowly at 2 °C/min to 300 °C, held there for 2 d, heated at 2 °C/min to 900 °C, held there for 7 d, and then cooled to room temperature over 2 d. The targeted compounds formed as powders, with excess I_2 deposited at the other end of the tubes.

Products were analyzed by powder X-ray diffraction (XRD) performed on an Inel powder diffractometer equipped with a curved position-sensitive detector (CPS 120) and a Cu $K\alpha_1$ radiation source operated at 40 kV and 20 mA. The XRD patterns were analyzed with use of the TOPAS Academic software package [20]. The background was modeled by a six-term polynomial function and a Pawley fit was applied (Fig. 1).

Small irregularly shaped crystals (light yellow or nearly colourless $La_3Ge_2S_8I$, yellow $Ce_3Ge_2S_8I$, and green $Pr_3Ge_2S_8I$) were found within the products which were examined on a JEOL JSM-6010LA InTouch-Scope scanning electron microscope, operated with an accelerating voltage of 15 kV. Energy-dispersive X-ray (EDX) analyses performed with acquisition times of 120 s on several points of multiple crystals (insets of Fig. 1) gave compositions of 19–25% *RE*, 10–16% Ge, 50–58% S, and

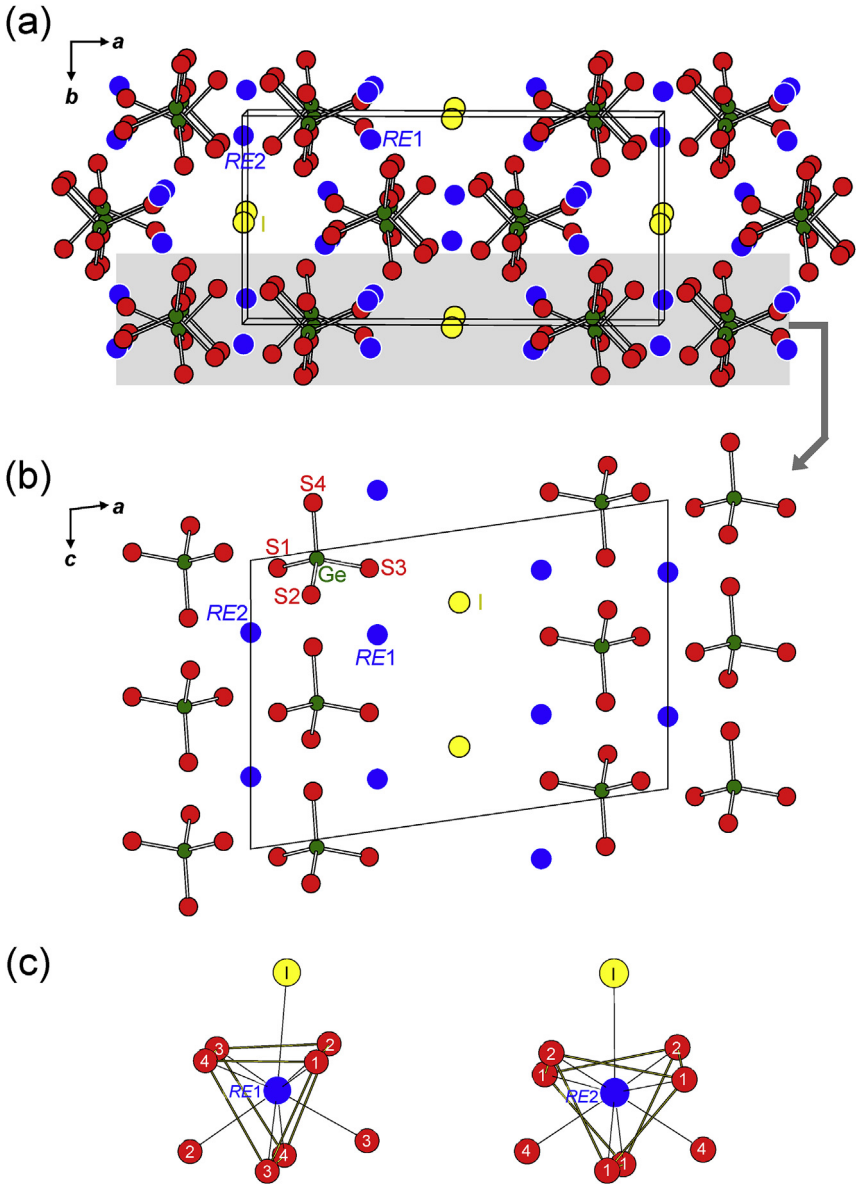

Fig. 2. Structure of $RE_3Ge_2S_8I$ (*RE* = La, Ce, Pr) (a) viewed down the *c*-direction revealing tunnels occupied by I atoms, (b) highlighting a slice parallel to the *ac*-plane containing isolated GeS_4 tetrahedra, and (c) showing the coordination environments around *RE* atoms.

Table 4
Bond valence sums in $RE_3Ge_2S_8I$.

	$La_3Ge_2S_8I$	$Ce_3Ge_2S_8I$	$Pr_3Ge_2S_8I$
*RE*1	2.97	2.99	2.94
*RE*2	2.74	2.75	2.73
Ge	4.24	4.22	4.25
S1	1.76	1.75	1.75
S2	2.07	2.07	2.07
S3	2.07	2.06	2.06
S4	2.27	2.29	2.26
I	0.81	0.84	0.82

8–13% I, in reasonable agreement with expectations (21% *RE*, 14% Ge, 57% S, 7% I). The high I content is attributed to surface deposition of some excess iodine which can be removed by washing the crystals with DMF.

Attempts were made to extend the *RE* substitution beyond Pr (e.g., *RE* = Nd, Sm, Eu, Gd, Tb, Dy, Ho, Er) and to prepare the analogous selenide series RE_3Ge_2SeI, using the same preparative conditions as indicated above, but these generally led to formation of ternary phases $RE_3Ge_{1+x}S_7$ or $RE_3Ge_{1+x}Se_7$. Attempts were also made to prepare the Cl or Br analogues through use of binary halide starting materials, but these were unsuccessful and led to complex multiphase mixtures.

2.2. Structure determination

Intensity data for $RE_3Ge_2S_8I$ (*RE* = La, Ce, Pr) were collected at room temperature on a Bruker PLATFORM diffractometer equipped with a SMART APEX II CCD area detector and a graphite-monochromated Mo *K*α radiation source, using ω scans at 7–8 different ϕ angles with a frame width of 0.3° and an exposure time of 10–12 s per frame. Face-indexed numerical absorption corrections were applied. Structure solution and refinement were carried out with use of the SHELXTL (version 6.12) program package [21]. The centrosymmetric monoclinic space group *C*2/*c* was chosen on the basis of Laue symmetry and intensity statistics. Initial positions of all atoms were easily found by direct methods, and structure refinement proceeded in a straightforward fashion. All sites were confirmed to be fully occupied when occupancies were refined. The displacement parameters for the I atom are slightly elevated compared to those of the other atoms, but this appears to be a recurring characteristic in related $RE_3Si_2S_6X$ structures associated with its location within a large tunnel and its relatively weak bonding to only three neighbouring *RE* atoms [11–17]. Atomic positions were standardized with the program STRUCTURE TIDY [22]. Table 1 lists crystal data, Table 2 lists atomic and displacement parameters, and Table 3 lists interatomic distances. CCDC 1890620–1890622 contain the supplementary crystallographic data for this paper. These data can be obtained free of charge from the Cambridge Crystallographic Data Centre via www.ccdc.cam.ac.uk/structures.

2.3. Electronic structure calculations

Tight-binding linear muffin-tin orbital (TB-LMTO) band structure calculations were performed on $La_3Ge_2S_8I$ within the local density and atomic-spheres approximation with the use of the Stuttgart TB-LMTO program [23]. The basis set consisted of La 6s/6p/5d/4f, Ge 4s/4p/4d, S 3s/3p/3d, and I 5s/5p/4d/4f orbitals, with the La 6p, Ge 4d, S 3d, and I 4d/4f orbitals being downfolded. Integrations in reciprocal space were carried out with an improved tetrahedron method over 78 irreducible *k* points within the first Brillouin zone. Crystal orbital Hamilton populations (COHP) were evaluated to analyze bonding interactions [24].

2.4. Diffuse reflectance spectroscopy

Optical diffuse reflectance spectra for all three compounds were measured from 200 nm (6.2 eV) to 2500 nm (0.50 eV) on a Cary 5000 UV–vis–NIR spectrophotometer equipped with a diffuse reflectance accessory, with a compacted pellet of $BaSO_4$ used as a 100% reflectance standard. These reflectance spectra were converted to optical absorption spectra using the Kubelka-Munk function, $F(R) = \alpha/S = (1-R)^2/2R$, where α is the Kubelka–Munk absorption coefficient, *S* is the scattering coefficient, and *R* is the reflectance [25].

2.5. Magnetic susceptibility measurements

Zero-field-cooled dc magnetic susceptibility measurements were made on $RE_3Ge_2S_8I$ (*RE* = Ce, Pr) between 2 and 300 K under an applied magnetic field of 0.5 T on a Quantum Design 9T–PPMS magnetometer. Susceptibility values were corrected for contributions from the holder and sample diamagnetism.

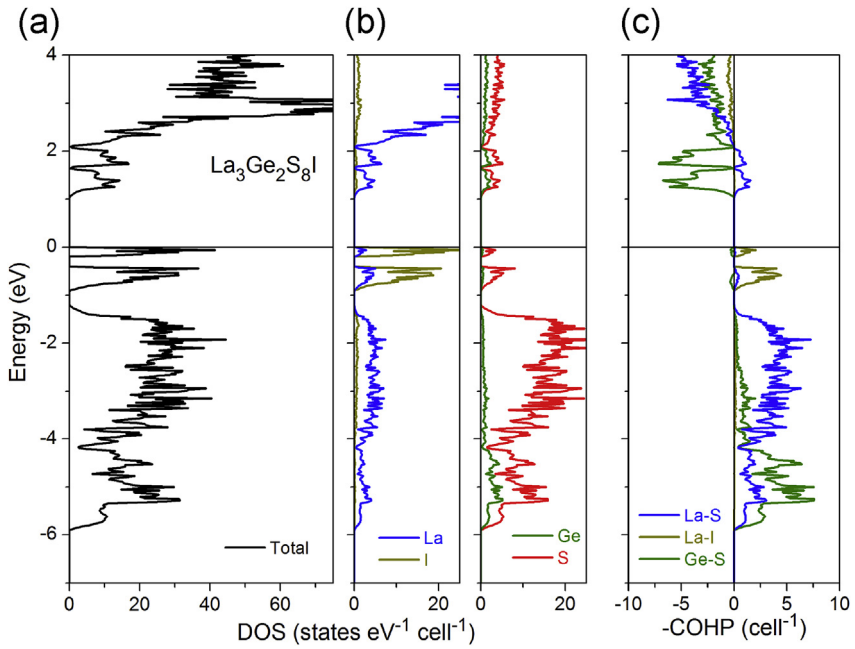

Fig. 3. (a) Density of states (DOS) (b) atomic projections, and (c) crystal orbital Hamilton population (–COHP) curves for $La_3Ge_2S_8I$.

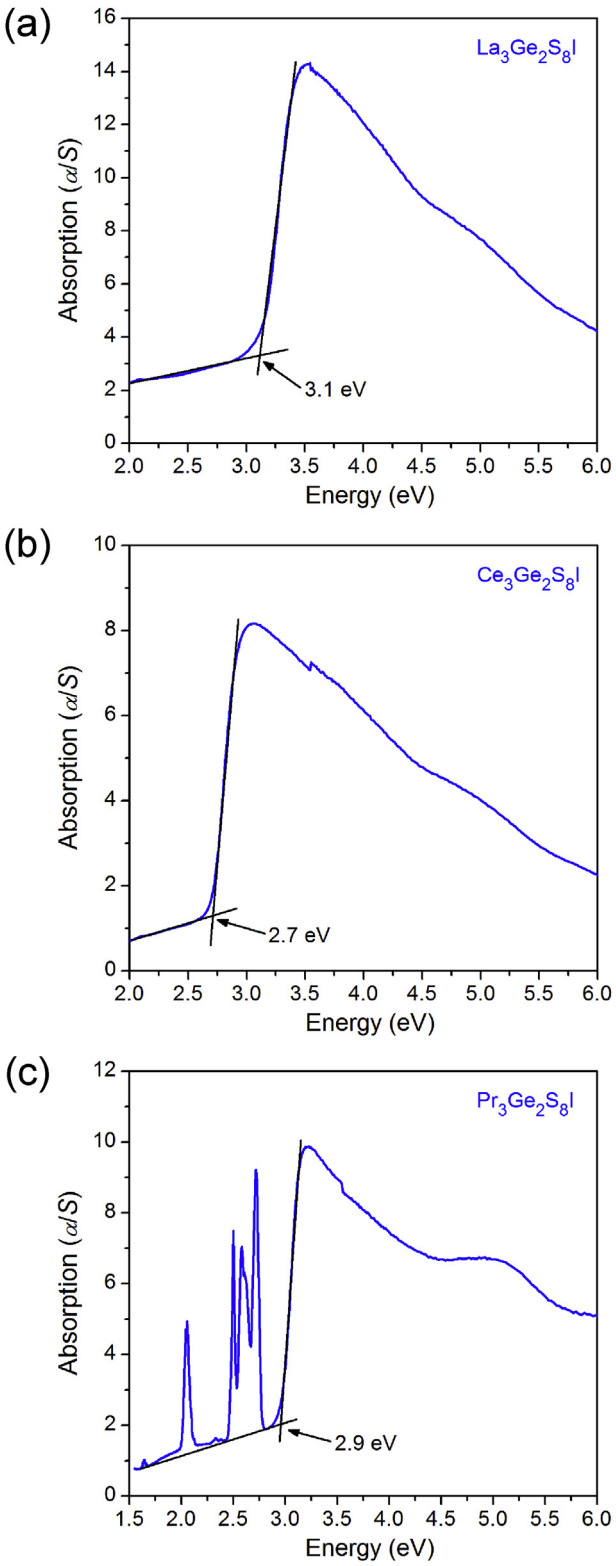

Fig. 4. Optical absorption spectra, converted from the diffuse reflectance spectra, for (a) $La_3Ge_2S_8I$, (b) $Ce_3Ge_2S_8I$, and (c) $Pr_3Ge_2S_8I$.

3. Results and discussion

The sulfide iodides $RE_3Ge_2S_8I$ were successfully prepared by reactions of the elements at 900 °C. They are the first quaternary phases found in the *RE*–Ge–S–I systems. As in the corresponding Si-containing compounds $RE_3Si_2S_8X$ (X = Cl, Br, I) [11–17], the range of *RE* substitution in

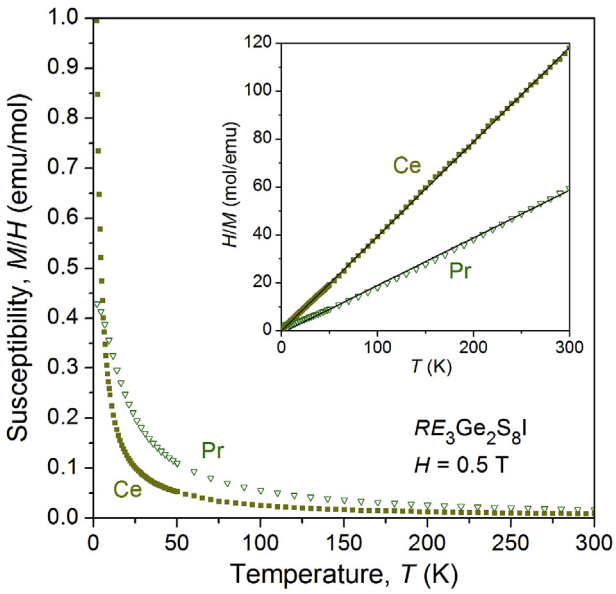

Fig. 5. Magnetic susceptibility and its inverse (inset) for $RE_3Ge_2S_8I$ (*RE* = Ce, Pr).

$RE_3Ge_2S_8I$ is limited to the lighter members (*RE* = La, Ce, Pr). The formula could also be written as $RE_3(GeS_4)_2I$ to emphasize the presence of thiogermanate groups, in analogy to the orthosilicate groups found in the $La_3(SiO_4)_2Cl$-type structure [26] to which these compounds are isostructural. The monoclinic structure (space group *C*2/*c*) consists of discrete anionic $[GeS_4]^{4-}$ tetrahedra arranged in stacks along the *c*-direction and separated by RE^{3+} cations; these stacks outline large tunnels occupied by I^- anions (Fig. 2a and b). The Ge-centred tetrahedra are quite regular with nearly equidistant Ge–S bonds (2.18–2.22 Å) that fall within the usual range (2.1–2.3 Å) found in other Ge-containing sulfides [27]. The two types of *RE* sites are each surrounded by one I and eight S atoms in roughly tricapped trigonal prismatic geometry, but the coordination environment around *RE*2 is quite irregular (Fig. 2c). These environments are asymmetric as a result of the presence of the two different kinds of ions, S^{2-} and I^-, around the RE^{3+} cations. The distances to the S atoms are shorter (La–S, 2.96–3.14 Å; Ce–S, 2.94–3.12 Å; Pr–S, 2.91–3.10 Å) than to the I atoms (La–I, 3.47 Å; Ce–I, 3.28 Å; Pr–I, 3.25 Å), and agree well with the sum of Shannon ionic radii (La^{3+}, 1.16 Å; Ce^{3+}, 1.14 Å; Pr^{3+}, 1.13 Å; S^{2-}, 1.84 Å; I^-, 2.20 Å) [28]. Bond valence sums (Table 4) [29] support the simple charge-balanced ionic formulation $(RE^{3+})_3(Ge^{4+})_2(S^{2-})_8(I^-)$.

Electronic structure calculations were performed on $La_3Ge_2S_8I$, whose closed-shell electron configurations for all atoms imply the presence of a band gap. The density of states (DOS) curve shows a gap between filled states below the Fermi level at 0 eV and empty states above 1.0 eV (Fig. 3a). The gap is a direct one at the Brillouin zone centre Γ, as revealed in a band dispersion diagram (not shown). The valence band results largely from mixing of S 3p with Ge 4p (from −6.0 to −1.2 eV) and I 5p states (from −0.9 to 0 eV), as indicated by the atomic projections of the DOS curve (Fig. 3b). The normal expectation is that the band gap is controlled by the strongest covalent interactions in the structure, namely that it would correspond to the separation of filled Ge–S bonding and empty Ge–S antibonding levels. As seen in the crystal orbital Hamilton population (–COHP) curves (Fig. 3c), this is indeed the case, but the band gap is considerably narrowed by the presence of the I-based states that lie higher in energy than the Ge-based states in the valence band. This feature was also observed in the electronic structure of $Ce_3Si_2S_8I$ [12]. Notwithstanding the ionic formulation indicated earlier, both La–S and La–I interactions bring important contributions to the covalent bonding stabilization of the structure. The integrated COHP values (–ICOHP) are 15.5 eV/cell for Ge–S, 14.0 eV/cell for La–S, and 1.5 eV/cell for La–I

interactions.

The optical band gaps are 3.1 eV for $La_3Ge_2S_8I$, 2.7 eV for $Ce_3Ge_2S_8I$, and 2.9 eV for $Pr_3Ge_2S_8I$, as extrapolated from the absorption edges of the UV–vis–NIR diffuse reflectance spectra, converted to absorption spectra (Fig. 4). For $La_3Ge_2S_8I$, the observed band gap is significantly larger than found in the electronic structure calculated from the LMTO method (with a discrepancy of similar magnitude as found for $Ce_3Si_2S_8I$ [12]), which tends to underestimate the gap, but it is consistent with the nearly colourless appearance of crystals of $La_3Ge_2S_8I$. For comparison, the experimental band gap of the Si-containing analogues are larger, 3.9 eV for $La_3Si_2S_8I$ and 2.9 eV for $Ce_3Si_2S_8I$ [13].

Magnetic susceptibility measurements made on $Ce_3Ge_2S_8I$ and $Pr_3Ge_2S_8I$, which contain *RE* components with unpaired f electrons, reveal simple paramagnetism with no obvious transitions down to 2 K (Fig. 5). The linear portions of the inverse magnetic susceptibility (over the entire temperature range for $Ce_3Ge_2S_8I$ and above ~20 K for $Pr_3Ge_2S_8I$) were fit to the Curie-Weiss law, $\chi = C/(T - \theta_p)$. The effective magnetic moments evaluated from the Curie constant, through $\mu_{eff} = (8C)^{1/2}$, were 4.51(1) μ_B/f.u. for $Ce_3Ge_2S_8I$ and 6.20(1) μ_B/f.u. for $Pr_3Ge_2S_8I$. If the *RE* atoms are assumed to be the only contribution to the effective magnetic moment, according to $\mu_{eff} = (3\mu_{RE}^2)^{1/2}$, the values of μ_{RE} are 2.60(1) μ_B/Ce for $Ce_3Ge_2S_8I$ and 3.63(1) μ_B/Pr for $Pr_3Ge_2S_8I$, in good agreement with the theoretical free-ion values of 2.54 μ_B for Ce^{3+} and 3.58 μ_B for Pr^{3+}. The paramagnetic Weiss constants are 0(1) K for $Ce_3Ge_2S_8I$ and 9(1) K for $Pr_3Ge_2S_8I$, implying little to no magnetic coupling of the *RE* atoms, which are quite far apart (4.5 Å) from each other. In comparison, $Ce_3Si_2S_8I$ also follows the Curie-Weiss law with $\mu_{eff} = 2.45(2)$ μ_B/Ce and $\theta_p = -4.7(3)$ K [12].

4. Conclusions

The Ge-substituted analogues of $RE_3Si_2S_8I$ (*RE* = La–Nd, Sm, Tb) have been successfully prepared, but the range of *RE* substitution is even more limited to just the largest components, $RE_3Ge_2S_8I$ (*RE* = La–Pr). The structures can be viewed as consisting of isolated $[GeS_4]^{4-}$ units in combination with monoatomic RE^{3+} and I^- ions. Preliminary experiments in which powders of these samples are exposed to a handheld UV light source showed no visibly detectable luminescence.

Acknowledgments

This work was supported by the Natural Sciences and Engineering Research Council of Canada (NSERC, through Discovery Grant RGPIN-2018-04294), the NSERC Collaborative Research and Training Experience Program (CREATE, through the Alberta/Technical University of Munich International Graduate School (ATUMS)), and the Canada First Research Excellence Fund (CFREF, through the Future Energy Systems Research Institute at the University of Alberta, Project T12-P01).

References

[1] H. Kageyama, K. Hayashi, K. Maeda, J.P. Attfield, Z. Hiroi, J.M. Rondinelli, K.R. Poeppelmeier, Expanding frontiers in materials chemistry and physics with multiple anions, Nat. Commun. 9 (2018), 772-1–772-15.
[2] N. Recham, J.-N. Chotard, L. Dupont, C. Delacourt, W. Walker, M. Armand, J.-M. Tarascon, A 3.6 V lithium-based fluorosulphate insertion positive electrode for lithium-ion batteries, Nat. Mater. 9 (2010) 68–74.
[3] K. Ueda, S. Inoue, S. Hirose, H. Kawazoe, H. Hosono, Transparent *p*-type semiconductor: LaCuOS layered oxysulfide, Appl. Phys. Lett. 77 (2000) 2701–2703.
[4] M. Jansen, H.P. Letschert, Inorganic yellow-red pigments without toxic metals, Nature 404 (2000) 980–982.
[5] Y. Kamihara, T. Watanabe, M. Hirano, H. Hosono, Iron-based layered superconductor $La[O_{1-x}F_x]FeAs$ ($x = 0.05$–0.12) with $T_c = 26$ K, J. Am. Chem. Soc. 130 (2008) 3296–3297.
[6] J.-R. Xiao, S.-H. Yang, F. Feng, H.-G. Xue, S.-P. Guo, A review of the structural chemistry and physical properties of metal chalcogenide halides, Coord. Chem. Rev. 347 (2017) 23–47.
[7] T. Nilges, S. Nilges, A. Pfitzner, T. Doert, P. Böttcher, Structure-property relations and diffusion pathways of the silver ion conductor Ag_5Te_2Cl, Chem. Mater. 16 (2004) 806–812.
[8] H. Shi, W. Ming, M.-H. Du, Bismuth chalcohalides and oxyhalides as optoelectronic materials, Phys. Rev. B 93 (2016), 104108-1–104108-7.
[9] Y.-Y. Li, P.-F. Liu, L. Hu, L. Chen, H. Lin, L.-J. Zhou, L.-M. Wu, Strong IR NLO material $Ba_4MGa_4Se_{10}Cl_2$: highly improved laser damage threshold via dual ion substitution synergy, Adv. Opt. Mater. 3 (2015) 957–966.
[10] S.L. Nguyen, C.D. Malliakas, J.A. Peters, Z. Liu, J. Im, L.-D. Zhao, M. Sebastian, H. Jin, H. Li, S. Johnsen, B.W. Wessels, A.J. Freeman, M.G. Kanatzidis, Photoconductivity in Tl_6SI_4: a novel semiconductor for hard radiation detection, Chem. Mater. 25 (2013) 2868–2877.
[11] G. Gauthier, S. Kawasaki, S. Jobic, P. Macaudière, R. Brec, J. Rouxel, Synthesis and structure of the first cerium iodothiosilicate: $Ce_3(SiS_4)_2I$, J. Alloys Compd. 275–277 (1998) 46–49.
[12] G. Gauthier, S. Kawasaki, S. Jobic, P. Macaudière, R. Brec, J. Rouxel, Characterization of $Ce_3(SiS_4)_2I$, a compound with a new structure type, J. Mater. Chem. 8 (1998) 179–186.
[13] R. Riccardi, D. Gout, G. Gauthier, F. Guillen, S. Jobic, A. Garcia, D. Huguenin, P. Macaudière, C. Fouassier, R. Brec, Structural investigation and luminescence properties of the $Ce_3(SiS_4)_2X$ (X = Cl, Br, I) family and the $La_{3-x}Ce_x(SiS_4)_2I$ ($0 \le x \le 1$) solid solution, J. Solid State Chem. 147 (1999) 259–268.
[14] S.T. Hatscher, W. Urland, Synthese und Kristallstrukturen von $Ln_3I(SiS_4)_2$ (Ln = Pr, Nd, Sm, Tb), Z. Anorg. Allg. Chem. 627 (2001) 2198–2200.
[15] S.T. Hatscher, W. Urland, Lanthanum iodide thiosilicate, $La_3I[SiS_4]_2$, Acta Crystallogr. Sect. E Struct. Rep. Online 58 (2002) i100–i102.
[16] S.T. Hatscher, W. Urland, Synthese und Kristallstrukturen von Bromid–Thiosilicaten $Ln_3Br[SiS_4]_2$ der Lanthanide (Ln = La, Ce, Pr, Nd, Sm, Gd), Z. Anorg. Allg. Chem. 628 (2002) 608–611.
[17] S.T. Hatscher, W. Urland, Synthesis and structures of chloride thiosilicates with lanthanides $Ln_3Cl[SiS_4]_2$ (Ln = La, Ce, Pr), Mater. Res. Bull. 37 (2002) 1239–1247.
[18] S.T. Hatscher, W. Urland, Samarium chloride sulfide thiosilicate, $Sm_3ClS_2[SiS_4]$, Acta Crystallogr. Sect. E Struct. Rep. Online 58 (2002) i124–i126.
[19] S.T. Hatscher, W. Urland, Synthesis, structure, and magnetic behavior of a new chloride thiosilicate with neodymium $Nd_3ClS_2[SiS_4]$, Mater. Res. Bull. 38 (2003) 99–112.
[20] A.A. Coelho, TOPAS-academic, Version 6, Coelho Software, Brisbane, Australia, 2007.
[21] G.M. Sheldrick, SHELXTL, Version 6.12, Bruker AXS Inc., Madison, WI, 2001.
[22] L.M. Gelato, E. Parthé, STRUCTURE TIDY – a computer program to standardize crystal structure data, J. Appl. Crystallogr. 20 (1987) 139–143.
[23] R. Tank, O. Jepsen, A. Burkhardt, O.K. Andersen, TB-LMTO-ASA Program, Version 4.7, Max Planck Institut für Festkörperforschung, Stuttgart, Germany, 1998.
[24] R. Dronskowski, P.E. Blöchl, Crystal orbital Hamilton populations (COHP). Energy-resolved visualization of chemical bonding in solids based on density-functional calculations, J. Phys. Chem. 97 (1993) 8617–8624.
[25] G. Kortüm, Reflectance Spectroscopy, Springer, New York, 1969.
[26] P. Gravereau, B. Es-Sakhi, C. Fouassier, $La_3(SiO_4)_2Cl$: a new structural type of rare-earth chloroorthosilicate, Acta Crystallogr. Sect. C Cryst. Struct. Commun. 44 (1988) 1884–1887.
[27] P. Villars, K. Cenzual, Pearson's Crystal Data – Crystal Structure Database for Inorganic Compounds (on DVD), Release 2016/17, ASM International, Materials Park, OH, USA.
[28] R.D. Shannon, Revised effective ionic radii and systematic studies of interatomic distances in halides and chalcogenides, Acta Crystallogr. Sect. A Cryst. Phys. Diffr. Theor. Gen. Crystallogr. 32 (1976) 751–767.
[29] N.E. Brese, M. O'Keeffe, Bond valence parameters for solids, Acta Crystallogr. Sect. B Struct. Sci. 47 (1991) 192–197.

4. Summary and Outlook

This work focusses on fabrication and characterization of new functional inorganic materials. In particular single-phased crystals or phosphorus-based compounds and TiO_2 nanotube hybrid materials, which exhibit great light harvesting application potential are investigated. Three single-phased quaternary sulfide iodides were found and analyzed for possible optoelectronic utilization. Hybrid materials, through heterojunction generation of TiO_2 nanotube arrays together with low-cost phosphorus allotropes and polyphosphides were manufactured and studied in regard to their photocatalytic activity.

TiO_2 nanotube arrays are commercially used in photovoltaics, photodetectors, sensors. Key drawbacks are addressed when shifting the absorption spectra more towards solar radiation and delaying charge carrier recombination. In this way its potential in visible-light-driven photocatalytic applications can be maximized in an easy approach *via* short way gas-phase transport reaction was accomplished. Successful decoration and infiltration of TiO_2 nanotubes with nanostructured phosphorus allotropes (fibrous red P, black P), binary and ternary polyphosphides (NaP_7, SnIP, $(CuI)_3P_{12}$) without material degradation was achieved. Elemental phosphorus deposition on the nanotube surface was accomplished with less effort than using binary and ternary compounds. The order of deposition is fibrous red P>black P>NaP_7>SnIP>$(CuI)_3P_{12}$. Photo-electrochemical investigation in water splitting experiments revealed overall enhanced photoconversion efficiencies of the hybrid materials compared to pristine TiO_2. Filling of phosphorus and polyphosphides into TiO_2 nanotubes was determined for NaP_7@TiO_2 all along the tubes. Moreover, NaP_7@TiO_2 showed 50% decoration of the array surfaces and full surface decoration was found for fibrous red P@TiO_2. However, the filling and decoration grade of the nanotube arrays are not directly correlated to their photocatalytic activities as they showed performance in the order of SnIP@TiO_2> $(CuI)_3P_{12}$@TiO_2> NaP_7@TiO_2> fibrous red P@TiO_2> black P@TiO_2. A crucial artificial Z-scheme junction formation was confirmed for all hybrid samples. Detailed energy level diagrams were constructed, illustrating efficient absorption of visible photons due to better charge carrier separation. Lowest double layer (Helmholtz) capacitance values were observed, resulting in a wider depletion layer at the SnIP-TiO_2 interface.

The hybrid materials are promising candidates as photocatalyst for future optoelectronic applications. An additional improvement in the field of water splitting can be realized by optimizing the semiconductor-electrolyte interface to an islands-like heterostructure, covering the TiO_2 surface only partially. As previously reported by Godart *et al.*,

metallic islands photoelectrochemically deposited onto *p*-InSe in sizes ≤0.5 µm lead to an increase of photogenerated hydrogen.[94] Applying a solvothermal synthesis route, by generating the respective nanofibers and -layers under reduced temperature and pressure on ultrasonicated TiO_2 nanotubes in a suitable solvent should be studied to further enhance the hybrid materials' photocatalytic performance. Thus, a selective growth on the nanotube surface forming a heterojunction at the interfaces could be achieved.

Chalcogenide halides were first classified with the aid of mathematical models in terms of their estimated optical properties. Therefore, data collection and building of in-house selection routines served as systematical approach. Three new rare-earth chalcogenidehalide $RE_3Ge_2S_8I$ (*RE* = La, Ce, Pr) were successfully prepared and investigated in terms of structure, optical band gap and magnetic properties. The quaternary mixed-anion compounds crystalize in the $La_3(SiO_4)_2Cl$ structure type, in space group *C*2/c. An experimental optical band gap of $La_3Ge_2S_8I$ was determined to be 3.1 eV (400 nm). Measurements on magnetic susceptibility for paramagnetic $Ce_3Ge_2S_8I$ and $Pr_3Ge_2S_8I$ demonstrated Curie-Weiss behavior.

Future substitution experiments of iodine by chlorine and bromine could broaden the gap between 4f and 5d energy levels (Cl < Br < I) and may therefore play a role to improve these compounds as photovoltaic material. On the basis of estimated room-temperature luminescence, further research should be conducted to clarify whether they can be used in lighting and display applications, amplifiers, optical fibers or in electroluminescent devices.

5. Scientific Contributions

5.1. Referred Articles

1. E. Üzer, P. Kumar, R. Kisslinger, P. Kar, K. Shankar, T. Nilges; Vapor growth of binary and ternary phosphorus-based semiconductors into TiO_2 nanotube arrays and application in visible light driven water splitting, Nanoscale Advances (2019).

2. E. Üzer, P. Kumar, R. Kisslinger, P. Kar, K. Shankar, T. Nilges; Vapor growth of semiconducting P allotropes into TiO_2 nanotube arrays for photo-electrocatalytic water splitting applications; ACS Applied Nanomaterials (2019).

3. D. Mumbaraddi, A. K. Iyer, E. Üzer, V. Mishra, A. O. Oliynyk, T. Nilges, A. Mar; Synthesis, structure, and properties of rare-earth germanium sulfide iodides $RE_3Ge_2S_8I$ (*RE* = La, Ce, Pr); Journal of Solid-State Chemistry (2019).

5.2. Congress and Meeting Participations

1. D. Purschke, E. Üzer, C. Ott, M. Pielmeier, N. Amer, T. Nilges, F. Hegmann, Photoconductivity of SnIP Semiconducting Inorganic Double Helices, 8th International Conference on Optical Terahertz Science and Technology, *Santa Fe*, *USA* (March 2019).

2. J. Mock, A. Lyuleeva, E. Üzer, T. Nilges, M. Becherer, Semiconducting SnIP in Field-effect transistors, 4th ATUMS - International Graduate School of Science and Engineering Conference, *Garching*, *Germany* (November 2018).

3. E. Üzer, P. Kumar, R. Kisslinger, P. Kar, K. Shankar, T. Nilges; Vapor growth of semiconducting P allotropes into TiO_2 nanotube arrays for photo-electrocatalytic water splitting applications, 101st Canadian Chemistry Conference, *Edmonton*, *Canada* (May 2018).

4. D. Mumbaraddi, A. K. Iyer, E. Üzer, V. Mishra, A. O. Oliynyk, T. Nilges, A. Mar; Synthesis, structure, and properties of rare-earth germanium sulfide iodides $RE_3Ge_2S_8I$ (*RE* = La, Ce, Pr), 101st Canadian Chemistry Conference, *Edmonton*, *Canada* (May 2018).

Appendix

List of Figures

List of Tables

References

1. Bundesregierung, P.-u. I. d. https://www.bundesregierung.de/breg-de/suche/bundesregierung-beschliesst-ausstieg-aus-der-kernkraft-bis-2022-457246. (accessed 14 February 2019).
2. Bundesregierung, P.-u. I. d. https://www.bundesregierung.de/breg-de/suche/der-einstieg-in-den-kohleausstieg-1574264. (accessed 14 February 2019).
3. Handelsblatt https://www.handelsblatt.com/finanzen/anlagestrategie/zertifikate/nachrichten/anlagestrategie-rwe-und-die-angst-vor-der-energiewende/4689266-3.html.
4. Journalism, E. D. https://www.europeandatajournalism.eu/ger/Nachrichten/Daten-Nachrichten/Naechster-EU-Haushalt-zieht-Sicherheit-und-Forschung-der-Landwirtschaft-vor. (accessed 14 February 2019).
5. Worldbank http://wdi.worldbank.org/table/3.7. (accessed 14 February 2019).
6. Wirth, H.; Schneider, K., Aktuelle Fakten zur Photovoltaik in Deutschland. *Fraunhofer ISE* **2015**.
7. ISE, F.-I. f. S. E. https://www.energy-charts.de. (accessed 14 February 2019).
8. Henning, H.-M.; Palzer, A., 100% erneuerbare Energien für Strom und Wärme in Deutschland. *Freiburg (Germany) Fraunhofer-Institut für Solare Energiesysteme ISE* **2012**.
9. Unter Berücksichtigung, E. i. S., EE-STROM, WÄRME UND VERKEHR. **2015**.
10. Green, M. A.; Hishikawa, Y.; Dunlop, E. D.; Levi, D. H.; Hohl-Ebinger, J.; Yoshita, M.; Ho-Baillie, A. W. Y., Solar cell efficiency tables (Version 53). *Progress in Photovoltaics: Research and Applications* **2019,** *27* (1), 3-12.
11. Nazeeruddin, M. K.; Baranoff, E.; Graetzel, M., Dye-sensitized solar cells: A brief overview. *Sol. Energy* **2011,** *85* (6), 1172-1178.
12. Lewis, N. S., Toward cost-effective solar energy use. *Science* **2007,** *315* (5813), 798-801.
13. Shankar, K.; Basham, J. I.; Allam, N. K.; Varghese, O. K.; Mor, G. K.; Feng, X.; Paulose, M.; Seabold, J. A.; Choi, K.-S.; Grimes, C. A., Recent Advances in the Use of TiO_2 Nanotube and Nanowire Arrays for Oxidative Photoelectrochemistry. *The Journal of Physical Chemistry C* **2009,** *113* (16), 6327-6359.
14. Kuang, Y.; Di Vece, M.; Rath, J. K.; van Dijk, L.; Schropp, R. E., Elongated nanostructures for radial junction solar cells. *Reports on Progress in Physics* **2013,** *76* (10), 106502.
15. Fujishima, A.; Honda, K., Electrochemical photolysis of water at a semiconductor electrode. *Nature* **1972,** *238* (5358), 37.
16. Schock, H.; Meissner, D., Solarzellen-Physikalische Grundlagen und Anwendungen in der Photovoltaik. *Vieweg & Sohn: Wiesbaden* **1993**.
17. Van de Krol, R., Principles of photoelectrochemical cells. In *Photoelectrochemical hydrogen production*, Springer: 2012; pp 13-67.
18. Michaelis, W.; Pilkuhn, M., Radiative recombination in silicon p-n junctions. *Physica Status Solidi (b)* **1969,** *36* (1), 311-319.
19. Herrmann, J.; Disdier, J.; Mozzanega, M.-N.; Pichat, P., Heterogeneous photocatalysis: in situ photoconductivity study of TiO_2 during oxidation of isobutane into acetone. *Journal of Catalysis* **1979,** *60* (3), 369-377.
20. Frederikse, H., Recent studies on rutile (TiO_2). *Journal of Applied Physics* **1961,** *32* (10), 2211-2215.
21. Beranek, R.; Tsuchiya, H.; Sugishima, T.; Macak, J.; Taveira, L.; Fujimoto, S.; Kisch, H.; Schmuki, P., Enhancement and limits of the photoelectrochemical response from anodic Ti O 2 nanotubes. *Applied Physics Letters* **2005,** *87* (24), 243114.
22. Navarro Yerga, R. M.; Alvarez Galvan, M. C.; Del Valle, F.; Villoria de la Mano, J. A.; Fierro, J. L., Water splitting on semiconductor catalysts under visible-light irradiation. *ChemSusChem: Chemistry & Sustainability Energy & Materials* **2009,** *2* (6), 471-485.
23. Mohammadpour, A.; Kar, P.; D Wiltshire, B.; M Askar, A.; Shankar, K., Electron transport, trapping and recombination in anodic TiO_2 nanotube arrays. *Current Nanoscience* **2015,** *11* (5), 593-614.
24. Meissner, D.; Reineke, R., Photoelektrochemische Solarenergienutzung. *Nachrichten aus Chemie, Technik und Laboratorium* **1990,** *38* (12), 1490-1498.
25. Meissner, D., Photoelektrochemische Solarzellen. In *Solarzellen*, Springer: 1993; pp 137-150.

26. Roy, P.; Berger, S.; Schmuki, P., TiO_2 nanotubes: synthesis and applications. *Angewandte Chemie International Edition* **2011,** *50* (13), 2904-2939.
27. Moniz, S. J.; Shevlin, S. A.; Martin, D. J.; Guo, Z.-X.; Tang, J., Visible-light driven heterojunction photocatalysts for water splitting–a critical review. *Energy & Environmental Science* **2015,** *8* (3), 731-759.
28. Su, J.; Guo, L.; Bao, N.; Grimes, C. A., Nanostructured WO3/BiVO4 heterojunction films for efficient photoelectrochemical water splitting. *Nano letters* **2011,** *11* (5), 1928-1933.
29. Fukuda, M., *Optical semiconductor devices*. John Wiley & Sons: 1999; Vol. 46.
30. Kittel, C., Einführung in die Festkörperphysik (German Edition). Oldenbourg Wissenschaftsverlag: 2017, 561-613.
31. Li, L.; Salvador, P. A.; Rohrer, G. S., Photocatalysts with internal electric fields. *Nanoscale* **2014,** *6* (1), 24-42.
32. Huheey, J. E.; Keiter, E. A.; Keiter, R. L.; Medhi, O. K., *Inorganic chemistry: principles of structure and reactivity*. Pearson Education India: 2006, 11-50.
33. Laube, P. https://www.halbleiter.org/en/fundamentals/conductors-insulators-semiconductors/. (accessed 02 April 2019).
34. Vollath, D., *Nanoparticles-Nanocomposites–Nanomaterials: An Introduction for Beginners*. John Wiley & Sons: 2013, 167-203.
35. Smith, A. M.; Nie, S., Semiconductor nanocrystals: structure, properties, and band gap engineering. *Accounts of chemical research* **2009,** *43* (2), 190-200.
36. Kittel, C.; Krömer, H., *Thermodynamik*. Oldenbourg Verlag: 2013, 21-56.
37. Cahay, M. In *Quantum confinement VI: Nanostructured materials and devices: Proceedings of the International Symposium*, The Electrochemical Society: 2001.
38. Wulf, U. https://www.physik.tu-cottbus.de/users/wulf/Vorlesungen/lehre.html. (accessed 03 April 2019).
39. Paiella, R., Quantum cascade lasers. **2011**.
40. Pfister, D. Reaktivität von Phosphor mit Hauptgruppenmetallhalogeniden. Ph.D. Thesis, Technische Universität München, 2017, 91-139.
41. Shatruk, M. M.; Kovnir, K. A.; Shevelkov, A. V.; Presniakov, I. A.; Popovkin, B. A., First tin pnictide halides $Sn_{24}P_{19.3}I_8$ and $Sn_{24}As_{19.3}I_8$: synthesis and the clathrate-I type of the crystal structure. *Inorganic chemistry* **1999,** *38* (15), 3455-3457.
42. Pfister, D.; Schäfer, K.; Ott, C.; Gerke, B.; Pöttgen, R.; Janka, O.; Baumgartner, M.; Efimova, A.; Hohmann, A.; Schmidt, P.; Venkatachalam, S.; van Wüllen, L.; Schuermann, U.; Kienle, L.; Duppel, V.; Parzinger, E.; Miller, B.; Becker, J.; Holleitner, A.; Weihrich, R.; Nilges, T., Inorganic Double Helices in Semiconducting SnIP. *Adv. Mater. (Weinheim, Ger.)* **2016,** *28* (44), 9783-9791.
43. Baumgartner, M. P. Über die Eigenschaften niedrigdimensionaler Polyphosphide. Ph.D. Thesis, Technische Universität München, 2017, 73-80.
44. Möller, M.; Jeitschko, W., Preparation, properties, and crystal structure of the solid electrolytes $Cu_2P_3I_2$ and $Ag_2P_3I_2$. *Journal of Solid State Chemistry* **1986,** *65* (2), 178-189.
45. Pfitzner, A.; Freudenthaler, E., $(CuI)_3P_{12}$: ein Festkörper mit einer neuartigen, theoretisch vorhergesagten Form des Phosphors. *Angewandte Chemie* **1995,** *107* (15), 1784-1786.
46. Pfitzner, A.; Freudenthaler, E., $(CuI)_2P_{14}$: ein neues Phosphorpolymer in einer Kupferhalogenid-Matrix/$(CuI)_2P_{14}$: a Novel Phosphorus Polymer in a Copper Halide Matrix. *Zeitschrift für Naturforschung B* **1997,** *52* (2), 199-202.
47. Ruck, M.; Hoppe, D.; Wahl, B.; Simon, P.; Wang, Y.; Seifert, G., Faserförmiger roter phosphor. *Angewandte Chemie* **2005,** *117* (46), 7788-7792.
48. Baudler, M., Ketten-und ringförmige Phosphorverbindungen–Analogien zwischen Phosphor-und Kohlenstoffchemie. *Angewandte Chemie* **1982,** *94* (7), 520-539.
49. Baudler, M., Polyphosphorverbindungen–neue Ergebnisse und Perspektiven. *Angewandte Chemie* **1987,** *99* (5), 429-451.
50. Baudler, M.; Glinka, K., Contributions to the chemistry of phosphorus. 218. Monocyclic and polycyclic phosphines. *Chemical reviews* **1993,** *93* (4), 1623-1667.
51. Pfitzner, A.; Bräu, M. F.; Zweck, J.; Brunklaus, G.; Eckert, H., Phosphorus Nanorods—Two Allotropic Modifications of a Long-Known Element. *Angewandte Chemie International Edition* **2004,** *43* (32), 4228-4231.

52. Grotz, C.; Köpf, M.; Baumgartner, M.; Jantke, L. A.; Raudaschl-Sieber, G.; Fässler, T. F.; Nilges, T., Synthesis, Structure, and Properties of NaP_7, a Phosphorus-rich Polyphosphide. *Zeitschrift für anorganische und allgemeine Chemie* **2015,** *641* (8-9), 1395-1399.
53. Schmidt, P.; Binnewies, M.; Glaum, R.; Schmidt, M., Chemical Vapor Transport Reactions–Methods, Materials, Modeling. In *Advanced Topics on Crystal Growth*, IntechOpen: 2013.
54. Binnewies, M.; Glaum, R.; Schmidt, M.; Schmidt, P., *Chemical vapor transport reactions*. Walter de Gruyter: 2012, 117-159.
55. Tschulik, K.; Ruck, M.; Binnewies, M.; Milke, E.; Hoffmann, S.; Schnelle, W.; Fokwa, B. P.; Gilleßen, M.; Schmidt, P., Chemistry and Physical Properties of the Phosphide Telluride Zr_2PTe_2. *European journal of inorganic chemistry* **2009,** *2009* (21), 3102-3110.
56. Ansari, S. A.; Khan, Z.; Ansari, M. O.; Cho, M. H., Earth-abundant stable elemental semiconductor red phosphorus-based hybrids for environmental remediation and energy storage applications. *RSC Advances* **2016,** *6* (50), 44616-44629.
57. Hu, Z.; Yuan, L.; Liu, Z.; Shen, Z.; Yu, J. C., An elemental phosphorus photocatalyst with a record high hydrogen evolution efficiency. *Angewandte Chemie International Edition* **2016,** *55* (33), 9580-9585.
58. Brown, A.; Rundqvist, S., Refinement of the crystal structure of black phosphorus. *Acta Crystallographica* **1965,** *19* (4), 684-685.
59. Li, L.; Yu, Y.; Ye, G. J.; Ge, Q.; Ou, X.; Wu, H.; Feng, D.; Chen, X. H.; Zhang, Y., Black phosphorus field-effect transistors. *Nature nanotechnology* **2014,** *9* (5), 372.
60. Viti, L.; Hu, J.; Coquillat, D.; Knap, W.; Tredicucci, A.; Politano, A.; Vitiello, M. S., Black-phosphorus Terahertz photodetectors. *arXiv preprint arXiv:1805.00735* **2018**.
61. Yuan, H.; Liu, X.; Afshinmanesh, F.; Li, W.; Xu, G.; Sun, J.; Lian, B.; Curto, A. G.; Ye, G.; Hikita, Y., Polarization-sensitive broadband photodetector using a black phosphorus vertical p–n junction. *Nature nanotechnology* **2015,** *10* (8), 707.
62. Liu, B.; Köpf, M.; Abbas, A. N.; Wang, X.; Guo, Q.; Jia, Y.; Xia, F.; Weihrich, R.; Bachhuber, F.; Pielnhofer, F., Black arsenic–phosphorus: layered anisotropic infrared semiconductors with highly tunable compositions and properties. *Advanced Materials* **2015,** *27* (30), 4423-4429.
63. Keyes, R. W., The electrical properties of black phosphorus. *Physical Review* **1953,** *92* (3), 580.
64. Guo, H.; Lu, N.; Dai, J.; Wu, X.; Zeng, X. C., Phosphorene nanoribbons, phosphorus nanotubes, and van der Waals multilayers. *The Journal of Physical Chemistry C* **2014,** *118* (25), 14051-14059.
65. Morita, A., Semiconducting black phosphorus. *Applied Physics A* **1986,** *39* (4), 227-242.
66. Yan, J.; Ji, Y.; Kong, L.; Li, Y.; Navlani-García, M.; Liu, S.; Kuwahara, Y.; Mori, K.; Che, M.; Yamashita, H., Black Phosphorus-Based Compound with Few Layers for Photocatalytic Water Oxidation. *ChemCatChem* **2018,** *10* (16), 3424-3428.
67. Wood, J. D.; Wells, S. A.; Jariwala, D.; Chen, K.-S.; Cho, E.; Sangwan, V. K.; Liu, X.; Lauhon, L. J.; Marks, T. J.; Hersam, M. C., Effective passivation of exfoliated black phosphorus transistors against ambient degradation. *Nano letters* **2014,** *14* (12), 6964-6970.
68. Na, J.; Lee, Y. T.; Lim, J. A.; Hwang, D. K.; Kim, G.-T.; Choi, W. K.; Song, Y.-W., Few-layer black phosphorus field-effect transistors with reduced current fluctuation. *ACS nano* **2014,** *8* (11), 11753-11762.
69. Bahat-Treidel, E.; Hilt, O.; Zhytnytska, R.; Wentzel, A.; Meliani, C.; Wurfl, J.; Trankle, G., Fast-switching GaN-based lateral power Schottky barrier diodes with low onset voltage and strong reverse blocking. *IEEE Electron Device Letters* **2012,** *33* (3), 357-359.
70. Nakato, Y.; Ueda, K.; Yano, H.; Tsubomura, H., Effect of microscopic discontinuity of metal overlayers on the photovoltages in metal-coated semiconductor-liquid junction photoelectrochemical cells for efficient solar energy conversion. *The Journal of Physical Chemistry* **1988,** *92* (8), 2316-2324.
71. Köpf, M.; Eckstein, N.; Pfister, D.; Grotz, C.; Krüger, I.; Greiwe, M.; Hansen, T.; Kohlmann, H.; Nilges, T., Access and in situ growth of phosphorene-precursor black phosphorus. *Journal of crystal growth* **2014,** *405*, 6-10.
72. Wibowo, A. C.; Malliakas, C. D.; Liu, Z.; Peters, J. A.; Sebastian, M.; Chung, D. Y.; Wessels, B. W.; Kanatzidis, M. G., Photoconductivity in the chalcohalide semiconductor, SbSeI: a new candidate for hard radiation detection. *Inorganic chemistry* **2013,** *52* (12), 7045-7050.

73. Aliev, Z.; Musaeva, S.; Babanly, D.; Shevelkov, A.; Babanly, M., Phase diagram of the Sb–Se–I system and thermodynamic properties of SbSeI. *Journal of Alloys and Compounds* **2010,** *505* (2), 450-455.
74. Alward, J.; Fong, C.; El-Batanouny, M.; Wooten, F., Electronic and optical properties of SbSBr, SbSI and SbSeI. *Solid State Communications* **1978,** *25* (5), 307-310.
75. Arivuoli, D.; Gnanam, F.; Ramasamy, P., Microindentation studies of chalcohalides of antimony and bismuth. *Journal of Physics D: Applied Physics* **1988,** *21* (6), 1019.
76. Oppermann, H.; Petasch, U., Zu den pseudobinären Zustandssystemen Bi2Ch3-BiX3 und den ternären Phasen auf diesen Schnitten (Ch= S, Se, Te; X= Cl, Br, I), I: Bismutsulfidhalogenide/The Pseudobinary Systems Bi_2Ch_3-BiX_3 and the Ternary Phases on their Boundary Lines (Ch= S, Se, Te; X= Cl, Br, I), I: Bismuth Sulfide Halides. *Zeitschrift für Naturforschung B* **2003,** *58* (8), 725-740.
77. Jin, M.-S.; Park, K.-H.; Kim, H.-G.; Choe, S.-H.; Park, B.-S.; Hyun, S.-C.; Kim, W.-T., Optical properties of undoped and Co-doped SbSBr and BiSBr single crystals. *Semiconductor science and technology* **1995,** *10* (8), 1167.
78. Nilges, S. Untersuchungen zur Stabilisierung von neutralen Phosphorchalkogenid-Molekülen durch Kupfer (I)-halogenide. Ph.D. Thesis, Universität Regensburg, 2006.
79. Dectris. https://www.dectris.com/mythen_overview.html, (accessed 08 April 2013).
80. WinXPOW, S., Stoe & Cie GmbH. Darmstadt: 2011.
81. Villars, P.; Cenzual, K., *Pearson's crystal data®: crystal structure database for inorganic compounds*. ASM International Materials Park, Ohio, USA: 2007.
82. Gelato, L.; Parthé, E., STRUCTURE TIDY–a computer program to standardize crystal structure data. *Journal of Applied Crystallography* **1987,** *20* (2), 139-143.
83. Sheldrick, G., SHELXTL/PC Version 6.12 for Windows XP. *Bruker AXS Inc., Madison, Wisconsin, USA* **2001**.
84. Brandenburg, K.; Putz, H., DIAMOND–crystal and molecular structure visualization. *Crystal Impact GbR, Bonn* **2012**.
85. Kortüm, G., *Reflectance spectroscopy: principles, methods, applications*. Springer Science & Business Media: 2012.
86. Tauc, J.; Grigorovici, R.; Vancu, A., Optical properties and electronic structure of amorphous germanium. *physica status solidi (b)* **1966,** *15* (2), 627-637.
87. Tauc, J., Optical properties of amorphous semiconductors. In *Amorphous and Liquid Semiconductors*, Springer: 1974; pp 159-220.
88. Thakur, U.; Kisslinger, R.; Shankar, K., One-dimensional electron transport layers for perovskite solar cells. *Nanomaterials* **2017,** *7* (5), 95.
89. Mor, G. K.; Shankar, K.; Paulose, M.; Varghese, O. K.; Grimes, C. A., Use of highly-ordered TiO_2 nanotube arrays in dye-sensitized solar cells. *Nano letters* **2006,** *6* (2), 215-218.
90. Mor, G. K.; Varghese, O. K.; Paulose, M.; Shankar, K.; Grimes, C. A., A review on highly ordered, vertically oriented TiO_2 nanotube arrays: Fabrication, material properties, and solar energy applications. *Solar Energy Materials and Solar Cells* **2006,** *90* (14), 2011-2075.
91. Ravi, P.; Rao, V. N.; Shankar, M.; Sathish, M., CuOCr2O3 core-shell structured co-catalysts on TiO_2 for efficient photocatalytic water splitting using direct solar light. *International Journal of Hydrogen Energy* **2018,** *43* (8), 3976-3987.
92. Gauthier, G.; Kawasaki, S.; Jobic, S.; Macaudière, P.; Brec, R.; Rouxel, J., Characterization of Ce 3 (SiS 4) 2 I, a compound with a new structure type. *Journal of Materials Chemistry* **1998,** *8* (1), 179-186.
93. Riccardi, R.; Gout, D.; Gauthier, G.; Guillen, F.; Jobic, S.; Garcia, A.; Huguenin, D.; Macaudière, P.; Fouassier, C.; Brec, R., Structural Investigation and Luminescence Properties of the Ce3 $(SiS_4)_2X$ (X= Cl, Br, I) Family and the $La_{3-x}Ce_x(SiS_4)_2I$ (0≤ x≤ 1) Solid Solution. *Journal of Solid State Chemistry* **1999,** *147* (1), 259-268.
94. Sedaries, D.; Levy-Clement, C.; Godart, C., Photoelectrodeposition of Noble Metal Islands onto p-InSe Characterization and SEXAFS Study. *Journal of The Electrochemical Society* **1990,** *137* (6), 1733-1739.